Primary brain cells in in vitro controlled microenvironments : single cell behaviors for collective functions

Caterina Tomba

UNIVERSITÉ DE GRENOBLE

THÈSE

Pour obtenir le grade de

DOCTEUR DE L'UNIVERSITÉ DE GRENOBLE

Spécialité : **Physique pour les sciences du vivant**

Arrêté ministériel : 7 août 2006

Présentée par

Caterina TOMBA

Thèse dirigée par **Catherine VILLARD**
et codirigée par **Alice NICOLAS**

préparée au sein du l' **Institut Néel** et du **Laboratoire des Technologies de la Microélectronique**
dans l'**Ecole Doctorale de Physique de Grenoble**

Primary brain cells in *in vitro* controlled microenvironments

single cell behaviors for collective functions

Thèse soutenue publiquement le **05/12/2014**,
devant le jury composé de :

Christine METIN
Institut du Fer à Moulin, Rapporteur
Vincent STUDER
Institut interdisciplinaire de Neurosciences, Rapporteur
Yves COUDER
Laboratoire Matière et Systèmes Complexes, Examinateur
Frédéric SAUDOU
Grenoble Institut des Neurosciences, Examinateur
Catherine VILLARD
Institut Néel, Directeur de thèse
Alice NICOLAS
Laboratoire des Technologies de la Microélectronique, Co-Directeur de thèse

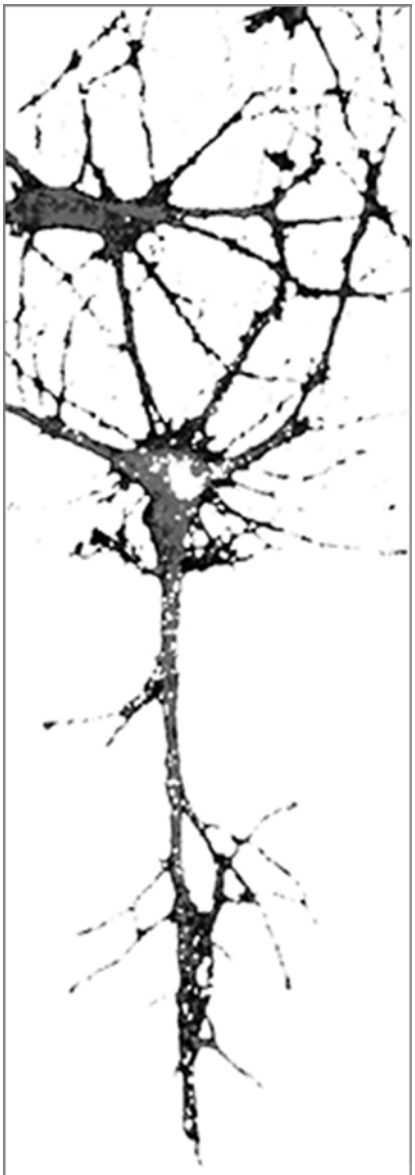

Rien n'est figé

Cellules primaires du cerveau en microenvironnements contrôlés *in vitro*

Résumé : Du fait de sa complexité, le fonctionnement du cerveau est exploré par des méthodes très diverses, telles que la neurophysiologie et les neurosciences cognitives, et à des échelles variées, allant de l'observation de l'organe dans son ensemble jusqu'aux molécules impliquées dans les processus biologiques. Ici, nous proposons une étude à l'échelle cellulaire qui s'intéresse à deux briques élémentaires du cerveau : les neurones et les cellules gliales. L'approche choisie est la biophysique, de part les outils utilisés et les questions abordées sous l'angle de la physique.

L'originalité de ce travail est d'utiliser des cellules primaires du cerveau dans un souci de proximité avec l'*in vivo*, au sein de systèmes *in vitro* dont la structure chimique et physique est contrôlée à l'échelle micrométrique. Utilisant les outils de la microélectronique pour un contrôle robuste des paramètres physico-chimiques de l'environnement cellulaire, ce travail s'intéresse à deux aspects de la biologie du cerveau : la polarisation neuronale, et la sensibilité des cellules gliales aux propriétés mécaniques de leur environnement. A noter que ces deux questions sont étroitement imbriquées lors de la réparation d'une lésion. La première est cruciale pour la directionalité de la transmission de signaux électriques et chimiques et se traduit par une rupture de symétrie dans la morphologie du neurone. La seconde intervient dans les mécanismes de recolonisation des lésions, dont les propriétés mécaniques sont altérées. Les études quantitatives menées au cours de cette thèse portent essentiellement sur la phénoménologie de la croissance de ces deux types de cellules et leur réponse à des contraintes géométriques ou mécaniques. L'objectif *in fine* est d'élucider quelques mécanismes moléculaires associés aux modifications de la structure cellulaire et donc du cytosquelette.

Un des résultats significatifs de ce travail est le contrôle de la polarisation neuronale par le simple contrôle de la morphologie cellulaire. Ce résultat ouvre la possibilité de développer des architectures neuronales contrôlées *in vitro* à l'échelle de la cellule individuelle.

Mots clés : Cellules primaires du cerveau, neurones d'hippocampe, polarisation neuronale, cellules gliales du cortex cérébral, motifs d'adhésion et de rigidité, mécanique cellulaire, mécanosensibilité, cytosquelette, biophysique

Primary brain cells in *in vitro* controlled microenvironments

Abstract: The complex structure of the brain is explored by various methods, such as neurophysiology and cognitive neuroscience. This exploration occurs at different scales, from the observation of this organ as a whole entity to molecules involved in biological processes. Here, we propose a study at the cellular scale that focuses on two building elements of brain: neurons and glial cells. Our approach reaches biophysics field for two main reasons: tools that are used and the physical approach to the issues.

The originality of our work is to keep close to the *in vivo* by using primary brain cells in *in vitro* systems, where chemical and physical environments are controlled at micrometric scale. Microelectronic tools are employed to provide a reliable control of the physical and chemical cellular environment. This work focuses on two aspects of brain cell biology: neuronal polarization and glial cell sensitivity to mechanical properties of their environment. As an example, these two issues are involved in injured brains. The first is crucial for the directionality of the transmission of electrical and chemical signals and is associated to a break of symmetry in neuron morphology. The second occurs in recolonization mechanisms of lesions, whose mechanical properties are impaired. During this thesis, quantitative studies are performed on these two cell types, focusing on their growth and their response to geometrical and mechanical constraints. The final aim is to elucidate some molecular mechanisms underlying changes of the cellular structure, and therefore of the cytoskeleton.

A significant outcome of this work is the control of the neuronal polarization by a simple control of cell morphology. This result opens the possibility to develop controlled neural architectures *in vitro* with a single cell precision.

Keywords: Primary brain cells, hippocampal neurons, neuronal polarization, cortical glial cells, chemical and mechanical pattering, cellular mechanics, mechanosensitivity, cytoskeleton, biophysics

Acknowledgments, remerciements

First of all, I would like to thank you, the reader, for your interest in this PhD work.
For these few pages, I prefer to switch to my daily language, the French, in order to say "un grand merci" to all the people I had the chance to meet during my PhD and that contributed to realize this experience.

Ces trois ans m'ont donné l'occasion de nourrir ma curiosité pour le monde qui nous entoure et de plonger dans le monde de la biophysique. La richesse de cette aventure a pour protagonistes la vitalité, la passion et la curiosité des différentes personnes qui ont participé de façon active à la réalisation de ce projet de thèse ou que j'ai connu grâce aux collaborations et les conférences auxquelles j'ai pu participer. Je ne pourrai pas les citer toutes mais j'en suis très reconnaissante.

Je tiens à remercier en quelques lignes ici mes directrices de thèse, Catherine Villard et Alice Nicolas, grâce à qui j'ai pu découvrir la beauté de ce domaine de recherche et son approche. Merci pour m'avoir toujours soutenue et encouragée par votre optimisme et confiance. Je vous remercie pour votre dynamisme qui m'a permis d'explorer différents laboratoires et de m'approcher de leurs compétences de biologistes. Merci pour ces trois ans de travail intense et amusant.

Je tiens également à remercier tous les membres du jury, Christine Métin, Vincent Studer, Yves Couder et Frédéric Saudou, d'avoir accepté d'évaluer mon travail, pour leur commentaires et leur regard intéressé et critique très enrichissant.

Je souhaite remercier mes équipes, l'équipe Termodynamique des Petits Systèmes à l'Institut Néel dirigée par Olivier Bourgeois, et l'équipe Micronanotechnologies pour la santé au LTM dirigée par David Peyrade. Je tiens à remercier Alain Schuhl, Pierre-Etienne Wolf et Benjamin Canals à l'Institut Néel et Olivier Joubert et Jumana Boussey au LTM pour leur soutient comme aussi André Sulpice et tout le personnel du CRETA pour leur accueil toujours chaleureux.

Un merci spécial à Antoine Triller de l'IBENS pour m'avoir accueilli dans son laboratoire jusqu'à que je puisse être autonome dès les premières étapes nécessaires pour mes manips et merci à toute l'équipe, en particulier à Sabrina Colasse pour sa patience et délicatesse utilisée pour m'amener à apprendre les techniques de dissection.
Je tiens à rappeler la générosité et l'hospitalité également de :

- Isabelle Marty, Julien Fauré et en particulier Julie Brocard du GIN à Grenoble pour l'initiation et le rodage à la culture cellulaire,
- Catherine Picart et Claire Monge du LMGP à Grenoble pour leur échanges sur les cellules musculaires,
- Giorgio Scita et Andrea Disanza, Amanda Oldani, Dario Parazzoli et Massimiliano Garrè

de l'Imaging group de l'IFOM-IEO à Milan grâce à qui j'ai eu l'émotion de filmer la première vagues d'actine en fluorescence,
- Casper Hoogenraad, Ines Ferreira et Kah Wai Yau de l'Université de Utrecht pour leur sympathie et persévérance,
- Laurent Malaquin et toute l'équipe à l'Institut Curie de Paris pour leur investissement dans l'aventure des cellules primaires aimantées dans des systèmes microfluidiques,
- Patricia Bassereau et Thomas Bornschlögl de l'Institut Curie de Paris pour la courte mais enthousiasmante expérience avec les pinces optiques,
- Giovanni Longo et Simone Ruggeri à l'EPFL à Lausanne pour leur maitrise avec l'AFM qui a battu l'élasticité imparable des neurones,
- Christine Métin à l'institut du Fer à Moulin à Paris qui a fait tout le possible pour réussir les manips,
- Lionel Bureau du LiPhy à Grenoble pour sa disponibilité à partager la fabrication des brosses de PNIPAM.

Merci beaucoup aussi à :

- Nir Gov du Weizmann Institute à Rehovot pour les échanges enrichissants et son intérêt insatiable pour notre système,
- Nora Dempsey, Frédéric Dumas-Bouchiat, Luiz Fernando Zanini et Damien Le Roy pour leur enthousiasme et sourire malgré les contraintes de manipuler des objets vivants,
- toute la formidable et impeccable équipe de Nanofab,
- Pierre Brosse pour ses questions sur les neurones parmi ses conseils patients et utiles pour apprendre à me servir du tour,
- Laetitia Marty, Vincent Bouchiat et Graziella Kavaklian pour leur aide à Nanochimie,
- Ghislain Bugnicourt qui a rendu son manuscrit à mon premier jour de thèse et qui n'a jamais manqué de me transmettre son enthousiasme et des bons conseils pour démarrer au mieux cette aventure,
- Céline Braïni qui a pris la suite du passage de témoin, avant lequel j'ai pu profiter de sa bonne compagnie et soutient, que ce soit en salle blanche ou devant une tasse de thé et muffins,
- les stagiaires Beilun Wu, Soha Souk et Yohan Lecomte pour leurs questions et les bons moments gourmands passés ensemble

... de l'Institut Néel et à...

- Michel Moussus pour m'avoir toujours soutenue et motivée, pour son sang froid, ses conseils en béton et le meilleur café français,
- David Fuard qui m'a initiée à la salle blanche et a su toujours intervenir avec la bonne solution dans les moments cruciaux,
- Abbas Mgharbel pour ses explications et conseils sur les gels et pour avoir renoncé à sa yaourtière pour assurer un confort essentiel des neurones entre Paris et Grenoble,
- Nicolas Bouchonville d'avoir pris à coeur la suite des mesures AFM,
- Olivier Lecarme, Julien Cordeiro, Thibault Honegger, Clarisse Benoit, Kevin Berton, Maxime Darnon, Camille Petit-Etienne... pour leur vitalité contagieuse et motrice et pour la bonne ambiance au labo et à l'extérieure

... du LTM,
... sans oublier Danielle Gulino, qui a relu mon manuscrit avec beaucoup d'intérêt en apportant des remarques constructives aussi bien avant qu'après la rédaction, Camille Migdal, pour un travail d'équipe hyper efficace et plaisant, Marie Courçon, Alexandre Morel, Mélanie Charbit, Helena Polena et Isabelle Vilgrain du C3 au CEA à qui je dois un merci particulier pour leur bonne humeur toujours présente, comme aussi pour les petits délices qui soulageaient les longues journées au labo.

Je tiens également à remercier Stéphanie Lacour et Cédric Paulou de l'EPFL à Lausanne, Cédric Allier et Srikanth Vinjimore Kesavan du CEA à Grenoble pour les courtes mais très enrichissantes manips ensemble, le Prof. Balestra de l'Université de Turin pour ses conseils.
Une grande partie des résultats de ce travail n'aurait pas pu être observée sans l'accès aux microscopes mis à disposition par Odile Fihol-Cochet et Didier Grunwald du CEA, Jean-Philippe Kleman de l'IBS et Michaël Betton du LiPhy à Grenoble, que je souhaite tous remercier pour leurs conseils et présence importante.
Au GIN de Grenoble, je voudrais remercier aussi Antoine Depaulis, pour sa bonne humeur, toujours disponible pour des bons conseils, et Mireille Albrieux, de nous avoir accueilli dans son labo pour nos premières aventures de dissection à Grenoble.
Merci beaucoup à Christine Martinelli, Patricia Poirier, Carméline Meli, Mathilde Mauro, Louise Infuso de l'Institut Néel, Sylvaine Cetra et Marielle Clot du LTM, Sandrine Ferrari de l'école doctorale de Physique et toutes les gestionnaires qui ont toujours fait leur mieux pour simplifier les démarches parfois emmêlées du système administratif, à Cécile Nemiche de la repro pour ses conseils et compréhension.

Un souvenir spécial à Franck Omnès qui m'a guidée à la découverte de l'Institut Néel la toute première fois que je rentrais au labo et qui m'a transmis son enthousiasme pour la recherche à l'interface entre physique et biologie.

Mille mercis à ...
Stéphanie Monfront pour la riche expérience avec la Fondation Nanosciences, l'équipe d'Innov-Doc pour la belle synergie, Sandrine, Julien, Jonathan et Jonathan pour leur accueil chaleureux pendant mes visites à Paris, ma troupe de Percevalière pour son énergie puissante et les moments ensemble inoubliables, les autres covoitureurs franco-italiens pour les conversations dépaysantes et les questions motivantes sur mon sujet de recherche.

Je vais terminer par remercier de tout coeur toutes les personnes chaleureuses dont la présence a marqué le cheminement de ma thèse et qui ont alimenté mon enthousiasme au cours de la rédaction, pour leur curiosité assidue pour mon travail et leur esprit critique, leur soutient jour par jour et les renforts culinaires, les pique-niques régénérants en montagne : ma famille qui a fait tout le possible pour assister à la soutenance et qui a assuré la réussite du pot, Ben, Sania, Rachel, Alex, Raph, Antho, Virginie, Yann, Daniela, Véro, Cyril, Sofia, Luca, Layal, Antoine, Cec, Jerem, Six, Marta, Vale... Grazie!

Contents

Introduction

Since the pioneering observations of Ramón y Cajal more than one century ago, the very fast development of imaging technologies has given the possibility to investigate living systems, and in particularly the brain, from submicrometric scale to the level of the whole organ. Therefore, it does not surprise the growing charm around the understanding of the brain organization and working. Although some knowledge about nervous system are now well established and largely diffused, this complex system is far from being understood and still attract the attention of scientists and people in general.

The complexity of the nervous system is partially due to its large panel of functions and properties of mechanical, electrical and chemical origins, that distinguishes it from most other tissues or organs. Therefore, the study of this biological system is approached from different points of view. Nervous system can be considered for its morphological properties, as well as for its capabilities to respond to a stimulus, to propagate and transfer nerve impulses, or for its role in interaction with other organs. Nevertheless, it is crucial to consider nervous system as relatively autonomous but fundamentally integrated in a larger biological system. In the same way, single neurons are entities with independent functions that have to be taken into account as a component of a larger computational entity that is the nervous system.

The surge of innovative technologies giving access to the cell and sub-cell scale environment has allowed significant advances in the understanding of nervous system. The variety of tools coming from genetics, physics, chemistry and optics opens new approaches and new questions that motivate scientists. This context gives the great advantage to promote the encounter of diverse disciplines that, each of them, provides its portion of knowledge and a combinatory of approaches. The interest for the brain is that way addressed from both a computational and a cellular point of view. These two angles of study enrich one another and are associated to complex questions like the information processing in neuronal networks and the mechanisms underlying the origin and the development of neurodegenerative diseases and brain cancers.

This PhD project has mainly taken place in a laboratory of physics. The point of view of a physician is the guideline of this work, supported by enriching interactions with biologists. Indeed, several collaborations and exchanges with biologists in France and Europe have been undertaken along this PhD to maintain a constructive dialog between these two domains of research. The particular context of Grenoble has played a fundamental role thanks to a large proximity of several laboratories of research and to a technological environment highly developed in the microelectronic context.

In this PhD thesis, we focus on the issue of brain cell growth from a morphological point of view at the scale of single cells. In particular, our interest is oriented towards the interplay between cell morphology and its functions. From this point of view, a neuron is characterized by a rather spherical cell body, named the soma, and arboreal extensions, called neurites, that in polarized functional neurons differentiate into two types: dendrites and axons. Dendrites are organized into a tree structure that collects the electrical activity produced by pre–synaptic neurons, whereas the axon represents the long extension that conveys the output signal toward post–synaptic neurons.

During this PhD project, experiments have been performed using primary brain cells. These kind of cells differentiate from cell lines, that are quasi immortal cells with a nearly unlimited capability of division. Cell lines have thus characteristics similar to cancer cells and are populations that became stable after several steps *in vitro*, far from their original environment *in vivo*. Contrarily, primary cells are more sensitive to their environment and better reflect the properties of the organ of their origin.

Primary brain cells have been obtained from rodent embryos. Indeed, at least for studies on cell brain behavior, rodents are considered as the best experimental compromise between availability and pertinence of brain tissues and ethical aspects. In particular, we have studied the *in vitro* behavior of hippocampal neurons and cortical glial cells. Neurons from hippocampus are a basic reference of primary brain cells but they are still poorly employed in microstructured *in vitro* environments. Glial cells are another fundamental cell type in brain. They are known for their metabolic and regulatory role of neuron activity but they are also at the origin of most of brain cancers and of the mechanical changes in injured brains. This work is thus constituted of two main topics. Firstly, the establishment of the neuronal polarization, or differentiation, as a function of morphological changes associated to this crucial phenomenon in the neuron development. Secondly, the sensitivity of glial cells to the physical and mechanical properties of cell environment.

Our study highlights the importance of the interactions of cells with the physical and chemical properties of their environment. These interactions are at the basis of the development of a single cell and of its specific functions. In that sense, our approach is humbly inspired by the work on the living system geometrical organization of the Scottish D'Arcy Thompson (*On Growth and Form*, 1917) until the Chilean H. Maturana (*Autopoiesis and Cognition: The Realization of the Living*, with F. Varela, 1980).

The methodology employed in this work is based on the fabrication of controlled environments in order to investigate the neurons and glial cells response to topographical, mechanical and chemical cues. Indeed, although the nervous system is a complex network of interconnected cells, one way to understand its complexity is to dissect it into simpler elements. For that, it is necessary to study the properties of its cellular components, that are mainly neuronal and glial cells. This is currently possible thanks to the contribution of microelectronic technologies and of the development of instruments of microscopic observation that give access to a fine control of the physical and chemical properties of the cell environment, as well as to a deep analysis at the single cell level.

In the **first chapter** of this manuscript, we will introduce the general context of our work in order to describe the basics of cell neurobiology, the specific vocabulary associated to brain cells (highlighted in bold) and the main steps of neuronal development *in vitro*. This section will give some motivations underlying the studies on the cellular microenvironment and an overview of the principal examples reported by the literature. We will mainly focus on studies with primary brain cells, for the same reason we have made the choice to work with this kind of cells, that is to keep a close relationship with the *in vivo* real environment.

The subject of the **second chapter** will be the methods employed as well as some additional methods we have developed and tested, but not used for the results exposed in this manuscript. The different techniques explored reflect the growing impact of microelectronics technologies into life science. We will conclude this chapter with the presentation of some techniques to trap cells in controlled microstructured substrates whose principles are based on magnetic interactions.

In the two last chapters, we will report experimental results about neuronal and glial cell responses to chemical and physical contraints of their environment. In the **third chapter**, we will analyze the influence of the adhesion geometry on the neuronal growth. We will especially focus on the neurite elongation and the neuronal polarization. More precisely, we will report observations on neurons whose branches differ in width or number. Possible biophysical mechanisms underlying the control of the neurite growth and polarization will be proposed and discussed, eventually based on theoretical models.

In the **fourth chapter**, we will discuss about the mechanosensitivity of glial cells on patterns of rigidity at different scales. This work represents a new exploratory study of the role played by the chemistry of the glial cell environment in their sensitivity to the mechanical properties of their substrates. A short section about the glial cell response to topography will conclude this chapter.

At the end of each of these two last chapters we will provide a summary of our results. Finally, more significant results will be recapitulated in a general conclusion discussing the various perspectives that have come to light from this PhD work.

Introduction

Depuis les observations pionnières de Ramón y Cajal il y a plus d'un siècle, le développement très rapide des technologies d'imagerie a ouvert la possibilité d'étudier les systèmes vivants, et en particulier le cerveau, de l'échelle submicrométrique à celle de l'organe vu dans son ensemble. Ces techniques d'imagerie toujours plus résolues ont engendré un véritable engouement vers la compréhension de l'organisation du cerveau et de son fonctionnement. Bien que certaines connaissances sur le système nerveux soient maintenant bien établies et largement diffusées, ce système complexe est loin d'être compris et attire encore fortement l'attention à la fois des scientifiques et du grand public.

La complexité du système nerveux est en partie due à sa variété de fonctions, associées à un environnement mécanique, électrique et chimique, qui le distingue de la plupart des autres tissus ou organes. De ce fait, l'étude de ce système biologique est abordé sous différents points de vue. Le système nerveux peut aussi être observé pour ses propriétés morphologiques, pour sa capacité à répondre à un stimulus et à propager et transférer l'influx nerveux, ou pour son rôle dans l'interaction avec d'autres organes. Il est crucial de considérer le système nerveux comme relativement autonome mais fondamentalement intégré dans un système biologique plus grand. De la même manière, les neurones sont des entités ayant des fonctions indépendantes qui doivent être pris en compte en tant que composants d'une entité plus grande qui est le système nerveux.

L'émergence de technologies innovantes donnant accès à l'environnement à l'échelle cellulaire et sub-cellulaire a permis des avancées significatives dans la compréhension du système nerveux. La variété des outils issus de la génétique, de la physique, de la chimie et de l'optique ouvre de nouvelles approches et de nouvelles questions qui motivent les scientifiques. Ce contexte donne le grand avantage de favoriser la rencontre de disciplines différentes qui, chacune d'entre elles, apportant sa part de connaissances et d'approches possibles. Une spécificité du cerveau est l'importance d'approcher son fonctionnement à la fois avec un point de vue cellulaire et un point de vue in silico. Ces deux angles d'étude s'enrichissent l'un l'autre et sont associées à des questions complexes comme le traitement de l'information dans des réseaux neuronaux, les mécanismes sous-jacents à l'origine et au développement de maladies neurodégénératives ou l'invasion de cancers du cerveau.

Ce projet de thèse a principalement eu lieu dans un laboratoire de physique. Le point de vue

d'un physicien est la ligne directrice de ce travail, soutenu par l'enrichissement des interactions avec les biologistes. En effet, plusieurs collaborations et échanges avec des biologistes en France et en Europe ont été entreprises le long de cette thèse afin d'assurer un dialogue constructif entre ces deux domaines de recherche. Le contexte particulier de la ville de Grenoble a joué un rôle fondamental grâce à une grande proximité de plusieurs laboratoires de recherche et à un environnement technologique très développé dans le contexte de la microélectronique.

Dans cette thèse, nous nous concentrons sur la question de la croissance des cellules du cerveau à partir d'une analyse morphologique à l'échelle de cellules individuelles. En particulier, notre intérêt est orienté vers l'interaction entre la morphologie des cellules et leurs fonctions. De ce point de vue, un neurone est caractérisé par un corps cellulaire plutôt sphérique, appelé soma, et des ramifications, nommées neurites, qui dans les neurones fonctionnels une fois polarisés se différencient en deux types : les dendrites et les axones. Les dendrites sont organisées en une structure arborescente qui recueille l'activité électrique produite par les neurones pré–synaptiques, alors que l'axone représente une longue extension qui transmet le signal de sortie vers les neurones post–synaptiques.

Au cours de ce projet de thèse, des expériences ont été effectuées en utilisant des cellules primaires du cerveau. Ce type de cellules se différencie des lignées cellulaires, devenues stables après plusieurs étapes *in vitro*, loin de leur milieu d'origine *in vivo*. Bien que plus contraignantes à manipuler, les cellules primaires sont plus sensibles à leur environnement et reflètent mieux les propriétés de l'organe d'origine.

Les cellules primaires du cerveau ont été extraites d'embryons de rongeurs. En effet, au moins pour les études sur le comportement des cellules du cerveau, les rongeurs sont considérés comme le meilleur compromis expérimental entre la disponibilité et la pertinence des tissus du cerveau et les aspects éthiques. Nous avons étudié le comportement *in vitro* des neurones issus d'une région cérébrale appelée hippocampe et des cellules gliales corticales. Les neurones de l'hippocampe sont une référence fondamentale des cellules primaires du cerveau, mais ils sont encore peu utilisés dans des environnements microstructurés *in vitro*. Les cellules gliales constituent l'autre grand type de cellules du cerveau. Elles sont connues pour leur rôle métabolique et régulateur et de l'activité neuronale. Elles sont également à l'origine des cancers du cerveau et du remodelage de l'environnement cellulaire dans les cerveaux blessés. Ce travail est donc constitué de deux thèmes principaux : la mise en place de la polarisation neuronale (ou différenciation axonale), en fonction de changements morphologiques associés à cette étape clé de développement, puis la sensibilité des cellules gliales aux propriétés physiques et mécaniques du micro-environnement cellulaire.

Notre étude met en évidence l'importance des interactions des cellules avec les propriétés

physiques et chimiques de leur environnement. Ces interactions sont déterminantes pour la croissance d'une cellule isolée et ses fonctions spécifiques. Dans ce contexte, notre approche est modestement inspiré par le travail sur l'organisation géométrique des systèmes vivants de l'écossais D'Arcy Thompson (*On Growth and Form*, 1917) jusqu'au chilien H. Maturana (*Autopoiesis and Cognition : The Realization of the Living*, avec F. Varela, 1980).

La méthodologie utilisée dans ce travail est basée sur la fabrication d'environnements contrôlés afin d'étudier la réponse des neurones et des cellules gliales à des signaux topographiques, mécaniques et chimiques. En effet, bien que le système nerveux soit un réseau complexe de cellules interconnectées, une façon de comprendre sa complexité est de le subdiviser en éléments plus simples. Pour cela, il est nécessaire d'étudier les propriétés de ses composants cellulaires, qui sont principalement des cellules neuronales et gliales. Ceci est actuellement possible grâce à la contribution des technologies de la microélectronique qui donnent accès à un contrôle subcellulaire des propriétés physiques et chimiques de l'environnement de la cellule, et à l'élaboration d'instruments d'observation microscopique qui permettent une analyse approfondie des mécanismes cellulaires.

Dans le **premier chapitre** de ce manuscrit, nous allons présenter le contexte général de notre travail afin de décrire les bases de neurobiologie cellulaire, le vocabulaire spécifique associé aux cellules du cerveau (indiqués en gras) et les principales étapes du développement neuronal *in vitro*. Cette section donnera les motivations sous-jacentes des études effectuées dans des micro-environnements artificiels contrôlés et un aperçu des principaux exemples rapportés par la littérature. Nous nous concentrerons principalement sur l'état de l'art portant sur des cellules primaires du cerveau, pour la même raison que celles pour lesquelles nous avons fait le choix de travailler avec ce type de cellules.
Le sujet du **deuxième chapitre** sera dédié aux méthodes employées ainsi qu'à d'autres méthodes que nous avons développées et testées, mais qui ne sont pas utilisés pour les résultats exposés dans ce manuscrit. Les différentes techniques explorées reflètent l'impact croissant des technologies de la microélectronique dans les sciences de la vie. Nous terminerons ce chapitre par la présentation de quelques techniques basées sur des interactions magnétiques permettant de capturer des cellules sur des sites prédéterminés lors de l'étape d ?ensemencement.
Les deux derniers chapitres suivants sont dédiés spécifiquement aux réponses des cellules neuronales et gliales à des contraintes chimiques et physiques de leur environnement. Dans le **troisième chapitre**, nous analyserons l'influence de la géométrie d'adhésion sur la croissance neuronale. Nous mettrons l'accent sur l'élongation neuritique et la polarisation neuronale. Plus précisément, nous rapporterons nos observations sur des neurones dont les branches varient en largeur ou en nombre. De possibles mécanismes biophysiques sous-jacents contrôlant la croissance des neurites et la polarisation seront proposés et discutés, éventuellement basés sur des

modèles théoriques.

Dans le **quatrième chapitre**, nous discuterons de la sensibilité des cellules gliales aux propriétés mécaniques de leur environnement sur des motifs de rigidité à différentes échelles. Ce travail présente une étude exploratoire du rôle joué par la chimie de l'environnement des cellules gliales dans leur réponse aux propriétés mécaniques de ce même environnement. Une courte section sur la réponse des cellules gliales à la topographie terminera ce chapitre.

À la fin de chacun de ces deux derniers chapitres, nous fournirons un résumé de nos résultats. Enfin, les résultats les plus significatifs seront récapitulés dans une conclusion générale qui discutera les différentes perspectives résultant de ce travail de thèse.

Chapter I

Introduction to brain cells

Contents

Chapitre I : résumé

Dans ce chapitre d'introduction nous présentons quelques propriétés fondamentales de l'organisation cellulaire et subcellulaire des cellules du cerveau, les processus impliqués dans leur développement et leur différentiation. Cela permet de poser le contexte biophysique et d'introduire les éléments nécessaires à la compréhension de ce travail de thèse. Une étude bibliographique portant sur l'interaction des cellules primaires du cerveau avec des microenvironnements contrôlés décrit et compare les travaux récents. Ce chapitre se termine par une présentation succinte de la finalité et la validité des méthodes et des approches expérimentales choisies.

List of abbreviations and nomenclatures

AIS ..... Axonal Initial Segment

AnkG ..... AnkirinG

CAMs ..... Cell Adhesion Molecules

CAMSAPs ..... Calmodulin–regulated spectrin–associated proteins

CNS ..... Central Nervous System

DIV ..... Days In Vitro

DRG ..... Dorsal-Root Ganglia neurons

EB ..... End–Binding proteins

ECM ..... Extracellular matrix

FAs ..... Focal Adhesions

FAK ..... Focal Adhesion Kinase

GFAP ..... Glial Fibrillary Acid Protein

MAPs ..... Microtubule–Associated Proteins

PDMS ..... PolyDiMethylSiloxane

PLL, PDL ..... Poly-L-lysine, Poly-D-lysine

PLL–PEG ..... Poly-L-lysine PolyEthyleneGlycol

PLO ..... Poly-ornithine

PNS ..... Peripheral Nervous System

μCP ..... Microcontact printing

3D, 2D, 1D ..... 3, 2 and 1 dimensions

I.1 Functions and morphology

The nervous system assures the survival of living organisms by its capacity to orchestrate their interaction with the external environment, which at the most basic level means to coordinate the movements produced by the body and to process the signals from the various organs, including sensory organs. The centralized control role played by the nervous system is characterized by its complex and very quick capabilities to integrate information. During the course of the Evolution, the nervous system has gained in complexity and efficiency, reaching its higher level in primates with the emergence of consciousness. A high brain plasticity and development throughout life is what distinguishes humans from the others primates. The level of complexity of the nervous system in the organisms is often associated to a corresponding capacity to acquire new learning and to adjust behaviors in reaction to the external environment. All responses to the various internal or external stimuli determines the organism behavior. In that respect, the brain function is strongly associated to the foundation of biological individuality, to such an extent that the existing legislation in most of the world equates the cessation of all brain activity to death. Most questions about identity, consciousness and intelligence are still open, gathering the joined efforts of neuroscientists, psychologists and philosophers.

In vertebrate organisms, the nervous system is composed of the central (**CNS**) and of the peripheral (**PNS**) nervous system. The CNS includes the brain and the spinal cord and results in a centralized control of the information coming both from the organism and its environment. The CNS and the PNS are surrounded by three sheets of connective tissues forming the meninges. The PNS is constituted of nerves leading from and to the CNS and of a set of ganglia that are groups of nerve cells providing intermediary connections with the CNS. Cells from the CNS will be the focus of this work. The CNS is mainly composed of neurons and of more numerous glial cells.

Glial cells name takes origin from the Greek word "glue", thanks to their first known role of support and protection of the nervous tissue. Glial cells are grouped in three principal types (Figure I.1): astrocytes, microglia and oligodendrocytes.

Astrocytes, taking their name from their star-like shape, ensure several functions in the nervous system: they supply glucose to neurons, they contribute to regulate the composition of the interstitial fluid in the nervous tissue and to the formation of the blood-brain barrier, they modulate synaptic activity, releasing and uptaking for example glutamate [1]. In the fourth chapter we will discuss their interaction with neurons on mechanosensitive aspects. Microglia are macrophage cells with an immune defense role. The third kind of glial cells has a similar role than Schwann cells in the PNS, i.e. to wrap a myelin sheath around neuronal extensions.

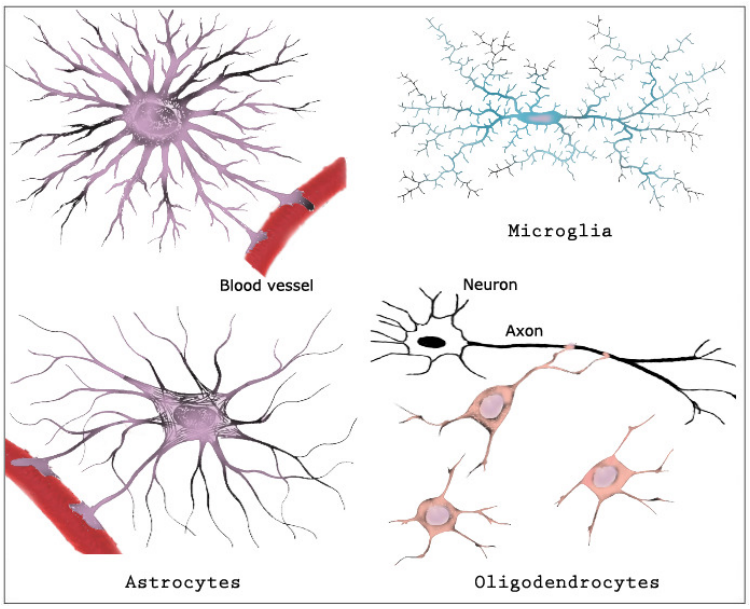

Figure I.1: **Morphologies of the three principal types of glial cells**: astrocytes, microglia and oligodendrocytes. Adapted from Ganong W.F., Review of Medical Physiology, 22nd Edition, 2005.

There is a growing interest for glial cells in general and for their active involvement in various brain functions, including the regulation of the strength of neuronal connections [2, 3]. Glial cells, unlike mature neurons where the mitotic cell cycle is arrested [4], may retain the potential to divide and this capacity is one of the reasons of the glial origin of most of brain cancers. They are also associated to the mechanical changes observed in the injured brain.

Neurons are excitable cells characterized by a resting intra-cellular potential ($\sim$ -70 mV) induced by the difference of ions concentrations, mainly choloride (Cl^-), sodium (Na^+) and potassium (K^+), on opposite sides of the cellular membrane. The membrane potential can locally switch to positive values in neuronal processes conveying electrical signals. The neuron morphology reflects its function to collect, process and transmit electrical signals through chemical junction named **synapses**. From a mature neuron cell body, or **soma**, emerge one **axon** (sometimes two in specific neuronal types) that conveys the output signal toward post-synaptic neurons, and multiple **dendrites** organized into a tree structure that collects the electrical activity produced by pre-synaptic neurons. Soma and dendrites mainly compose the **grey matter** of the CNS whereas the **white matter** is composed of bundles of myelinated axons. In mammals, the typical size of a soma is on the order of 10 μm, the axon and dendrites diameter of less than 1 μm [5]. The different steps of neuronal maturation *in vitro* will be described in Section I.3.

There are over 200 different varieties of neuronal cells. The geometry of axons and dendrites and synapses localization change strongly with the cell type, depending on their role in the neural circuit (Figure I.2). For this reason, a better understanding of the interplay between morphologies and associated functions is crucial.

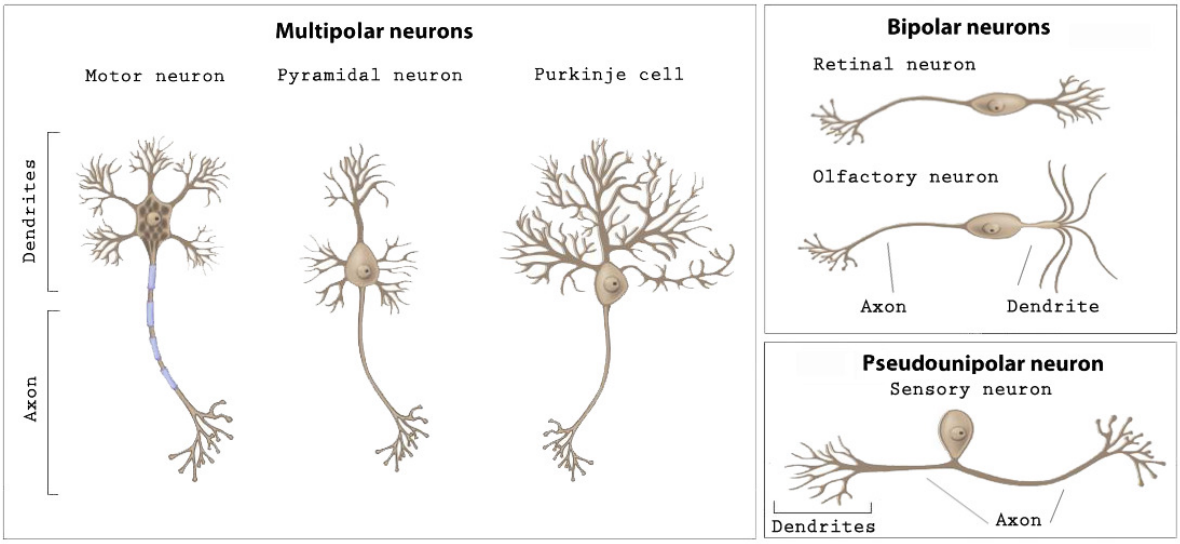

Figure I.2: **Basic neuron types of different brain areas, classed by their morphology**. Adapted from wiseGEEK.com.

Brain can be divided into functional areas, which dimensions are species-dependent. Their local architecture is nevertheless quite conserved, in relation to their biological function. For example, the olfactory bulb is more developed in mice than in human beings, where the cerebral cortex is the most developed region (Figure I.3).

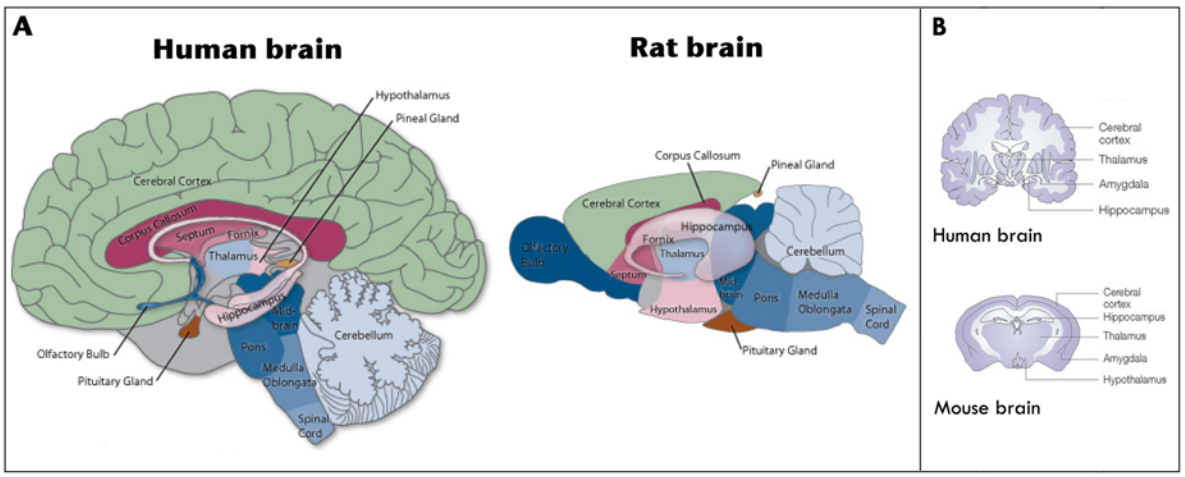

Figure I.3: Longitudinal (A) and transverse (B) sections of human and rat (A) or mouse (B) brains, showing functional similarities although in different proportions. Adapted from [6].

Interestingly, there are no qualitative differences between neurons of the human brain and those of other mammals or other vertebrates. However, numerous variables differentiate the brains of several species like their size, their number of neurons and glial cells, the number of their sub-types, the molecular nature of synapses [7] and the architecture of the connectivity between neurons.

The studies exposed in this manuscrit have been performed with neurons coming from the

hippocampus or the cortex of rodent embryos at eighteen days of gestation (E18 embryos). The main reason is that the dissociated hippocampal tissue provides a relatively homogeneous cell population. Indeed, pyramidal neurons, so-called for their pyramidal-shaped soma, are the predominant neuron type present in the hippocampus at this stage of development. These cells are excitatory glutamatergic neurons, whereas the majority of the remaining neurons are interneurons, GABAergic cells making inhibitory synaptic terminals [8]. Moreover, the hippocampus development has been well-characterized *in vitro*. On a functional point of view, the hippocampus plays an important role in spatial memory and in learning processes, it is essential for the consolidation of long-term memories, acquired from experiences, and it may be necessary in the encoding of novel associative information in short-term memory. Cerebral cortex encompasses about two-thirds of the brain mass and it is responsible, amongst other functions, of consciousness, memory, language and thinking.

I.2 Brain cells structure

Neurons, as all eukaryotic cells including glial cells (Figure I.4), have a common envelope named the **plasma membrane**. This membrane, that contains many transmembrane proteins and macromolecules, is at the interface between the **extracellular matrix** (ECM) and the internal **cytoplasm**. The cytoplasm is composed of a medium called the cytosol where are immersed the **nucleus** containing genes, various organelles (e.g. the **mitochondria** which provides energy, the **Golgi's apparatus** and the **ribosomes** that are able to synthesize proteins) and three types of filaments. These filaments are **microtubules**, **actin** and **intermediate filaments** that, organized in a network, form the **cytoskeleton** of the cell. These three important structures will be detailed in the following subsections (I.2.1, I.2.2, I.2.3). The cytoskeleton plays a critical role in the dynamical properties of the cell, e.g. migration, polarization, forces generation and external signals transduction. In neurons, the cytoskeleton adopts specific organizations that will be described in the subsections entitled: **axon**, **dendrites** and **growth cone** (I.2.4, I.2.5).

I.2.1 Microtubules

Microtubules are nucleated from the **centrosome**, an organelle composed of two **centrioles**, and they form the mitotic spindles that guide the chromosomes during cell division. Recent studies have shown that most of microtubules dispersed in the different regions of neurons are not only nucleated and released from the centrosome [9] but they can originate from a acentrosomal assembly [10]. This phenomenon already known from plants and yeasts [11], could be important for axonal specification, thanks for example to the presence in the axon of some microtubule severing proteins like katanin [4].

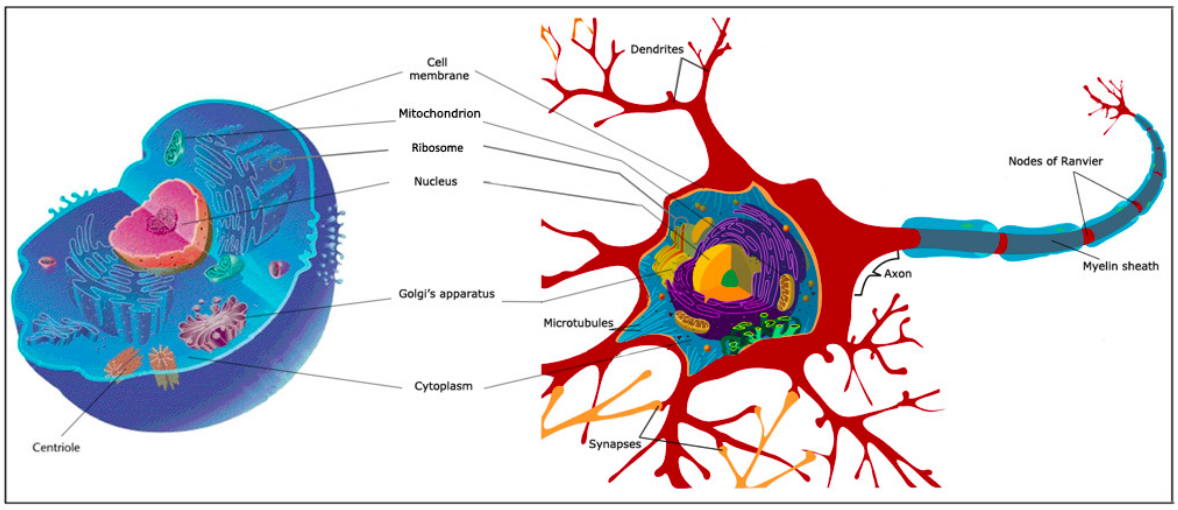

Figure I.4: **Common components between a typical eukaryotic animal cell (left), like glial cells, and a neuron (right).** Adapted from Wikimedia Commons.

Microtubules are highly dynamic structures, with an external and internal diameter typically of 22 nm and 12 nm and a length varying between fraction to tens of microns [12]. Their tubular architecture makes them the stiffest filaments in the cytoskeleton, giving structural support to cell shapes. The tubular structure of these protofilaments is polarized with a **plus** (+) **end** (polymerization) and a **minus** (−) **end** (depolymerization) and is made up of α and β-tubulin dimers (Figure I.5).

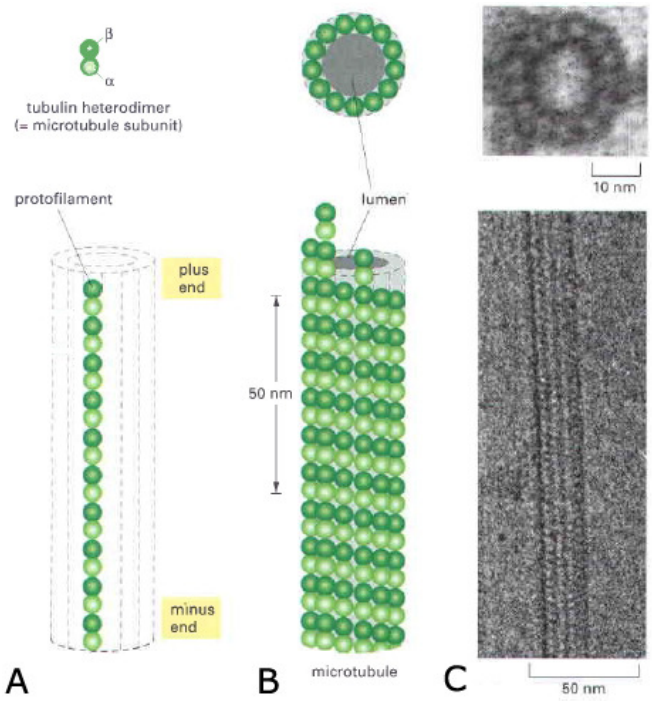

Figure I.5: **Schematic representation of microtubule structure.** A) Tubulin heterodimer (α and β subunits) and a polarized protofilament. B) Protofilament network composed of parallel protofilaments with the same orientation. C) Electronic image of a microtubule segment showing a ring of 13 protofilaments [13].

Of note, the growth of the microtubule + end is coordinated by the **end–binding** (EB) **proteins** family, composed of three members (EB1 – 3) [14]. In neurons, EB1 is implicated in axonal transport [15], whereas EB3 plays the role of a molecular link between microtubules and the actin cytoskeleton [16]. The polarization of microtubules determines the direction of motion of vesicles and organelles along the filaments. **Kinesin** and **dynein** are the molecular motors associated to microtubules, moving respectively toward their + and - ends. A more recent family of microtubule **minus–end binding proteins** called calmodulin–regulated spectrin–associated proteins (CAMSAPs) have been described for their role of regulation of microtubules dynamics. It has been shown that mammalian CAMSAP family members bind specifically to microtubule minus–ends and protect them against kinesin-13–induced depolymerization [17]. In particular, CAMSAP2 specifically localizes to noncentrosomal microtubule minus–ends. In neurons, it stabilizes the free microtubule minus–ends in order to control neuronal polarity and development, playing a key role for proper microtubule organization [18].
In general, **microtubule–associated proteins** (MAPs) localized along microtubules promote their stabilization and organization.

I.2.2 Actin filaments

Actin filaments, or F-actin, are organized in a double helix of 7 – 9 nm of diameter and composed of monomers of globular actin, or G-actin. They are polarized and dynamic like microtubules and their thin structure makes them very flexible (Figure I.6.A). Actin polymerization is stimulated by nucleating factors, e.g. formins and Arp2/3 complex.
Actin filaments self assemble in 3D, 2D or 1D structures such as **cortex**, **lamellipodium** and **filopodium** (Figure I.6.B). Lamellipodia are large projections of the leading edge of the cell used to explore its environment and to move. Thin filopodia are filled with oriented, bundled actin filaments that usually spread beyond the front of the lamellipodium with the + end toward the protrusion direction. Actin-binding proteins, such as Eps8, are enriched in the growth cones, in particular in the focal adhesions and in the filopodium. These regulatory proteins are involved in the axonal filopodia formation and, more in general, in the control of the actin dynamics in developing neurons [19]. Actin self assembly and bundling are the result of the cooperation of numerous proteins, e.g. IRSp53, Ena/VASP, WASp/Scar. Antiparallel associations of actin filaments are found in stress fibers, making possible the production of mechanical forces inside the cell by shifting actin filaments respectivly to each others. The actin filaments relative motion involved in cell contractility is allowed by myosin-II, an ATP–dependent motor protein (Figure I.6.C).

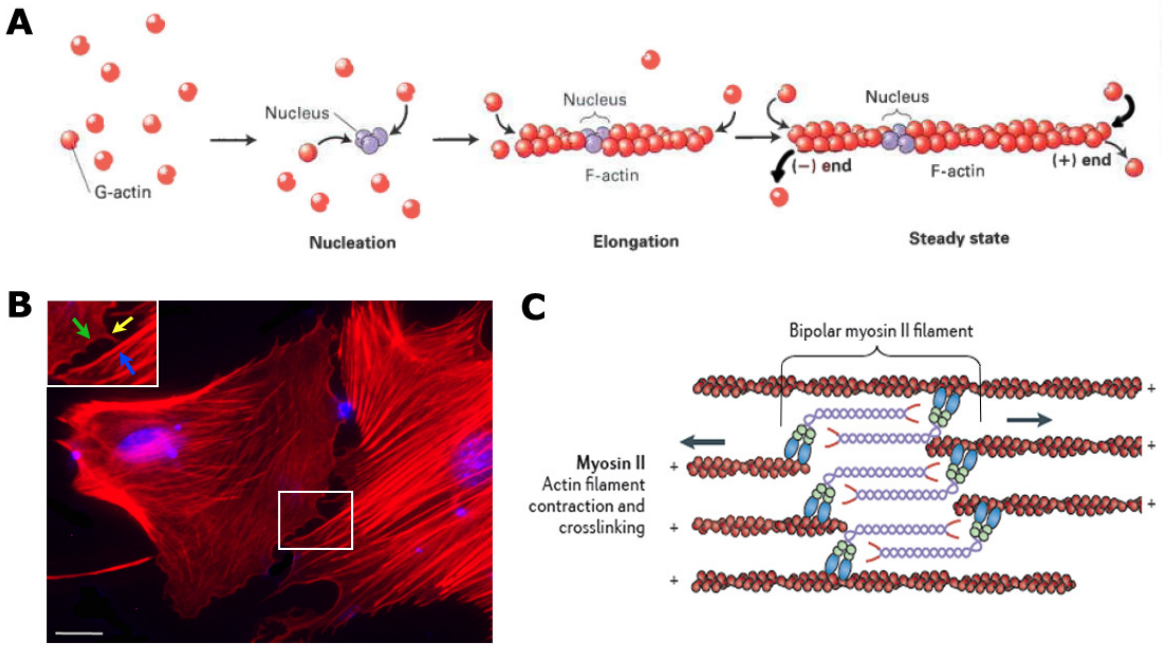

Figure I.6: A) Actin polymerization stages: from nucleation of G-actin monomers (red), to intermediary stable actin complexes (violet) to a gradual elongation of actin filaments (F-actin). In the steady state, actin filaments are organized in a polarized double helix [20]. B) Example of actin structures in glial cells at 2 DIV. The grey rectangle corresponds to the zoom in the inset: lamellipodium (green arrow), filopodia (yellow arrow) and stress fibers (blue arrow). Red, phalloidin. Blue, nucleus. Scale bar: 20 μm. C) Myosin II molecules (in blue and in white) are associated in an antiparallel fashion to move (see arrows) towards the + ends of antiparallel actin filaments leading to acto-myosin contractility [21].

I.2.3 Intermediate filaments

Intermediate filaments are responsible for structural support. They are less dynamic than the two others polymers (microtubules and actin filaments) and they are not polarized. Their molecular structure depends on the cell type but they generally adopt an helical shape composed of dimer proteins organized in protofilaments, with a typical diameter of 10 nm, i.e. an intermediate size between the diameters of microtubules and of actin filaments.
In neurons, they are called **neurofilaments** and play a major role in the maturation and the maintenance of axonal integrity as well as in the establishment of axonal diameter [13]. Their defective trafficking and mutations have also been implicated in mechanisms involved in several neurological disorders, e.g. Parkinson's disease and amyotrophic lateral sclerosis, and in neuronal death [22].
Astrocytes in the CNS express a specific type of intermediate filament proteins: the **glial fibrillary acid protein** (GFAP). In embryonic glial cells, the vimentin intermediate filament, a protein characteristic of mesenchymal cells (e.g. fibroblasts), is also present.

I.2.4 Axon and dendrites

Axons and dendrites are neuronal protrusions grouped under the generic term of **neurites**. These cylindrical membrane protrusions are essentially composed of a bundle of axial microtubules, a small proportion of neurofilaments and a peripheral actin cortex. **Tau** and **MAP2** are distinctive microtubule-associated proteins of axons and dendrites respectively. Both play a role in promoting microtubule stabilization.
Axon, the transmitter pole of neurons, morphologically differs from dendrites by its more homogeneous aspect and its thinner and constant diameter. Its length varies depending on the neuron type from hundreds of microns to a few meters in large animals. Microtubules are all oriented with their + end towards the tip of the axon [23]. The proximal region of the axon near the soma is called **axonal initial segment** (AIS). In this area, a high density of sodium ($Na+$) channels fulfills the necessary conditions to initiate the action potential [24]. A diffusion barrier is established at the AIS level, associated to the segregation of specific axonal proteins like **ankyrinG** (ankG) [25]. The interplay between ankG and AIS microtubules that support the maintenance of neuronal polarity is coordinated by microtubule plus–end–binding proteins EB1 and EB3 [26].
The characteristic length of the AIS is typically 30 – 40 μm. A similar characteristic length has been revealed in axotomy experiments where the remaining stump retains a memory of its axonal nature only when longer than 35 μm [27] (Figure I.7).

An axonal length threshold of 40 μm is also critical to stabilize the polarized state [28].

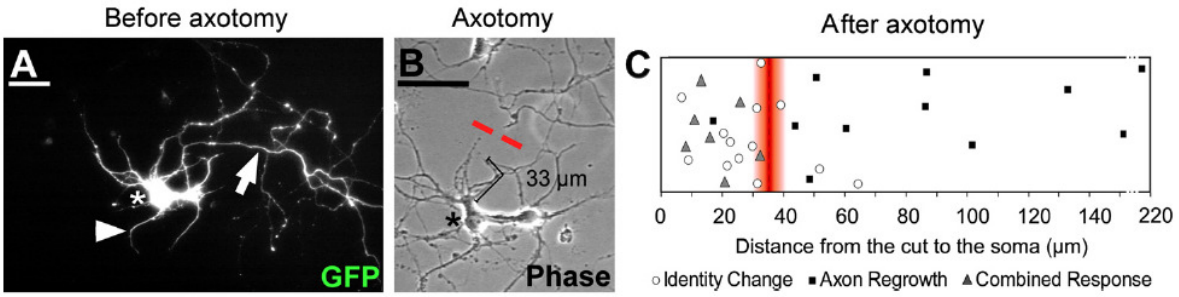

Figure I.7: A) GFP-positive hippocampal neuron at 10 DIV. Axon is identified by the arrow. B) Axon is cut at 33 μm from the cell body (red dashed line). C) Responses of axotomized neurons: above a threshold of $\sim$ 35 μm neurons mostly regrow their original axon. From [27].

In the myelinated axons of vertebrates, clustered $Na+$ channels are then activated at the nodes of Ranvier to rapidly propagate action potentials along the axon [29]. **Nodes of Ranvier** (see Figure I.4) represent myelin sheath gaps of approximately 1 μm in length, leading to uninsulated areas in axons that are necessary for their electrical processes.

The terminal region of the axon generally includes several branches, ending with a specialized area called the **synaptic button**. This is the presynaptic part of the synapse. It contains an actin network that mainly represents the site where neurotransmitter vesicles and the energy suppliers mitochondria are localized. Kinesins allow directional transfer of molecules from soma to axon terminals, i.e. using vesicles to lead along microtubules materials required for renewal of the membrane.

Unlike axons, **dendrites**, the receptors poles of neurons, possess microtubules with reverse polarities, i.e. with their + or - ends directed toward the same side of the cell.

Some observations have shown that microtubules are involved in mRNA localization. Moreover, ribosomes, whose function is to decode mRNA information, have been observed closely associated to microtubules. A specific distribution of mRNA triggers a locally controlled synthesis of proteins, e.g. mRNA coding for MAP2 that is localized to dendrites [30]. For instance, cytoskeletal proteins involved in the formation of **dendritic spines**, small membrane protrusions that are the main sites of excitatory synaptic inputs [31], could be synthesized in the dendrites. Of note, in mammal PNS axons the ability to synthesize proteins is higher than in the CNS, that might be directly correlated to the high capacity of axon spontaneous regeneration observed in the peripheral nervous system [32].

Recently, the development of high-resolution techniques *in vitro* gives the possibility to analyse the structural organization of axon and dendrites. Stochastic optical reconstruction microscopy (STORM) has revealed periodical ringlike structures around the axon circumference at a submicrometric scale [33]. These rings are composed of actin and adducin, an actin-capping protein, with a periodicity of $\sim$ 180 to 190 nm and alternated with spectrin rings, a cytoskeletal protein. Interestingly, these periodic rings have not been observed in dendrites (Figure I.8).

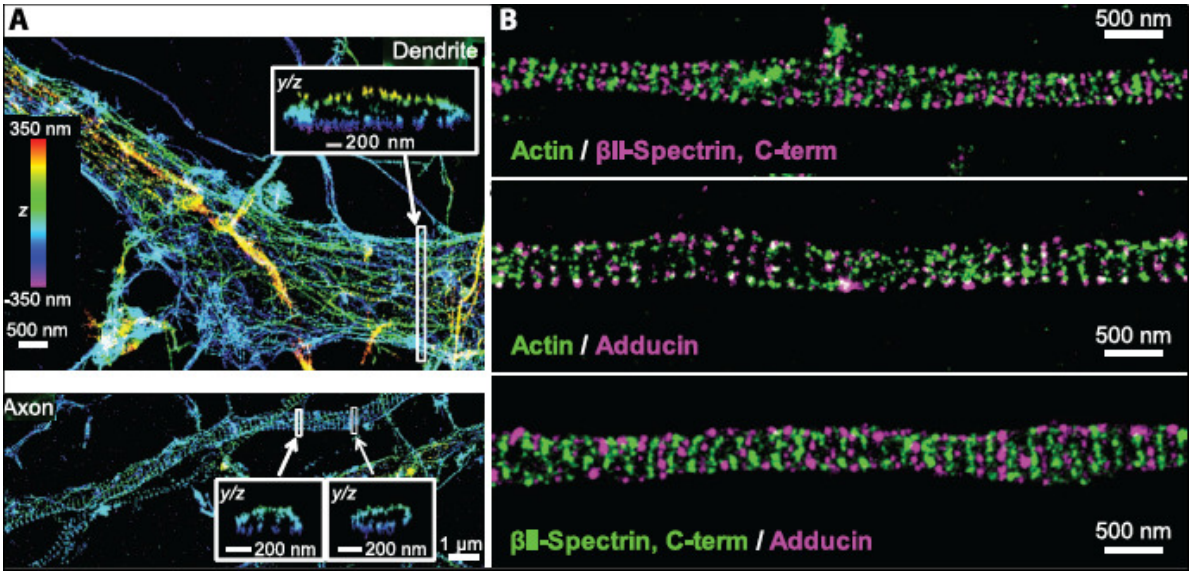

Figure I.8: **STORM imaging of cytoskeletal organization of axons and dendrites in hippocampal neurons al 7 DIV** [33]. A) Three-dimensional image of actin in a dendrite (top) and an axon (bottom). Color-scale shows from violet to red the z positions closest to farthest from the substratum, respectively. B) Actin, adducing and βII-Spectrin immunostaining in an axon.

The consequence of these actin structures in the regulation of shape and adhesive properties of axons and dendrites remains an open issue. The state of the art of our knowledge on the molecular features of neuronal adhesions will be exposed in a dedicated section (I.4).

I.2.5 Growth cone

The growth cone is another important specific structure of neurons. The growth cone is formed at the neurite tip during development to ensure neurite guidance. Its high dynamics and sensitivity toward guidance molecules play a key role in neuronal growth and polarization, as much as in neuronal adhesion, as will be discuss in next sections (I.3, I.4). Beside, it has been shown that a growth cone produce mechanical forces.

Structurally, a growth cone is composed of three areas that determine its shape and motion: a central zone filled with microtubules, an intermediary zone and a peripheral one, composed of lamellipodia and filopodia (Figure I.9). The intermediary area is made of an actin arc enclosing the microtubules coming from the shaft and receiving the retrograde actin flow from the peripheral zone. Myosin II, a main component of the actin arc, seems to actively constrain microtubules of the central domain through acto–myosin contractility, leading to the stabilization of microtubules [34].

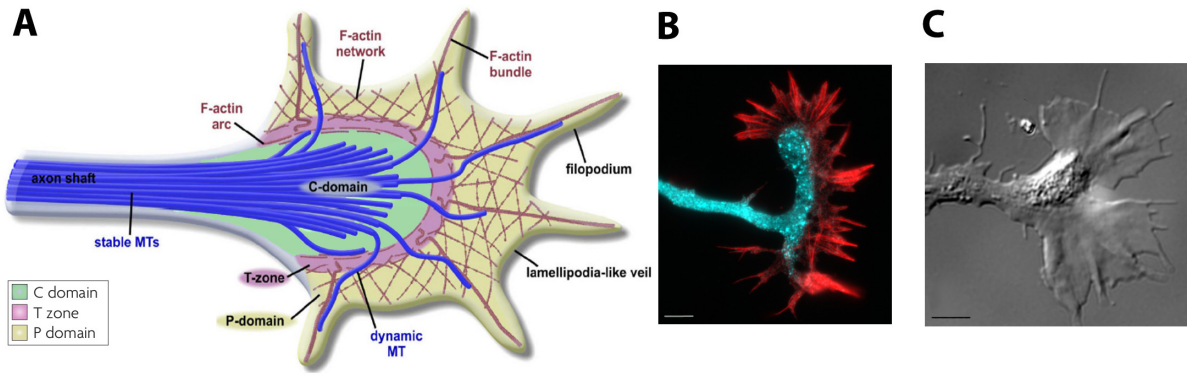

Figure I.9: **Growth cone.** A) Schematic representation of the three areas of a growth cone: the central (C) domain with stables microtubules, the transitional (T) zone with the actin arc enriched of myosin II and the peripheral domain (P), composed of lamellipodia and filopodia. Adapted from [34]. B) Example of growth cone in a mouse hippocampal neuron at 2 DIV. Cyan: synapsin. Red: phalloidin. Scale bar: 10 μm. C) Differential Interference Contrast image of a growth cone of a Xenopus spinal neuron [35]. Scale bar: 5 μm.

I.3 Neuronal cell growth and polarization

Embryonic **cortical** and **hippocampal neurons** development *in vitro* has been described by several stages identified by the morphological changes that occur during maturation [36, 37, 38] (Figure I.10). Soon after plating, lamellipodia and filopodia are observed at the periphery of the soma. After several hours, these structures become immature neurites [39]. The navigation of neurites in this phase is mainly guided by the presence of the **growth cone**. Then, one neurite starts to elongate faster than the other. This longest neurite will progressively acquire the molecular specificities of the axon and the other neurites will later fully differentiate into dendrites. Finally, the dendritic spines that characterize a mature functional network will appear after about two weeks of culture.

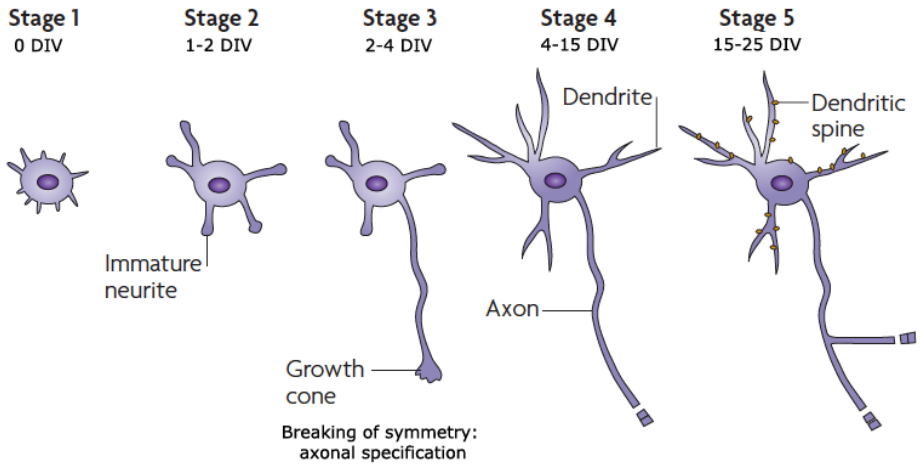

Figure I.10: **The generic stages of development of cortical/hippocampal neurons.** Time refers to mouse hippocampal neurons, expressed in Days In Vitro (DIV). Adapted from [38].

I.3.1 Mechanisms of neuronal polarization process

Neuronal polarization is the event that leads to the **axonal specification**. The common denominator of neuronal polarization both *in vivo* and *in vitro* is the **symmetry breaking** expressed by the distinct specific molecular and morphological characteristics of axons and dendrites [38] (Figure I.10).

Contrarily to the non–uniform chemical and topographical *in vivo* environment where numerous signals may orient the cell asymmetry associated with the polarization process, the emergence of a structural asymmetry *in vitro* results from a stochastic process leading to a random choice of the localization of axonal specification [40].

The mechanisms at the base of the breaking of symmetry associated to axonal specification during neuronal polarization are more and more investigated. Recent studies have focused on the interplay between extracellular signals and cytoskeletal organization, i.e. actin stability and microtubule protrusion [40]. Local instability of the actin network restricted to a single growth cone is a physiological signal that triggers neuronal polarization [41]. Axon specification is also associated with an increased microtubule stabilization in one of the neurites, but it is actually unclear how this stability is achieved.

Recently, it has been shown that, in cultured hippocampal neurons and in cortical slices, laminin promotes neuronal polarization, i.e. axon specification and growth, through adhesive contacts and a resultant regulation of directional microtubule assembly [42]. Both in vertebrate and invertebrate species, growth cones interact with their environment, i.e. with other cells, the physical substrate or diffusive molecular gradients. These aspects will be the subject of the next subsection.

I.3.2 Molecular neuronal growth and guidance

Over the past decade, a large effort has been made in developmental neurobiology to identify the repulsive and attractive molecules that guide axons.

Proteins that promote axonal outgrowth have been arranged in three distinct classes: **diffusible molecules**, such as trophic factors, **components of the ECM** and **cell adhesion molecules** (CAMs) [43]. **Trophic factors** regulate neuron growth and survival, as it was demonstrated by V. Hamburger and R. Levi Montalcini [44], who received the Nobel Prize in 1986 for the purification of the first trophic factor in the 1950s: the nerve growth factor (NGF). **ECM constituents** will be more detailed in a dedicate section (I.4). Let us mention here that **proteoglycan proteins** specifically regulate the structural organisation of the ECM, modulate growth factor activities and cellular adhesive and motility events, such as cell migration and axon outgrowth [45]. **CAMs** include calcium independent (immunoglobulin superfamily and integrins) and dependent (cadherins and selectins) proteins.

N-CAM and L1 belong to the immunoglobulin superfamily. L1 is mainly observed on fasciculating axons (i.e. axons growing on top of each others) whereas N-CAM is predominantly involved in the stabilization of the cell contacts and in the interactions between glial cells and neurons [46]. They also contribute to more complex processes like axonal pathfinding, target recognition, synapse formation and synaptic plasticity.
The main proteins that contribute to axonal navigation are the **semaphorins**. They act as axonal guidance during brain development of vertebrates by the capacity of growth cones to sense their signals.
Semaphorin-3A (Sema3A), the first discovered semaphorin, in 1993 [47], is repulsive for the axon and attractive for the dendrites of cortical neurons [48]. More generally, semaphorins are able to drive nerve fiber fasciculation as shown for example by the capacity of Sema3A to inhibit the branching of cortical axons growing on two-dimensional substrates [49].
Amongst others guidance molecules, we report the most commonly known netrins, slits and ephrins families.

Growth and guidance of CNS axons are also crucially influenced by the interaction with astroglial cells. Neurite outgrowth and growth cone motility are mainly mediated by two receptors: **N–cadherin** and **β1–class integrin**. The first one is a Ca^{2+}–dependent cell adhesion molecule, the second one is an ECM receptor. Chick ciliary ganglion neurons grown on cultured astrocytes had shown to be strongly influenced by these receptors at E8, whereas the influence of β1–integrin vanished at later stages [50]. The reduction of the integrin function during development, i.e. the interactions with several ECM proteins, including laminin, could be associated to the limited ability of adult CNS neurons to regenerate, in coherence with the regenerative potential played by laminin [51].
N-cadherin may have a primary importance in neuritic growth and it could be also implicated in adhesion between nerve and muscle *in vivo* [52], as well as in synaptogenesis [53].

I.3.3 Waves

To conclude this short introduction to neuronal growth and polarization, this section gives the basics of **growth cone–like structures** named "waves" that have been first observed in *in vitro* rat hippocampus cultures, mainly during the first stages (i.e. 2 and 3, Figure I.10) [54]. Waves are created at the soma level and travel to the neurite tip at a speed of approximately 3 $\mu m/min$ [54] (Figure I.11.A-C). They occasionally move in a retrograde direction (less than 5% of waves). These structures are similar to growth cones in their dynamics and composition [55]. Some previous works have suggested that these dynamical membrane deformations may recruit many actin–binding proteins, like GAP–43, Ezrin, Cortactin and the axon–promoting Shootin–1 protein [54, 56]. However, a global understanding of their molecular structure is

still missing.

The wave arrival at the neurite tip is systematically correlated with an initial retraction followed by an elongation of the neurite, leading to a net elongation, as well as an increase in the growth cone dynamics [57] (Figure I.11.D).

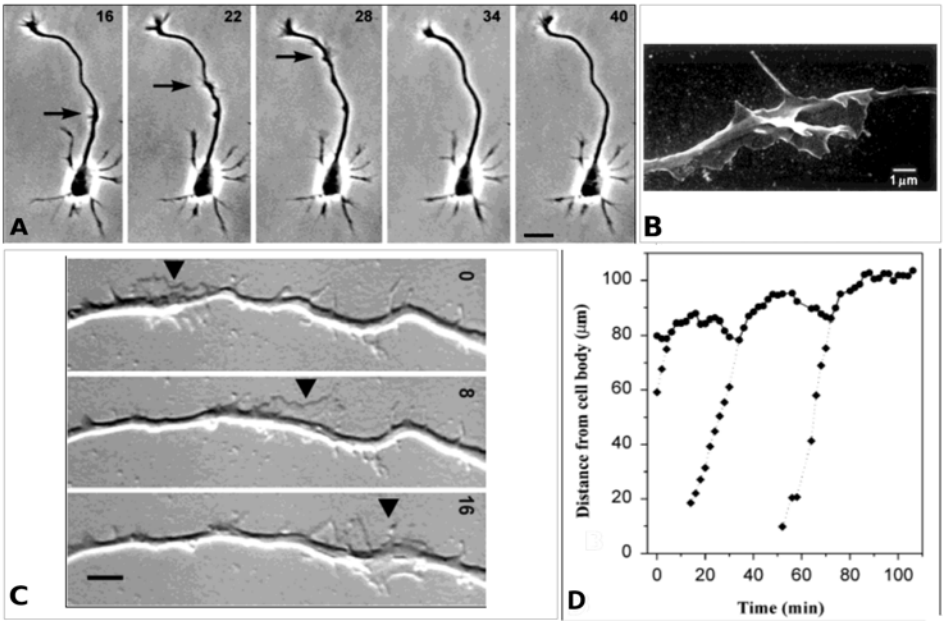

Figure I.11: A) Wave propagation along an axon (see arrows): phase contrast image of a rat hippocampal neuron after approximately 30 h in culture. Times are shown in minutes and correspond to the respective times in the graph in D). Scale bar: 20 μm. B) Scanning electron image showing 3D wave morphology of the rat hippocampal neuron. Scale bar: 1 μm. C) Wave propagation (see arrows) toward the growth cone of a rat hippocampal neuron (out-field), recorded after approximately 24 h in culture. Times are shown in minutes. Scale bar: 5 μm. D) Diagram of axon tip (circles) and wave (diamonds) positions in function of time during the wave propagation. Wave arrival is associated to an axon retraction and a subsequent elongation. Adapted from [57, 54].

Waves also contribute to the axon growth and to the creation of new branches [55]. The frequency of these waves is higher along the nascent axon (approximately 2 times more than in other neurites). Moreover, they were observed in hippocampal slices, confirming that they are not *in vitro* artifacts [55]. Several fundamental open issues related to waves remain, like their mechanisms of propagation and their possible role in the neuronal polarization process as well as in the axonal transport mechanism [55, 56].

I.4 Brain cell adhesion *in vitro*

Cell adhesion mechanisms are involved at all levels, i.e. from the maintenance of the cohesion of the neural tissue to the regulation of synaptic contacts in the mature nervous system. Cell adhesion molecules directly or indirectly interact with cytoplasmic proteins and cytoskeletal structures and therefore actively participate to various processes like cell spreading,

differentiation or motility [58].
Of note, the identities and functions of many cytoplasmic proteins in association with the ECM proteins are presently better understood in non-neural tissues, although several molecular and cellular mechanisms, like the regulation of cell adhesion and cell motility, are fundamentally similar in all cell types.

I.4.1 Extracellular matrix receptors and adhesion proteins

The main **ECM proteins** found in the brain are **laminin**, known to specifically foster axonal growth [59], **fibronectin**, **collagen** (e.g. collagen IV [60] is one of the main component of the basement membrane and collagen XVII has been observed mainly in the soma and proximal axons of CNS neurons but not in glial cells [61]) and the **heparan sulfate proteoglycan** [60]. It has been also reported that ECM proteins regulate the balance of neuronal (laminin and heparan sulfate) and glial (fibronectin) cell differentiation [62]. These basement membrane and fibrous matrix proteins are mainly present in the embryonic brain. It has been showed that laminin is expressed by astrocytes *in vitro* [63] and *in vivo* [64], that is coherent with a role for laminin in neuron-astrocyte interactions. Conversely, the main components of the ECM of the adult brain tissue are **lecticans**, a family of proteoglycans. This unique composition may exist in order to better resist against invasion by tumoral cells of non-neuronal origin [65].
Although these three kinds of ECM proteins are widely used as *in vitro* substrates of adhesion, non-specific adhesive molecules, i.e. **poly-L-lysine** (or its enantiomer **poly-D-lysine**, PLL and PDL respectively) and **poly-ornithine** (PLO), are also commonly employed. Due to the non-specific property of these positively-charged adhesive molecules, they are not directly linked to a specific receptor of the cell membrane and they are often employed as control. Of note, *in vitro* culture conditions have to be optimized for each kind of cells and complemented with specific supplements (e.g. serum, growth factors and glutamine) in order to achieve the best conditions of cell adhesion and survival [66].

For most cells, the membrane is attached to the ECM by integrin dependent adhesions called **focal adhesions** (FAs). In addition, a complex network of cytoplasmic proteins mediates the transmembrane interactions with the internal actin cytoskeleton. FAs play a central role in cell migration, morphology, proliferation, differentiation and death.
In neurons, the organization of these proteins of adhesion and the cell response to the ECM properties are poorly known. Due to its crucial role in neurite outgrowth and axonal guidance, the **growth cone** has been for a long time the focus of most studies on neuron adhesion.
In vitro rat Dorsal-Root Ganglia (DRG) neurons cultured on laminin substrate shows integrin clusters over the entire growth cone surface. The central domain of growth cones and the tips of filopodia present an high concentration of **vinculin**, an intracellular protein specifically

associated with FAs points and implicated in the control of growth cone motility, and of **paxillin** and **talin**, two cytoskeletal proteins colocalized with β1–integrins (Figure I.12).

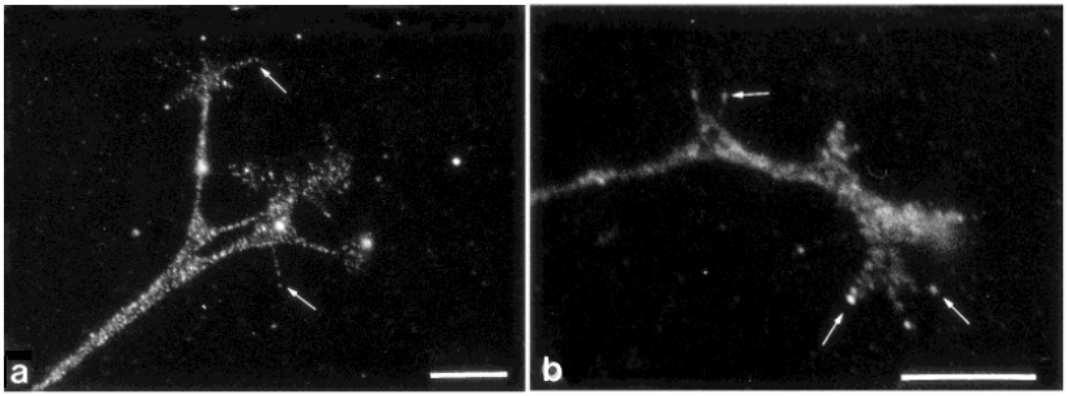

Figure I.12: **Growth cones focal adhesions of primary Dorsal-Root Ganglia neurons on laminin coated surfaces.** β1–integrin (A) and vinculin (B) immunoreaction (see arrows). Scale bar: 10 μm. Adapted from [67].

The rhoGTPases proteins RhoA, RhoB, and Cdc42, that activate the signaling pathways associated to actin polymerization and myosin activity, have been observed in growth cones, eventually colocalized with vinculin [67]. Another signal transduction protein, the focal adhesion kinase (FAK), was also observed in growth cones. **FAK** is a non-receptor tyrosine kinase that is required for the formation of growth cone adhesions. In non–neuronal cells, FAK is indispensable for the assembly of FAs, where it participates to adhesion-dependent intracellular signalling. FAK also promotes rapid neurite outgrowth by stabilizing lamellipodial protrusions on permissive ECM substrata, suggesting that FAK may control axon pathfinding *in vivo* [68, 69]. Biochemical analysis has revealed the presence of FAK immunoreactivity in cells neuronal lineage [70] and in CNS [71]. FAK is highly expressed in the CNS both during development and in the adult brain. FAK+, an isoform of FAK selectively enriched in neurons, is responsible for the localization of FAK to FAs. In hippocampal growth cones in culture, they overlap with F–actin enrichments but not with vinculin, showing a dependence of FAK distribution on F–actin organization [72]. Controversially, it has also been shown that primary hippocampal neurons display abundant FAK immunoreactivity in nerve cell bodies, neurites and growth cones, coinciding with clusters of vinculin [73]. It has also been showed in hippocampal neurons that FAKs ablation abolishes axon remodeling induced by Sema3A, a growth cone guidance molecule [74].

Recently, the role of adhesion proteins has also been investigated in more detail in neurites and especially in the axon. **Neurofascin** (NF186) and **neuron-glia related cell adhesion molecule** (NrCAM) are members of the L1–family, i.e. the immunoglobulin superfamily (IgSF

CAM) described in the subsection I.3.2. These proteins have been observed in the nodes of Ranvier, where they contribute to the nodes formation in both the PNS [75] and the CNS (excepted for NrCAM) [76], and in the axonal initial segment (AIS, see I.2.4). Their role in the AIS is still unclear. NF186 *in vivo* and *in vitro* could be necessary for AIS maintenance and NrCAM recruitment, whereas AnkG could be already required to coordinate AIS assembly [77]. The AIS stabilization could also be ensured by the NF186 ability to link key extracellular and membrane components, e.g. AnkG and gephyrin, the postsynaptic scaffolding protein that is required for clustering GABA receptors [29] (Figure I.13).

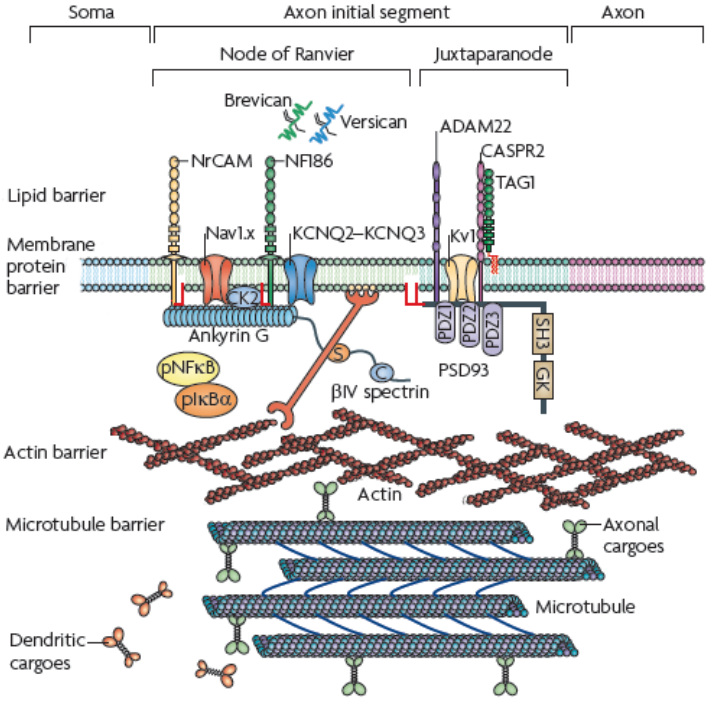

Figure I.13: **Neurofascin (NF186) and neuron-glia related cell adhesion molecule (NrCAM) in the axon initial segment (AIS) barrier.** The model proposed here suggests that a lipid barrier built up the AIS plasma membrane may influence diffusion rates in the AIS. The membrane protein barrier (including NF186 and NrCAM), established through binding to ankyrin G, limits the lateral mobility of other transmembrane proteins and lipids at the AIS. Actin filaments could contribute to the maintenance of the AIS barrier and the neuronal polarity by limiting the entry of cytoplasmic proteins into the axon through interactions with βIV spectrin. Microtubules should contribute to the maintenance of neuronal polarity allowing axonal but not dendritic cargoes to enter the axon [29].

In conclusion, cell adhesion proteins contribute to mediate axon guidance and growth by a direct influence on the cytoskeleton dynamics. In addition to these molecular approaches, a fine control of the microenvironment has interestingly allowed to dissect the specific role of the various chemical or physical features that promote neuronal growth and polarization. This will be the focus of the following section.

I.5 Brain cell response in controlled microenvironments

In this section, we will give an overview of a few important results on brain cell properties obtained in controlled microenvironments. Some are directly associated to the core of this work, some are more peripheral, but all illustrates the importance of micro-nanotechnological tools to either isolate the cell response to specific stimuli or to reveal properties that would be hidden in more conventional culture conditions.

I.5.1 Chemical, mechanical and topographical stimuli

In the developing embryonic brain, neurons undergo migration, growth, polarization and branching. These early features persist into the mature brain both in physiological conditions thanks to the existence of neurogenesis areas, and after injury where neuronal branches display a regrowth ability if provided with a suitable environment. The *in vivo* environment is the result of intricate guidance cues including diffusible factors and substrate-bound molecules (i.e. the ECM) as exposed in section I.3.2, but also rigidity and topography.
These three aspects and their roles will be separately dissected in the following sub-sections.

I.5.1.1 Guidance cues

Either the migration of neural precursors or the necessity for mature neurons to connect distant (at the scale of a soma) target sites imply guidance cues and a sensory machinery located at the growth cone. Directing neuronal navigation *in vitro* requires to reconstruct, eventually element by element, a migration microenvironment offering a combination of signaling, adhesive, and migration events. Since the seminal experiments based on co-cultures, where one cell type is used to secrete guidance factors for the surrounding neurons, a local release of guidance molecules have been implemented using glass micropipettes [78] or more sophisticated optical-based techniques [79]. However, only microfluidic tools allow a fine control of the concentration gradients (down to a few percent on the micrometric scale, i.e. more than ten times better than other techniques) and to follow multiple neuronal processes in the same experimental run [80]. These tools are particularly suitable to explore how living systems produce complexity and non-linearity from the combination of few elementary bricks. A first example is the use of the γ–aminobutyric acid (GABA)–A neurotransmitter in inhibitory synapses as a guidance molecule in the embryonic brain [81]. In addition, repulsive or attracting effects can be set up from a combinatory of a few sets of molecules like Netrin (Figure I.14) or Slit. It has recently been reported *in vivo* in a brain structure named the corridor that a combination of Slit (a repulsive cue) and Netrin (that does not trigger any chemiotactic effect) gradients generates an attractive effect on the axons crossing this brain area [82]. The ability of microfluidic tools to produce controlled multiple gradients of diffusible molecules will therefore

be an invaluable tool to decipher the molecule guidance alphabet of the brain. Moreover, the study of haptotaxis (i.e. the cell response to an adhesive gradient) is also an exploration field opened by microfluidic tools, as already demonstrated by Dertinger et al. [83], and by a novel promising multiplexed optical device enabling surface grafting at the micron scale ("Digital Mirror Device", [84]). If associated, these tools would enable the study of the cell responses to a combination of adhesive and diffusive gradients in *in vitro* systems, similarly to what occurs in the embryonic brain.

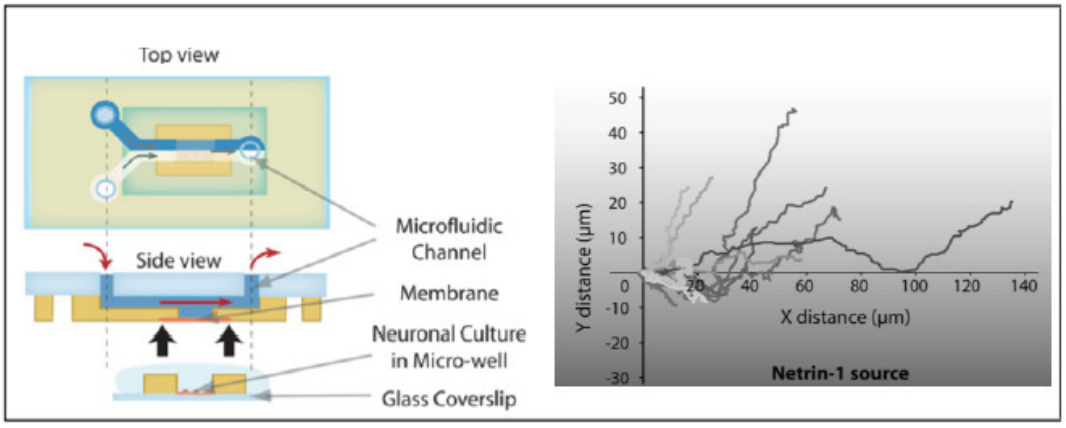

Figure I.14: **Cell response to guidance cues.** The chemical attractant, here Netrin delivered as a gradient within a microfluidic channel (left). The graph shows the repulsive effect of Netrin on the growth cone navigation (right) [81].

I.5.1.2 Rigidity

Cells regulate their morphology and adhesion by reaching the minimization of the total free energy in their interactions with the environment. Significant changes on the cell structure and functions in response to the substrate rigidity have been observed in many cell types. Nevertheless, brain cell mechanosensitivity has still to be clarified. In addition, the stiffness of brain cells themselves is another important aspect of the mechanics of the nervous system. Passive mechanical properties of the ECM and active forces inside the brain tissue influence neuronal development, e.g. axonal elongation and guidance [85, 86]. Moreover, knowledge on the mechanical properties of brain cells or tissues should increase our understanding of healthy versus diseased tissues, which often reveal distinct stiffness and mechanical sensitivity. Besides, brain implants could gain in biocompatibility and efficiency by coupling a control of their chemical, mechanical and eventually electrical properties [87].

Stiffness of the whole healthy brain has been estimated to be of several hundred Pa [88] taking into account that its precise value can be affected by conditions of the tissue preparation as well as by the age of the brain tissue [89, 90]. From a macroscopic point of view, brain

appears to be the softest tissue in comparison with relaxed muscles fibers (8 – 21 kPa) [91, 92], skin (∼102 kPa) [93] and rigid bones (∼106 kPa) [94]. The injured brain characterized by the higher presence of glial cells seems to be stiffer [95, 96] although neuron soma appears to be around one and a half stiffer that glial cells [97]. Generally, in the context of brain studies, "hard" and "soft" words are employed for elastic moduli respectively higher or lower of the limit value of a normal brain (∼1 kPa).

Neurite elongation in DRG neuron-glial cell co-cultures was significantly diminished on PLL coated visco-elastic polydimethylsiloxane (PDMS) substrates compared to rigid glass coverslip, with the observation of an optimum of neurite elongation and cell attachment on semi-rigid (∼88 kPa) substrates compared to the two other studied values of 18 and 173 kPa [98]. Another example of substrates was provided by self-assembled randomly oriented peptide nanofibers which display rigidities in the range 7 – 23 kPa according to the fiber density. An earlier axonal specification was observed for hippocampal mice neurons grown on these substrates [99]. However, in these two last examples, the adhesive chemistry (different on PDMS compared to glass coverslips) or the topography (fibers) are not deconvoluted from the rigidity parameter. To work with pure soft elastic and planar substrates, one has to use bis-acrylamide crosslinked polyacrylamide hydrogels. On such substrates, a rigidity as low as 200 – 300 Pa resulted in an increased neurite branching [100] and neurite number [101] without however changing the overall aspects of cells, e.g. the neurite length in the particular case of spinal cord [101] and cortical neurons [102]. Interestingly, the variation of the neurite number displayed a minimum in the range ∼30 – 100 kPa [101]. An intermediate stiffness range between 6 and 30 kPa has been achieved using a new class of polyacrylamide hydrogels cross-linked by DNA [103]. Inconsistently with other studies, an increase of the neurite number was observed toward the highest stiffness, associated to shorter axons and to a reduction in FAK expression. However, no significant difference in dendritic length were reported on these DNA-crosslinked gels for spinal cord neurons.

A similar trend of neuron length versus rigidity was found in pure neurons culture (95%) except for a two-fold increase in the number of adherent neurons between gel stiffness of 300 Pa and 230 kPa [101]. This observation suggests that the interaction between neurons and astrocytes might affect the neuronal response to the surface stiffness, especially on stiff gels, where well adherent astrocytes usually play a role of support. Although within a narrower range of rigidity (6 – 30 kPa), a later study has reported a similar trend also in mixed cultures [103]. Contrarily to neurons, astrocytes are very sensitive to rigidity in a large range between ∼250 Pa to more than 50 kPa. Indeed, these cells do not spread and show fewer stress fibers on soft gels coated with laminin (∼250 Pa) [102], or matrigel (mainly composed of laminin and collagen IV, ∼50 – 550 Pa) [100]. Similar effects were obtained on intermediate rigidities of ∼50 kPa [99]. Another study has confirmed a larger cell spreading on stiff gels and demonstrated that rigidity,

rather than a difference in the concentration of the PDL coating, was the parameter controlling this effect [104]. Interestingly, when adherent, astrocytes may adopt on soft gels the star-like shape characteristic of their *in vivo* morphology [104]. To summarize, astrocytes show similar responses to rigidity in both mixed and pure cultures.

In conclusion, the analysis of neuronal mechanosensing in a wide range of stiffness values has revealed the difficulty to achieve a global and consistent understanding for this quite unique cellular type in its response to rigidity. However, one important point is that neurons seem to be the only cell type that is able to polymerize F-actin on soft gels, compared with e.g. astrocytes, myotubes, fibroblasts and endothelial cells. These observations suggest that actin-myosin contractions in growth cone and in the lamellipodium of other cell types could not have the same role despite their structural similarity [102]. The high growth cone sensitivity to the mechanical properties could be due to its very low elastic modulus ($\sim$100 Pa) and internal stress ($\sim$30 $pN/\mu\text{m}^2$) [105]. At present time, only few results have been published. They have showed that the mechanosensitivity of neurons might be associated to several morphological changes: number of adherent cells, number and length of dendrites and axons. More investigations should be made in order to identify the differences and similarities among the neuronal cell types. This point highlights the crucial importance to decipher the relative importance between different factors of the ECM environment, e.g. topographical and structural aspects, substrate and medium chemical components, presence of other cells. For example, the issue of the mechanical interaction between neuron and glial cells [97] should be considered in future works. Actually, the critical challenge is to master the possibility to separate all these aspects taking into account the final context of application. Soft and intermediate rigidity substrates appear as promising tools to support neuronal development while impairing astrocytes proliferation (Figure I.15), and would be therefore suitable for applications concerning the nervous system regeneration [99].

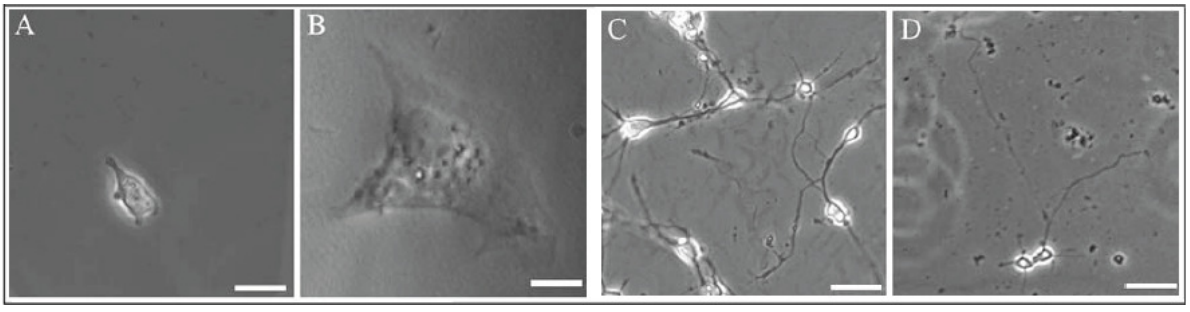

Figure I.15: **Cell response to rigidity.** Astrocytes appear more spread on hard gels, whereas neurons show insignificant differences. Phase contrast images of astrocytes (A, B) and cortical neurons (C, D) on soft (A and C respectively) and hard (B and D respectively) LN–coated gels at 2 Days *In Vitro*. Scale bars: 50 μm (A, B) and 25 μm (C, D) [102].

I.5.1.3 Topography: grooves and curvatures

Digging grooves, offering neurons to navigate on fibers may partially reproduce some key topographical cues found in the *in vivo* environment. In this subsection, the modalities of neuron interaction with grooves and curvatures will be discussed.

Grooves topography is characterized by depth, width and pitch values and it was the first to be implemented in usual protocols of cell cultures to mimic the aligned fibers of the extracellular matrix in a context of regenerative medicine. After the seminal work of Brunette [047] reporting an orientation effect of fibroblasts and epithelial cells on grooves, Clark et al. [048] have shown that the alignment of chick embryo cerebral neurites was inversely proportional to the grating pitch in the range 4 – 24 μm (2 μm deep and wide grooves). In the same line, experiments reported by Rajnicek et al. [106] demonstrated that a set of 1, 2 and 4 μm wide parallel grooves as faint as 14 nm in depth, separated by distances of 1 – 4 μm, could orient xenopus and hippocampal neurites either parallel or perpendicularly to the groove direction (Figure I.16.A). Interestingly, parallel guidance was enhanced for the largest pitch distance (i.e. 4 μm) and the neurite tendency to grow perpendicular was higher in hippocampal neurons extracted from early stage embryos (i.e. 16 days of gestation instead of 19). Of note, such a feature was also reported by Nagata et al. on neuroblasts [107].

The purpose with curvature structures is to reproduce the specific curvatures of 3D brain structures like blood vessels (diameters in the range 5 – 50 μm for capillary to small veins or artery [108]), myelinated bundled fibers ($\sim$10 μm [109]) and, at a the micrometric scale, the elongated radial glial cells providing tracks for neuronal migration [110].
A curvature induced neuritic guidance has been observed in two complementary studies. In the work of Smeal using isolated extruded polypropylene solid tubes of diameters ranging between 500 μm to 35 μm, therefore mimicking blood vessel diameters, the neurite guidance along the tube long axis increases continuously toward the finest fibers (Figure I.16.B) [111]. A similar result has been found on a collection of oriented sub-micrometric (150 nm to 400 nm) fibers [112], i.e. in the range of the characteristic sizes of neurite or radial glia processes. Moreover, it was found by previous works performed in our team that the neurite curvature imposed by curved adhesive stripes built from half–circles of diameter R inhibits axonal differentiation [113]. For R within the range 5 – 40 μm, the smallest curvature provides the largest discriminative effect between axon and dendrites specification.

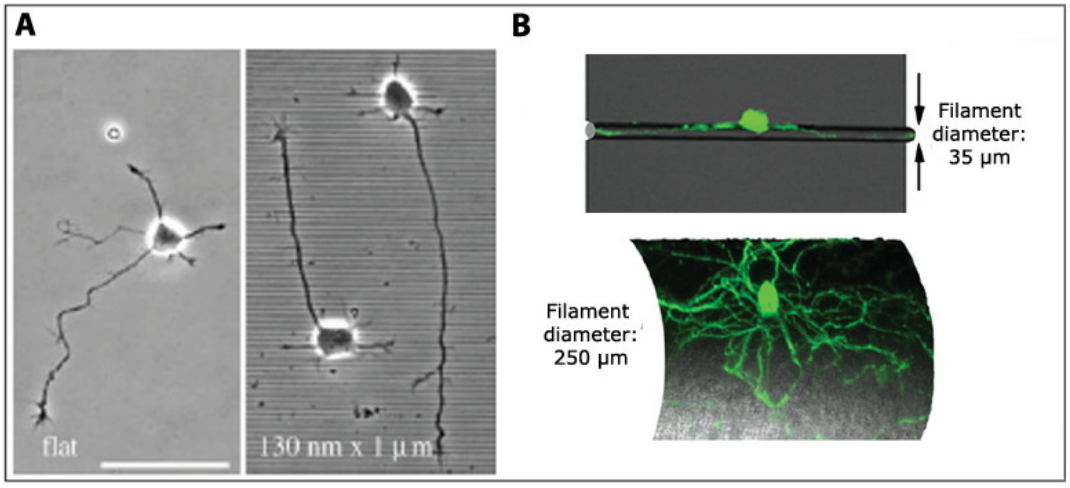

Figure I.16: **Cell response to topography: grooves and curvatures.** A) The effect of nanogrooves (1 μm wide, 130 nm deep) on Xenopus neuron growth, showing perpendicular and parallel extension of neurites with respects to grooves (right). Growth on a flat surface (left) is displayed as a control. Scale bar: 50 μm [106]. B) Curvature–induced alignment of DRG neurons on 35 μm (top) and 500 μm (bottom) fiber diameters [111].

In conclusion, these results highlight the responses of brain cells, and in particular neurons, in terms of adhesion, elongation or orientation phenomena. These responses ensue from various properties of the microenvironment reproducing to a certain extent typical *in vivo* features. More artificial growth conditions like micro or nanopillared surfaces, can reveal some neuronal properties that would be hidden in a more conventional context. This aspect will be developed in the next section.

I.5.2 Mechanical properties of neuronal cells

A fundamental aspect that will be developed in this subsection is related to the mechanical properties of neuronal extensions and their ability to generate forces. The seminal work of Bray [114] has suggested, from a vectorial analysis of the directions of neurite outgrowth on flat surfaces, that growth cones exerted a mechanical tension all along neurites. 3D topographies or micropatterns of adhesion have since allowed to visualize the tensile state of neurite.

I.5.2.1 Neurite tension and mechanical forces

The bending of highly flexible GaP nanowires by neurite transverse filopodia reported in the work of Hällström et al. [115] has revealed the mechanical forces exerted by these generic sub-cellular structures in the case of mice DRG neurons. When confronted to deep PDMS grooves in the range of tens to hundreds of microns, DRG neurite can exert forces sufficient to pull onto a cell body to suspend it above a groove between two ridges separated by 30 μm (Figure I.17) [116].

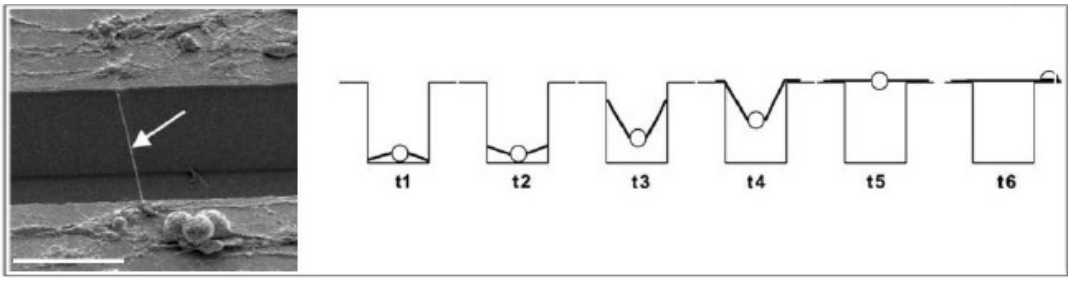

Figure I.17: **Neurite tension.** DRG neurons crossing deep PDMS grooves (arrow: suspended neurite). The sketch displays the sequence of events involving neuritic force generation leading to the configuration shows in the scanning electron microscopy image [116].

It has been previously shown by our team[1] using curvatures imposed by adhesive PLL micropatterns, that axons were under a higher tensile stress than minor processes [117]. Tension is then expressed by a curvature–dependent rate of neurite unhooking events that occur when adhesive forces are overcome by mechanical forces. Interestingly, quantitative values can be obtained indirectly from the neuronal response to topographical constraints like the neurite tension (in the range 1 – 10 nN) [117] or the bending stiffness $D \sim 10^{-27}\ Nm^2$ [111].
Concerning now neuron-neuron interactions, the use of ∼15 μm diameter carbon nanotubes islands located at 50 μm from each other (center to center distance) has revealed that extending neurites (locust frontal ganglion neurons) need to successfully reach a target situated on a neighboring adhesive site in order to be maintained [118]. This observation identifies the neurite tension as a key factor for the stabilization of axonal branches and possibly for the subsequent formation of synaptic contacts. The hypothesis that the mechanical tension behaves as a control signal modulating synaptic plasticity was similarly proposed by Siechen et al. [119] for neuromuscular synapses. Lastly, carbon nanotubes islands have been also employed to decipher the role of neurite tension in the mechanism of soma migration during the establishment of neuronal connections [120].

I.5.2.2 Discrete adhesive contacts

There is a significant literature about cellular interaction with pillared surfaces in the context of cell mechanics: the forces produced by the cells can be evaluated from pillars bending [121]. However, due the weak values (in the range of the nN) of both neurite tensions and the forces exerted by neurites on the growth cones [105], pillars are not the adequate substrate for a direct exploration of the mechanical properties of neurons. Basically, the principal interest of plating neurons on pillars was to explore the combined effects of a discontinuous surface of adhesion and of a pseudo 3D environment. The first review on the subject of neuron/topography interaction mentioning a neurite guidance effect on micropillars is dated from 2001 [122]. Since then, the micro- and nanotechnologies have produced a wide range of nanopil-

[1] in collaboration with the Grenoble Institute of Neuroscience

lar sizes to highlight the consequence of discontinuous adhesive contacts on neuronal growth. The accelerated neurite elongation and neuronal polarization observed in discontinuous or restricted adhesive conditions still requires a molecular understanding. However, this effect has been attributed to the discontinuous adhesive path associated to all these microenvironments that induces the formation of actin patches between which neurites might build mechanical forces [123]. Interestingly, this hypothesis brings together (i) the several lines of evidence suggesting that the fast elongating axon (relatively to the other neuronal processes) is the most tensed neurite [117, 124] and (ii) the recent discovery of the existence of periodic actin rings along the axon of hippocampal neurons (see Section I.2.4 and Figure I.8) [33]. Together, these two findings suggest that a high neurite elongation rate might require a discrete actin structure, either spontaneous (as the one built within the axon), or provided by artificial pillared surfaces. Another hypothesis relies on a possible channeling effect provided by topographies. Neurite directional choices were either clearly [123], or indirectly [125] evidenced on pillared surfaces, which might reduce the time required for the growth cone decision–making and consequently might trigger a faster elongation rate. To go further into this channeling effect hypothesis, a mechanism for accelerated growth based on the integration of signals emanating from non–aligned and aligned filopodia on a grooved surface was proposed [126].
Interestingly, these phenomenological effects might be already exploited for the design of implants to foster brain reparation after injuries.

In summary, this section has shown that the chemical and physical properties of the environment seem to behave as key players in the establishment or the stability of neuronal architectures. In particular, these signals can deeply enhance the neurite elongation rate and the directionality of neuronal branches. More generally, the features revealed by the interaction of neurons with their environment can provide useful tools to build controlled and stable neuronal networks, as discussed in the next section.

I.6 Control from single cell to population

Different levels of organization of neuronal assemblies characterize the brain. In order to meet this essential feature of the *in vivo* circuits, studies on neuronal adhesion and neurite guidance must at some point converge into methods allowing to built custom *in vitro* microcircuits of defined architecture, polarity and connectivity. This section gives an overview of the attempts to fulfill these three requirements in *in vitro* studies, considering neuronal assemblies either at the population or at the single cell level, and starting with the challenging issue of placing dissociated soma on their dedicated adhesive sites during the seeding step.

I.6.1 Active cell entrapment and long term soma positioning

When starting from a cell suspension, the filling of specific adhesive sites relies on the stochastic process of sedimentation: the remaining cells falling on non-adhesive surfaces are washed away shortly after seeding. This process inherently leads to a non-uniform and a low occupancy rate of the adhesive sites, ruled out by a Poisson distribution [127]. The cell occupancy rate of these sites could in principle be enhanced by increasing the cell concentration of the initial suspension or by taking advantage of cell motility [128]. However, due to the presence of thin adhesive lines guiding neuronal connections, the design of the adhesive micropatterns associated to neuronal microcircuits offers natural interstitial adhesive sites. Therefore, active strategies have to be implemented in order to increase the rate of soma site occupancy relatively to the rate of interstitial cells. Lastly, due to the mechanical tension produced by neurons, long term (i.e. from cell seeding to synapse formation) cell positioning implies not only to initially locate the soma but also to maintain its initial position despite the mechanical forces exerted by neurites.

Capturing individual soma was performed using a micropipette [129, 130], a laser guidance technique [131] or dielectrophoresis [132]. The phenomenon of dielectrophoresis is the motion of dielectric, i.e. non charged particles, under the influence of a non-uniform electric field. A cell can be attracted or repelled from a region of high magnetic field strength depending on the orientation of the electric dipole induced by the external electric field gradient. Dielectrophoresis presents the advantage to be intrinsically fast compared to individual cell positioning methods. An other promising methodology is the magnetic–based technique where magnetically labeled target cells can be efficiently captured thanks to the high magnetic field gradients generated by the microflux sources. Its efficacy has been demonstrated on bacteria [133] and on the mouse embryonic fibroblast cell line NIH/3T3 [134]. This large scale, multiplexed technique that could ultimately be pushed toward a single cell control is intrinsically transposable to other cells, e.g. neurons [135].

The other aspect associated to soma positioning is the issue of the long-term stability of soma localization. Up to now, stable soma pinning was mainly achieved from a physical confinement strategy using microchambers. These chambers can be simple wells [089], PDMS membranes [131, 136], arrays of picket fences [129] or more sophisticated structures like parylen neurocages (Figure II.26) that trap soma into 40 μm diameter open wells and let neurites free to colonize the outside substrate through 10 μm wide, 1 μm high tunnels [130]. However, dielectrophoresis or magnetic entrapment should also intrinsically offer active solutions for long term soma positioning.

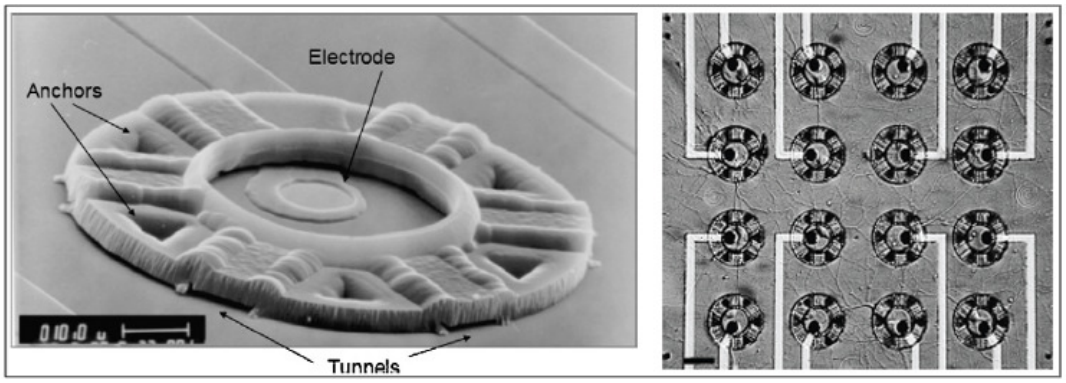

Figure I.18: **Neurochip and soma trapping.** Scanning Electron Microscope image of the parylene neurocage design (left), showing the central area for neurons placement, near the gold electrode, and the tunnels to allow axons and dendrites to grow through and to connect other neurons. Scale bar: 10 μm. 10 Days In Vitro culture of hippocampal cells (right) showing neurons trapped in the neurocages and a mesh of neurites outside cages. Scale bar: 30 μm [130].

I.6.2 Neuronal architecture and polarity

The control of neuronal architectures has been largely investigated by means of patterned substrates, although more exotic substrates like oriented carbon nanotubes (CNT) square arrays has proved to be interesting guiding structures for hippocampal neurons (Figure I.19.A) [137]. More generally, the versatility in the design of micropattern geometries has highlighted the cells ability to organize their cytoskeleton as a function of external constraints to control fundamental features such as neuronal adhesion, growth and neuronal polarization [138].

Photolitography and microcontact printing (μCP) techniques have been employed to create adhesive micropatterns characterized by various adhesive (e.g. ECM and CAM molecules) and non-adhesive surfaces (e.g. PLL–PEG [139] or agarose layer [140]). As an example, the number of adherent neurons, the soma spreading and the neurite number are observed to increase on PLL coated glass surfaces, compared to matrigel or laminin. On the other hand, matrigel and laminin promote neurite elongation. Fibronectin mainly selects non-neuronal cells adhesion and therefore is discarded for neuronal cultures.

An optimized design of the adhesive patters is necessary to build neuron networks and to preserve functional properties. As a preliminary step toward interconnected architectures, the use of minimal geometries of uniformly wide adhesive stripes was reported almost two decades ago [141]. This study enlightened the differences in the spatial range of the growth cone exploration between different neuron types (12 μm in chick embryo brain neurons, and 50 μm for mouse neonatal DRG neurons), setting the minimal distance between branches of a neuronal network. Then, more complex micropatterns built from non-parallel lines connected through relatively large spots dedicated to soma localization have been used to produce *in*

vitro organized neuronal networks [142, 143]. Patch-clamps recordings have been performed on mature neuronal networks growing on such patterned surfaces (Figure I.19.B) [144, 140] to validate their physiologic properties over several weeks.

The second step toward a full control of neuronal architectures is to force the axonal specification of a given neurite, eventually at the single cell level, thereby setting the axo–dendritic polarity of the network. It has been shown that axon guidance can be induced by stripes of triangles of different heights and widths in the range $10 - 70$ μm. Axons elongate from triangle to triangle preferentially through their tips rather than along the reverse direction [145]. A gradient of PLL or PLL and laminin achieved from the geometrical arrangement of rectangles of increasing length and decreasing gaps can play a similar role than stripes of triangles. A maximum rate of 84% of guided axons along a 4 μm–wide pattern of PLL along the direction of increasing concentration was then reported [146]. Rather than a succession of adhesive and non adhesive surfaces, an alternation of PLL, laminin and neuron–glia cell adhesion molecules (NgCAM) stripes have shown that (i) growth cone preferentially guides axons on laminin and NgCAM surfaces, and that (ii) crossing the frontier between the different coatings promotes axonal specification independently of the direction of crossing [59]. In the same line, mixed patterns of axonal–specific adhesive molecules superimposed to PLL lines have also been reported to achieve axonal positioning. In this work, a PLL pattern achieved by μCP was used to guide the elongation of minor neurites (i.e. the future dendrites) whereas the axonal specification and guidance was ensured by stripes coated with L1, a transmembrane adhesion protein expressed on the axon surface [147].

As already mentioned in section I.5.1.3 about previous works in our team, Roth et al. have shown that a combination of somatic and neuritic constraints (i.e. curvatures) can set the localization of axonal specification with a 87% selectivity (Figure I.19.C) [113].

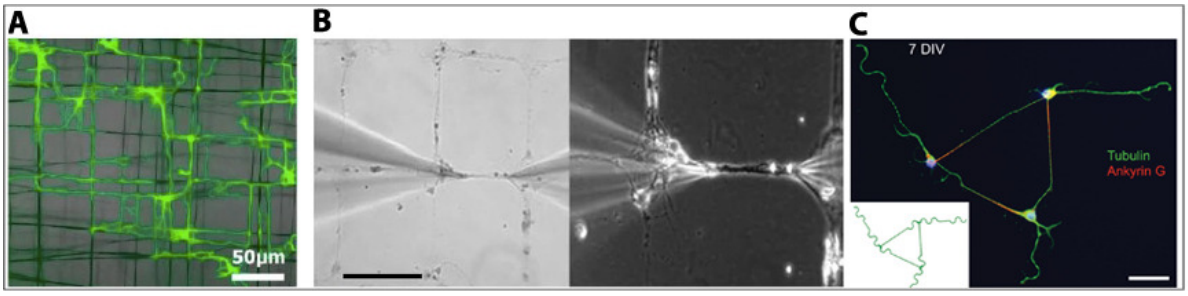

Figure I.19: **Neuronal controlled architectures.** A) E18 rat hippocampal neurons along cross–linked carbon nanotube yarn patterned substrate at 5 DIV. Neurons were incubated in Calcein–AM (30 $\mu g/ml$) (DojinDO, Japan) solution at 37 °C in 5% CO_2 for 25 min for staining. Dark lines: carbon nanotubes. Scale bar: 50 μm [137]. B) Bright field (left) and phase contrast (right) images illustrating patch–clamp recording performed on a square hippocampal neuronal network of PLL μCP patterns. Scale bar: 200 μm [140]. C) Three-neurons triangular network at 7 DIV guided by the microadhesive pattern shown in green in inset. Green: anti-tyrosinated tubulin, microtubules. Red: anti-ankyrinG, axon initial segment. Blue: Hoechst, nuclei. Scale bar: 50 μm [113].

Lastly, let us remark that one motivation for mastering neuronal architectures and polarity is to achieve a control of synaptic localization. In this context, the approach developed by Czöndör et al. [148] provided a novel and robust strategy to achieve a precise distribution of synaptic contacts by substituting the post-synaptic structure by micro-dots coated with various synaptogenetic adhesion molecules (e.g. neurexin–1β, SynCAM1).

I.6.3 Neuronal polarity at population levels

Complementarily to the search of a single-cell precision in *in vitro* neural architectures, connecting neuronal populations in a controlled way might be relevant to collect biological material in sufficient amount, or to induce collective effects reminiscent of the *in vivo* large networks. Distinct elegant strategies have been employed to re-create *in vitro* controlled architectures and unidirectional axon connectivity using microfluidic tools. In a seminal work, Taylor et al. [149] took advantage of the fast axonal elongation compared to minor processes to design a microfluidic axonal sorter using 10 μm wide, 3 μm high, and up to 900 μm long microchannels (Figure I.20).

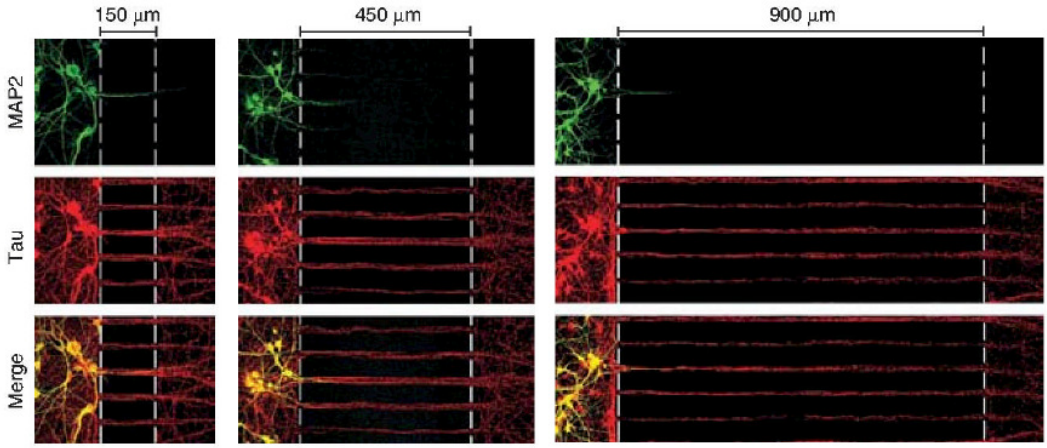

Figure I.20: **Neuronal populations controlled by microfluidics.** 150 to 900 μm wide barriers isolate axons from soma and dendrites at 14 DIV with an increasing efficacy according with barrier width. Red: Tau, axons. Green: MAP2, dendrites. Dashed lines indicate the barrier region [149].

An hydrostatic pressure difference on either side of the channel was established to maintained fluidic isolation and eventually to collect axonal RNA. In the same line, Peyrin et al. [150] fabricated asymmetrical funnel-shaped micro-channels named "axon diodes" to ensure an unidirectional axon connectivity with 97% selectivity using 15 to 3 μm funnels. Interestingly, this work has demonstrated the ability of microfluidic devices to interconnect neuron population of different cell types, e.g. cortical, hippocampal or striatal neurons, forming cortico–striatal or cortico–hippocampal functional synapses. Adhesive patterns in the millimiter range have also been employed to create another type of axonal diodes: in the work of Feinerman et al. [151], the 50 μm wide restricted contact zones joining millimeter sized triangles induced a preferential

unidirectional crossing of the axons toward the tip of these geometric shapes.
Some recent successful attempts have pushed the microfluidic approach toward single neuron precision. In the technique of Compartmentalized Neuron Arraying (CAN) developed by Dinh et al. [152], microfluidic channels were combined with a novel patterning method to use minimal neuronal inputs (about 1000 cells, i.e. 10 – 100-fold less than existing systems) and to increase by one order of magnitude the proportion of axons connecting two compartments. CAN is therefore a suitable method for the studies on rare cells like substantia nigra or dopaminergic neurons involved in Parkinson's research.

I.6.4 Coming research approaches and applications

Although surface topographies give an access to the cellular behavior in a 3D environment, true 3D substrates with comparable dimensions in the three directions of space were very recently developed [153, 154]. These structures should bring new insights in cell biology. Indeed, cell microenvironment is 3D and heterogeneous, whereas many studies are still achieved on 2D flat substrates that may induce different spatial distribution of cell interactions with ECM. For example, β1–integrin and FAK molecules in DRG neurons have shown to decrease their locally intracellular concentrations in 3D compared to 2D environments, altering cytoskeletal dynamics, i.e. cell adhesion and neurite length [155]. It would therefore be extremely interesting to see how 3D scaffolds might be used in neuroscience. A first attempt of neuronal culture on 3D porous scaffolds has been reported by Tian et al. [156] and constitutes a striking proof of concept of integrating nanoelectronics into a 3D cellular network.

Lastly, the possibility to master axonal guidance and positioning meets medical needs. The ability to reconstruct oriented and mixed neuronal networks in 3D microfluidics channels represents a stirring approach to develop suitable drugs for therapies of neurodegenerative syndromes, such as Alzheimer's and Parkinson's diseases [157]. Microengineering surfaces could also contribute to fulfill the challenging aim of guiding nerve repair and replacing the autograft approach [158]. Nerve guides are actually used for peripheral nerve regeneration (maximal curable nerve gaps from 3 to 8 cm) and different biocompatible materials are employed, both synthetic [159] and natural, i.e. collagen, silicon, skeletal muscles and mesothelial chambers [160]. A recent review in the field shows some examples of grafts successfully executed on human patients [161]. Direct applications of microengineering techniques, e.g. pores, grooves and polymer fibers, in the design of neuronal scaffolds are already illustrated by several reviews [162, 163, 164].

I.7 Context and objective of this work

In this first chapter, we have introduced the context of the present work. Firstly, we have provided the basics of brain cell structure and development, related to the biological aspects addressed in this manuscript. Then, we have reported the state-of-art of studies based on biophysical approaches, where microelectronic techniques meet brain cells. We have mainly focused on the works employing primary brain cells, as a first step towards a better understanding of brain tissue. We have concluded with some possible future evolutions of these works and their applications.

All these researches, including this PhD work, have become possible thanks to important progresses both from a point of view of microscopic observations and thanks to the achievable control at the micron and nanometric scale in the fabrication or the manipulation of objects. We highlight here some significant examples, fundamental for the realization of this work: the study of the cell dynamics thanks to the possibility to access to their microscopic scale and to manage a large amount of data, the techniques of immunofluorescence (or in general the visualisation techniques associated to fluorescent proteins) and the parallel development of fluorescent microscopes (with higher and higher resolutions) allowing the observation of specific internal properties of cells and, finally, the numerous microfabrication techniques coming from the microelectronics, such as the photolithography, to create micro or nano structured substrates for cell cultures.

These techniques have strongly contributed to the development of biophysics, and in particular of cell biophysics, which this work is part of. In this way, the physical approach is combined with the biological one. Physical methodologies tend to simplify and to quantify the expression of a specific character belonging to a more complex system. In general, the ultimate aim is to the develop a theoretical model giving the possibility to generalize or to predict a phenomenon, as well as to provide explanatory frameworks to some experimental observations. On the other hand, biology needs to reiterate experiments to obtain statistically robust results, compensating the biological variability. This PhD thesis research has been conducted with this double approach.

In the following chapters we will get to the heart of this PhD project. The focus of this work has been the study of fundamental questions linked to brain cell growth. In particular, we have investigated the phenomenon of the neuronal polarization and the glial cells sensitivity to the mechanical properties of their environment. These issues, poorly explored in the peculiar case of glial cell mechanosensitivity, have been studied here with a point of view that highlights cell interaction with its environment. For that, we have employed some methodologies coming from microelectronic technologies in order to reliably control the properties of the *in vitro* cell environment, using chemical and the physical patterns. Consistent with the purpose of the

state-of-art presented in this chapter and with the idea to remain close to the real biological system, we have made the choice to conduct this research using primary brain cells only.

Bibliography

[1] Philip G Haydon. Glia: listening and talking to the synapse. *Nature Reviews Neuroscience*, 2(3):185–193, 2001. 14

[2] Andrea Volterra and Jacopo Meldolesi. Astrocytes, from brain glue to communication elements: the revolution continues. *Nature Reviews Neuroscience*, 6(8):626–640, 2005. 15

[3] Andrew Koob. The root of thought: what do glial cells do. *Scientific American*, 2009. 15

[4] Michael Stiess and Frank Bradke. Neuronal polarization: the cytoskeleton leads the way. *Developmental neurobiology*, 71(6):430–444, 2011. 15, 17

[5] A Aldo Faisal and Simon B Laughlin. Stochastic simulations on the reliability of action potential propagation in thin axons. *PLoS computational biology*, 3(5):e79, 2007. 15

[6] John F Cryan and Andrew Holmes. The ascent of mouse: advances in modelling human depression and anxiety. *Nature reviews Drug discovery*, 4(9):775–790, 2005. 16

[7] Cécile Charrier, Kaumudi Joshi, Jaeda Coutinho-Budd, Ji-Eun Kim, Nelle Lambert, Jacqueline De Marchena, Wei-Lin Jin, Pierre Vanderhaeghen, Anirvan Ghosh, Takayuki Sassa, et al. Inhibition of srgap2 function by its human-specific paralogs induces neoteny during spine maturation. *Cell*, 149(4):923–935, 2012. 16

[8] DL Benson, FH Watkins, O Steward, and G Banker. Characterization of gabaergic neurons in hippocampal cell cultures. *Journal of neurocytology*, 23(5):279–295, 1994. 17, 110

[9] Wenqian Yu, Victoria E Centonze, Fridoon J Ahmad, and Peter W Baas. Microtubule nucleation and release from the neuronal centrosome. *The Journal of cell biology*, 122(2):349–359, 1993. 17

[10] Michael Stiess, Nicola Maghelli, Lukas C Kapitein, Susana Gomis-Rüth, Michaela Wilsch-Bräuninger, Casper C Hoogenraad, Iva M Tolić-Nørrelykke, and Frank Bradke. Axon extension occurs independently of centrosomal microtubule nucleation. *Science*, 327(5966):704–707, 2010. 17

[11] Francesca Bartolini and Gregg G Gundersen. Generation of noncentrosomal microtubule arrays. *Journal of cell science*, 119(20):4155–4163, 2006. 17

[12] Wenqian Yu and Peter W Baas. Changes in microtubule number and length during axon differentiation. *The Journal of neuroscience*, 14(5):2818–2829, 1994. 18

[13] Bruce Alberts, Alexander Johnson, Julian Lewis, Martin Raff, Keith Roberts, and Peter Walter. *Molecular biology of the cell, 5th edition*. Garland Science, 2007. 18, 21

[14] Anna Akhmanova and Michel O Steinmetz. Tracking the ends: a dynamic protein network controls the fate of microtubule tips. *Nature reviews Molecular cell biology*, 9(4):309–322, 2008. 19

[15] Chen Gu, Wei Zhou, Manojkumar A Puthenveedu, Mingxuan Xu, Yuh Nung Jan, and Lily Yeh Jan. The microtubule plus-end tracking protein eb1 is required for kv1 voltage-gated k^+ channel axonal targeting. *Neuron*, 52(5):803–816, 2006. 19

[16] Sara Geraldo, Umme K Khanzada, Maddy Parsons, John K Chilton, and Phillip R Gordon-Weeks. Targeting of the f-actin-binding protein drebrin by the microtubule plus-tip protein eb3 is required for neuritogenesis. *Nature cell biology*, 10(10):1181–1189, 2008. 19

[17] Melissa C Hendershott and Ronald D Vale. Regulation of microtubule minus-end dynamics by camsaps and patronin. *Proceedings of the National Academy of Sciences*, 111(16):5860–5865, 2014. 19

[18] Kah Wai Yau, Sam FB van Beuningen, Inês Cunha-Ferreira, Bas Cloin, Eljo Y van Battum, Lena Will, Philipp Schätzle, Roderick P Tas, Jaap van Krugten, Eugene A Katrukha, et al. Microtubule minus-end binding protein camsap2 controls axon specification and dendrite development. *Neuron*, 82(5):1058–1073, 2014. 19

[19] Elisabetta Menna, Andrea Disanza, Cinzia Cagnoli, Ursula Schenk, Giuliana Gelsomino, Emanuela Frittoli, Maud Hertzog, Nina Offenhauser, Corinna Sawallisch, Hans-Jürgen Kreienkamp, et al. Eps8 regulates axonal filopodia in hippocampal neurons in response to brain-derived neurotrophic factor (bdnf). *PLoS biology*, 7(6):e1000138, 2009. 19, 165

[20] Harvey Lodish, Arnold Berk, Paul Matsudaira, Chris A. Kaiser, Monty Krieger, Matthew P. Scott, Lawrence Zipursky, and James Darnell. *Molecular cell biology, 5th edition*. Freeman and Co., 2004. 20

[21] Matthias Kneussel and Wolfgang Wagner. Myosin motors at neuronal synapses: drivers of membrane transport and actin dynamics. *Nature Reviews Neuroscience*, 14(4):233–247, 2013. 20

[22] Heather Wood. Directing neurofilament traffic. *Nature Reviews Neuroscience*, 5(4):260–260, 2004. 21

[23] Peter W Baas, Jeffrey S Deitch, Mark M Black, and Gary A Banker. Polarity orientation of microtubules in hippocampal neurons: uniformity in the axon and nonuniformity in the dendrite. *Proceedings of the National Academy of Sciences*, 85(21):8335–8339, 1988. 21

[24] Zofia M Lasiecka, Chan Choo Yap, Max Vakulenko, and Bettina Winckler. Compartmentalizing the neuronal plasma membrane: From axon initial segments to synapses. *International review of cell and molecular biology*, 272:303–389, 2008. 21

[25] Anna Brachet, Christophe Leterrier, Marie Irondelle, Marie-Pierre Fache, Victor Racine, Jean-Baptiste Sibarita, Daniel Choquet, and Benedicte Dargent. Ankyrin g restricts ion channel diffusion at the axonal initial segment before the establishment of the diffusion barrier. *J Cell Biol*, 191(2):383–395, Oct 2010. 21

[26] Christophe Leterrier, Hélène Vacher, Marie-Pierre Fache, Stéphanie Angles d'Ortoli, Francis Castets, Amapola Autillo-Touati, and Bénédicte Dargent. End-binding proteins eb3 and eb1 link microtubules to ankyrin g in the axon initial segment. *Proceedings of the National Academy of Sciences*, 108(21):8826–8831, 2011. 21

[27] Susana Gomis-Rüth, Corette J Wierenga, and Frank Bradke. Plasticity of polarization: changing dendrites into axons in neurons integrated in neuronal circuits. *Current Biology*, 18(13):992–1000, 2008. 21, 22, 116

[28] Hideaki Yamamoto, Takanori Demura, Mayu Morita, Gary A Banker, Takashi Tanii, and Shun Nakamura. Differential neurite outgrowth is required for axon specification by cultured hippocampal neurons. *Journal of neurochemistry*, 123(6):904–910, 2012. 21, 125, 129

[29] Matthew N Rasband. The axon initial segment and the maintenance of neuronal polarity. *Nature Reviews Neuroscience*, 11(8):552–562, 2010. 22, 30

[30] Kathy A Suprenant. Microtubules, ribosomes, and rna: evidence for cytoplasmic localization and translational regulation. *Cell motility and the cytoskeleton*, 25(1):1–9, 1993. 22

[31] Fiala John C, Spacek Josef, and Harris Kristen M. Dendritic spine pathology: cause or consequence of neurological disorders? *Brain Research Reviews*, 39(1):29–54, 2002. 22

[32] Jeffery L Twiss and Mike Fainzilber. Ribosomes in axons–scrounging from the neighbors? *Trends in cell biology*, 19(5):236–243, 2009. 22

[33] Ke Xu, Guisheng Zhong, and Xiaowei Zhuang. Actin, spectrin, and associated proteins form a periodic cytoskeletal structure in axons. *Science*, 339(6118):452–456, 2013. 22, 23, 38

[34] Laura Anne Lowery and David Van Vactor. The trip of the tip: understanding the growth cone machinery. *Nature reviews Molecular cell biology*, 10(5):332–343, 2009. 23, 24

[35] Jacob H Hines, Steven J Henle, Lucas P Carlstrom, Mohammad Abu-Rub, and John R Henley. Single vesicle imaging indicates distinct modes of rapid membrane retrieval during nerve growth. *BMC biology*, 10(1):4, 2012. 24

[36] Carlos G Dotti, Christopher A Sullivan, and Gary A Banker. The establishment of polarity by hippocampal neurons in culture. *The Journal of neuroscience*, 8(4):1454–1468, 1988. 24

[37] Anthony P Barnes and Franck Polleux. Establishment of axon-dendrite polarity in developing neurons. *Annual review of neuroscience*, 32:347, 2009. 24

[38] Nariko Arimura and Kozo Kaibuchi. Neuronal polarity: from extracellular signals to intracellular mechanisms. *Nature Reviews Neuroscience*, 8(3):194–205, 2007. 24, 25

[39] Leif Dehmelt and Shelley Halpain. Actin and microtubules in neurite initiation: are maps the missing link? *Journal of neurobiology*, 58(1):18–33, 2004. 24

[40] Frank Bradke and Carlos G Dotti. Establishment of neuronal polarity: lessons from cultured hippocampal neurons. *Current opinion in neurobiology*, 10(5):574–581, 2000. 25

[41] Frank Bradke and Carlos G Dotti. The role of local actin instability in axon formation. *Science*, 283(5409):1931–1934, 1999. 25

[42] Wen-Liang Lei, Shi-Ge Xing, Cai-Yun Deng, Xiang-Chun Ju, Xing-Yu Jiang, and Zhen-Ge Luo. Laminin/β1 integrin signal triggers axon formation by promoting microtubule assembly and stabilization. *Cell research*, 22(6):954–972, 2012. 25

[43] Louis F Reichardt, JL Bixby, DE Hall, MJ Ignatius, KM Neugebauer, and KJ Tomaselli. Integrins and cell adhesion molecules: neuronal receptors that regulate axon growth on extracellular matrices and cell surfaces. *Developmental neuroscience*, 11(4-5):332–347, 1989. 25

[44] Rita Levi-Montalcini. The nerve growth factor 35 years later. *Science*, 237(4819):1154–1162, 1987. 25

[45] Paola Bovolenta and Isabel Fernaud-Espinosa. Nervous system proteoglycans as modulators of neurite outgrowth. *Progress in neurobiology*, 61(2):113–132, 2000. 25

[46] E Persohn and M Schachner. Immunohistological localization of the neural adhesion molecules l1 and n-cam in the developing hippocampus of the mouse. *Journal of neurocytology*, 19(6):807–819, 1990. 26

[47] Yuling Luo, David Raible, and Jonathan A Raper. Collapsin: a protein in brain that induces the collapse and paralysis of neuronal growth cones. *Cell*, 75(2):217–227, 1993. 26

[48] Dominique Bagnard. *Neuropilin: From Nervous System to Vascular and Tumor Biology*. Kluwer Academic/Plenum Pub., 2002. 26

[49] Dominique Bagnard, Marion Lohrum, Daniela Uziel, AW Puschel, and Jürgen Bolz. Semaphorins act as attractive and repulsive guidance signals during the development of cortical projections. *Development*, 125(24):5043–5053, 1998. 26

[50] Kevin J Tomaselli, Karla M Neugebauer, John L Bixby, Jack Lilien, and Louis F Reichard. N-cadherin and integrins: two receptor systems that mediate neuronal process outgrowth on astrocyte surfaces. *Neuron*, 1(1):33–43, 1988. 26

[51] Paivi Liesi. Laminin-immunoreactive glia distinguish regenerative adult cns systems from non-regenerative ones. *The EMBO journal*, 4(10):2505, 1985. 26

[52] Kohei Hatta, Shin Takagi, Hajime Fujisawa, and Masatoshi Takeichi. Spatial and temporal expression pattern of n-cadherin cell adhesion molecules correlated with morphogenetic processes of chicken embryos. *Developmental biology*, 120(1):215–227, 1987. 26

[53] Olivier Thoumine, Mireille Lambert, René-Marc Mège, and Daniel Choquet. Regulation of n-cadherin dynamics at neuronal contacts by ligand binding and cytoskeletal coupling. *Molecular biology of the cell*, 17(2):862–875, 2006. 26

[54] Gordon Ruthel and Gary Banker. Actin-dependent anterograde movement of growth-cone-like structures along growing hippocampal axons: A novel form of axonal transport? *Cell motility and the cytoskeleton*, 40(2):160–173, 1998. 26, 27, 129, 133

[55] Kevin C Flynn, Chi W Pak, Alisa E Shaw, Frank Bradke, and James R Bamburg. Growth cone-like waves transport actin and promote axonogenesis and neurite branching. *Developmental neurobiology*, 69(12):761–779, 2009. 26, 27, 129, 133

[56] Michinori Toriyama, Tadayuki Shimada, Ki Bum Kim, Mari Mitsuba, Eiko Nomura, Kazuhiro Katsuta, Yuichi Sakumura, Peter Roepstorff, and Naoyuki Inagaki. Shootin1: A protein involved in the organization of an asymmetric signal for neuronal polarization. *The Journal of cell biology*, 175(1):147–157, 2006. 26, 27

[57] Gordon Ruthel and Gary Banker. Role of moving growth cone–like "wave" structures in the outgrowth of cultured hippocampal axons and dendrites. *Journal of neurobiology*, 39(1):97–106, 1999. 27, 95, 133, 134

[58] Barry M Gumbiner. Proteins associated with with cytoplasmic surface of adhesion molecules. *Neuron*, 11(4):551–564, 1993. 28

[59] Teresa Esch, Vance Lemmon, and Gary Banker. Local presentation of substrate molecules directs axon specification by cultured hippocampal neurons. *The Journal of neuroscience*, 19(15):6417–6426, 1999. 28, 41, 67, 167

[60] Lorraine W Lau, Rowena Cua, Michael B Keough, Sarah Haylock-Jacobs, and V Wee Yong. Pathophysiology of the brain extracellular matrix: a new target for remyelination. *Nature Reviews Neuroscience*, 14(10):722–729, 2013. 28

[61] Allan Seppänen, Tiina Suuronen, Silke C Hofmann, Kari Majamaa, and Irina Alafuzoff. Distribution of collagen xvii in the human brain. *Brain research*, 1158:50–56, 2007. 28

[62] Yan Li, Meimei Liu, Yuanwei Yan, and Shang-Tian Yang. Neural differentiation from pluripotent stem cells: The role of natural and synthetic extracellular matrix. *World journal of stem cells*, 6(1):11, 2014. 28

[63] Ivan Selak, Jean-Michel Foidart, and Gustave Moonen. Laminin promotes cerebellar granule cells migration in vitro and is synthesized by cultured astrocytes. *Developmental neuroscience*, 7(5-6):278–285, 1985. 28

[64] James Cohen, Julia F Burne, Calum McKinlay, and Janet Winter. The role of laminin and the laminin/fibronectin receptor complex in the outgrowth of retinal ganglion cell axons. *Developmental biology*, 122(2):407–418, 1987. 28

[65] Erkki Ruoslahti. Brain extracellular matrix. *Glycobiology*, 6(5):489–492, 1996. 28

[66] Stefanie Kaech and Gary Banker. Culturing hippocampal neurons. *Nature protocols*, 1(5):2406–2415, 2007. 28, 84

[67] A Renaudin, M Lehmann, JA Girault, and L McKerracher. Organization of point contacts in neuronal growth cones. *Journal of neuroscience research*, 55(4):458–471, 1999. 29

[68] Estuardo Robles and Timothy M Gomez. Focal adhesion kinase signaling at sites of integrin-mediated adhesion controls axon pathfinding. *Nature neuroscience*, 9(10):1274–1283, 2006. 29

[69] Ana I Navarro and Beatriz Rico. Focal adhesion kinase function in neuronal development. *Current opinion in neurobiology*, 27:89–95, 2014. 29

[70] Chi Zhang, Mary P Lambert, Chris Bunch, Kirsten Barber, Warren S Wade, Grant A Krafft, and William L Klein. Focal adhesion kinase expressed by nerve cell lines shows increased tyrosine phosphorylation in response to alzheimer's a beta peptide. *Journal of Biological Chemistry*, 269(41):25247–25250, 1994. 29

[71] Ferran Burgaya, Andrea Menegon, Mathias Menegoz, Flavia Valtorta, and Jean-Antoine Girault. Focal adhesion kinase in rat central nervous system. *European Journal of Neuroscience*, 7(8):1810–1821, 1995. 29

[72] Andrea Contestabile, Dario Bonanomi, Ferran Burgaya, Jean-Antoine Girault, and Flavia Valtorta. Localization of focal adhesion kinase isoforms in cells of the central nervous system. *International journal of developmental neuroscience*, 21(2):83–93, 2003. 29

[73] Gerin R Stevens, Chi Zhang, Margaret M Berg, Mary P Lambert, Kirsten Barber, Isabel Cantallops, Aryeh Routtenberg, and William L Klein. Cns neuronal focal adhesion kinase forms clusters that co-localize with vinculin. *Journal of neuroscience research*, 46(4):445–455, 1996. 29

[74] Mariola R Chacón, Gloria Fernández, and Beatriz Rico. Focal adhesion kinase functions downstream of sema3a signaling during axonal remodeling. *Molecular and Cellular Neuroscience*, 44(1):30–42, 2010. 29

[75] Yael Eshed, Konstantin Feinberg, Sebastian Poliak, Helena Sabanay, Offra Sarig-Nadir, Ivo Spiegel, John R Bermingham Jr, and Elior Peles. Gliomedin mediates schwann cell-axon interaction and the molecular assembly of the nodes of ranvier. *Neuron*, 47(2):215–229, 2005. 30

[76] Barbara Zonta, Steven Tait, Shona Melrose, Heather Anderson, Sheila Harroch, Jennifer Higginson, Diane L Sherman, and Peter J Brophy. Glial and neuronal isoforms of neurofascin have distinct roles in the assembly of nodes of ranvier in the central nervous system. *The Journal of cell biology*, 181(7):1169–1177, 2008. 30

[77] Barbara Zonta, Anne Desmazieres, Arianna Rinaldi, Steven Tait, Diane L Sherman, Matthew F Nolan, and Peter J Brophy. A critical role for neurofascin in regulating action potential initiation through maintenance of the axon initial segment. *Neuron*, 69(5):945–956, 2011. 30

[78] Guo-li Ming, Ann M Lohof, and James Q Zheng. Acute morphogenic and chemotropic effects of neurotrophins on cultured embryonic xenopus spinal neurons. *The Journal of neuroscience*, 17(20):7860–7871, 1997. 31

[79] Dirk Sieger, Christian Moritz, Thomas Ziegenhals, Sergey Prykhozhij, and Francesca Peri. Long-range ca< sup> 2+</sup> waves transmit brain-damage signals to microglia. *Developmental cell*, 22(6):1138–1148, 2012. 31

[80] Nirveek Bhattacharjee, Nianzhen Li, Thomas M Keenan, and Albert Folch. A neuron-benign microfluidic gradient generator for studying the response of mammalian neurons towards axon guidance factors. *Integrative Biology*, 2(11-12):669–679, 2010. 31

[81] Mathieu Morel, Vasyl Shynkar, Jean-Christophe Galas, Isabelle Dupin, Cedric Bouzigues, Vincent Studer, and Maxime Dahan. Amplification and temporal filtering during gradient sensing by nerve growth cones probed with a microfluidic assay. *Biophysical journal*, 103(8):1648–1656, 2012. 31, 32

[82] Franck Bielle, Paula Marcos-Mondéjar, Eduardo Leyva-Díaz, Ludmilla Lokmane, Erik Mire, Caroline Mailhes, Maryama Keita, Noelia García, Marc Tessier-Lavigne, Sonia Garel, et al. Emergent growth cone responses to combinations of slit1 and netrin 1 in thalamocortical axon topography. *Current Biology*, 21(20):1748–1755, 2011. 31

[83] Stephan KW Dertinger, Xingyu Jiang, Zhiying Li, Venkatesh N Murthy, and George M Whitesides. Gradients of substrate-bound laminin orient axonal specification of neurons. *Proceedings of the National Academy of Sciences*, 99(20):12542–12547, 2002. 32, 167

[84] Kevin J Luebke, Duane E Carter, Harold R Garner, and Kathlynn C Brown. Patterning adhesion of mammalian cells with visible light, tris (bipyridyl) ruthenium (ii) chloride, and a digital micromirror array. *Journal of Biomedical Materials Research Part A*, 68(4):696–703, 2004. 32

[85] Daniel M Suter and Kyle E Miller. The emerging role of forces in axonal elongation. *Progress in neurobiology*, 94(2):91–101, 2011. 32

[86] Kristian Franze. The mechanical control of nervous system development. *Development*, 140(15):3069–3077, 2013. 32

[87] Pouria Moshayedi, Gilbert Ng, Jessica CF Kwok, Giles SH Yeo, Clare E Bryant, James W Fawcett, Kristian Franze, and Jochen Guck. The relationship between glial cell mechanosensitivity and foreign body reactions in the central nervous system. *Biomaterials*, 35(13):3919–3925, 2014. 32

[88] Amit Gefen and Susan S Margulies. Are in vivo and in situ brain tissues mechanically similar? *Journal of biomechanics*, 37(9):1339–1352, 2004. 32, 180

[89] Kirk L Thibault and Susan S Margulies. Age-dependent material properties of the porcine cerebrum: effect on pediatric inertial head injury criteria. *Journal of biomechanics*, 31(12):1119–1126, 1998. 32

[90] Ilya Levental, Penelope C Georges, and Paul A Janmey. Soft biological materials and their impact on cell function. *Soft Matter*, 3(3):299–306, 2007. 32

[91] Yoshiki Umazume and Norikatsu Kasuga. Radial stiffness of frog skinned muscle fibers in relaxed and rigor conditions. *Biophysical journal*, 45(4):783–788, 1984. 33

[92] Adam J Engler, Ludovic Richert, Joyce Y Wong, Catherine Picart, and Dennis E Discher. Surface probe measurements of the elasticity of sectioned tissue, thin gels and polyelectrolyte multilayer films: correlations between substrate stiffness and cell adhesion. *Surface Science*, 570(1):142–154, 2004. 33

[93] S Diridollou, F Patat, F Gens, L Vaillant, D Black, JM Lagarde, Y Gall, and M Berson. In vivo model of the mechanical properties of the human skin under suction. *Skin Research and technology*, 6(4):214–221, 2000. 33

[94] Adam J Engler, Shamik Sen, H Lee Sweeney, and Dennis E Discher. Matrix elasticity directs stem cell lineage specification. *Cell*, 126(4):677–689, 2006. 33, 76

[95] Philip J Horner and Fred H Gage. Regenerating the damaged central nervous system. *Nature*, 407(6807):963–970, 2000. 33

[96] Yun-Bi Lu, Ianors Iandiev, Margrit Hollborn, Nicole Körber, Elke Ulbricht, Petra G Hirrlinger, Thomas Pannicke, Er-Qing Wei, Andreas Bringmann, Hartwig Wolburg, et al. Reactive glial cells: increased stiffness correlates with increased intermediate filament expression. *The FASEB Journal*, 25(2):624–631, 2011. 33, 180

[97] Yun-Bi Lu, Kristian Franze, Gerald Seifert, Christian Steinhäuser, Frank Kirchhoff, Hartwig Wolburg, Jochen Guck, Paul Janmey, Er-Qing Wei, Josef Käs, et al. Viscoelastic properties of individual glial cells and neurons in the cns. *Proceedings of the National Academy of Sciences*, 103(47):17759–17764, 2006. 33, 34

[98] Chao-Min Cheng, Philip R LeDuc, and Yi-Wen Lin. Localized bimodal response of neurite extensions and structural proteins in dorsal-root ganglion neurons with controlled polydimethylsiloxane substrate stiffness. *Journal of biomechanics*, 44(5):856–862, 2011. 33, 180

[99] Shantanu Sur, Christina J Newcomb, Matthew J Webber, and Samuel I Stupp. Tuning supramolecular mechanics to guide neuron development. *Biomaterials*, 34(20):4749–4757, 2013. 33, 34, 180

[100] Lisa A Flanagan, Yo-El Ju, Beatrice Marg, Miriam Osterfield, and Paul A Janmey. Neurite branching on deformable substrates. *Neuroreport*, 13(18):2411, 2002. 33, 180

[101] Xue Jiang, Penelope C Georges, Baogang Li, Yangzhou Du, Melinda K Kutzing, Michelle L Previtera, Noshir A Langrana, and Bonnie L Firestein. Cell growth in response to mechanical stiffness is affected by neuron-astroglia interactions. *The Open Neuroscience Journal*, 1(1):7–14, 2007. 33

[102] Penelope C Georges, William J Miller, David F Meaney, Evelyn S Sawyer, and Paul A Janmey. Matrices with compliance comparable to that of brain tissue select neuronal over glial growth in mixed cortical cultures. *Biophysical journal*, 90(8):3012–3018, 2006. 33, 34, 76, 180

[103] Frank Xue Jiang, Bernard Yurke, Bonnie L Firestein, and Noshir A Langrana. Neurite outgrowth on a dna crosslinked hydrogel with tunable stiffnesses. *Annals of biomedical engineering*, 36(9):1565–1579, 2008. 33

[104] Pouria Moshayedi, Luciano da F Costa, Andreas Christ, Stephanie P Lacour, James Fawcett, Jochen Guck, and Kristian Franze. Mechanosensitivity of astrocytes on optimized polyacrylamide gels analyzed by quantitative morphometry. *Journal of Physics: Condensed Matter*, 22(19):194114, 2010. 34, 180

[105] Timo Betz, Daniel Koch, Yun-Bi Lu, Kristian Franze, and Josef A Käs. Growth cones as soft and weak force generators. *Proceedings of the National Academy of Sciences*, 108(33):13420–13425, 2011. 34, 37, 146, 147

[106] A Rajnicek, Stephen Britland, and C McCaig. Contact guidance of cns neurites on grooved quartz: influence of groove dimensions, neuronal age and cell type. *Journal of cell science*, 110(23):2905–2913, 1997. 35, 36

[107] Isao Nagata, Akio Kawana, and Norio Nakatsuji. Perpendicular contact guidance of cns neuroblasts on artificial microstructures. *Development*, 117(1):401–408, 1993. 35

[108] Mary P Wiedeman. Dimensions of blood vessels from distributing artery to collecting vein. *Circulation research*, 12(4):375–378, 1963. 35

[109] Tessa Gordon and Victor F Rafuse. Size of myelinated nerve fibres is not increased by expansion of the peripheral field in cats. *The Journal of physiology*, 532(3):835–849, 2001. 35

[110] H Troy Ghashghaei, Cary Lai, and ES Anton. Neuronal migration in the adult brain: are we there yet? *Nature Reviews Neuroscience*, 8(2):141–151, 2007. 35

[111] Roy M Smeal, Richard Rabbitt, Roy Biran, and Patrick A Tresco. Substrate curvature influences the direction of nerve outgrowth. *Annals of Biomedical Engineering*, 33(3):376–382, 2005. 35, 36, 37

[112] N Dubey, PC Letourneau, and RT Tranquillo. Neuronal contact guidance in magnetically aligned fibrin gels: effect of variation in gel mechano-structural properties. *Biomaterials*, 22(10):1065–1075, 2001. 35

[113] Sophie Roth, Ghislain Bugnicourt, Mariano Bisbal, Sylvie Gory-Fauré, Jacques Brocard, and Catherine Villard. Neuronal architectures with axo-dendritic polarity above silicon nanowires. *Small*, 8(5):671–675, 2012. 35, 41

[114] D Bray. Mechanical tension produced by nerve cells in tissue culture. *Journal of cell science*, 37(1):391–410, 1979. 36

[115] Waldemar Hällström, Christelle N Prinz, Dmitry Suyatin, Lars Samuelson, Lars Montelius, and Martin Kanje. Rectifying and sorting of regenerating axons by free-standing nanowire patterns: A highway for nerve fibers. *Langmuir*, 25(8):4343–4346, 2009. 36

[116] Joshua S Goldner, Jan M Bruder, Grace Li, Daniele Gazzola, and Diane Hoffman-Kim. Neurite bridging across micropatterned grooves. *Biomaterials*, 27(3):460–472, 2006. 36, 37

[117] Sophie Roth, Mariano Bisbal, Jacques Brocard, Ghislain Bugnicourt, Yasmina Saoudi, Annie Andrieux, Sylvie Gory-Fauré, and Catherine Villard. How morphological constraints affect axonal polarity in mouse neurons. *PloS one*, 7(3):e33623, 2012. 37, 38, 141

[118] Sarit Anava, Alon Greenbaum, Eshel Ben Jacob, Yael Hanein, and Amir Ayali. The regulative role of neurite mechanical tension in network development. *Biophysical journal*, 96(4):1661–1670, 2009. 37

[119] Scott Siechen, Shengyuan Yang, Akira Chiba, and Taher Saif. Mechanical tension contributes to clustering of neurotransmitter vesicles at presynaptic terminals. *Proceedings of the National Academy of Sciences*, 106(31):12611–12616, 2009. 37

[120] Y Hanein, O Tadmor, S Anava, and A Ayali. Neuronal soma migration is determined by neurite tension. *Neuroscience*, 172:572–579, 2011. 37

[121] Léa Trichet, Jimmy Le Digabel, Rhoda J Hawkins, Sri Ram Krishna Vedula, Mukund Gupta, Claire Ribrault, Pascal Hersen, Raphaël Voituriez, and Benoît Ladoux. Evidence of a large-scale mechanosensing mechanism for cellular adaptation to substrate stiffness. *Proceedings of the National Academy of Sciences*, 109(18):6933–6938, 2012. 37

[122] HG Craighead, CD James, and AMP Turner. Chemical and topographical patterning for directed cell attachment. *Current opinion in solid state and materials science*, 5(2):177–184, 2001. 37

[123] Liesbeth Micholt, Annette Gärtner, Dimiter Prodanov, Dries Braeken, Carlos G Dotti, and Carmen Bartic. Substrate topography determines neuronal polarization and growth in vitro. *PloS one*, 8(6):e66170, 2013. 38

[124] Phillip Lamoureux, Gordon Ruthel, Robert E Buxbaum, and Steven R Heidemann. Mechanical tension can specify axonal fate in hippocampal neurons. *The Journal of cell biology*, 159(3):499–508, 2002. 38, 141, 142

[125] Ghislain Bugnicourt, Jacques Brocard, Alice Nicolas, and Catherine Villard. Nanoscale surface topography reshapes neuronal growth in culture. *Langmuir*, 30(15):4441–4449, 2014. 38

[126] Kyung-Jin Jang, Min Sung Kim, Daniel Feltrin, Noo Li Jeon, Kahp-Yang Suh, and Olivier Pertz. Two distinct filopodia populations at the growth cone allow to sense nanotopographical extracellular matrix cues to guide neurite outgrowth. *PloS one*, 5(12):e15966, 2010. 38

[127] Kosuke Ino, Mina Okochi, Nao Konishi, Masahiro Nakatochi, Rentaro Imai, Mitsuhiro Shikida, Akira Ito, and Hiroyuki Honda. Cell culture arrays using magnetic force-based cell patterning for dynamic single cell analysis. *Lab on a Chip*, 8(1):134–142, 2008. 39

[128] Peter JF Röttgermann, Alicia Piera Alberola, and Joachim O Rädler. Cellular self-organization on micro-structured surfaces. *Soft matter*, 10(14):2397–2404, 2014. 39

[129] Günther Zeck and Peter Fromherz. Noninvasive neuroelectronic interfacing with synaptically connected snail neurons immobilized on a semiconductor chip. *Proceedings of the National Academy of Sciences*, 98(18):10457–10462, 2001. 39

[130] Jonathan Erickson, Angela Tooker, Y-C Tai, and Jerome Pine. Caged neuron mea: A system for long-term investigation of cultured neural network connectivity. *Journal of neuroscience methods*, 175(1):1–16, 2008. 39, 40

[131] Russell Kirk Pirlo, Xiang Peng, Xiaocong Yuan, and Bruce Zhi Gao. Microfabrication, surface modification, and laser guidance techniques to create a neuron biochip. *Optoelectronics letters*, 4(5):387–390, 2008. 39

[132] Shalini Prasad, Xuan Zhang, Mo Yang, Yingchun Ni, Vladimir Parpura, Cengiz S Ozkan, and Mihrimah Ozkan. Separation of individual neurons using dielectrophoretic alternative current fields. *Journal of neuroscience methods*, 135(1):79–88, 2004. 39

[133] Jérémy Pivetal, Sylvain Toru, Marie Frenea-Robin, Naoufel Haddour, Sébastien Cecillon, Nora M Dempsey, Frédéric Dumas-Bouchiat, and Pascal Simonet. Selective isolation of bacterial cells within a microfluidic device using magnetic probe-based cell fishing. *Sensors and Actuators B: Chemical*, 195:581–589, 2014. 39

[134] NM Dempsey, D Le Roy, H Marelli-Mathevon, Gorky Shaw, A Dias, RBG Kramer, M Kustov, LF Zanini, C Villard, K Hasselbach, C Tomba, and F Dumas-Bouchiat. Micro-magnetic imprinting of high field gradient magnetic flux sources. *Applied Physics Letters*, 104(26):262401, 2014. 39, 97

[135] Cécile Delacour, Ghislain Bugnicourt, Nora M Dempsey, Frédéric Dumas-Bouchiat, and Catherine Villard. Combined magnetic and chemical patterning for neural architectures. *Journal of Physics D: Applied Physics*, 47(42):425403, 2014. 39, 96

[136] Laurent Griscom, Patrick Degenaar, Bruno LePioufle, Eiichi Tamiya, and Hiroyuki Fujita. Techniques for patterning and guidance of primary culture neurons on microelectrode arrays. *Sensors and Actuators B: Chemical*, 83(1):15–21, 2002. 39

[137] Li Fan, Chen Feng, Wenmei Zhao, Li Qian, Yuquan Wang, and Yadong Li. Directional neurite outgrowth on superaligned carbon nanotube yarn patterned substrate. *Nano letters*, 12(7):3668–3673, 2012. 40, 41

[138] Joseph M Corey and Eva L Feldman. Substrate patterning: an emerging technology for the study of neuronal behavior. *Experimental neurology*, 184:89–96, 2003. 40, 62, 65

[139] Sébastien G Ricoult, Jennifer S Goldman, David Stellwagen, David Juncker, and Timothy E Kennedy. Generation of microisland cultures using microcontact printing to pattern protein substrates. *Journal of neuroscience methods*, 208(1):10–17, 2012. 40, 69

[140] Emanuele Marconi, Thierry Nieus, Alessandro Maccione, Pierluigi Valente, Alessandro Simi, Mirko Messa, Silvia Dante, Pietro Baldelli, Luca Berdondini, and Fabio Benfenati. Emergent functional properties of neuronal networks with controlled topology. *PloS one*, 7(4):e34648, 2012. 40, 41

[141] Peter Clark, Stephen Britland, and Patricia Connolly. Growth cone guidance and neuron morphology on micropatterned laminin surfaces. *Journal of cell science*, 105(1):203–212, 1993. 40

[142] Angela K Vogt, Lars Lauer, Wolfgang Knoll, and Andreas Offenhäusser. Micropatterned substrates for the growth of functional neuronal networks of defined geometry. *Biotechnology progress*, 19(5):1562–1568, 2003. 41

[143] Alessia Petrelli, Emanuele Marconi, Marco Salerno, Davide De Pietri Tonelli, Luca Berdondini, and Silvia Dante. Nano-volume drop patterning for rapid on-chip neuronal connect-ability assays. *Lab on a Chip*, 13(22):4419–4429, 2013. 41

[144] Claire Wyart, Christophe Ybert, Laurent Bourdieu, Catherine Herr, Christelle Prinz, and Didier Chatenay. Constrained synaptic connectivity in functional mammalian neuronal networks grown on patterned surfaces. *Journal of neuroscience methods*, 117(2):123–131, 2002. 41

[145] Mark A Scott, Zachary D Wissner-Gross, and Mehmet Fatih Yanik. Ultra-rapid laser protein micropatterning: screening for directed polarization of single neurons. *Lab on a Chip*, 12(12):2265–2276, 2012. 41

[146] Rita Fricke, Peter D Zentis, Lionel T Rajappa, Boris Hofmann, Marko Banzet, Andreas Offenhäusser, and Simone H Meffert. Axon guidance of rat cortical neurons by microcontact printed gradients. *Biomaterials*, 32(8):2070–2076, 2011. 41, 167

[147] Anthony A Oliva Jr, Conrad D James, Caroline E Kingman, Harold G Craighead, and Gary A Banker. Patterning axonal guidance molecules using a novel strategy for microcontact printing. *Neurochemical research*, 28(11):1639–1648, 2003. 41, 167

[148] Katalin Czöndör, Mikael Garcia, Amélie Argento, Audrey Constals, Christelle Breillat, Béatrice Tessier, and Olivier Thoumine. Micropatterned substrates coated with neuronal adhesion molecules for high-content study of synapse formation. *Nature communications*, 4, 2013. 42

[149] Anne M Taylor, Mathew Blurton-Jones, Seog Woo Rhee, David H Cribbs, Carl W Cotman, and Noo Li Jeon. A microfluidic culture platform for cns axonal injury, regeneration and transport. *Nature methods*, 2(8):599–605, 2005. 42

[150] Jean-Michel Peyrin, Bérangère Deleglise, Laure Saias, Maéva Vignes, Paul Gougis, Sebastien Magnifico, Sandrine Betuing, Mathéa Pietri, Jocelyne Caboche, Peter Vanhoutte, et al. Axon diodes for the reconstruction of oriented neuronal networks in microfluidic chambers. *Lab on a Chip*, 11(21):3663–3673, 2011. 42

[151] Ofer Feinerman, Assaf Rotem, and Elisha Moses. Reliable neuronal logic devices from patterned hippocampal cultures. *Nature Physics*, 4(12):967–973, 2008. 42

[152] Ngoc-Duy Dinh, Ya-Yu Chiang, Heike Hardelauf, Jenny Baumann, Emily Jackson, Sarah Waide, Julia Sisnaiske, Jean-Philippe Frimat, Christoph van Thriel, Dirk Janasek, et al. Microfluidic construction of minimalistic neuronal co-cultures. *Lab on a Chip*, 13(7):1402–1412, 2013. 43

[153] Franziska Klein, Benjamin Richter, Thomas Striebel, Clemens M Franz, Georg von Freymann, Martin Wegener, and Martin Bastmeyer. Two-component polymer scaffolds for controlled three-dimensional cell culture. *Advanced materials*, 23(11):1341–1345, 2011. 43

[154] Tiemo Bückmann, Nicolas Stenger, Muamer Kadic, Johannes Kaschke, Andreas Frölich, Tobias Kennerknecht, Christoph Eberl, Michael Thiel, and Martin Wegener. Tailored 3d mechanical metamaterials made by dip-in direct-laser-writing optical lithography. *Advanced Materials*, 24(20):2710–2714, 2012. 43

[155] Andreia Ribeiro, S Balasubramanian, D Hughes, S Vargo, EM Powell, and JB Leach. β1-integrin cytoskeletal signaling regulates sensory neuron response to matrix dimensionality. *Neuroscience*, 248:67–78, 2013. 43

[156] Bozhi Tian, Jia Liu, Tal Dvir, Lihua Jin, Jonathan H Tsui, Quan Qing, Zhigang Suo, Robert Langer, Daniel S Kohane, and Charles M Lieber. Macroporous nanowire nanoelectronic scaffolds for synthetic tissues. *Nature materials*, 11(11):986–994, 2012. 43

[157] Bérangère Deleglise, Benjamin Lassus, Vaneyssa Soubeyre, Aurélie Alleaume-Butaux, Johannes J Hjorth, Maéva Vignes, Benoit Schneider, Bernard Brugg, Jean-Louis Viovy, and Jean-Michel Peyrin. Synapto-protective drugs evaluation in reconstructed neuronal network. *PloS one*, 8(8):e71103, 2013. 43

[158] Amélie Béduer, Inès Gonzales-Calvo, Christophe Vieu, Isabelle Loubinoux, and Laurence Vaysse. Investigation of the competition between cell/surface and cell/cell interactions during neuronal cell culture on a micro-engineered surface. *Macromolecular bioscience*, 13(11):1546–1555, 2013. 43

[159] Xu Jiang, Shawn H Lim, Hai-Quan Mao, and Sing Yian Chew. Current applications and future perspectives of artificial nerve conduits. *Experimental neurology*, 223(1):86–101, 2010. 43

[160] Elizabeth O Johnson and Panayotis N Soucacos. Nerve repair: experimental and clinical evaluation of biodegradable artificial nerve guides. *Injury*, 39(3):30–36, 2008. 43

[161] Xiaosong Gu, Fei Ding, Yumin Yang, and Jie Liu. Construction of tissue engineered nerve grafts and their application in peripheral nerve regeneration. *Progress in neurobiology*, 93(2):204–230, 2011. 43

[162] Nicolas N Madigan, Siobhan McMahon, Timothy OíBrien, Michael J Yaszemski, and Anthony J Windebank. Current tissue engineering and novel therapeutic approaches to axonal regeneration following spinal cord injury using polymer scaffolds. *Respiratory physiology & neurobiology*, 169(2):183–199, 2009. 43

[163] Laura MY Yu, Nic D Leipzig, and Molly S Shoichet. Promoting neuron adhesion and growth. *Materials today*, 11(5):36–43, 2008. 43

[164] P Roach, T Parker, N Gadegaard, and MR Alexander. Surface strategies for control of neuronal cell adhesion: a review. *Surface Science Reports*, 65(6):145–173, 2010. 43

Chapter II

Materials and Methods

Contents

Chapitre II : résumé

Dans ce chapitre nous présentons l'ensemble des méthodes utilisées avec une description détaillée des protocoles expérimentaux : les différentes méthodes de préparation des substrats microstructurés et leur fonctionalisation, les techniques de cultures et de marquages de cellules primaires du cerveau, les techniques d'observation et d'analyse employées. Cette partie méthodologique est très développée en raison de la variété des approches employées au cours de ce travail de thèse. Ce chapitre se termine par la présentation d'une méthode utilisant des sites magnétiques pour positionner de façon contrôlée les cellules, avec un intérêt particulier pour les corps cellulaires des neurones.

List of abbreviations and nomenclatures

AFM ..... Atomic Force Microscope

ATRP ..... Atom Transfer Radical Polymerization

BSA ..... Bovine Serum Albumin

CAMs ..... Cell Adhesion Molecules

DHM ..... Digital Holographic Microscope

DI ..... Deionized

DIV ..... Days In Vitro

DMEMs ..... Dulbecco's Modified Eagle Medium ("s" is for "supplemented")

ECM ..... Extracellular matrix

EDTA ..... Ethylene-Diamine-Tetra-Acetic acid

FN ..... Fibronectin

GFAP ..... Glial Fibrillary Acid Protein

LN ..... Laminin

MEMs ..... Minimum Essential Medium ("s" is for "supplemented")

NBs ..... NeuroBasal ("s" is for "supplemented")

PA ..... PolyAcrylamide

PBS ..... Phosphate buffered saline

PDMS ..... PolyDiMethylSiloxane

PLL ..... Poly-L-lysine

PLO ..... Poly-ornithine

PNIPAM ..... Poly(N-isopropylacrylamide)

UV ..... Ultraviolet

3D, 2D ..... 3 and 2 dimensions

In this chapter we will present the protocols, the instrumentations and the methods employed during this PhD project. As methodologies are a common denominator of experiments discussed in separated contexts, we have made the choice to group them in a dedicated chapter.

We will describe the preparation of the substrates for cell seeding, the protocols employed for the neuronal and the glial cell cultures and the different microscopy set–ups. We will illustrate the principles of the protocols in the figures, their successive steps will be in details described in the text and the product information will be found in the footnotes.
These sections will be followed by a section dedicated to the methods of data analysis and by a last one describing a few techniques to control the cell positioning *in vitro*.

II.1 Patterned substrates

The substrate is one of the critical aspects of the *in vitro* experiments. Indeed, it constitutes both the physical and chemical support of cellular growth.
We have here employed microstructured substrates and created patterns of chemical, structural or mechanical properties.

II.1.1 Chemical patterns

Photolithography and micropatterning techniques have been largely employed to create controlled adhesive surfaces, in order to investigate the cell sensitivity to their environment. This technique gives the possibility to analyse cell response to chemical stimuli (mainly ECM and CAM molecules) as well as to control the cell morphology, by the control of the surface of adhesion. These tools have highlighted the cells ability to organize their cytoskeleton, i.e. morphology and functions. They have therefore contributed to analyse the mechanical properties involved in cell adhesion and growth, e.g the axonal polarization in neurons [1].
We describe the various steps of preparation of our substrates. We have used glass coverslips of different size and shapes (circular or square) depending on the application (thickness of 170 μm). Firstly, the surface is treated so as to acquire anti-adhesive properties, then the patterns are formed with a photolithographic step followed by the incubation of adhesive molecules. The first steps take place in a cleanroom. The last step is performed under the hood of the culture room in order to avoid any contaminations.

II.1.1.1 Silanization: hydrophobic treatment

The silanization is a reaction that makes a surface hydrophobic. The generic formula of the silanes presented in this section is $X-(CH_2)_n-Si(OR)_3$, where X is a functional group reacting with organic materials, located on the hydrophobic side of the chain and OR

is a functional group reacting with inorganic materials, like glass. The $(OR)_3$ group gives a relative stability to the molecule. The fact remains that silanes are very reactive with water in air, liberating for example methanol or ethanol.

Silanes employed and methods of deposition

The 3GPS[1] silane has been validated for *in vitro* neuronal preparations as anti-adhesive molecule since then used by our group. This silane needs to be prepared in liquid phase in an atmosphere with controlled low hygrometry (e.g. working in a glovebox) to prevent any degradation. During this PhD, we have made the choice to replace it by the APTES[2], a silane less sensitive to light and air moisture. Moreover, APTES presents the great advantage to be part of a automated vapor–phase set–up, recently acquired at the Néel Institute. The Bind Silane[3] in liquid phase has also been successfully employed and we will expose the protocol used for this silane in the section dedicated to the hydrogel fabrication (II.1.2.2). All these silanes present the advantage to be sufficiently hydrophilic to obtain an uniform spreading of the photoresist during the photolithography step, as exposed in the next subsection, but also sufficiently hydrophobic to avoid the neuronal cell adhesion.

The silane molecules are covalently linked at the surface and their fixation is improved by a previous step of oxygen plasma of few minutes enabling the formation of free radicals at the glass surface (Figure II.1). The oxygen plasma is also useful to clean the surface and therefore to create a reproducible "start condition".

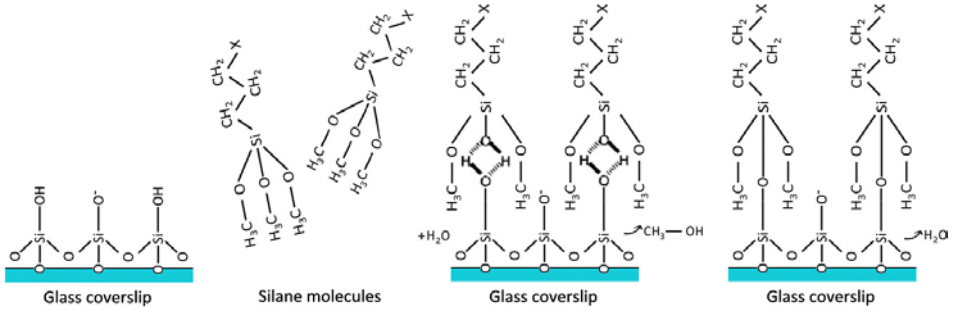

Figure II.1: **Steps of silanization.** From left to right: O_2 plasma oxidation forming free O^- and OH^- radicals, followed by silane deposition. A final phase of hydrolysis binds the silane molecules to the glass coverslip.

The success of the silanization step can be checked by the measure of the contact angle (Figure II.2), typically of 60 ° for the silanes employed here.

[1] 3-glycidoxypropyl-trimethoxysilane: $(C_3H_5O_2) - (CH_2)_3 - Si(OCH_3)_3$, Sigma-aldrich.
[2] 3-aminopropyl-triethoxysilane: $NH_2 - (CH_2)_3 - Si(OCH_2CH_3)_3$, Sigma-aldrich.
[3] 3-methacryloxypropyl-trimethoxysilane: $(C_4H_5O_2) - (CH_2)_3 - Si(OCH_3)_3$, Ficher Scientific.

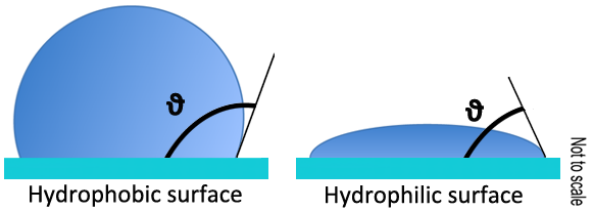

Figure II.2: **Contact angle measurement**: θ is the angle between the surface of the substrate and the tangent of the liquid/vapor interface of the liquid drop placed on the surface. The contact angle θ quantifies the wettability of the surface as a measurement of the surface tension between the substrate and the liquid. It indicates that a surface is hydrophobic if $\theta > 90\,^\circ$ (left) or hydrophilic if $\theta > 90\,^\circ$ (right). Light blue: glass coverslip. Dark blue: water drop.

II.1.1.2 Photolitography: pattern designs

Patterns are defined using UV classical photolithography, whose steps are reported in Figure II.3 and described below.

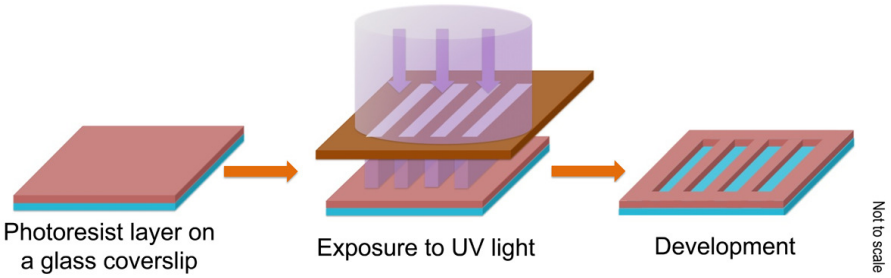

Figure II.3: **Steps of the photolithography process**. From left to right: spinning of the photoresist layer and annealing, exposition to ultraviolet (UV) light through a chromed mask, photoresist development to dissolve the exposed regions of the photoresist layer (in the case of a positive photoresist) followed by a washing step in deionized (DI) water. Light blue: glass coverslip. Red: photoresist. Brown: chromed regions on the mask.

Experimental protocol

- Shipley S1805 **photoresist spinning**[4];
- **annealing** step at 115 °C on a hotplate during 1 min;
- **exposure** of the resist through a mask;
- photoresist **development**[5] during 1 min.

The chosen parameters of rotation speed (4000 rpm) and duration (30 s) define the final thickness depending on the photoresist viscosity (0.5 μm in the case of the S1805 photoresist from Shipley that we used). With the annealing step the solvents are removed, allowing a drying of the resist. The sample is then exposed to the UV light through a mask thanks to a MJB4 aligner (Karl Süss KG München-Garching, mercury-vapor lamp, wavelength $\lambda = 365\ nm$). The

[4] 4000 rpm/s^2 of initial acceleration, 4000 rpm of speed during 30 s, thickness 0.5 μm.
[5] 1:1 dilution in DI water, Microposit^{tm} Developer concentrate, Shipley.

time of exposure depends on the type of resist used and the power of the lamp[6]. During the development the exposed areas of a positive resist like the S1805 are dissolved. The substrate is finally washed in DI water in order to stop the process of dissolution of the resist.

Patterns on the mask

The areas without resist obtained after the development step, correspond to the patterns designed on the mask. To design the geometry of the patterns we use the software Elphy (other free softwares like KLayout are also adapted for this purpose). The masks we use are made of quartz or glass (Soda–lime). The glass masks can be used only with lamps emitting in the conventional UV spectrum ($\lambda = 365\ nm$). We report in Figure II.4 the transmission spectra of glass and quartz masks, showing that only quartz is transparent in the whole range of UV light[7].

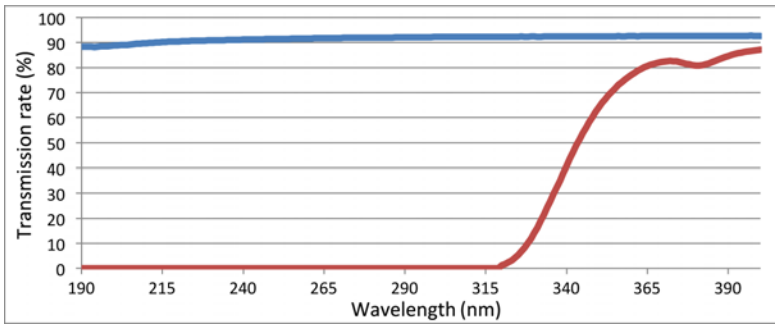

Figure II.4: **Spectrum of transmission** in the range between 190 and 400 nm (UV light). Transmission rate versus the wavelength of a mask made in quartz (blue line) and in glass (red line), showing that glass is opaque in the range of the UV light below 320 nm while quartz is transparent in the whole UV spectrum.

The patterns used during this PhD have a width varying from 2 to about ten μm. These dimensions correspond to the size of neurons and glial cells, justifying the need of a photolithographic process using a cleanroom aligner, whose resolution in the 1 μm range[8] could not be achieved by other techniques like for example the microcontact printing method, based on the utilization of PolyDiMethylSiloxane (PDMS) moulds [1]. The distance between parallel stripe patterns was typically set to 100 – 150 μm, providing both a sufficient separation to prevent neurites to jump between stripes and a reasonable density of neurons, promoting their survival [2]. Our micropattern design is well adapted for mouse cell cultures, in particular a stripe width of 2 μm. For slightly bigger rat cells, we have observed that larger stripes ($\sim$ 3 μm) would be more adapted.

[6]The UV dose for the S1805 resist is of 15 $mJ \cdot cm^{-2}$, given by the power lamp ($mW \cdot cm^{-2}$) multiplied for the exposition time (s).

[7]Measurements have been performed with a spectrometer *Lambda900* (Perkin Elmer Inc.), equipped with a deuterium lamp for the UV light emission until 319.2 nm and a tungsten lamp for the higher wavelengths.

[8]MJB4 Mask Aligner data sheet, www.suss.com.

Finally, we have designed specific patterns to create some visible marks on the glass coverslips. This is particularly useful in a context where a selection of cells is required, like in time-lapse experiments (Figure II.5).

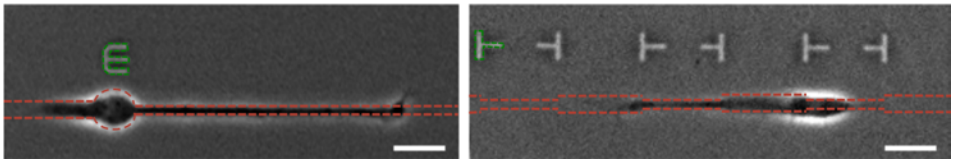

Figure II.5: **Mouse hippocampal neurons at 2 Days In Vitro on patterned glass coverslips with etched markers to localize the pattern shape.** Red dashed lines delimit the PLO adhesive patterns of 2 or 6 μm wide stripes. Green dashed lines delimit the markers: "E" indicates the localization of a 15 μm disk to anchor the cell body, a 6 μm branch on the left and a 2 μm branch on the right of the disk (left image). Horizontal "T" indicates the begin and end of 2 μm wide stripes, alternated with 6 μm wide stripes (right image).

For that, a first photolithography step is followed by an etching process (reactive ion etching in CH_3 vapor phase) of the glass coverslip[9]. The photoresist is then removed during a 3 min sonication step in pure ethanol. The patterns for the cell adhesion are then made by a new process of photoresist coating, exposure and development. In this case, an alignement step has to be performed in order to get the adhesive patterns in correspondance with the etched glass motifs.

II.1.1.3 Functionalization: selective adhesive treatment

At the end of the photolithography process we obtain substrates with regions protected by the resist and free areas devoted to be covered by the adhesive coating. Figure II.17 describes the technological steps of lift-off that leads to the final substrate characterized by an alternation of adhesive and non-adhesive regions.

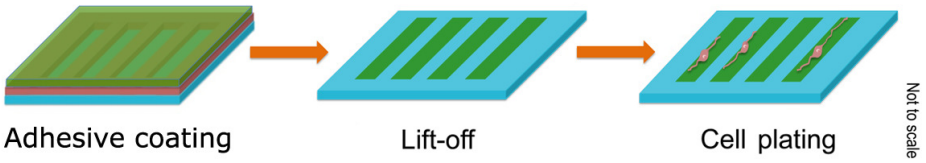

Figure II.6: **Steps of the functionalization with adhesive molecules**. Form left to right: the patterned substrate is incubated in a solution of molecules of adhesion. By a lift-off step of sonication in ethanol, the photoresist is removed leaving the proteins only in the regions initially free of photoresist. Cells are finally plated on the patterned substrate and will adhere only on coated (green) region. Light blue: glass coverslip. Green: molecules of adhesion. Red: photoresist.

[9]Etching process of the markers on the glass coverslip: CH_3, 15 cc, 50 W, 2 $\cdot 10^{-2}$ $mbar$, during 20 min.

Activation of the surface and adhesive coating

The transfer of the proteins of adhesion on the substrates needs a step of activation by oxygen plasma. Its duration depends on the power of the plasma[10] but must be sufficient to make the surface hydrophilic by producing free radicals (O^-, OH^-) on the glass surface. These charged molecules allow electrostatic interactions with the polycationic molecules that constitute the adhesive coating (PLO or PLL[11]). Of note, the oxygen plasma also reacts with the photoresist, removing eventual residues of photoresist at the level of developed areas. By eliminating all the organic impurities on the substrate, the oxygen plasma sterilizes the samples before their transfer from the cleanroom to the cell culture room.

Free radicals having a short life time, the plasma step has to to be performed at maximum 1 h before the incubation of the adhesive molecules. We mainly employ PLL or PLO, two widely used polycationic coating for their non-specific properties. Laminin[12] (LN) is a component of the ECM and is commonly employed to foster axonal growth [3]. Therefore, it can be useful in some experimental conditions. Importantly, we have quantitatively checked that PLL and PLO provide equivalent results in terms of neurite elongation rate. We report in the Table II.1 the parameters of incubation employed for neurons and glial cells.

Cell type	Molecule	Character	Molecular weight (kDa)	Concentr. ($\mu g/cm^2$)	Solution ($\mu g/ml$)	Buffer	Duration of incubation	Washing
Primary neurons	PLL	Non specific	70 – 150	60	1 000	Borate[a]	over-night	2 shorts 1 long (20 min) in water
	PLO	Non specific	3 – 15	2 – 2.5	80	PBS[b]	over-night	2 shorts in PBS
	LN	Specific	900	0.3	10	PBS	30 - 60 min	2 shorts in PBS
Glial cells	PLO	Non specific	3 – 15	3.5 – 4.5	150	PBS	min. 4 h	2 shorts in PBS

[a] Borate buffer composition for 100 ml of water: boric acid (0.31 g) and sodium tetraborate (0.28 g); filter; 0.1 M; pH 8.5. [b] Phosphate buffered saline; pH 7.4.

Table II.1: **Key elements of the protocols associated to the different coatings for cellular adhesion: molecules, parameters and associated cell types.** All incubations are performed at room temperature. See the text for the protocol of deposition of the proteins and note the specific protocol need for the LN.

[10] The duration of the oxygen plasma can varying between 15 and 120 s.
[11] PLO: Poly-ornithine. PLL: Poly-L-Lysine. Sigma-aldrich.
[12] LN: laminin. Sigma-aldrich.

Lift-off

The lift-off is performed using a sonication step in pure ethanol for 60 to 90 s. It is very important to completely dissolve the resist in order to reveal the silanized regions as repulsive surface for the cell adhesion. On the other hand, the adhesive molecules would be denatured by a too long sonication in a solvent like ethanol. This solvent being toxic for cells, some shorts washings after the lift-off are done. Of note, the ethanol sterilizes a last time the samples before using them for the cell culture.
We will describe in the Section II.2, dedicated to the cell cultures, the protocol employed to plate cells on these micropatterned substrates.

Alternative methods successfully tested to improve the protocol of adhesive functionalization

Motivated by the need to transport our samples in other laboratories, in the frame of the different collaborations undertaken during this PhD project, we have done some tests in order to simplify the process of sample preparation. For example, reasonable neuron confinement into micropatterns has been achieved by doubling the concentration of PLO and drying the samples after the lift-off and the washing steps. These functionalized substrates can be used just at the moment of the cell culture, after a step of rehydration in PBS of a few minutes before cell seeding. This methods has been qualitatively validated. A quantification of cell growth (e.g. neurite length or the chemical constrain effect) on these substrates should be performed to check the equivalence between the standard and the dried method. Moreover, the protocol should be optimized in terms of best conditions of work (adhesive molecule concentration, rehydration time, conservation of adhesive molecules over time, ...) to save time and limit the use of consumables.

Finally, let us remark that LN does not adhere directly on glass and that it is easily denatured by solvents. Thus, we have tested two protocol to make patterns of PLO and LN, using the PLO as intermediary chemical layer to graft the proteins, or LN deposition by multi–step coating.
The first method includes to incubate the LN just after the lift-off step of PLO. The method is based on the greater affinity existing between the LN and the PLO than with the silanized regions around the PLO patterns. The LN concentration indicated in the Table II.1 and a duration of incubation of 30 min are the good conditions to avoid the deposition of the LN on the entire surface, impairing the micropattern design. This protocol should be further tested and optimized to insure a good reproducibility and to better understand the selective adhesion mechanisms of LN.

The second method requires to incubate a secondary antibody over-night at 4 °C (dilution 1/200 in PBS), then to make a second incubation of the primary antibody recognizing the LN during 1 h at the room temperature (dilution 1/100 in PBS) and finally to deposit LN at the required concentration. In this case the well-definition of the adhesive patterns, i.e. the contrast between the adhesive and the repulsive regions, is ensured since contrarily to the first method the molecules of adhesion are not put in contact with the silanized surface. This method presents the disadvantage to require three steps of incubation molecules and to need the application of an alternative technique of patterning without the lift-off step in pure ethanol as the proteins would be denatured. We refer to the next paragraph for the description of some alternative methods to lift-off.

II.1.1.4 Functionalization: anti-adhesive treatment

The silanization process described at the beginning of this section (II.1.1.1) has shown to be very efficient to restrain neuronal cell adhesion only on pre-determined areas. Nevertheless, the non-adhesive properties of silanes are not sufficient for long term neuronal cultures (longer than 1 – 2 weeks *in vitro*) and for most types of cells that are able to secrete their own ECM, like glial cells. We report in this paragraph some alternative techniques we have employed to obtain adhesive micropatterns surrounded by repulsive areas.

◊ PLL-g-PEG

Poly-L-Lysine-grafted-PolyEthylene Glycol is a copolymer largely employed for cell patterning techniques [4, 5, 6]. We have adopted this compound as a first option for long term neuronal cultures or for glial cell patterning.

Experimental protocol

The different steps of our protocol have been adapted from the works of M. Théry and M. Piel [5] as described below:

- ethanol **cleaning** of the glass coverslip;
- surface **oxidation** by O_2 oxygen plasma;
- incubation of the **cross-linker** (EDC–NHS diluted in DI water[13]) during 30 min followed by twice DI gentle **washings**;
- incubation of the **PLL-PEG** molecules (diluted in PBS or HEPES[14]) during 1 h followed by twice DI gentle **washings** (the reactions leading to the covalent linking of the PLL-

[13] EDC–NHS solution: 19.2 mg/ml and 11.5 mg/ml respectively. Avoid light exposition. EDC: N-(3-Dimethylaminopropyl)-N'-ethylcarbodiimide hydrochloride: $C_8H_{17}N_3 \cdot HCl$, Sigma-aldrich.; NHS: N-Hydroxysuccinimide: $C_4H_5NO_3$, Sigma-aldrich.

[14] PLL-PEG concentration: $\sim 10 - 15\ \mu g/cm^2$. PBS: phosphate buffered saline, Sigma-aldrich; HEPES: 2-[4-(2-hydroxyethyl)piperazin-1-yl]ethanesulfonic acid, Invitrogen, ref: 15630-049.

PEG to the surface via the EDC–NHS cross-linker are reported in Figure II.7)[15];

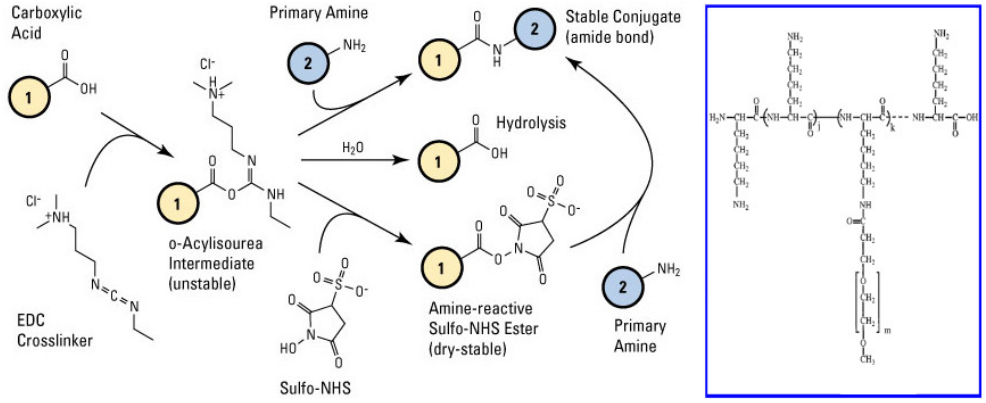

Figure II.7: **Chemical reactions linking the PLL-PEG to the surface via the EDC–NHS intermediary.** Representation of the interaction between the EDC–NHS cross-linker with the oxidized glass surface (represented by the number "1" yellow point) and with the PLL-PEG molecules (represented by the number "2" blue point). From www.piercenet.com. The PLL-PEG copolymer is employed as non-adhesive functionalization and its molecular structure is reported in the blue rectangle on the right [4].

- **oxidation** of the mask surface by an O_2 oxygen plasma[16] during 3 min;
- **exposure** of the sample through a chromed mask with a lamp emitting deep UV radiations[17] ($\lambda < 200\ nm$) during 6 min in order to ablate the PLL-g-PEG;
- gentle **washings** (twice with DI water and twice with PBS);
- then proceed with the **functionalization** of the adhesive regions.

Functionalization of the adhesive regions

The process of functionalization of the PLL-g-PEG patterned substrates is represented in Figure II.8.

Of note, the non-adhesive property of the PLL-g-PEG is given by its chain–like structure (see the molecular formula in Figure II.7). For this reason, the PLL-PEG concentration can be modulated as a function of the chain density (in the range 0.5 – 0.1 mg/ml) but it is not advisable to increase it. Indeed, this can lead to the deposition of multilayer films of disordered chains of PLL-PEG. This may position the hydrophilic PLL side of the copolymer at the interface with the culture medium rather than at surface with the glass substrate, suppressing the non-adhesive properties of the copolymer.

[15]The sample functionalized with the PLL-g-PEG can be dried and so stored up to 1 week. A rehydration of the substrate in DI water during 30 min is required before the exposure step. We have observed a better repulsive effect on the patterned structures when the substrates had been conserved in water (4 °C) or dried (room temperature) compared to when conserved in PBS (4 °C).

[16]The plasma on the mask makes its surface hydrophilic, increasing the wettability and the contact with the sample. A minimal distance between the mask and the glass coverslip is fundamental in order to get a good respect of the size of the patterns.

[17]UVO Cleaner Model 342–220, Jelight company, intensity 30 – 33 mW/cm^2 measured at 254 nm with distance of 4 mm.

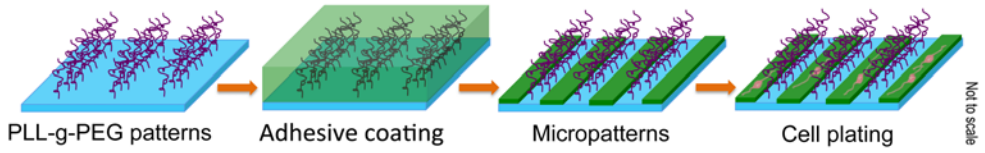

Figure II.8: **Steps of functionalization of the PLL-g-PEG patterned substrates.** From left to right: adhesive molecules are put in incubation on the patterned substrate. Deposition on the glass surface is prevented in the regions occupied by the chains of PLL-g-PEG, leading to adhesive and repulsive patterned areas. Cells are finally plated on the microstructured substrate. Light blue: glass coverslip. Violet: chains of PLL-g-PEG. Green: proteins of adhesion.

We have optimized this method by using cells that are easier to manipulate than primary neurons. These preliminary experiments have given us the opportunity to collaborate with two groups focusing their researches, amongst other subjects, on the muscle pathologies and the engineering of 2D and 3D muscle tissues: respectively, the I. Marty's team at the Grenoble Institute of Neuroscience and the C. Picart's team at the LMGP (materials and physical engineering laboratory) in Grenoble. For this reason, these experiments have been performed with L6 and C2C12 cells[18] and they have confirmed the repulsive properties of PLL-g-PEG toward cell adhesion for at least 10 days *in vitro*.
We report in Figure II.9 the details of our protocol for cell plating.

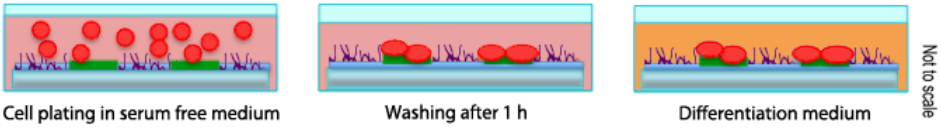

Figure II.9: **Steps of cell plating on the PLL-g-PEG patterned substrates.** Cells are plated at a concentration of $\sim 550\ cells/mm^2$ in a serum free medium, after 1 h a washing with the same medium removes the cells died or weakly adherent outside of the adhesive patterns and finally medium is replaced by a differentiation one. Light blue: glass coverslip. Violet: chains of PLL-g-PEG. Green: proteins of adhesion. Red: cells.

C2C12 cell development has been compared on glass and polystyrene micropatterned substrates (Figure II.10).

We have observed a better cellular confinement on polystyrene[19], where the proteins adhere more efficiently and therefore the coating density is expected to be higher. Moreover, on glass substrates the fusion of myoblasts at 5 DIV in a differentiation medium[20] was not observed, while on polystyrene substrates cells displayed features resembling striations, indicating a more mature stage of cell differentiation, similar to the cell development on non-patterned polystyrene substrates.

[18] L6 and C2C12 are two myoblast cell lines, from rat and mouse respectively.
[19] Polystyrene coverslips have been obtained by cutting circular substrates with a lathe from conventional Petri dishes.
[20] DMEM Glutamax low glucose (Life Technologies, ref: 21885-108) supplemented with 2% horse serum (Life Technologies, ref: 26050-070) and 1% Penicillin / Streptomycin (Life Technologies, ref: 15140-122).

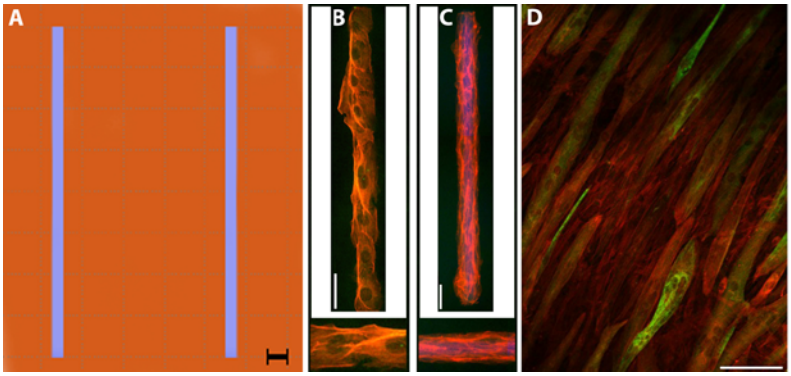

Figure II.10: **C2C12 cells on PLL-g-PEG/FN patterned substrates at 5 DIV.** A) Pattern design of the mask used for the experiments. Blue: transparent regions where PLL-g-PEG chains are exposed to the deep UV light and subsequently covered by FN. Brown: chromed regions. B) C2C12 cells on glass patterned substrates, before the fusion stage (see inset). C) C2C12 cells on polystyrene patterned substrates, aligned and in fusion (see inset), before the striation stage. D) C2C12 cells on Petri dish (control), showing some myotubes not still in the striation stage. In B, C and D: Green: MHC (myosin heavy chain), myotubes. Red: phalloidin, actin. Blue: Hoechst, nuclei. Scale bars: 50 μm.

Remarks about the molecules of adhesion for PLL-g-PEG patterned substrates

Some remarks can be made about the choice of the proteins of adhesion. The fibronectin (FN, Roche Applied Science) is a protein suitable for the majority of the cell cultures. It is particularly adapted for this protocol thanks to its molecular weight of $\sim 440\ kDa$, that is large enough to prevent FN adhesion in the regions occupied by the PLL-g-PEG chains[21]. Of note, proteins like fibrinogen and collagen should be employed with a maximal concentration of 10 $\mu g/ml$ because they tend to form a continuous film over the PEG surface [7].

Alternative method to achieve an adhesive coating of molecules with a low molecular weight on PLL-g-PEG patterned substrates

Contrarily to FN, polycationic polymers like PLL or PLO are very small molecules (molecular weight of $\sim 70-150\ kDa$ and $\sim 3-15\ kDa$ respectively, Sigma-aldrich). They can thus penetrate within the PLL-g-PEG chains and impair their repulsive effect. These molecules are commercially available with greater molecular weight and different concentration of incubation should be tested to check if it is possible to adapt the protocol of the PLL-g-PEG functionalization with PLL and PLO coatings. Alternatively, we propose here a variation of the protocol described above to obtain low molecular weight PLL adhesive patterns surrounded by PLL-g-PEG repulsive areas. This method consists in an inversion between the PLL-g-PEG incubation and the adhesive coating deposition. PLL is firstly incubated during 1 h at $\sim 60\ \mu g/cm^2$ (solution of 1 mg/ml diluted in the borate buffer, see Table II.1) and then selectively removed by an exposition to deep UV light through a mask with negative patterns in comparison with the

[21] The advised concentration of FN is $\sim 1\ \mu g/cm^2$ during 1 h (solution $\sim 10-25\ \mu g/ml$ diluted in PBS) .

previous method. Finally the PLL-PEG is incubated during 1 h at $\sim$ 25 $\mu g/cm^2$ (solution of 0.5 mg/ml diluted in PBS), leading to the formation of a repulsive layer outside the PLL patterns.

This method is very efficient to confine cells for long times. We report in Figure II.11 some examples of L6 and neurons growing on this kind of substrate, still following the pattern design after 17 DIV.

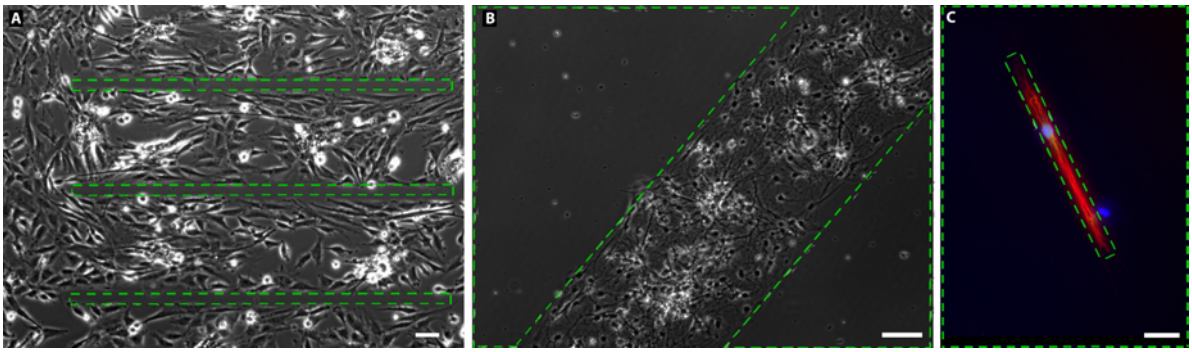

Figure II.11: **Long term cell confinement on PLL/PLL-g-PEG patterned substrates.** A) Phase contrast image of L6 cells at 7 DIV. Phase contrast (B) and fluorescence (C) images of mouse cortical neurons at 17 DIV. In C: Red: MAP2, neurons. Blue: Hoechst, nuclei. The green dashed lines delimit the PLL-g-PEG regions. Scale bars: 50 μm.

Finally, to graft LN (Sigma) on the glass surface, we refer to the methods exposed at the end of the II.1.1.3 subsection, proposing to incubate the LN after the PLO or the PLL deposition or to deposit the LN by the multi–step coating.

◊ Polymer brushes

We propose in this section an alternative solution to PLL-g-PEG functionalization that present two advantages: patterned substrates can be stored for at least 2 months (dried at room temperature and protected from light as compared with only few weeks in water at 4 °C or dried at room temperature for PLL-g-PEG) and the cost of fabrication is much cheeper.

The non-adhesive regions are made via the grafting of polymer brushes, a protocol developed by L. Bureau at the LIPhy (Interdisciplinary Laboratory of Physics) in Grenoble [8]. In the last decades, polymer brushes have inspired several research works investigating macromolecule phenomena in confined environment and have been largely employed from the early 1990s thanks to the development of rapid protocols based on user-friendly chemistry [9]. This technique has been elaborated by the L. Bureau's team to study for example cell dynamics in polymer brush-coated microcapillaries, mimicking the glycocalyx, a macromolecular layer coating the inner walls of blood vessels *in vivo* [10].

Experimental protocol

The steps of fabrication of the PNIPAM[22] polymer brushes are described in Figure II.12.

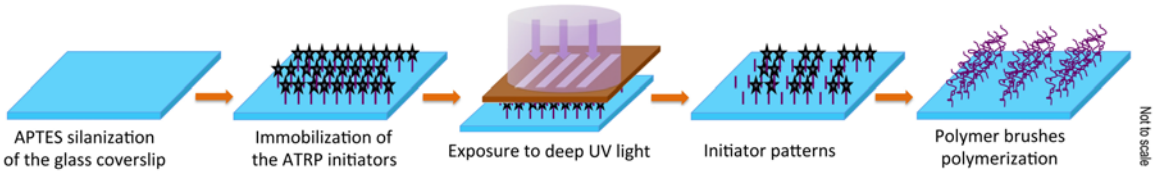

Figure II.12: **Polymer brushes of PNIPAM chains grafting based on the atom transfer radical polymerization (ATRP) method.** From left to right: glass coverslips are cleaned and silanized, before the immobilization at the surface of ATRP initiators, followed by the exposure by deep UV light through a chromed mask and the PNIPAM chain polymerization at the level of the initiators. Light blue: glass coverslip. Black stars: ATRP initiators. Brown: chromed regions on the mask. Violet: PNIPAM polymer brushes.

Polymer brushes are produced by a "grafting–from" technique, i.e. growing from a layer of polymerization initiators first grafted on the substrate. We resume the procedure below from [8]:

- cleaning of the surface by an **oxidation step** using O_2 oxygen plasma;
- APTES **silanization** in liquid solution[23] during 2 h;
- **monomer immobilization** on the surface of the ATRP initiators in a dichloromethane solution[24] during 5 min, leading thus to bromine–terminated surfaces from which ATRP can be initiated;
- **washing** with pure dichloromethane, ethanol and water before being dried;
- **exposure** of the substrate trough the mask with a lamp emitting deep UV radiations ($\lambda < 200\ nm$) during 2 min in order to ablate the active polymerization initiators in the regions exposed to the light corresponding to the transparent regions of the mask[25];
- a water solution of NIPAN[26] and PMDETA[27] is prepared in a flask and bubbled with argon or nitrogen gas during 30 min before adding a $CuCl$ catalyzer[28];
- immersion in the solution leading to the **polymerization of the polymer brushes** of PNIPAM from the initiator molecules. The time duration of the immersion in this solution determines the polymer brush height (e.g. a duration of 5 min gives brushes 55 nm high).

The substrates are then dried and stored at room temperature or directly incubated with

[22] Poly(N-isopropylacrylamide).
[23] 3-aminopropyl-triethoxysilane: $NH_2 - (CH_2)_3 - Si(OCH_2CH_3)_3$, concentration: $8.5 \cdot 10^{-3}\ M$, Merck.
[24] 4.8% of TEA (triethylamine) and 1% of BMPB (2-bromo-2-methylpropionyl bromide, 98%, Acros Organics).
[25] UVO Cleaner Model 342–220, Jelight company, intensity 30 – 33 mW/cm^2 measured at 254 nm with distance of 4 mm.
[26] N-isopropylacrylamide, 30 mg/ml.
[27] 1,1,7,7-Pentamethyldiethylenetriamine, 0.75%.
[28] $CuCl$ catalyzer, 3.75 mg/ml.

proteins of adhesion before the cell seeding step.

An example of glial cells growing on this kind of patterned substrate[29] is reported in Figure II.13 and compared to silanized patterned substrates.

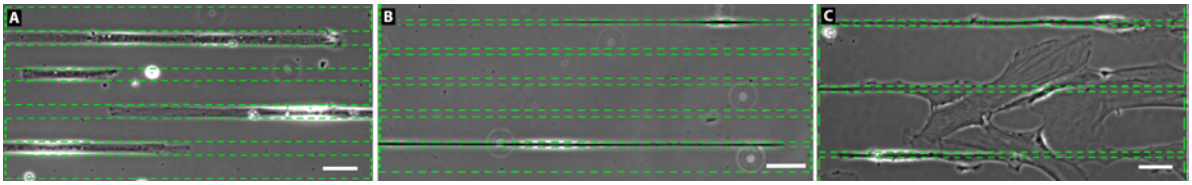

Figure II.13: **Comparison of glial cells growing on PNIPAM and silanized patterned substrates.** Phase contrast images. Adhesive PLO patterns, alternated with repulsive regions occupied by the PNIPAM polymer brushes at 2 (A) and 9 (B) DIV. C) Adhesive PLO patterns, alternated with APTES silanized regions at 4 DIV. Cell growth is perfectly constrained by PNIPAM polymer brushes patterns until 9 DIV, whereas at 4 DIV glial cell morphology on silanized surfaces does not respect the pattern design. The green dashed lines delimit the PNIPAM (A, B) or the silanized (C) regions. Scale bars: 50 μm.

This technique appears as quite promising for long term neuronal cultures. In the initial protocol, substrates stick to the mask thanks to the capillary forces provided by a liquid layer of hexadecane. The thickness of this intermediate layer is responsible for the broadening of the pattern size (typically of 1 – 2 μm at each stripe edge). Therefore, a reduction of the contact distance between the coverslips and the mask should be achieved, or the initial sizes of the patterns on the mask should be reduced, in order to fabricate 2 – 3 μm wide adhesive stripes.

II.1.2 Physical patterns

II.1.2.1 Structural properties: glass etching

We have described in the previous section (see Figure II.5) the possibility to etch patterns on glass substrates in order to design some visible markers enabling the localization of the adhesive patterns on the substrate. The same etching protocol can be used to obtain physical patterns on the substrate. After the development step at the end of the photolithography process (Figure II.3), the substrate is etched by reactive ion etching. The functionalization can be achieved before or after the lift-off, depending on the objectif to obtain an adhesive coating on the whole surface or to combine physical and chemical patterns.
We report in Figure II.14 the measured etching velocity of the glass with the CH_3 gaz[30].

We note that reasonable thicknesses in the range of a few hundreds of nm are obtained with this method for reasonable etching duration in the scale of minutes. To obtain larger depth

[29] **Details of functionalization and culture of the PNIPAM patterned glass coverslip.** PNIPAM polymerization during 5 min (polymer brushes 55 nm high). PLO ~ 4.5 $\mu g/cm^2$ (150 $\mu g/ml$ solution) during 5 h. Seeding conditions: ~ 30 $cells/mm^2$ in DMEMs culture medium.

[30] Etching process of the markers on the glass coverslip (SiO_2 protocol): CH_3, 15 cc, 50 W, $2 \cdot 10^{-2}$ $mbar$.

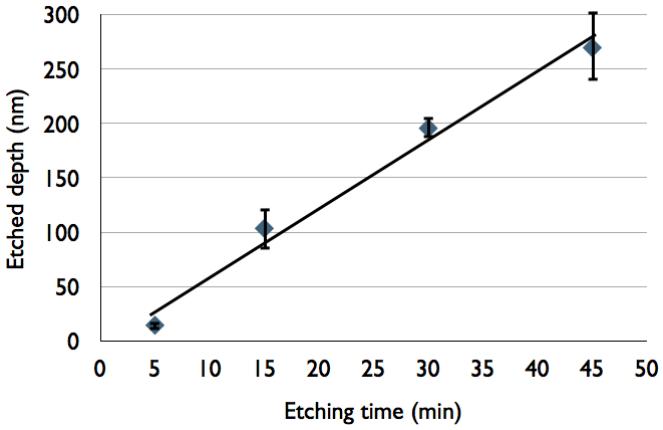

Figure II.14: **Experimental calibration of the glass etching.** Measured depth (mean values ± SD) versus time (1 glass coverslip and 4 measurements for each condition). Best linear fit: $y = 6.3\ x - 3.2$, giving an etching velocity of about 6 nm/min.

through a plasma process, we refer to the last section dedicated to the methods developed to achieve a control of cell positioning (Section II.5.2).

Chemical etching with hydrofluoric acid (HF) is very efficient but also strongly corrosive. We have made the choice to not adopt this technique also because the etched profiles are isotropic. Structures with high aspect ratios would therefore be impossible to achieve.

II.1.2.2 Mechanical properties: hydrogels

Hydrogels are largely used as substrates for cell cultures in order to modulate the stiffness of the cell in *in vitro* environment [11, 12].
We describe in this section the methods employed during this PhD work to fabricate polyacrylamide (PA) hydrogels of uniform stiffness or with patterns of rigidity. The advantages of the PA gels toward other soft materials are numerous [13, 14]:

- Stiffness modulation in a wide range of rigidities, between hundreds of Pa to several tens or hundreds of kPa, thus enclosing physiological rigidities of the *in vivo* ECM.
- Weak non-specific adsorption of the proteins to uncoated gel surface.
- Non degradable, preventing degradation by cells.
- Transparency.
- Cell penetration is avoided thanks to the existence of pores in the range of 100 nm.

Moreover, these physical and chemical properties remain quite constant during cell cultures.

Photopolymerization

Our group in LTM in collaboration with Danielle Gulino in CEA Grenoble has developed a method of photopolymerization [15] inspired by [16] that presents the advantage to locally modulate the mechanical properties of the hydrogel. This enables the fabrication of stiffness

micropatterns down the micron range. Moreover, the polymerization with this technique is more uniform than with the usual chemical technique described in the follow paragraph entitled "Chemical polymerization".

The principle of this method is to use a photoinitiator activated by UV light to enable the local polymerization of the gel through a mask. The steps of fabrication are reported in Figure II.15 and described below:

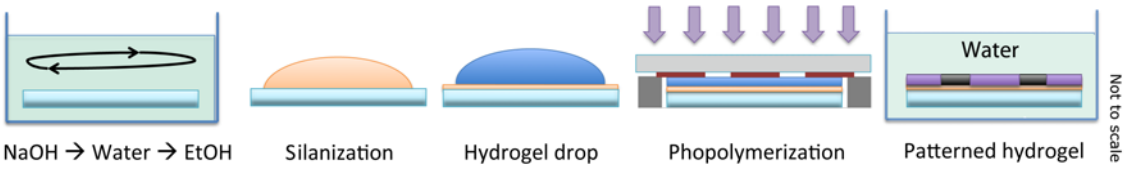

Figure II.15: **PA hydrogel fabrication steps.** Glass coverslips are cleaned and silanized before the photopolymerization step. Polymerization occurs by a UV light exposition through a mask. Hydrogels are finally swollen in ultra-pure water. Orange: Bind Silane solution. Dark blue: hydrogel solution. Dark grey: wedges of 40 μm. Red: chromed regions on the mask (light grey). Violet: softer regions (protected from the chrome, lower dose of light) of the hydrogel. Black: stiffer regions (higher dose of light) of the hydrogel.

- glass coverslips ($\phi = 30\ mm$) are **cleaned** in soda ($NaOH$, 0.1 M), washed in ultra-pure water (0.22 μm filter, 18,2 $M\Omega \cdot cm$ at 25°C), then in ethanol ($EtOH$), each step during 10 min and upon a mixing platform (20 rpm), and finally dried;
- glass coverslips are **silanized** in order to covalently graft the PA hydrogels to the surface: a drop of 500 μl of Bind Silane solution[31] is applied on the surface during few minutes and dried with a cleanroom wiper (dust-free, microfiber);
- a drop of 30 μl of **hydrogel solution**[32] is deposited on the silanized surface of the coverslip on a support equipped with 40 μm thick wedges in order to control the final hydrogel height;
- **polymerization** occurs by UV exposition[33] of the hydrogel solution through a chromed or transparent mask (with hydrophobic treatment) that is gently removed after 15 – 45 min and the gel is allowed to swell in ultra-pure water for 24 h;
- **patterned (or uniform) hydrogels** are obtained according to the mask design.

[31] Bind Silane, 3-methacryloxypropyl-trimethoxysilane: $(C_4H_5O_2) - (CH_2)_3 - Si(OCH_3)_3$, Ficher Scientific. Solution for 15 ml of ethanol (absolute, ≥99.8%, Sigma-aldrich): acetic acid (484 μl) and Bind Silane (56 μl). Glass coverslips can be so stored up to 1 month at room temperature and protected from air.

[32] hydrogel solution: 10% acrylamide (C_3H_5NO, 40% w/v stock solution, Sigma-aldrich), and 0.5% bis-acrylamide (N,N'-Methylenebisacrylamide, $C_7H_{10}N_2O_2$, 2% w/v stock solution, Sigma-aldrich). Patent CEA/CNRS FR2983201. Fluorescent beads can be added to the solution (usual concentration of 100 $\mu l/ml$, i.e. 0.22% v/v, if for Tracking Force Microscopy experiments, 0.2 μm, 2% solid red beads, Molecular Probes).

[33] Fiber lamp Panacol/Eleco UVP281, $\lambda = 350 - 450\ nm$ light, 18 mW/cm^2.

Chemical polymerization

This technique is based on a polymerization initiated by a solution of TEMED[34] and APS[35] in a water solution of a monomer and a cross-linker: respectively the acrylamide[36] and the bis-acrylamide[37], like for the photopolymerization method. The hydrogel stiffness is modulated by the concentration of these last two components.
A droplet of 35 μl of this solution is deposited on a glass coverslip ($\phi = 30\ mm$) cleaned and silanized as described previously for the photopolymerization method and covered with a hydrophobic treated silicon slide, gently removed after a given time necessary for the hydrogel polymerization (10 – 30 min).

This protocol is the most commonly method employed in the literature and the parameters chosen for our study have been adapted from [17] in order to obtain ultra–soft hydrogels. Although it can be easier to obtain ultra–soft gels with the chemical method, the polymerization in this case is longer (minutes compared to seconds) than with the photopolymerization method and it is less homogeneous. Importantly, it is not possible with this technique to fabricate hydrogels with micropatterns of rigidity.

Hydrogel stiffness characterization by atomic force microscopy

The hydrogel stiffness has been characterized by atomic force microscopy (AFM), that gives an access to the Young's modulus with a precision of $\sim 0.5\ kPa$.

The AFM set–up[38] is located at the LIPhy (Interdisciplinary Laboratory of Physics) in Grenoble. AFM probes were (MLCT, Bruker)[39] V–shaped silicon nitride cantilevers with silicon nitride tips (Figure II.16.A), ideal for contact imaging modes, force modulation microscopy and liquid operation. We used cantilevers with spring constant of 0.01 and 0.03 N/m in order to cover the range of elastic moduli of about 0.1 to 100 kPa, characterizing the PA hydrogels. Characterizations have been performed in PBS at $\sim 30\,°C$, as well as cantilever calibrations. The influence of the temperature on the stiffness was also measured and was on the order of magnitude of the error. We have employed the so-called "force mapping" mode which corresponds to record multiple "force volume" curves (i.e. force spectra of the force evolution as a function of the probe–sample distance) on a predefined grid. Typically, maps were constituted

[34] Tetramethylethylenediamine, final concentration employed: 0.2%.
[35] Ammonium persulfate, 10% w/v, final concentration employed: 0.5%.
[36] Acrylamide, Bio-Rad, 40% w/v stock solution, final concentration employed: 3%.
[37] Bis-acrylamide, Bio-Rad, 2% w/v stock solution, final concentration employed: 0.06%.
[38] NanoWizard II BioScience AFM set–up on Zeiss Axio Observer, JPK Instruments AG, objective 10X, www.jpk.com.
[39] MLCT non-conductive triangular Bruker's Microlever, with minimal – maximal resonant frequencies and minimal – maximal spring constant respectively of 4 – 10 kHz and 0.005 – 0.02 N/m (shape "C") or 10 – 20 kHz and 0.01 – 0.06 N/m (shape "D"), www.brukerafmprobes.com.

of $5\,x\,5$ points on a $50\,x\,50\ \mu m^2$ area on the hydrogel surface in order to obtain a mean value of stiffness on a surface similar to the cell size. It is advisable to measure various maps in order to probe the stiffness uniformity at the level of the entire surface.

Data analysis have been performed with the software "JPK Data Processing". They are based on the Hertz model of the study of the deformation of two solids in contact, assuming that the AFM tip presses on an infinite surface. Practically, with a maximal indentation of less than 5% of the total hydrogel height, the Hertz's model is applicable. This model does not take into account potential adhesion forces between the tip and the sample. In that case the relation between the applied force (F_e[40]) and the indentation depth is [18]:

$$F_e = \frac{4E^* \cdot \tan\alpha}{\pi\sqrt{\pi}}\, h^2 \tag{II.1}$$

For the analysis, we use the approach curves in a range of indentation depth between 0.2 and $1-2\ \mu m$ in order to always take into account the same window, where the elastic behvior of the gel is predominant (Figure II.16.B).

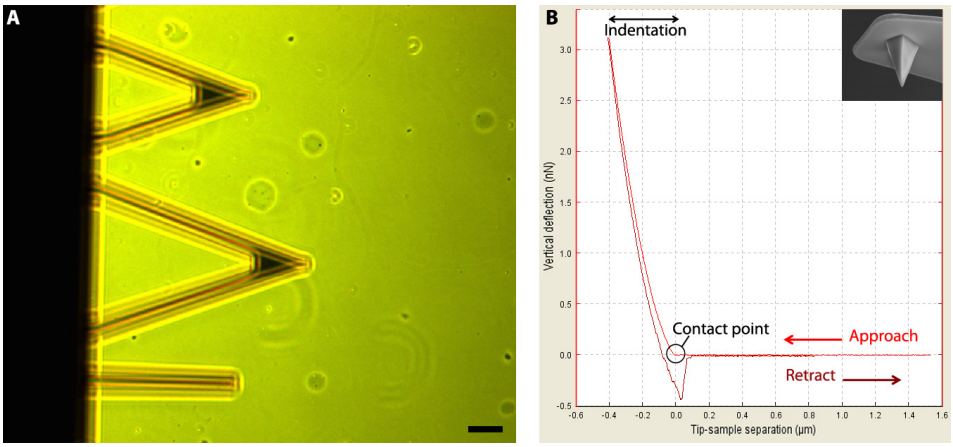

Figure II.16: **Atomic force microscopy hydrogel characterization.** A) Picture of triangular cantilevers used for the AFM measurements on a hydrogel surface. Scale bar: 50 μm. B) Example of curve analyzed with the software "JPK Data Processing": vertical tip deflection versus the tip distance from the hydrogel surface. The vertical deflection corresponds to the contact force with the substrate, by an equivalence given by the calibration of the spring constant of the cantilever that leads to the calculation of the Young's modulus of the hydrogel. Curves represent the approach and the retraction of the AFM tip to the surface. A picture of a pyramidal tip is reported in the inset. Refer to the text for the parameters of analysis.

On ultra–soft hydrogels the window of analysis is reduced between 0.4 and $1-2\ \mu m$ in order to discard the adhesive effects of the tip to the surface at the contact point level.

Data are smoothed, a baseline is automatically subtracted to keep to zero the line of approach, the contact point (offset) is automatically set to zero and finally the elastic modulus of the

[40] $E^* = \frac{E}{(1-\nu^2)}$ with E the Young's modulus, $0.33 < \nu < 0.45$ for the Poisson's ratio of the polyacrylamide, α the angle of the pyramidal tip and h the indentation depth of the tip into the hydrogel.

sample is determined by fitting the curve with the formula II.1. The parameters used are the tip shape (quadratic pyramid with an half-angle to face of 18.75 °C) and the Poisson's ratio (0.45). Moreover, thanks to complementary experiments we have observed that (i) the result is not influenced by the approach speed of the cantilever in a range between 1 and 16 $\mu m/s$ (ii) nor by the substrate functionalization[41] and (iii) in a temperature range between 27 and 37 °C the result decreases by only ~ 6 % (which is lower than the error due for example to the choice of the Poisson's coefficient value). Neverthless, the preparation of the hydrogel solution remains a bit experimentalist–dependent, probably due to the residual air in the solution that has a strong impact on the polymerization speed.

The AFM characterization is fundamental for the hydrogels fabricated with the photopolymerization method whose stiffness is scarcely predictable. Indeed, this parameter depends on the duration of the exposure and the lamp power but it is also dependent on the ratio between the soft and the stiff surfaces. As the component concentration is homogeneous, regions receiving an higher dose of light will pump the monomers proportionally to their surfaces, leading to a reduction of the amount of hydrogel components in the soft, less illuminated, regions. For this reason, a small stiff area will tend to be stiffer that expected for the same exposition time on uniform substrates as the hydrogel components will be concentrated in a smaller volume. In the same way, if the stiff region is very large in comparison with the soft one, the high concentration of hydrogel components pumped in the stiff region from the soft region will prevent the hydrogel polymerization of the soft area.

Hydrogel functionalization

PA hydrogels are quite inert from a chemical point of view, making difficult to covalently link proteins to their surface. We describe here the methods developed to graft the proteins of adhesion necessary for brain cell cultures, i.e. FN or PLL/LN (Figure II.17).

As reported in Figure II.17, the method to covalently attach proteins of adhesion to the hydrogels slightly change for the FN or the PLL/LN functionalization. Both are based on the application of a heterobifunctional reagent named Sulfo-LC-SDA[42], that thanks to its photosensitive diazirine group is more stable and more reactive compared with other commonly employed compounds, like the Sulfo–SANPAH[43].

The functionalization steps are described below:

[41] FN functionalization, 0.8 $\mu g/cm^2$.

[42] Sulfosuccinimidyl 6-[4,4-azipentanamido]hexanoate, succinimidyl-ester diazirine (SDA) reagent, Pierce Biotechnology.

[43] N–sulfosuccinimidyl–6–[4'–azido–2'–nitrophenylamino]–hexanoate.

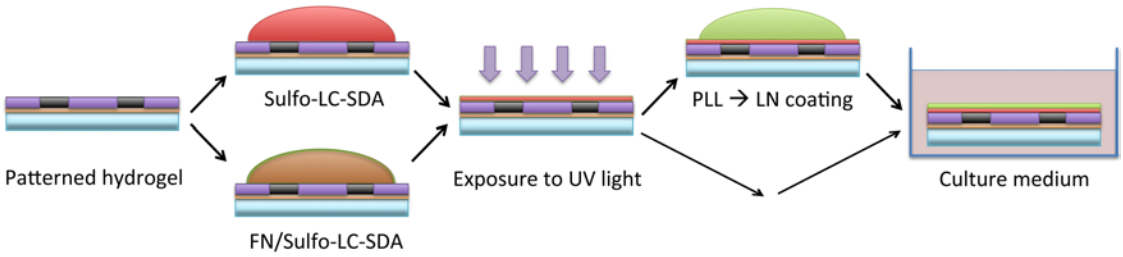

Figure II.17: **Steps of functionalization of the polyacrylamide hydrogels.** Adhesive molecules are covalently grafted to the surface of patterned (or uniform) hydrogels using a photoactivable reagent named Sulfo–LC–SDA. Refer to the bullet list into the text for a detailed description in case of PLL/LN or FN coating. Light blue: glass coverslip. Orange: Bind Silane solution. Violet: softer regions (protected from the chrome, lower dose of light) of the hydrogel. Black: stiffer regions (higher dose of light) of the hydrogel. Red: Sulfo–LC–SDA solution. Green/Red: FN/Sulfo–LC–SDA solution. Green: PLL then LN solution.

- hydrogels are **dehydrated**[44];
- **Sulfo–LC–SDA** solution[45] (PLL/LN coating) or **FN/Sulfo–LC–SDA** solution[46] (FN coating) is poured on the surface of the hydrogel and incubated during 2 h (PLL/LN coating) or 1 h (FN coating) protected from light;
- hydrogels are **dehydrated** again and exposed to **UV light**[47] during 5 min;
- hydrogels for **PLL/LN coating** are washed with water and 3 times with PBS before incubation of the PLL solution[48] during 1 h, followed by the LN solution[49] incubation during 1 h;
- finally, for both coatings, hydrogels are washed 3 times in PBS and incubated with **cell culture medium** 1 h before cell seeding.

The covalent link of the proteins to the hydrogel surface occurs via the Sulfo–LC–SDA bifunctional reagent, according to the representation reported in Figure II.18.

Of note, the functionalization via the bifunctional cross-linker is the critical aspect of this method of functionalization. Indeed, this molecule is quite instable and the homogeneity of the final distribution of the proteins of adhesion is not guaranteed. In particular, the succinimide group is the most instable and for example, in the protocol with the FN, the quality of the interaction is improved because it firstly reacts with the proteins, differently from the case of the PLL coating. Moreover, the non-specific reaction of the diazirine group with inert molecules, like water or polyacrylamide, makes difficult to control its attachement to the surface. The

[44]The dehydration time depends on the hydrogel stiffness and it is variable between 10 and 55 min (fractures on the surface of ultra–soft gels can appear for too long periods of dehydration.
[45]Sulfo–LC–SDA concentration: 70 $\mu g/cm^2$ in water (0.44 mg/ml solution).
[46]FN/Sulfo–LC–SDA concentration: 3.5/2.8 – 1.1/0.9 $\mu g/cm^2$ in PBS. Fibronectin from human plasma (Roche Applied Science).
[47]Fiber lamp Panacol/Eleco UV-P281, $\lambda = 365\ nm$, 18 mW/cm^2.
[48]PLL concentration: 115 $\mu g/cm^2$ in borate buffer (1 mg/ml solution).
[49]LN concentration: 1.1 $\mu g/cm^2$ in PBS (10 $\mu g/ml$ solution).

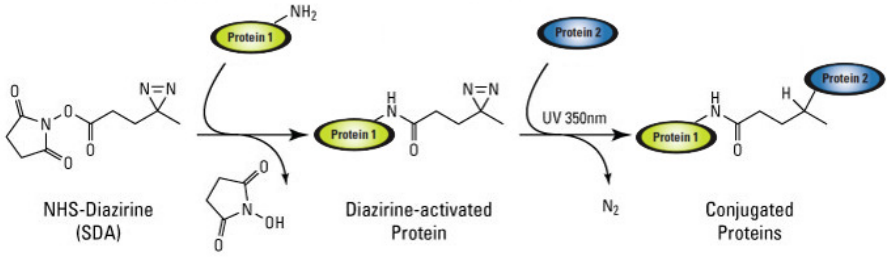

Figure II.18: **Chemical reactions linking the proteins of adhesions to the hydrogel surface via the Sulfo–LC–SDA intermediary.** Representation of the interaction between the N-Hydroxysuccinimide (NHS) esters of the Sulfo–LC–SDA reagent with the amine group (NH_2) of the PLL or the FN (represented by the yellow point named "Protein 1") and of the photoactivated ($\lambda = 330 - 370\ nm$) interaction of the diazirine esters of the Sulfo–LC–SDA reagent with the inert polyacrylamide of the hydrogel surface (represented by the blue point named "Protein 2"). Adapted from www.piercenet.com.

technique described for the FN coating has been developed in our group, considerably improving the homogeneity of the functionalization and minimizing the dependency of the protein attachment on the hydrogel stiffness. This point is fundamental to guarantee an homogenous controlled chemical coating on the surface, moreover independent of the gel stiffness, providing optimized conditions to study of cell mechanosensitivity. For that, we have map the coating density by confocal microscopy.

Functionalization characterization by confocal microscopy

To evaluate the attachment homogeneity of the proteins of adhesion to the hydrogel surface by confocal imaging requires to label the proteins by immunofluorescence, similarly to the protocol used for the cell labeling (Section II.2):

- incubation during 30 min of the **saturation buffer**[50] upon a mixing platform (10 rpm);
- incubation during 1 h of the **primary antibody**[51] upon a mixing platform (10 rpm), rinsed 3 times with the saturation buffer;
- incubation during 1 h of the **secondary antibody**[52] upon a mixing platform (10 rpm) protected by light, rinsed 3 times with the saturation buffer and stored in PBS.

Hydrogels have been analyzed with a confocal microscope located at the CEA[53], giving access to a quantification of the fluorescent proteins of adhesion on the surface, with a z resolution of $\sim 0.5\ \mu m$ (water immersion objective 40X).

[50] Saturation buffer in PBS: Tween–20 (polyoxyethylene (20) sorbitan monolaurate, Sigma-Aldrich) 0.1% and BSA (bovine serum albumin, Euromédex) 2%.
[51] Polyclonal FN or LN–antibody, dilution: 1:400 in the saturation buffer.
[52] Donkey α–rabbit antibody (Alexa 488), dilution: 1:2000 in the saturation buffer.
[53] Leica TCS SP2 microscope.

We report in Figure II.19 few examples for both FN and PLL coatings.

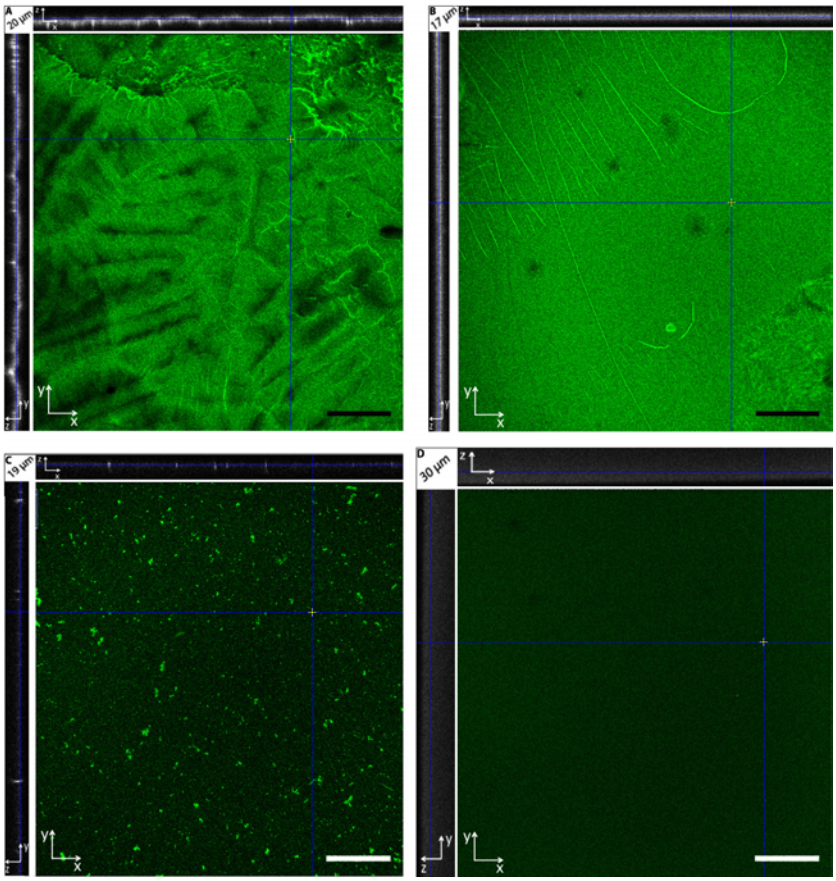

Figure II.19: **Characterization of the FN and PLL functionalization quality on the polyacrylamide (PA) hydrogel surface.** A, B) Confocal images of a soft ($\sim$ 1 kPa, A) and a stiff ($\sim$ 45 kPa, B) PA hydrogels showing a quite homogenous distribution of the FN and a more irregular surface of the soft hydrogel, due to its low stiffness. Green: α–LN. C, D) Confocal images of stiff ($\sim$ 30 kPa, C and $\sim$ 20 kPa, D) PA hydrogels showing a quite weak control of the distribution of the PLL (irregular on the left and homogenous on the right, but very faint compared to the FN coating). The images represent the xy view and the relative projections yz (left) and xz (top). Green: FITC–PLL. Scale bars: 50 μm. Step between two consecutively z slices: 0.28 μm.

Of note, the effective concentration of FN bound to the hydrogel surface has been quantified in our group with well reproducible results. The amount obtained by ELISA (enzyme-linked immunosorbent assay) tests is of $90 \pm 5\%$ of the protein concentration diluted from the stock.

II.2 Primary cell cultures

Most experiments reported in this manuscript have employed embryos from the C57 Black 6 inbred strain of laboratory mice and, occasionally, rat embryos.

II.2.1 Neuronal and mixed neuronal–glial cell cultures

Neuronal and mixed cell cultures are respectively achieved using hippocampus or cortex of mouse embryos at eighteen days of gestation. This corresponds to the phase just before their birth, since the gestation period is about 19 – 21 days. The reasons of this choice are that (i) hippocampus development has been well-characterized *in vitro*, (ii) young cells result more adaptable in constrained *in vitro* environments and (iii) dissociated hippocampal tissues provide a relatively homogeneous cell population, mainly composed of pyramidal neurons and a very low concentration of glial cells (less than 1% [2]). This point is fundamental to study isolated neurons. Indeed, glial cells can secrete the necessary proteins enabling them to colonize the initially repulsive space between patterns, if not blocked with polymer brushes or PLL-g-PEG molecules non-adhesive molecules, therefore providing a substrate for non-controlled neuronal adhesion.
The culture protocol employed is based on the method developed by Banker [19, 20] and the medium compositions have been kindly provided by the group of A. Triller (IBENS, Paris, France).

Exceptionally, in the context of collaborations with other groups of research, rat embryos at nineteen days of gestation (rat development requires about two additional days in comparison with mice) have been employed. This will be specified in the legend of the figures.

II.2.1.1 Dissection: hippocampus and cortex

The quality of the dissection of embryo brains is critical to guarantee the achievement of experiments and the cell survival *in vitro*. $1-2\ h$ is the maximum duration recommend between the animal euthanasia and the cell seeding. The dissection is made using a stereomicroscope, narrow pincers and scissors (Fine Science Tools).
The Figure II.20 illustrates the main steps of dissection of hippocampus and cortex from mouse embryonic brains. The typical length of a mouse embryonic hippocampus (at 18 days of gestation) is about 2 *mm* when straightened and slightly greater in rats.

Tissues are extracted in the dissection medium[54] at $\sim 4\,^{\circ}C$. Hippocampi are then incubated during 10 *min* at $37\,^{\circ}C$ in 3 *ml* of the same medium supplemented with 10% of Trypsin without EDTA (2.5%, Life Technologies), rinsed three times with the dissection medium at

[54] Dissection medium: Hank's HBSS 10x (10%) and Hepes 1 *M* (2%) diluted in sterile water. Gibco Invitrogen.

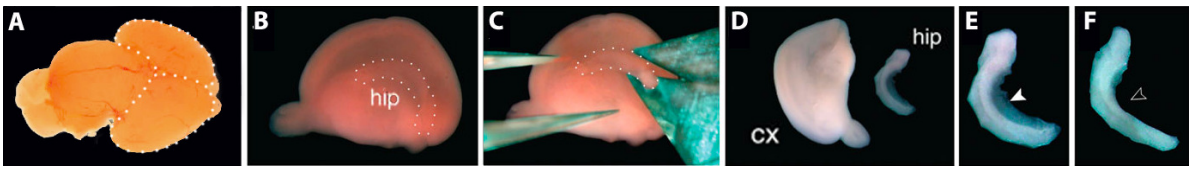

Figure II.20: **Dissection of hippocampus and cortex from mouse embryonic brains.** A) Fetal mouse brain. Left and right hemispheres of the cerebral cortex are delimited by the dashed white line (external view). B) Right hemisphere (inner view) and the olfactory bulb. Hippocampus ("hip") is delimited by the dashed white line. Meninges surrounding each hemisphere are removed. C) The hippocampus is removed with a microscissor. D) Cortex ("cx") and hippocampus ("hip") are separated. E, F) The fimbriae (arrowhead) on the concave side of the hippocampus are removed (open arrowhead). Adapted from [21].

room temperature and dissociated with a 1 ml pipette in 1 ml (20 passages max. through the tip) of MEMs medium[55] at 37 °C.

II.2.1.2 Cell seeding and standard culture conditions

One hippocampus usually provides about 0.3 – 0.7 millions neurons and one cortical hemisphere about 2 – 3 millions of cells. Substrates are prepared (see Section II.1) before the dissection and kept in PBS at room temperature until the seeding step. Around 1 h before the cell seeding, samples can be also incubated in MEMs medium at 37 °C (especially in the case of hydrogel substrates, Section II.1.2.2). PBS or MEMs is aspirated by taking care of not drying the substrates. Cells are then plated at a given concentration[56] in the MEMs medium. In the case of hippocampal neurons, after 3 – 4 h in the incubator at 37 °C and controlled atmosphere of 5% of CO_2, MEMs medium is quickly replaced by the maintenance NBs medium[57].

II.2.1.3 Variations from standard protocols: remarks about influence of the culture medium in cell confinement

As described in the previous paragraph, a culture medium supplemented with serum is commonly used from 1 h before to 3 h after the cell seeding step. We have investigated by immunofluorescence if this incubation step in presence of serum proteins could modify the initial chemical coating of our substrates. For that purpose, we have incubated a PLO-patterned substrates (alternation of PLO or silanized stripes) with various culture mediums for different periods of times, from 24 h before fixation or cell seeding to 24 h after cell seeding. After fixation, proteins of interest were immunolabeled (see the corresponding protocols in the following subsections). Finally, samples were observed under identical exposition conditions (i.e. duration and intensity), in order to achieve reliable quantifications of the relative protein

[55] MEMs medium: horse serum (10%), L–Glutamine 200 mM (1%), Sodium pyruvate 100 mM (1%) and Penicillin / Streptomycin (0.05%) in MEM. Invitrogen. Filtered at 220 nm.

[56] Usual cell density in 3 ml of medium in 6-well plates: $\sim 4 \cdot 10^3$ $cells/cm^2$ for observations at 1 – 2 DIV, $\sim 3 \cdot 10^3$ $cells/cm^2$ for longer cultures.

[57] NBs medium: B27 (2%), L–Glutamine 200 mM (1%) and Penicillin / Streptomycin (0.05%) in Neurobasal. Invitrogen. Filtered at 220 nm.

concentrations as a function of the incubation time.

We summarize below some conclusive remarks about FN and LN coatings induced by different culture medium on patterned glass substrates (see Section II.1.1 for the fabrication protocol of these substrates).

- MEMs vs NBs medium: FN and LN coatings are observed only with MEMs medium, i.e. in the presence of serum.
- Surface activation by O_2 plasma: FN and LN concentrations are slightly increased.
- Adhesive coating with PLO: FN and LN concentrations are slightly increased by the presence of a PLO adhesive layer on the substrates.
- 1 h, 6 h and 24 h of MEMs incubation: FN and LN concentrations are constant and the cell confinement in the adhesive patterns is not impaired.
- 1 h, 6 h and 24 h of MEMs incubation after the cell seeding: the cell confinement in the adhesive patterns is not impaired.

Interestingly, the surface silanization does not avoid the FN and LN deposition, even though their concentration appears higher on the patterns exposed to the O_2 plasma and/or incubated with adhesive molecules. Nevertheless, neuronal cell confinement is not influenced.

II.2.1.4 Cell preparation for fluorescence time-lapse microscopy: transfections and infections

Transfections by electroporation and virus infections techniques have been employed for live-imaging experiments of GFP labeled neurons.

Electroporation

The process of electroporation is based on the application of an external electrical field to permeabilize the cell plasma membrane and thus to introduce some substances inside, like nucleic acids (DNA plasmids). We have employed the Neon transfection system (Invitrogen). This system is especially adapted for primary cells compared with the traditional Amaxa Nuclefector system (Lonza) thanks to a new pipette chamber that generates a more uniform electric field [22]. Moreover, this system requires only some μl of medium volume and allows customs protocols to optimize the infected–died cell ratio. Below, the protocol we employed:

- **hippocampi dissection and dissociation** (refer to the Section II.2.1.1);
- **centrifugation step** (400 rpm, 5 min) to re-suspend cells in a concentration of 20 000 $cells/\mu l$[58];

[58] A final concentration of $\sim 6 \cdot 10^4$ $cells/cm^2$ on the substrates is replaced by the usually concentration of $\sim 4 \cdot 10^4$ $cells/cm^2$ used for live-imaging at 1 – 2 DIV, taking into account an estimation of around 30% of cell death during electroporation.

- **electroporation parameters:** 1 $pulse$, 20 ms, 1600 V and 0.5 μm of DNA in the culture medium without Penicillin / Streptomycin;
- **cell seeding** (refer to the Section II.2.1.2).

These experimental conditions have been optimized thanks to some preliminary experiments performed during a couple of weeks spent in C. Métin's group at the Institut du Fer à Moulin in Paris (France). Experiments whose results are reported in this manuscript have been then performed in G. Scita's group at the IFOM in Milan (FIRC Institute of Molecular Oncology, Italy).

Virus infection

Virus infections can be achieved by using retroviruses or lentiviruses. With the latter technique, viral RNA is delivered into the genome of the host cell without the need of a process of cell division by mitosis. Lentiviral infections are therefore particularly adapted to neurons.

Lentivirus constructs used in our experiments have been developed in G. Scita's group at the IFOM in Milan (FIRC Institute of Molecular Oncology, Italy). Double infections have been performed at 1 DIV with the following protocol:

- **first infection**: 10 or 20 μl in 0.5 ml (1 ml) of NBs medium for a 12–well (6–well) plate;
- **changing medium** after 3 h;
- **second infection**: 10 or 20 μl in 0.5 ml (1 ml) of NBs medium for a 12–well (6–well) plate;
- **changing medium** after 3 h (overday condition) or after one night (overday / overnight condition).

II.2.2 Pure glial cell cultures

Keeping cell cultures in DMEMs medium[59] improves glial cell proliferation and leads to a pure glial population. The protocol described in this section provides the cellular preparation commonly employed to obtain the conditioned medium used for long term neuronal cultures. By maintaining glial cells at confluence in NBs, this medium is enriched the nutriments (e.g thrombospondin [23, 24]) secreted by glial cells to in particular foster synaptogenesis.

II.2.2.1 Cell seeding

Cells are obtained as described in the previous section for the mixed neuronal–glial cell cultures (Section II.2.1), whit the difference that the dissociation step and cell seeding occur in DMEMs medium. Cells are plated in 100 mm Petri dishes previously functionalized with a

[59] DMEMs medium: Fetal bovine serum (10%), L–Glutamine 200 mM (1%), Sodium pyruvate 100 mM (1%) and Penicillin / Streptomycin (0.05%) in DMEM. Invitrogen. Filtered at 220 nm.

PLO coating[60] at concentration of $\sim 4 \cdot 10^4$ $cells/cm^2$ in 10 ml of medium ($\sim 3 \cdot 10^6$ $cells$/P100, P100: 100 mm Petri dish).

II.2.2.2 Cell maintenance

Medium is replaced by fresh DMEMs medium at 1 and 3 DIV. At 7 DIV cells usually reach confluence. Then medium needs to be replaced only once a week. This preparation can be used for preparing conditioned medium for neuron cultures or, as described below, to perform studies on glial cells (e.g. adhesion and proliferation).

II.2.2.3 Glial cell replating

P100 petri dishes covered by confluent glial cells are washed with warm PBS (37 °C) and incubated with 2 ml of Trypsin with EDTA (0.05%, Life Technologies) during 6 min at 37 °C. Cells are then gently detached from the surface with a 1 ml pipette in the trypsin solution diluted with 2 or 3 ml of warm DMEMs medium in order to stop the trypsin action. Two options are then possible: (i) cells are re-suspended and plated at a given concentration, and the medium is replaced after 3 h (i.e. once glial cells have adhered) in order to completely wash the trypsin; (ii) cells are centrifuged (1000 rpm, 5 min), the trypsin containing supernatant is removed, replaced by culture medium, and the cells are gently re-suspended and plated.

II.2.3 Fixation

Several methods of cell fixation exist. They are adapted to the antibody we used and to the kind of microscope employed for observations (e.g. glutaraldehyde fixation creates a stronger cross–linking of proteins inside cells and it is especially adapted for scanning electron microscopy [25]). For the experiments reported in this manuscript, we have employed paraformaldehyde, with the following protocol: after an optional washing with warm PBS (37 °C), neurons are fixed in 4% paraformaldehyde (PBS dilution) during 10 – 20 min. Paraformaldehyde can be also directly diluted in the culture medium. Indeed, PBS can be a stress factor for cells but it is also useful to rince the substrates from died cells and cellular fragments. Importantly, paraformaldehyde has to be at room temperature or lukewarm, in order to not depolymerize microtubules during fixation. Cells are then washed three times with PBS at room temperature and used for immunofluorescence or stored at 4 °C in PBS. In this case, as the paraformaldehyde can have a reversible effect, a new fixation just before the immunofluorescence might be advisable.
For EB3 staining we have fixed cells with methanol (MetOH) during 10 min at −20 °C, followed by three PBS washings of 5 min at room temperature.

[60] PLO concentration: 0.2 $\mu g/cm^2$ diluted in DI water (15 μg in 10 ml). PLO is incubated over night at room temperature and Petri dish surface is later dried.

For EB1–CAMSAP2 staining we have fixed cells with methanol (MetOH) during 5 *min* at −20 °C, followed by one PBS washing at room temperature and by a second fixation step in 4% paraformaldehyde / 4% sucrose during 5 *min* at room temperature, followed by three PBS washings of 5 *min* at room temperature.

II.2.4 Immunofluorescence

Once cells are fixed, they can be labeled by immunofluorescence. The principle of the immunostaining technique is to incubate cells with a first antibody that binds the target molecule or antigen. This first (primary) antibody is produced in a specific animal. Cells are then incubated with a secondary antibody, always labeled with a fluorophore, that recognizes the host animal specie of the primary antibody. Primary antibodies can be incubated together, as well as the secondary antibodies, being careful not to use primary antibodies made with the same animal specie, otherwise the secondary antibody will label all the molecules bound to the primary ones.

This technique requires a previous step of permeabilization and blocking of non-specific binding of the antibodies[61]. Cells are first washed with PBS and immunolabeling is achieved with the following protocol (all steps are made at room temperature):

- **primary antibodies** incubation, diluted in PBS–X[62], during 1 *h*[63];
- **three washings** in PBS, during 3 *min* upon a mixing platform (20 *rpm*);
- **secondary antibodies** incubation, diluted in PBS–X, during 45 – 60 *min* protected from light[64];
- **three washings** in PBS, during 3 *min* upon a mixing platform (20 *rpm*);
- **Hoechst**[65] incubation for nuclei staining, diluted in PBS–X, during 5 *min*;
- **short washings** in PBS–X, then in PBS and finally in water.

Finally, coverslips are mounted with a drop of a mounting medium on a microscope slide and let dried at 4 °C, until microscopic observations.

II.2.4.1 Antibodies employed in this work

Primary and secondary antibodies employed for the results exposed in this manuscript are summarized in the Table below.

[61] Permeabilization and blocking solution: bovine serum albumin (BSA, 0.2 – 2%) and Triton X–100 (0.1 – 0.2%) in PBS. Incubation during 10 – 30 *min* at room temperature. Of note, Triton X–100 is a detergent that can be replaced with the Tween–20.

[62] PBS–X: Triton X–100 (0.1%) in PBS. As an alternative, antibodies can be diluted in a 1 – 2% BSA solution in PBS.

[63] As an alternative, primary antibody can be incubated overnight at 4 °C.

[64] An optional fixation in 4% paraformaldehyde during 5 *min* can be achieved to fixe the secondary antibody.

[65] Hoechst 33258, an DNA binding, dilution employed: 1 $\mu g/ml$.

Indirect immunofluorescence				
Primary antibodies				
Target molecule	Target localization	Host animal	Dilution	Brand or Kindly provided by
Tyr–Tubulin[a]	Microtubules	Rat	1:850 – 1:1000	Laboratory product
βIII tubulin		Rabbit	1:1000	C. Hoogenraad
Monoclonal Tau–1	Axon specific MAPs	Mouse	1:500	Millipore
Synapsin I	Synaptic vesicles	Rabbit	1:200	
AnkyrinG	Axonal initial segment	Mouse	1:200	C. Hoogenraad
Actin	Actin	Mouse	1:200	
MAP2	Dendrites	Mouse	1:500	Invitrogen
		Chicken	1:10000	C. Hoogenraad
EB1	End–binding protein of microtubules	Mouse	1:100	
EB3		Rabbit	1:400	
CAMSAP2		Rabbit	1:300	
GFAP	Astrocyte cytoskeleton	Rabbit	1:250	A. Triller
N–cadherin	Cell-cell adhesions	Mouse	1:200	D. Gulino
Vinculin	Focal adhesions	Mouse	1:300	
Myosin heavy chain	Myotubes			C. Picart
Fibronectin	Protein of adhesion	Rabbit	1:100	D. Gulino
Laminin	Protein of adhesion	Rabbit	1:100	Sigma
GFP	GFP	Rabbit		G. Scita
Secondary antibodies				
Target animal	Fluorophore	Host animal	Dilution	Brand
Mouse	Alexa Fluor 488	Goat	1:300	Invitrogen
	Cyanine 3	Goat	1:300	Invitrogen
Rabbit	Alexa Fluor 488	Goat	1:300	Invitrogen
	Alexa Fluor 647	Goat	1:400	C. Hoogenraad
	Alexa Fluor 568	Goat	1:400	
Chicken	Alexa Fluor 647	Goat	1:400	
Rat	Alexa Fluor 488	Donkey	1:300	Invitrogen
Direct immunofluorescence				
Target molecule	Target localization	Fluorophore	Dilution	Brand
Phalloidin	Actin	Alexa Fluor 594	1:150	Invitrogen
DNA[b]	Nuclei	Blue	1:1000	Invitrogen

[a] YL1/2 antibody. It detects the tyrosinated form of the α-tubulin subunit.

[b] Hoechst or DAPI antibody.

Indirect immunofluorescence includes primary and secondary antibodies, while direct immunofluorescence is based on antibodies chemically linked to a fluorophore. In this case, antibodies are incubated with the secondary ones.
In the Table, we have reported the target molecule and its localization, the host animal used for the antibody production, the used dilutions for cell labelings and the brand name or the name of the group leader that has kindly provided the antibody for our experiments.

II.3 Microscopy observations

II.3.1 Time-lapse experiments

Images of living neurons were acquired using several inverted microscopes: Olympus IX71, Leica confocal spinning disk microscope (SP8 SMD), Zeiss Axiovert 200M, Nikon Eclipse Ti (equipped with an UltraView VoX spinning disk confocal unit, Perkin Elmer), and Leica AM TIRF MC (Total Internal Reflection Fluorescence) microscopes. All were equipped with a heated workplate or incubator, a humidifier, a CO_2 delivery system and a motorized stage to allow multi-position and multi-condition acquisitions. Microscopes were usually piloted by the Metamorph or the Cellˆ R softwares.
Time-lapse observations requires some compromises. Typically the interval between two acquisitions has to be (i) sufficiently short to follow the event dynamics (e.g. waves along the neurites) and (ii) sufficiently long in order to reduce the stress induced by phototoxicity. Neurons have been usually observed to follow the waves propagations along the neurites ($\sim 3\ \mu m/min$), with an interval of $2 - 4\ min$ and a duration of $4 - 12\ h$. Time-lapse experiments with glial cells have been performed to observe their proliferation, that occurs on a time window in the order of hours. In this case, we have used an interval of $15 - 30\ min$ and duration of $24 - 72\ h$.

II.3.2 Fixed cells

Optical microscopes

Isolated fixed and eventually immunostained neurons were analyzed by phase contrast or fluorescence imaging with a right Olympus BX51WI or an inverted Olympus CKX41 microscope, both piloted by the Cellˆ B software.

Confocal microscopes

Fixed and immunostained cells were observed with an higher resolution using Leica TCS SP2 microscopes.

Atomic force microscope (AFM)

AFM investigations of neuron 3D morphology were performed using JPK Nanowizard III microscope (JPK Instruments AG, Berlin, Germany). The AFM head is coupled to a commercial inverted optical microscope (Axio Observer.A1, Carl Zeiss, Göttingen, Germany). Analyses were performed in PBS using Bruker DNP-10 cantilevers (Bruker probes, Berlin, Germany), with a nominal spring constant of 0.35 N/m. Before each experiment, we calibrated the mechanical properties of the tip using the JPK software. All images were obtained by working in the quantitative imaging (QI) modality, an evolution of the force-volume mode in which the AFM tip is placed in fast oscillation over the sample and the deformation of the cantilever is recorded to reconstruct an image formed by a large number of force distance (FD) curves. Typical images contain up to 256x256 pixels and, for every pixel, 2048 points per FD curves were collected. The tip-sample interaction was limited to a maximum cantilever deflection of 3 nm (i.e. 1 nN).

Digital holographic microscope (DHM)

Phase images of neurons were acquired with a transmission Digital Holographic Microscope (DHM T1000, Lyncée tec, Switzerland).

II.4 Analysis methods

II.4.1 Neurite length of isolated cells

Cells growth on micropatterned substrates were recognized as "isolated" when separated from neighbor cells by at least ~ 30 μm, in order to discard cells whose elongation is limited by external factors. In the case of patterns with adhesive disks for the cell body localization, cells were selected only if about half of the nucleus was on the disk. The neurite length is measured from the edge of the soma to the extremity of the neurite tip.

II.4.2 Statistical tests

The statistical analyses of our experimental data have been performed with the GraphPad Prism software that provides a large panel of statistical tests. In our studies, we often deal with large populations, i.e. samples greater than 100 cells. As most of biological data, measured data follow bell-shaped distributions. When samples are huge, they can be often approximated to Gaussian distributions and parametric tests are quite robust. However, in order to also process data obtained on smaller samples, we have mainly adopted non parametric tests. These tests make few assumptions about the distribution of the data and result adapted both for Gaussian distributions and for smaller samples. We will describe in this section the main tests we used

depending on the type of available data.

◊ **Mann–Whitney test**

The unpaired nonparametric Mann–Whitney test was employed to compare for example two series of cells belonging to the same culture batch but experiencing different growth conditions (for example two kinds of patterns). Samples are independent and may have different sizes.

◊ **Kruskal–Wallis test**

The nonparametric Kruskal–Wallis test was employed as an extension of the Mann–Whitney test to compare more than two groups of samples.

◊ **Fisher's and Chi-square tests**

Theses tests were used to compare frequency values. Contingency tables are created, where the categories defining the rows and columns must be mutually exclusive. Theses tests can for example be dedicated to the comparison between the polarization rates between two populations of cells grown on two different types of patterns or to a random condition (i.e. to a probability of 50%). For series of small sizes, the Fisher's test is considered more accurate than the Chi-square test.

◊ **Linear regression: slope comparison**

Linear trends are fitted by linear curves with methods based on the least squares approach. Slopes are compared between two similar interpolation fits or with a null slope in order to identify a significant linear trend.

Data sets collected from equivalent experimental conditions and configurations in different samples and cell cultures are pooled together only once checked that they are not significantly different.

In all these cases, the null hypothesis when comparing two populations is that they are the same. In this manuscript, we will report the experimental results giving the two-tailed P value associated to the adapted statistical test. P values provide an indication of the probability that the null hypothesis is true, with a significance level depending on the confidence interval. Commonly, a 95% of confiance threshold is chosen and it indicates how precisely the P value is determined. We adopt the common asterisk code to describe values levels of statistical significance according to the table below.

P value	Code	Interpretation
< 0.001	***	Extremely significant
0.001 to 0.01	**	Very significant
0.01 to 0.05	*	Significant
> 0.05	ns	Not significant

Table II.2: **Asterisk code employed to describe values levels of statistical significance.** Threshold values are set by the conventional significance levels associated to the confidence intervals of 99.9%, 99% and 95%.

II.4.3 Neurite volume: atomic force and digital holographic microscopes

Neurite 3D profiles were measured and compared using atomic force (AFM) and digital holographic (DHM) microscopes. Figure II.21 illustrates typical cartographies obtained with both microscopes and the method adopted on the corresponding neurite height profiles to calculate the neurite volume.

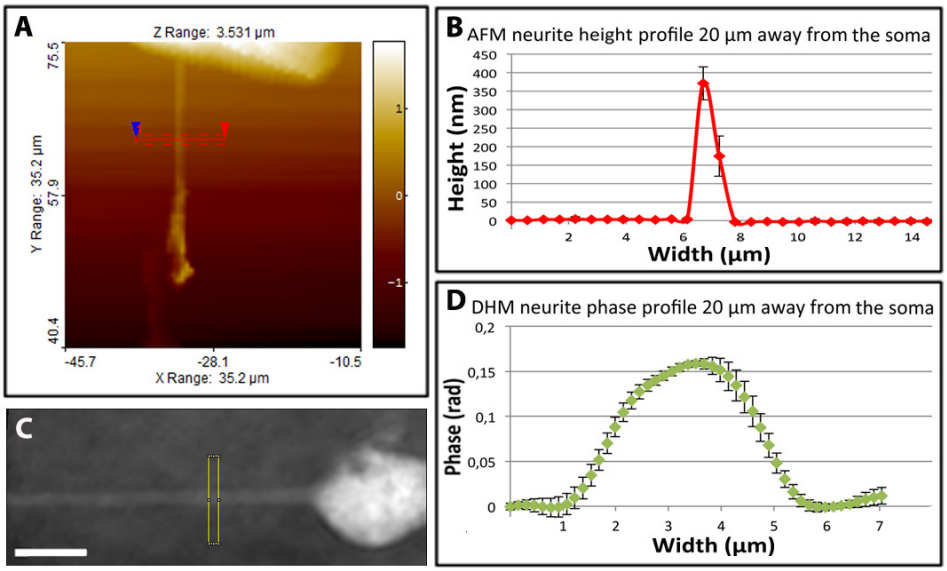

Figure II.21: **AFM and DHM imaging of neurons on patterned substrates.** A) AFM map of one neurite of a neuron on a 2 μm wide stripe pattern. The red line represents the cross section and the dashed lines delimit the zone ($\pm$ 1 μm) where the mean is calculated to get the neurite height profile. B) Height profile of the cross section represented in (A). C) DHM phase image of a neuron on a 2 μm wide stripe pattern. The green line represents the cross section ($\pm$ 1 μm) where the mean is calculated to get the neurite height profile. Scale bar: 10 μm. D) Phase profile of the cross section represented in (C). Error bars denote standard deviations.

AFM cartographies were analyzed with the SPIP software. Cross section profiles were traced on neurites every 5 μm from the end of the soma to the end of the neurite, with a mean of 2 μm along the neurite. To adjust these profiles, we treated them by a "plane correction". They provided us mean surfaces of the neurite cross sections at different points,

used as indications of the neurite thickness along its length. The total neuritic volume could be accessed by treating the whole length of the neurite. DHM phase acquisitions were saved as text files and profiles were traced in equivalent positons along the neurite, as reported for AFM data.

II.4.4 Waves detection

Waves are very dynamic structures, and therefore of very changeable morphology. We thus used a manual recognition of their positions like in [26]. Only propagative membrane deformations on at least three consecutive images are identified as actin waves. Waves being very extended structures, the determination of their coordinates is intrinsically affected by a large uncertainty. We nevertheless retained as the most reliable and reproducible structural mark the boundary between a relatively dense, central area, and the lamellipodium–like structure, more transparent, at the front of the wave (Figure II.22).

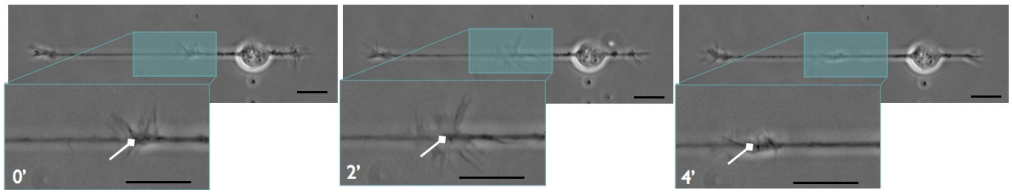

Figure II.22: **Actin wave** in a neuron on an adhesive pattern of 2 μm wide stripes spaced of disks for the soma localization. Insets show the zoomed areas with wave. Numbers indicate in minutes the respective acquisitions of the time-lapse experiment. Only propagative membrane deformations on at least three consecutive images are identified as actin waves. Then, the position of this structure is determined manually from the boundary between a relatively dense and central area and the lamellipodium–like structure, more transparent, at the front of the actin wave (white arrows). A similar manual recognition is performed to follow the neurite tip. Scale bars: 14 μm.

From each video, we created a text file that recapitulates the coordinates of the soma center, the neurite tips and the waves. Zeros encode the absence of waves and authorize an automatic recognition of the occurrence of these structures through a set of routines written in GNU Octave [27]. These routines were then used to automatically extract the following informations:

- the wave and soma instantaneous and mean speeds (from linear fits);
- the total distance traveled by wave and soma;
- the neuritic lengths.

In time-lapse acquisitions of GFP–infected or transfected neurons we identified waves by differential interference contrast (DIC) microscopy or by higher concentrations of fluorescent actin associated to waves (Lifeact staining).

II.4.5 Optical tweezers

Optical tweezer experiments were performed with a Nikon eclipse TE2000 confocal microscope, equipped with a custom built optical tarp using a Ytterbium fiber laser at 1.064 nm (IPG Photonics). Carboxylated 2.8 μm-diameter beads (Spherotech) are poured onto the neuronal cultures. Microbeads are individually trapped by optical tweezers, whose principle is based on the attractive force played by a focused laser beam on the microbead. Beads are moved close to the cell and immobilized until an adhesive contact with the membrane is built. By pulling the bead away from the neurite a membrane tether is created, whose length is then gradually increased in the perpendicular direction. The force required to keep the microbead in a same position corresponds to the local membrane tension associated to the tether position along the neurite.

II.5 Cell positioning by magnetic traps

We will describe in this section some methods developed during this PhD in order to improve the rate of cells correctly positioned on the adhesive patterns. Enlarging locally adhesive stripes to form 15 μm adhesive disk increases the probability to retain soma in these areas and thus to impose controlled initial conditions (Figure II.23.A). However, most cells fall and attach outside the disks and further elongate to adopt different shapes than the ones initially expected (Figure II.23.B).

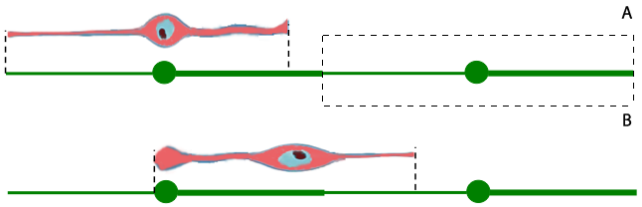

Figure II.23: **Neurons on patterned substrates.** Adhesive pattern module (green) is limited by the dashed square: two different stripe widths with a disk for the soma localization. A) Neuron (red) correctly growing on the pattern module, with the soma in correspondance of the disk. B) Neuron (red) growing outside the pattern module, resulting useless for analyses.

With standard methods, we can estimated the percentage of cells correctly positioned on the adhesive patterns to around 20% of all adherent cells. Magnetic patterned substrates have shown to be a promising tool to improve the control of the cell localization by significantly increasing for example the probability to fill a 3-neuron network [28]. We describe below two techniques we have developed during this PhD, based on the magnetic cell trapping either on PDMS or on glass substrates.

II.5.1 Micropatterned hard magnetic particles in PDMS

The first magnetic cell trapping method has been developed by the group of N. Dempsey at the Néel Institute [29]. The possibility to trap cells functionalized with superparamagnetic beads by micropatterned hard magnets embedded in a PDMS matrix has then been demonstrated. The fabrication principle is based on a patterning technique, named "micro Magnetic Imprinting" (μMI) [30], in which the local fields produced by a "magnetic hard mold" are used to imprint micron–scaled patterns of magnetic particles (average diameter $\sim 16\ \mu m$) in a non-magnetic soft matrix (PDMS in this case). The main steps of fabrication are reported in Figure II.24.

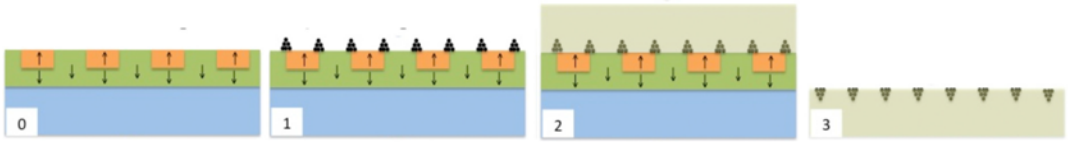

Figure II.24: **Micropatterned hard magnetic films on PDMS.** Schematic diagram of the micro magnetic imprinting process (side view perspective): 1) hard magnetic particles sprinkled onto master structure and magnetophoretically concentrated at the interfaces between neighbouring micro-magnets, 2) polymer poured over the hard magnetic powders to form a matrix, 3) the solid composite is peeled off the master structure.

We have validated this method with several cell types, like HEK293, NIH/3T3 and glial cells[66].

Nano- and microparticles

Cells are functionalized with superparamagnetic nano- or microbeads, respectively: nanoparticles passivated with silica (diameter = 200 nm, SiMAG-Silanol, Chemicell GmbH) or polystyrene-based red fluorescent beads (diameter = 2.8 μm, Fe-oxide inclusions, Micro-particles GmbH). Nanobeads present the advantage to be potentially internalized by endocytosis in the whole cell volume. Their interaction with the micromagnets on the substrate?s surface would results into a more homogeneous magnetic attraction at the cell scale compared to the configuration of isolated microbeads. In this way, the probability of magnetic trapping should increase. However, brain cells are characterized by a low rate of endocytosis and the possible effects of the nanobeads on the biological functions are still poorly known.

Cell functionalization

In a first step, a solution containing $5 \cdot 10^{10}$ nanobeads or 10^7 microbeads is mixed for 7 h into 1 ml of PLO (100 $\mu g/ml$, Sigma). After centrifugation (4000 rpm, 5 min), the supernatant

[66] HEK293 is a Human Embryonic Kidney cell line, NIH/3T3 is a mouse embryonic fibroblast cell line and glial cells comes from primary mouse embryonic brain cultures.

is removed and the beads are re-suspended in 5 ml of culture medium (DMEM GlutaMAX supplemented with 10% fetal bovine serum and 1% Peni-Streptomycine, Invitrogen). This solution is then poured onto a monolayer of cells at the bottom of a 100 mm Petri dish (ratio of nanobeads and of microbeads to cells $\sim 10^3$ and ~ 3 respectively). The cell preparation is left 8 h to allow the PLO coated beads to attach to the cells. The cells are then detached using 0.05% Trypsin–EDTA (Invitrogen).

Cell solution preparation

After a step of centrifugation (1000 rpm, 5 min), the trypsin containing supernatant is removed, replaced by culture medium, and the tagged cells are gently re-suspended using a 1 ml pipette. Hoechst stain is added (1:500) to label cell nuclei and therefore to allow a tracing of live cells trapping events on μMI structures by fluorescence.
Different methods can be then employed to trap cells on magnetic patterned substrates, as described below using HEK293, NIH/3T3 and glial cells.

Cell trapping methods

For experiments with NIH/3T3 and glial cells, tagged with microbeads, a solution of cells (250 000 $cells/ml$) was dropped onto the surface of PDMS-based μMI samples placed upon a mixing platform (Rotamax120, 50 rpm, 3 min) to favour the passage of cells close to the magnetic traps, and to prevent sedimentation in random positions. Then cells were fixed using 4% paraformaldehyde (Figure II.25.A–B). Based on the bead size and the volume content of magnetic nanoparticles associated to simulations of the magnetic field gradient, the trapping force was estimated to be on the order of about 10 nN.

For experiments with nanoparticles and HEK293 cells (a cell type known for its endocytosis properties), the cell suspension ($\sim 5 \cdot 10^6$ $cells/ml$) was introduced into a microfluidic PDMS channel (dimensions: 38 μm x 500 μm x 1.2 mm) to guide the cells above the magnetic patterns at a flow rate of approximately 2 – 3 $\mu l/min$. The trapping force was estimated to be about 0.4 nN. Of note, cells could be removed from the magnetic traps by increasing the flow rate by approximately a factor of 5 (Figure II.25.C).

The images of Figure II.25 clearly demonstrate that the magnetically functionalized cells are attracted and trapped by the regions of maximum magnetic field and field gradient at the surface of the μMI structure[67].
Of note, the stray fields produced by isolated hard magnetic particles embedded in the μMI matrix, are insufficient to trap the functionalized cells, though some do trap free magnetic beads. This illustrates the influence of the pattern size on trapping efficiency.

[67]Field gradients in the range of $10^4 - 10^5$ T/m are estimated for distances in the range 5 μm $-$ 100 nm above the μMI 100 x 100 μm structures.

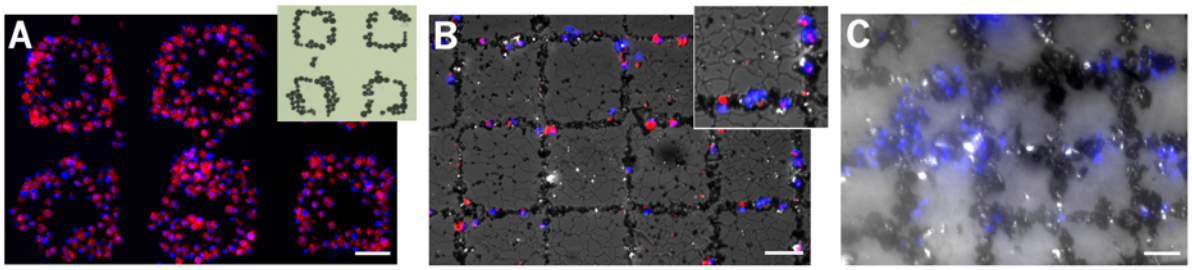

Figure II.25: **Trapped cells on micropatterned hard magnetic films on PDMS.** Superparamagnetic functionalized cells are trapped above the NdFeB powder patterns in the PDMS substrate. A – B) NIH/3T3 (A, fluorescence image) and glial (B, superposition of bright field and fluorescence images, main image and zoom) cells attached to polystyrene microbeads (red, $\phi = 2.8$ μm). In A, the μMI structure is illustrated by the bright field image in the inset. C) Superposition of bright field and fluorescence images of HEK293 cells functionalized by endocytosis with nanobeads ($\phi = 200$ nm) in a microfluidic PDMS channel (dimensions: 38 μm x 500 μm x 1.2 mm). Blue: Hoechst, nuclei. Scale bars: 50 μm.

II.5.2 Micropatterned soft magnetic particles in glass

The second magnetic cell trapping method has been developed to create soft magnetic patterns on glass substrates. The principle is to create cylindrical cavities in the glass substrate and to fill them with superparamagnetic microbeads. The methodology used to localize the microbeads on the surface is the capillary assembly process developed by L. Malaquin at the Curie Institute (Paris, France) [31]. Cells are functionalized with superparamagnetic beads as already described for the first method. the rotamax-assisted or the microfluidic methods to trap cells can be indifferently adopted for this kind of magnetic substrates. As magnetic patterns are built from superparamagnetic particles, the application of a permanent magnet below the substrate is in this case necessary to create the magnetic force required during cell seeding. On the other hand, once cells have been trapped, the permanent magnet can be removed and cells are no more exposed to the magnetic field.

We describe below the methodology developed to create soft magnetic patterns on glass coverslips.

Glass etching

- MicroChemicals AZ4562 **photoresist spinning**[68];
- **annealing** step at 95 °C on a hotplate during 2 min;
- **exposure** through a mask (UV dose necessary: 56 $mJ \cdot cm^{-2}$);
- photoresist **development**[69] during 1 min.
- second **annealing** step at 120 °C on a hotplate during 5 min;

[68] 3000 rpm/s^2 of initial acceleration, 3000 rpm of speed during 30 s, 7 μm of thickness.
[69] Pure Microposit^{tm} Developer, Shipley.

- high power **ion etching** of glass[70];
- surface **cleaning** with acetone with a cleanroom wiper (dust-free, microfiber) and a finale O_2 plasma during 2 min.

Samples are then silanized in order to improve the efficiency of the capillary assembly process. Samples are finally annealed at 200 °C during 1 h in order to heat the polystyrene shell of the microbeads deposited into the cavities in order to maintain them as a whole inside the glass holes. Doubling the cavity diameter from $\sim 3\ \mu m$ to $\sim 6-7\mu m$ is a easy and an optional solution that gives the possibility to localize up to three microbeads in the same cavity and thus increase the magnetic attractive efficiency. Of note, this technique can be also adapted with pure ferromagnetic particles in order to increase the magnetic force.

The advantage of using glass coverslips is the practical aspects associated to this kind of substrate both for adhesive pattern fabrication by photolithography (Figure II.26) and for cell observations under a microscope stage. Thus, this technique is a promising tool to improve the control of the cell localization on adhesive patterns.

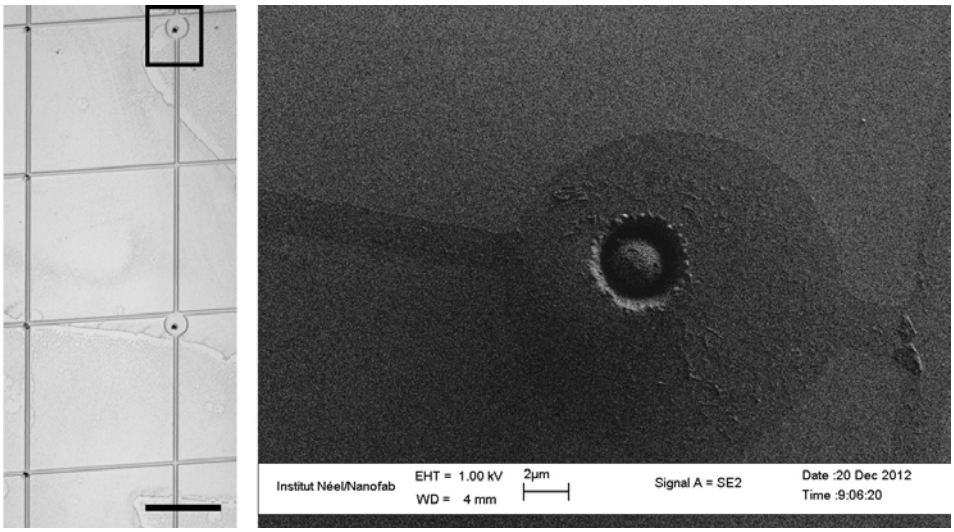

Figure II.26: **Soft magnetic microbeads patterns in glass coverslip.** Superparamagnetic polystyrene microbeads (diameter 2.8 μm) are assembled in patterns of etched cavities in glass. A) Optical image of photoresist patterns obtained by photolithoghraphy after an alignement step on patterns of magnetic particles. Microbeads are localized in the photoresist free regions of the center of the disk and at the crossing of the stripes. The black square delimits a region where a bead is inserted in a disk. Scale bar: 50 μm. B) Scanning electron microscope image of the region inside the black square in (A). Adhesive pattern (PLO coating) showing a 2 μm wide stripe pattern and a magnetic microbead located in a 15 μm in-diameter disk to anchor the cell body.

[70]Applied Materials eMAX™ magnetically-enhanced reactive ion etcher (MERIE). "Dry Clean" with a $O_2 - HI$ plasma on SiO_2 to create a "start point" condition of the chamber. "eMAX quartz" program (40 $sccm$ of CF_4, 10 $sccm$ of CH_2F_2, 800 W, 100 $mTorr$) during 120 s on samples fixed to a Si wafer. This cycle is repeated a number of time proportional to the depth required (etching rate $\sim$ 430 nm/min).

II.6 Summary

In this chapter we have presented the main techniques employed during this work. We have first described the methods of fabrication of chemical and physical patterns. For that, techniques such as photolithography on glass and photopolymerization of polyacrylamide hydrogels have been used. Some variations from standard protocols have been discussed. For example, some alternative surface chemistry with adhesive and non-adhesive patterns have been investigated in the perspective of long term neuronal cultures or to achieve a strong confinement of non neuronal cells, like glial cells.

The protocols to obtain primary brain cells have been described, as well as the techniques of patterned coverslip processing, including the list of the antibodies employed for the results described in the following chapters. The variety of techniques and microscopes (standard and non standard) employed in this work reflect a respective interplay between these tools and the scientific issues. Indeed, if cellular biophysics gains from the existence of these tools that may contribute to open new approaches and questions, biological experimental conditions encourage the development of new techniques.

The analysis methods used to obtain or process the results exposed in the following chapters have been also described. Finally we have presented two techniques to control the cell positioning by magnetic traps, either on PDMS or on glass substrates. Some experiments with different cell types have been reported, that validate these tools and show their potential to obtain an better control of cell localization on chemical patterns during the cell seeding step.

A good mastering of the methodologies would be very important to obtain reproducible experimental conditions and robust results. Moreover, well-defined and reproducible protocols usually lead to a gain of time during experiments. Let us remark, that such a robustness would pave the way to more elaborated or ultimately automatic protocols, and even to new techniques.

Bibliography

[1] Joseph M Corey and Eva L Feldman. Substrate patterning: an emerging technology for the study of neuronal behavior. *Experimental neurology*, 184:89–96, 2003. 40, 62, 65

[2] Y Ikegaya, Y Itsukaichi-Nishida, M Ishihara, D Tanaka, and N Matsuki. Distance of target search of isolated rat hippocampal neuron is about 150 μm. *Neuroscience*, 97(2):215–217, 2000. 65, 84

[3] Teresa Esch, Vance Lemmon, and Gary Banker. Local presentation of substrate molecules directs axon specification by cultured hippocampal neurons. *The Journal of neuroscience*, 19(15):6417–6426, 1999. 28, 41, 67, 167

[4] Ning-Ping Huang, Roger Michel, Janos Voros, Marcus Textor, Rolf Hofer, Antonella Rossi, Donald L Elbert, Jeffrey A Hubbell, and Nicholas D Spencer. Poly (l-lysine)-g-poly (ethylene glycol) layers on metal oxide surfaces: surface-analytical characterization and resistance to serum and fibrinogen adsorption. *Langmuir*, 17(2):489–498, 2001. 69, 70

[5] Ammar Azioune, Marko Storch, Michel Bornens, Manuel Théry, and Matthieu Piel. Simple and rapid process for single cell micro-patterning. *Lab on a chip*, 9(11):1640–1642, 2009. 69

[6] Sébastien G Ricoult, Jennifer S Goldman, David Stellwagen, David Juncker, and Timothy E Kennedy. Generation of microisland cultures using microcontact printing to pattern protein substrates. *Journal of neuroscience methods*, 208(1):10–17, 2012. 40, 69

[7] Ammar Azioune, Nicolas Carpi, Qingzong Tseng, Manuel Thery, and Matthieu Piel. Protein micropatterns: A direct printing protocol using deep uvs. *Methods in cell biology*, 97:133–146, 2010. 72

[8] Ibrahim B Malham and Lionel Bureau. Density effects on collapse, compression, and adhesion of thermoresponsive polymer brushes. *Langmuir*, 26(7):4762–4768, 2009. 73, 74

[9] Rigoberto C Advincula, William J Brittain, Kenneth C Caster, and Jürgen Rühe. *Polymer brushes*. Wiley Online Library, 2004. 73

[10] Luca Lanotte, Giovanna Tomaiuolo, Chaouqi Misbah, Lionel Bureau, and Stefano Guido. Red blood cell dynamics in polymer brush-coated microcapillaries: A model of endothelial glycocalyx in vitro. *Biomicrofluidics*, 8(1):014104, 2014. 73

[11] Adam J Engler, Shamik Sen, H Lee Sweeney, and Dennis E Discher. Matrix elasticity directs stem cell lineage specification. *Cell*, 126(4):677–689, 2006. 33, 76

[12] Penelope C Georges, William J Miller, David F Meaney, Evelyn S Sawyer, and Paul A Janmey. Matrices with compliance comparable to that of brain tissue select neuronal over glial growth in mixed cortical cultures. *Biophysical journal*, 90(8):3012–3018, 2006. 33, 34, 76, 180

[13] Robert J Pelham and Yu-li Wang. Cell locomotion and focal adhesions are regulated by substrate flexibility. *Proceedings of the National Academy of Sciences*, 94(25):13661–13665, 1997. 76

[14] Penelope C Georges and Paul A Janmey. Cell type-specific response to growth on soft materials. *Journal of Applied Physiology*, 98(4):1547–1553, 2005. 76, 180

[15] Danielle Gulino, Abbas Mgharbel, and Alice Nicolas. Procédé de preparation d'une matrice en hydrogel par photopolymerisation, June 6 2013. WO Patent App. PCT/EP2012/066,781. 76, 150

[16] Joyce Y Wong, Alan Velasco, Padmavathy Rajagopalan, and Quynh Pham. Directed movement of vascular smooth muscle cells on gradient-compliant hydrogels. *Langmuir*, 19(5):1908–1913, 2003. 76

[17] Justin R Tse and Adam J Engler. Preparation of hydrogel substrates with tunable mechanical properties. *Current protocols in cell biology*, pages 10–16, 2010. 78, 152

[18] L Sirghi, J Ponti, F Broggi, and F Rossi. Probing elasticity and adhesion of live cells by atomic force microscopy indentation. *European Biophysics Journal*, 37(6):935–945, 2008. 79

[19] Gary A Banker and W Maxwell Cowan. Rat hippocampal neurons in dispersed cell culture. *Brain research*, 126(3):397–425, 1977. 84

[20] Stefanie Kaech and Gary Banker. Culturing hippocampal neurons. *Nature protocols*, 1(5):2406–2415, 2007. 28, 84

[21] Thomas Fath, Yazi D Ke, Peter Gunning, Jürgen Götz, and Lars M Ittner. Primary support cultures of hippocampal and substantia nigra neurons. *Nature protocols*, 4(1):78–85, 2008. 85

[22] Jeong Ah Kim, Keunchang Cho, Mi Sun Shin, Won Gu Lee, Neoncheol Jung, Chanil Chung, and Jun Keun Chang. A novel electroporation method using a capillary and wire-type electrode. *Biosensors and Bioelectronics*, 23(9):1353–1360, 2008. 86

[23] Adam S Asch, LL Leung, Joan Shapiro, and Ralph L Nachman. Human brain glial cells synthesize thrombospondin. *Proceedings of the National Academy of Sciences*, 83(9):2904–2908, 1986. 87

[24] Karen S Christopherson, Erik M Ullian, Caleb CA Stokes, Christine E Mullowney, Johannes W Hell, Azin Agah, Jack Lawler, Deane F Mosher, Paul Bornstein, and Ben A Barres. Thrombospondins are astrocyte-secreted proteins that promote cns synaptogenesis. *Cell*, 120(3):421–433, 2005. 87

[25] JD Eisenback. A comparison of techniques useful for preparing nematodes for scanning electron microscopy. *Journal of nematology*, 18(4):479, 1986. 88

[26] Gordon Ruthel and Gary Banker. Role of moving growth cone–like "wave" structures in the outgrowth of cultured hippocampal axons and dendrites. *Journal of neurobiology*, 39(1):97–106, 1999. 27, 95, 133, 134

[27] Ghislain Bugnicourt. *Adhésion, croissance et polarisation de neurones sur substrats micro- et nano-structurés*. PhD thesis, Grenoble, 2011. 95

[28] Cécile Delacour, Ghislain Bugnicourt, Nora M Dempsey, Frédéric Dumas-Bouchiat, and Catherine Villard. Combined magnetic and chemical patterning for neural architectures. *Journal of Physics D: Applied Physics*, 47(42):425403, 2014. 39, 96

[29] NM Dempsey, D Le Roy, H Marelli-Mathevon, Gorky Shaw, A Dias, RBG Kramer, M Kustov, LF Zanini, C Villard, K Hasselbach, C Tomba, and F Dumas-Bouchiat. Micromagnetic imprinting of high field gradient magnetic flux sources. *Applied Physics Letters*, 104(26):262401, 2014. 39, 97

[30] Nora M Dempsey and Frédéric Dumas-Bouchiat. Procédé de fabrication d'un film comprenant des microstructures magnétiques tridimensionnelles, November 29 2013. FR20120054667, US61/650,398. 97

[31] Laurent Malaquin, Tobias Kraus, Heinz Schmid, Emmanuel Delamarche, and Heiko Wolf. Controlled particle placement through convective and capillary assembly. *Langmuir*, 23(23):11513–11521, 2007. 99

Chapter III

Neuronal growth under chemical adhesive constraints

Contents

Chapitre III : résumé

Dans ce chapitre nous présentons les résultats expérimentaux portants sur la croissance contrôlée de neurones sous contraintes géométriques d'adhérence sur des substrats microstructurés. Deux résultats majeurs sont obtenus. Premièrement, la maîtrise parfaitement reproductible de la localisation de l'axone par le simple contrôle de la largeur neuritique, via le contrôle de la largeur des motifs de molécules d'adhérence à la surface des substrats. Un modèle théorique est proposé, qui reproduit les mesures quantitatives de la croissance neuritique en fonction de la géométrie des motifs d'adhérence. Ce modèle prédit l'existence d'une longueur critique au delà de laquelle la polarisation axonale est possible. Deuxièmement, nous démontrons la corrélation entre la fréquence d'émission des vagues d'actine dans les neurites et la vitesse de pousse des neurites et, par conséquence, de la polarisation neuronale. Ces deux résultats constituent un apport important pour la réalisation de réseaux neuronaux *in vitro* et la compréhension de la polarisation neuronale *in vivo* au cours du développement du cerveau.

List of abbreviations and nomenclatures

AFM ..... Atomic Force Microscope

AIS ..... Axonal Initial Segment

AnkG ..... AnkyrinG

CNS ..... Central Nervous System

DHM ..... Digital Holographic Microscope

DIV ..... Days In Vitro

DRG ..... Dorsal-Root Ganglia neurons

MAPs ..... Microtubule–Associated Proteins

NS ..... Not Significantly different

PA ..... PolyAcrylamide

PDMS ..... PolyDiMethylSiloxane

PIV ..... Particle Imaging Velocimetry

PLL ..... Poly-L-lysine

PLO ..... Poly-ornithine

PNS ..... Peripheral Nervous System

PTV ..... Particle Tracking Velocimetry

SD ..... Standard Deviation

SEM ..... Standard Error of the Mean

TFM ..... Traction Force Microscopy

x–x ..... Patterns of simple stripes, 2 branches

x:x, x:x:x, x:x:x:x ..... Patterns with a 15 μm adhesive disk, 2, 3 and 4 branches

Mature neurons clearly present a differentiation in the morphology of the neurites depending on their functions. Dendrites appear shorter than axons and organized in a dense ramification adapted to collect the informations from other neurons. Whereas axons are longer and thinner in order to reach also far neurons, muscles or glands, and thus to transmit the electrical and chemical signals. However, it is still unclear how developing neurons control their morphology and how this parameter participates in the establishment of neuronal polarization.

In the present work, we have investigated these issues by imposing morphological constraints to developing neurons. As our interest was focused on the establishment of the neuronal polarization, we have mainly studied the neuron growth until the three first stages of development *in vitro* (see Figure I.10). Typically, that corresponds to 3 – 4 Days In Vitro (DIV).
We have firstly played on the control of the neurite width to quantify how this element influences the neuron growth: the neurite 2D elongation and polarization as well as the neurite 3D growth, i.e. the volume. Then we have deeper investigate this parameter that have shown to be crucial in the neuron growth. Looking for the cell response to the control of the neurite width at the neurite level, we have achieved the development of a theoretical model putting in relation the neuronal morphology and the polarization process.
Then, the dynamics of so-called "waves" emitted from the soma and transmitted along the neurites has been studied for the role of these structures associated to the neurite growth. These analyses, again under a control of the neurite width, have led to a minimal model providing a possible explication at the base of the emission of these waves.
A section of this chapter will be dedicated to the forces associated to the propagation of the waves and then to a molecular high resolution investigation of the cytoskeletal organization when a wave is emitted.
We finally conclude with an application of this study for controlled neuronal networks *in vitro*.

Methodology

We have employed chemical adhesive micropatterns to constrain neuronal shapes. This control of the geometry of adhesion allows to dissect the link between morphologies and development.
In vitro hippocampal neurons developing on fully adhesive surfaces generate from their soma about four neurites on average [1]. The characteristic width of these branches is 1 – 2 μm. We have diverted these spontaneous morphological characteristics using various geometries of poly-L-lysine (PLL) or poly-ornithine (PLO) adhesive micropatterns.
We have first chosen micronwide stripes as the simplest pattern in order to analyze and quantify a few features of neuron development like length and polarization. In this configuration,

neurons are constrained to generate two neurites along different stripe widths, as represented in Figure III.1. Later in the text, simple stripes will be defined by the nomenclature x–x (with x = 2, 4, 6 and 8 μm corresponding to the stripe width, III.1.A). In a second type of patterns, stripes are intercalated with a 15 μm in–diameter disk to anchor the soma. The nomenclature of these patterns changes to x:x (III.1.B). We also designed patterns with 3 and 4 branches drawn from a central disk (the 2:2:2 and 2:2:2:2 patterns respectively, III.1.C).

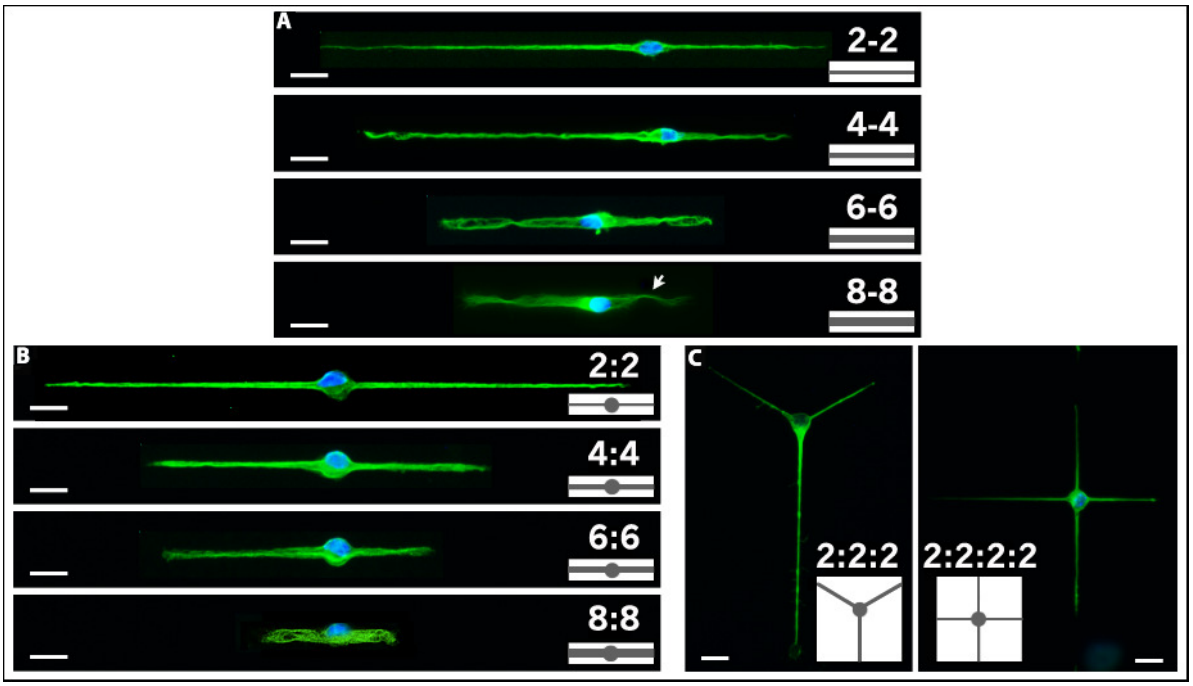

Figure III.1: **Micropatterns and neuronal morphologies at 2 DIV.** Mouse hippocampal neurons on the x–x (A) and x:x (B) patterns (x = 2, 4, 6 or 8 μm). The white arrow points to an instability in neurite adhesion. C) Mouse hippocampal neurons with 3 (2:2:2 pattern) and 4 (2:2:2:2 pattern) neurites on 2 μm wide stripes. Green: YL1/2, microtubules. Blue: Hoechst, nuclei. Adhesive patterns are shown in insets of the images. All neurons are fixed at 2 Days In Vitro (DIV). Scale bars: 20 μm.

I had the great opportunity to spend one month in the A. Triller's group at the Biology Institute of the Ecole Normale Supérieure (IBENS) in Paris (France) at the beginning of my PhD. During this period I learned the necessary techniques for the dissection of mice hippocampal and cortical neurons I have employed for all my experiences over the PhD. In addition, I had also the opportunity to achieve three consecutive cultures in the same conditions and to obtain the results reported in the next section for the x–x and x:x patterns.

III.1 How neurite width controls neuronal growth

The first striking feature we observed when enlarging the stripe width is that neurites tend to spread toward the adhesive stripe's edges. This emphasizes the neurite capability to increase its spontaneous width in culture by a factor of 3 to 6. However, dynamical instabilities in neurite width are sometimes observed, characterized by a transient local shrinking that preferentially occurs close to the edges of the adhesive stripes (e.g. neuron on the 8–8 pattern in Figure III.1.A). Of note, these instabilities were observed only on the largest patterns, i.e. on 6 μm wide stripes and most of all on the 8 μm wide stripes. This indicates that a length of about 8 μm delimits a territory outside which adhesive frontiers are not anymore perceived, and somehow gives an estimation of the lateral distance over which a neurite explore its environment. Why this specific size? In which terms the sensitivity and the adaptability of neurons exploring their environment influence the evolution of their growth? We will give in the next subsections some elements to approach these issues, discussing separately some aspects of the neuronal growth.

III.1.1 Neurite growth

We have performed a complete study of the neurite lengths on all the pattern geometries shown in Figure III.1 and we report in the Table III.1 data set information about the results shown below.

	Number of cells (n)			
	2 DIV		3 DIV	
Stripe width (μm)	Simple stripe x–x pattern	With disk x:x pattern	Simple stripe x–x pattern	With disk x:x pattern
2	180	162	180	180
4	180	165	180	180
6	180	169	180	180
8	167	78	180	39
Control	100		100	

Table III.1: **Statistics informations** about data shown in this section about mouse hippocampal neurons fixed at 2 and 3 DIV on x–x and x:x patterns (PLL coating). Control corresponds to cells on an uniform adhesive substrate. For all conditions: 3 cultures, 6 coverslips.

The expression "total neurite length" will state the sum of the neurite lengths. We have analyzed the total neurite length of isolated neurons fixed at 2 or 3 DIV (Table III.2).
The analyses of neurite length on patterns with different branches have been performed in the context of Celine Braïni and Beilun Wu's internships, two students I have co–supervised during my second year of PhD.

The first consideration is that the presence of an adhesive disk does not modify the total neurite length (Figure III.2.A). Importantly, both for x–x and for x:x series of patterns we report a significant decrease of the neurite length versus the stripe width (Figure III.2.B). Whereas, on the patterns with 2–4 branches, we have observed that neurons retain their overall length, a result that suggests a mechanism of cell length regulation independently of the number of neurites (Table III.3).

	Total neurite length (μm)			
	2 DIV		3 DIV	
Stripe width (μm)	Simple stripe x–x pattern	With disk x:x pattern	Simple stripe x–x pattern	With disk x:x pattern
2	189 ± 83	191 ± 62	320 ± 149	288 ± 124
4	145 ± 63	160 ± 64	248 ± 109	227 ± 82
6	104 ± 38	116 ± 42	178 ± 69	167 ± 64
8	95 ± 40	92 ± 43	149 ± 67	150 ± 63
Control	172 ± 86		252 ± 87	

Table III.2: **Total neurite length** (mean ± SD) of mouse hippocampal neurons fixed at 2 and 3 DIV on x–x and x:x patterns (PLL coating). Control corresponds to cells on an uniform adhesive substrate. Refer to Table III.1 for data informations.

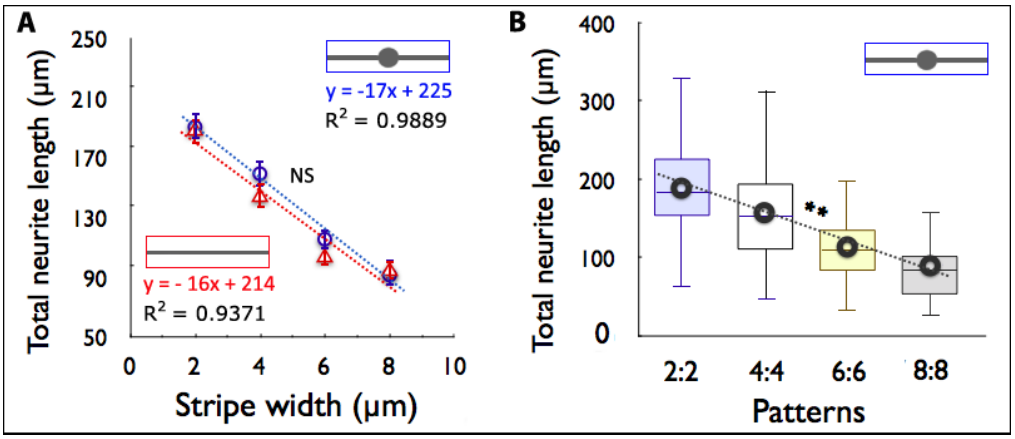

Figure III.2: **Influence of the stripe width on the total neurite length at 2 DIV.** Adhesive patterns are shown in insets of the graphs. A) Total neurite length comparison between x:x (blue circles) and x–x patterns (red triangles). Error bars denote SEM. Slope comparison between the two linear regression fits (blue and red): NS (p = 0.7808). The goodness of linear fits is indicated by the R^2 values associated to the respective equations (in blue and red). B) Decrease of the total neurite length versus the pattern width in x:x patterns. Refer to Table III.2 for data informations; p = 0.0056 (**, slope comparison with zero). Top and bottom of a box indicate 75th and 25th quartiles, respectively; whiskers indicate 10th and 90th percentiles; the middle line is the median. Symbols indicate the mean values.

Of note, the neurons plated on the 2 to 4 branches sets of patterns were grown in our culture room in Grenoble under slightly different conditions of culture (different serum batch, different mice type, different temperature set–point of the incubator) that prevents a direct comparison of the length data obtained from neurons grown at the IBENS on the x–x and x:x patterns.

Total neurite length (μm)			
x:x pattern	x:x:x pattern	x:x:x:x pattern	
308 ± 97	282 ± 88	284 ± 93	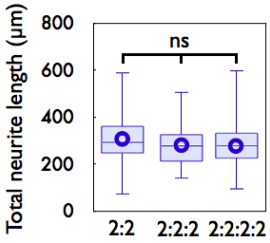

Table III.3: **Influence of the number of branches on the total neurite length at 2 DIV.** Total neurite length (mean ± SD) and graph showing the independence of the total neurite length on the number of neurites. Mouse hippocampal neurons, PLO coating, 2 cultures: n (number of coverslips) = 219 (7), 37 (4) and 81 (4) cells for the 2, 3 and 4 neurite conditions, respectively. NS, Kruskal–Wallis test. Top and bottom of a box indicate 75th and 25th quartiles, respectively; whiskers indicate 10th and 90th percentiles; the middle line is the median. Symbols indicate the mean values.

Interestingly, neuritic lengths of neurons on the 2:2 pattern (i.e the pattern with the 15 μm adhesive disk) are more asymmetric than on the 2–2 patterns (Table III.4). We have quantified how this asymmetry was expressed in terms of neuronal polarization rate and we report these results in the next subsection.

	Asymmetry factor (%)					
	2 DIV			3 DIV		
Stripe width (μm)	Simple stripe x–x pattern	With disk x:x pattern	Test	Simple stripe x–x pattern	With disk x:x pattern	Test
2	0.29 ± 0.22	0.39 ± 0.25	**	0.34 ± 0.23	0.43 ± 0.25	**
4	0.23 ± 0.18	0.28 ± 0.22	NS	0.29 ± 0.19	0.31 ± 0.21	NS
6	0.19 ± 0.15	0.24 ± 0.19	NS	0.27 ± 0.20	0.29 ± 0.19	NS
8	0.21 ± 0.17	0.26 ± 0.20	NS	0.25 ± 0.20	0.28 ± 0.18	NS

Table III.4: **Asymmetry factor** (mean ± SD) of cells fixed at 2 and 3 DIV on x–x and x:x patterns. It is computed as $(L_l - L_s)/(L_l + L_s)$, where L_l and L_s are respectively the length of the longest and shortest neurite. Refer to Table III.1 for data informations. Test values represent the results of the Mann–Whitney test.

III.1.2 Neuronal polarization

To investigate the neurite width influence on the neuronal polarization, we have analyzed cells fixed at stage 3 of cell development (Figure I.10). For that, we have quantitatively assessed the percentage of polarized neurons on all patterns by Tau-1 immunolabeling [2] at 2 and 3 DIV (Table III.5 and III.6 respectively).

We have measured that the percentage of polarized neurons decreases (i) when the number of branches increases from 2 to 4, and (ii) when the pattern width increases.

Polarization rate (%)			
x:x pattern	x:x:x pattern	x:x:x:x pattern	
57.6	45.7	27.3	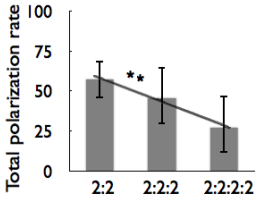

Table III.5: **Influence of the number of branches on the polarization rate at 2 DIV.** Error bars in the graph denote the 95% confidence intervals. p = 0.0044 (**, linear regression test, slope compared to zero). Refer to Table III.3 for data informations.

	Polarization rate (%)					
Stripe width (μm)	Simple stripe x–x pattern			With disk x:x pattern		
	Total	L_l	L_s	Total	L_l	L_s
2	65.6	99.1	9.3	73.3	96.2	12.1
4	60.6	93.6	13.8	63.9	99.1	5.2
6	42.7	98.7	1.3	47.2	95.3	10.6
8	42.2	94.7	3.9	36.8	100	0
Control	Total			57.0		

Table III.6: **Polarization rate** of cells fixed at 3 DIV on x–x and x:x patterns. The rate is obtained by the percentage of tau-1 gradient–positive neurons. It includes the total polarization rate and, among polarized cells: the polarization rate on the longest neurite (L_l) and the shortest one (L_s). Control corresponds to cells on an uniform adhesive substrate. Refer to Table III.1 for data informations.

Let us remark that the significantly higher asymmetry factor found at 2 DIV on the 2:2 pattern than on the 2–2 pattern did not result into a higher rate of polarization at 3 DIV. Note however that, at 3 DIV, the disparity of asymmetry factors for the two kinds of patterns is reduced. This observation suggests that the presence of the disk might induce a premature tendency to break the symmetry (see Table III.4, student's t–test at 2 DIV compared to at 3 DIV) but without leading to a significant difference between the polarization rates at a later stage. On the other hand, for both types of patterns the stripe width strongly influences the polarization rate and highlights the fact that a morphological constraint can tune the polarization rate at a given stage of development.

Similarly to what was reported in cultures on fully adhesive surface [3], double axons have also been observed in rare cases ($\sim$ 10% of the total number of polarized neurons, Table III.7).

	Double axons rate (%)	
Stripe width (μm)	Simple stripe x–x pattern	With disk x:x pattern
2	8.5 (4.7; 14.9)	8.3 (4.7; 14.3)
4	7.3 (3.8; 13.8)	4.4 (1.9; 9.9)
6	0 (0 ; 4.8)	5.9 (2.5; 13.0)
8	3.9 (1.3; 11.0)	0 (0; 21.5)
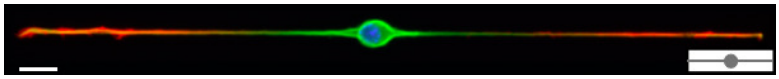		
Control	10.5 (4.9; 21.1)	

Table III.7: **Double axons rate** of cells fixed at 3 DIV on x–x and x:x patterns. Probability to observe doubles axons among polarized cells of Table III.6. Rate and the 95% confidence interval (lower limit; upper limit). Example of an mouse hippocampal neuron with double axon on a 2:2 pattern, fixed at 3 DIV. Red: tau-1, axons. Green: YL1/2, microtubules. Blue: Hoechst, nuclei. Adhesive pattern is shown in the inset of the image. Scale bar: 20 μm. Control corresponds to cells on an uniform adhesive substrate. Refer to Table III.1 for data informations.

III.1.2.1 Neuritic width control to master the localization of axonal specification

The specification of a neurite into an axon is supposed, as also exposed in Section I.2.4, to proceed through the crossing of a threshold of neurite length [4]. Having found a way to tune that length, we have designed a new type of pattern to try to control the process of axonal polarization in bipolar neurons (Figure III.3.A). This pattern is characterized by two lines of different widths, namely of 2 and 6 μm to maximize the expected growth difference while keeping the condition of an uniform neuritic spreading in-between the stripe's edges (this condition would not have been fulfilled using 8 μm wide stripes, Figure III.1.A). A 15 μm diameter disk is inserted at the junction between the two different stripes. In that way, the location of the soma is controlled as well as the width of the proximal segment of each neurite.

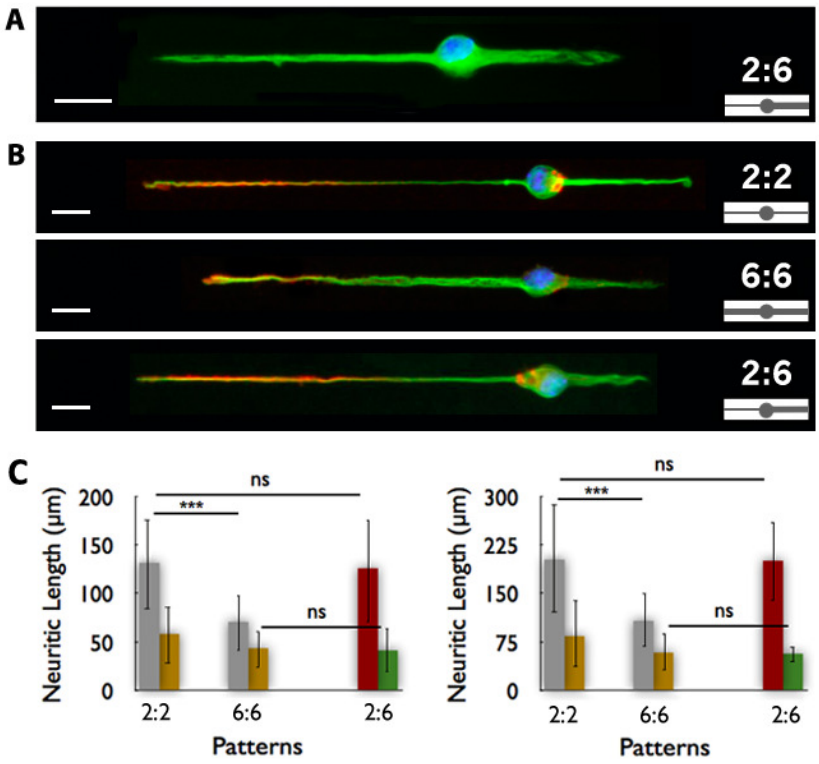

Figure III.3: **Micropatterns and neuronal morphologies at 2 and 3 DIV.** A) Mouse hippocampal neuron grown on the asymmetric 2:6 pattern fixed at 2 DIV. B) Mouse hippocampal neurons grown on symmetric (2:2 and 6:6) and asymmetric pattern (2:6) fixed at 3 DIV. Red: tau-1, axons. Green: YL1/2, microtubules. Blue: Hoechst, nuclei. Adhesive patterns are shown in insets of the images. Scale bars: 20 μm. C) Lengths of the longest (grey columns) and shortest (gold columns) neurites on 2:2 and 6:6 patterns compared to the lengths found on the 2:6 pattern (red column for the 2 μm branch and green columns for the 6 μm branch) of neurons fixed at 2 (left) and 3 DIV (right). Error bars denote SD. Refer to Table III.1 (x:x patterns) and III.8 (2:6 pattern) for data informations. Test values represent the results of the Mann–Whitney test.

We have performed the same analysis of length and polarization as above on this new pattern (Table III.8).

Total neurite length (μm)		Asymmetry factor (%)	
2 DIV	3 DIV	2 DIV	3 DIV
169 ± 60	259 ± 67	0.47 ± 0.26	0.55 ± 0.19

Polarization rate at 3 DIV (%)			
Total	2 μm	6 μm	Double Axons
89.4	100	0	0

Table III.8: **Characteristics of mouse hippocampal neurons growing on the 2:6 pattern** at 2 and 3 DIV: total neurite length (mean ± SD), asymmetry factor (% ± SD), total polarization rate (%) and, among polarized cells: the polarization rate on the 2: side (2 μm), on the :6 side (6 μm) and the probability to observe double axons. 3 cultures, PLL coating. 2 DIV: 18 coverslips, n = 181 cells, 3 DIV: 16 coverslips, n = 180 cells.

On the asymmetric 2:6 pattern, we have observed that neurites elongate differently on each branch with the longest neurite forming on the 2 μm–branch. The independent tuning of neuritic length in asymmetric patterns suggests a local regulation of length at the neurite scale.

A typical neuron on the 2:6 pattern is shown in Figure III.3.B and compared to neurons growing on the 2:2 and the 6:6 pattern. Interestingly, the shortest neurite of the 6:6 pattern and the neurite on the 6 μm–branch of the 2:6 patterns display the same length. Likewise, there is no significant difference between the length of the longest neurite on the 2:2 patterns and the neurite on the 2 μm–branch of the 2:6 patterns (Figure III.3.C). For further information, we report in the Table III.9 the neurite lengths for all patterns.

	Neurite length (μm)			
	2 DIV			
	Simple stripe x–x pattern		With disk x:x pattern	
Stripe width (μm)	Longest	Shortest	Longest	Shortest
2	124 ± 61	65 ± 35	133 ± 49	58 ± 33
4	90 ± 46	54 ± 25	102 ± 46	57 ± 30
6	63 ± 26	42 ± 16	72 ± 27	44 ± 20
8	58 ± 27	37 ± 17	59 ± 33	34 ± 15
	3 DIV			
	Simple stripe x–x pattern		With disk x:x pattern	
Stripe width (μm)	Longest	Shortest	Longest	Shortest
2	218 ± 113	102 ± 65	204 ± 49	58 ± 33
4	162 ± 80	86 ± 43	150 ± 65	77 ± 34
6	116 ± 55	63 ± 27	108 ± 48	59 ± 26
8	96 ± 52	53 ± 24	97 ± 49	53 ± 24
	2 DIV		3 DIV	
	2:	:6	2:	:6
2:6	126 ± 54	42 ± 21	202 ± 60	57 ± 24

Table III.9: **Neurite length** (mean ± SD) of cells fixed at 2 and 3 DIV on x–x, x:x patterns and the 2:6 asymmetric one. Neurite length (mean ± SD) of the longest and the shortest neurite. Refer to Table III.1 (x–x and x:x patterns) and III.8 (2:6 pattern) for data informations.

The 2:6 pattern therefore provides the highest asymmetry in neurite length of all patterns, recreating *in vitro* a bias favoring the rapid extension of one neurite to the detriment of the other, and this from the beginning of neuritic growth. It is therefore not surprising that the 2:6 pattern gives the significantly highest rate of polarization compared to all other symmetric configurations (Figure III.4.A) and even compared to unconstrained neurons (57.0%). Strikingly, this high polarization rate is associated to a deterministic location of the axon specification: among the population of polarized cells on the 2:6 pattern, 100% of them differentiated their axon on the thinnest line (Figure III.4.B). In support of this deterministic control of the axo-dendritic polarity, we have never observed double axons in the 2:6 configuration (Table III.8).

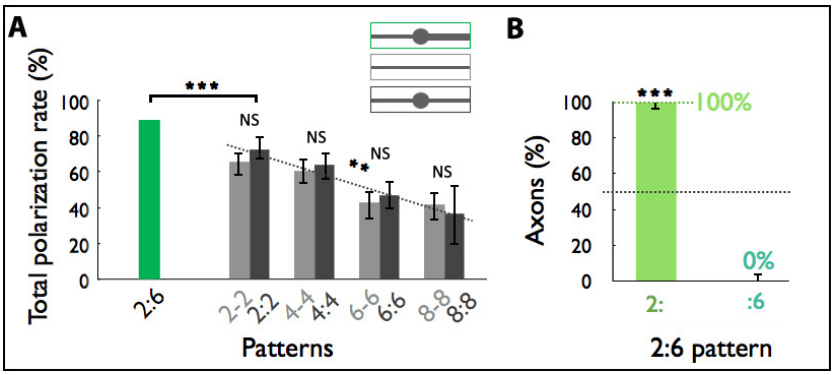

Figure III.4: **Polarization rate** at 3 DIV. Adhesive patterns are shown in insets of the graphs. A) Total polarization rate on the 2:6 asymmetric pattern (green) compared to the different geometries of symmetric patterns (light and dark grey). $p < 0.001$ (***, Fisher's test). NS (Fisher's test). $p = 0.0053$ (**, linear regression test of x:x patterns, slope compared to zero). Refer to Table III.1 (x–x and x:x patterns) and III.8 (2:6 pattern) for data informations. B) Localization of the axon on the 2 μm (2:, light green) and 6 μm (:6, light blue) wide stripes of the asymmetric 2:6 pattern. The dark dashed line corresponds to random (50%), $p < 0.001$ (***, Fisher's test, 3 cultures, $n = 161$ cells). Error bars denote the 95% confidence intervals.

III.1.3 Neurite volume

In the previous sections we have discussed how geometrical constraints on neuronal growth allows a control of neurite morphologies in two dimensions. In this section we address the issue of the third dimension, i.e. the neurite volume.

Atomic force microscopy (AFM) imaging is a method that is largely employed to study the 3D morphology of materials of various origins. It has been more and more adapted in the last decades to manipulate biological objects (e.g. DNA, proteins and cells [5, 6, 7]), and to study living cells [8, 9]. With this technique, the objects are probed with a nanometric tip at the extremity of a cantilever whose deflection reflects the sample topography or stiffness.

A more recent technique that has been developed to image living cells in 3D by optical microscopy is the digital holographic microscope (DHM) at the EPFL (École polytechnique fédérale de Lausanne, Switzerland). The operating principle is based on the measurement of the projected image of an object, recorded as a hologram that is consequently reconstructed by a dedicated algorithm [10, 11, 12].

The advantage of the AFM is that it provides a direct measurement of the topography of the object of analysis, whereas the DHM gives a measurement of the difference of optical path between a beam crossing the object and one of reference. This means that the measurement depends on the index of refraction of the object, which is difficult to assess for living objects. On another hand, AFM needs to scan the sample, which is rather invasive, time consuming and not directly adapted to follow dynamical events. In optimized experimental conditions

with the DHM (high magnification objectives, vibrations filtering, suppression of fluctuations of the liquid-air interface, ...), we could theoretically reach a vertical resolution of 0.2 °. Although we are improving our set-up in order to reduce the noise during acquisition, with our current experimental conditions we have a vertical resolution of about 1 °. Due to the working principle of this microscope, the phase-length conversion depends on the relative values of the refractive index of the medium and of the cell. With the available data, it corresponds to about 10 – 20 nm. As biological samples are quite inhomogeneous, this order of magnitude approaches fairly well the sub-nanometric vertical resolution provided by the AFM. Moreover, a higher lateral resolution can be achieved with the DHM than with the AFM ($\sim$ 150 nm compared to the $\sim$ 300 nm resolution obtained with the AFM).

We report here some measurements by AFM, providing preliminary indications about the neurite volume on pattern stripes of different widths. This issue will be only briefly discussed here as it is the focus of the PhD project of Céline Braïni, a PhD student in our team at the Néel Institute.
AFM measurements have been performed at the Laboratory of physics of living matter (LPMV) of the EPFL in the G. Dietler's team, during a couple of days spent in Lausanne. We have made the choice to select a set of neurons grown on the main significant pattern designs, i.e. symmetric 2–2 and 6–6 stripes and the asymmetric 2:6 pattern. The long duration that is necessary for each map did not give us the possibility to obtain a large set of data. The graph in Figure III.5 reports the mean neurite volume measured as a function of the neurite width on 4 neurons.

Let us remark that as AFM is a quite invasive method, a bias in the measurements during the lateral displacement of the AFM tip might be explain why the effective neurite width is lower that expected, according to the pattern width (especially for the neuron on the 6–6 pattern). About vertical resolution, the height measurements have an estimated erreur of 1 nm.

We note in the graph that the volumes displayed by neurites growing on symmetric patterns (2–2 and the 6–6) are not systematically different. Nevertheless, in both symmetric patterns, the neurite volume is always larger on the shortest neurite (see black stars in Figure III.5).

We have then measured in a first approximation the whole neurite volume by an accumulation of successive mean height profiles traced along the entire neurite. For both neurons on the symmetric patterns the volume results around 40 μm^3, with about a factor two between the shortest and highest neurite compared to the longest and thinnest one. These observations suggest that the neurite volume is quite independent of the neurite width, conversely to the

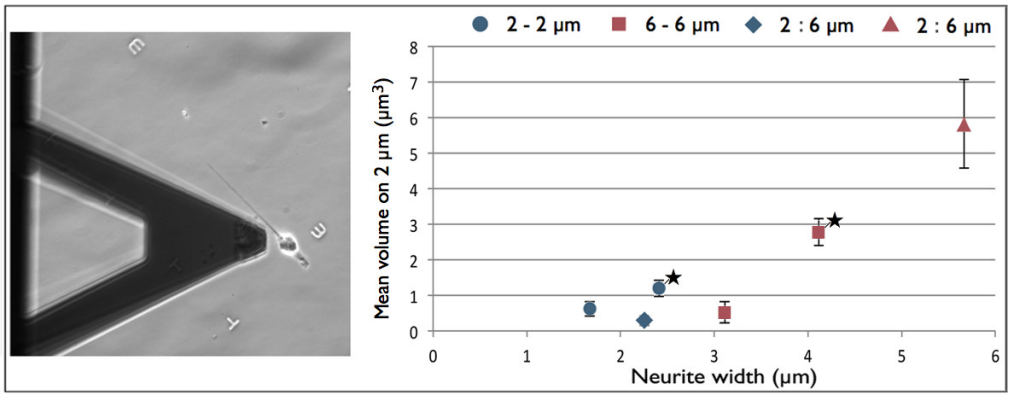

Figure III.5: **Atomic force microscope local measurements of neurite volume.** Hippocampal neuronal cells cultured on PLO patterns and fixed at 2 DIV. Mean volume (μm^3) measured on 2 μm of the neurite length at 15 μm from the soma versus neurite width (μm) measured at the base of the neurite profile. Symbols refer to the 4 neurons observed by AFM. The corresponding pattern designs are reported in the legend, blue (red) symbols indicate the nominal value of 2 μm (6 μm) of the adhesive stripes. Values pointed by the black stars are associated to the shortest neurite of the x – x pattern. The triangular cantilever used for the experiments is shown in the picture on the left, approaching a mouse hippocampal neuron on a 2:6 pattern where the landmark "E" indicates the localization of the 15 μm adhesive disk for the soma. Error bars denote SD.

neurite length that clearly varies with the width (see Section III.1). Moreover, the two neurites of neurons on the asymmetric 2:6 pattern display the lowest and the highest volume values compared to 2 and 6 μm stripes, respectively. Keeping in mind that in this asymmetric pattern the longest neurite is mainly observed on the 2 μm stripe (Figure III.3), this asymmetry imposed by the adhesive surface might impose a neurite volume regulation at the cell level, controlling the asymmetric volume values on the two branches.

These measurements suggest that neurites might regulate their volume in the course of the axonal polarization process. They also give important indications for future measurements with the DHM: firstly, data obtained on neurons growing on symmetric and asymmetric patterns should not be pooled. Secondly, it should be taken into account that as the neurite volume seems to depend on the neurite length, a deeper analysis along neurites would provide important information about the evolution of the neuron volume during its growth.

About neuron volume, we do not have at the moment sufficient data to conclude about its conservation at the cell level (at least when neurites of the same cell are not constrained to adopt different widths). Indications that the volume increases proportionally to the neurite width have to be confirmed. Similarly, preliminary results showing that an asymmetry in neurite width might lead to an asymmetry in both neurite length and volume have to be confirmed. This point would be in agreement with other previous studies reporting that dendrites are shorter, larger and thicker than axons [13, 14].

▶ AFM and DHM measurements to estimate the refractive index of neurites

These experiments have been performed on fixed neurons in order to compare the AFM measurements with the DHM observations on the same cells. We report an example of a 2 μm wide neurite measured with the two techniques, leading to the measurement of the index of refraction of the neurite, according to the relation [15]:

$$\Delta\phi = \frac{2\pi}{\lambda} \cdot \Delta OPL = \frac{2\pi}{\lambda} \cdot h_{cell} \cdot (n_{cell} - n_{medium}) \quad \text{(III.1)}$$

where $\Delta\phi$ is the phase measured with the DHM, $\lambda = 664.8\,nm$ the wavelength of the DHM laser, ΔOPL the difference of optical path length between a beam crossing the cell and one of reference, h_{cell} the height measured with the AFM and n the refractive index of the cell and of the medium (for these experiments in PBS, $n_{PBS} = 1.33$[1]). We used the maximal height obtained on the biggest neurite of that neuron (Figure III.5, 556 nm high and 2.4 μm wide, 2–2 pattern) and compared it with $\Delta\phi = 0.104\ rad$ measured with the DHM for the same region of the same cell, leading to an estimation of its refractive index ($n_{neurite} = 1.361$). This value is close to the value measured for the soma by Rappaz et al. [15] ($n_{soma} = 1.377$). However, the refractive index might not be constant between the soma and neurites, or between neurites of different width, or along the same neurite. More experiments are needed to conclude on that.

An interesting comparison might be performed with another technique, i.e. the fluorescence exclusion technique. This method is based on optical observations, presenting the same advantage of the DHM to provide measurements of the volume evolution at the cell level in real time. Its principle is to obtain a measurement of the cell volume by a negative staining, adding to the extracellular medium a non-cell-permeant fluorescent dye [16]. This technique has been recently implemented and improved at the Curie Institute (Paris, France), and a potential collaboration about this issue is already planned.

[1] PBS refractive index has been measured with an Optilab Rex (Wyatt) refractometer (Range 1.28 – 1.8 RIU; Sensitivity ± 0.002 RIU) at the IBS (Institut de Biologie Structurale, Grenoble).

III.1.4 Summary about the influence of neurite width in neuronal growth

In this section we have employed a geometrical control of neuronal morphology and investigate its role in the establishment of the neuronal polarization. This method has proved to finely control the neuron length and polarization, providing well reproducible experimental conditions.

More precisely, we have shown that:

- neurites can spread to achieve a width of 8 μm, therefore are capable to adopt a size much larger than their spontaneous diameter when constrained by micropatterns of adhesion;
- neurons growing with **wider neurites** are shorter and, interestingly, their rate of growth is not associated to a surface conservation but to a **surface increase**;
- changing the **neurite number** between two and four, with a constant width of 2 μm, does not modify the **total neurite length**;
- the **neuronal polarization** rate varies inversely to the neurite width and neurite number;
- **asymmetric adhesive patterns** imposing to neurons two different neurite widths (2 and 6 μm) lead neurons to a **neurite length regulation** where the thinnest neurite meanly elongates as the mean length of the longest neurite on symmetric 2 μm wide patterns and, similarly, the widest neurite adopt in average the mean length of the shortest neurite on symmetric 6 μm wide patterns;
- asymmetric adhesive patterns **perfectly control the localization of axonal polarization** on the 2 μm wide side of the pattern;
- preliminary experiments by atomic force microscope (AFM) observations show that the **total volume** of neurons growing on symmetric patterns seems to be **conserved**;

To recapitulate, we have achieved a control of neurite length and polarization leading to a deterministic localization of the axon with a novel pattern design. Doing so, we have provided an evidence, in this particular case of axonal polarization, that morphology controls functions.

III.2 Behind the role of the neurite width in the process of axonal specification

III.2.1 Changing the adhesive width along a same neurite

By using patterns with an asymmetric configuration of stripe width, we have achieved an independent tuning of individual neurite length and biased the neuritic competition to reach a perfect control of axonal positioning *in vitro* (Section III.1.2). We now wonder what would be the response in terms of growth and polarization of a neurite confronted to two successive stripe widths. This question is related to the issue of the possible existence of a critical length controlling the process of axonal polarization, as already suggested indirectly by several results (see for example Section I.2.4).

The adhesive patterns

We have designed fours series of geometric variations of the 2:6 pattern in which the lengths of either the 2 μm or the 6 μm wide stripe have been progressively reduced and replaced by a 6 μm or 2 μm wide portion of length l, respectively. More precisely, in the patterns on the left represented in Figure III.6, the non–modified portion of the 2:6 pattern remains near the adhesive disk (i.e. from the soma), on the contrary, on the patterns on the right, the 6 μm (top) or 2 μm (bottom) wide portions of length l depart from the circular disk. For these configurations, all patterns are defined by the nomenclature of type x:xy or y:xy expressing the spatial succession of the 2 and 6 μm wide stripes. These sets of patterns allow to control the neurite width during growth by the generation of a progressive cell shape asymmetry on either side of the cellular body.

Experiments and model in comparison

In this study, the neurite length has been systematically measured and the polarization rate analyzed.
In order to provide a complementary approach to this work, we have collaborated with Nir Gov of the Weizmann Institute of Science in Rehovot (Israel) to develop a model to be compared to the experimental data.

The model is based on (i) a width–dependent rate of neurite elongation and polarization, (ii) the existence of a critical neurite length that sets the axonal fate (Section I.2.4) and (iii) a growth rate dependent on the axonal or dendritic nature of the neuronal branch after the polarization decision.

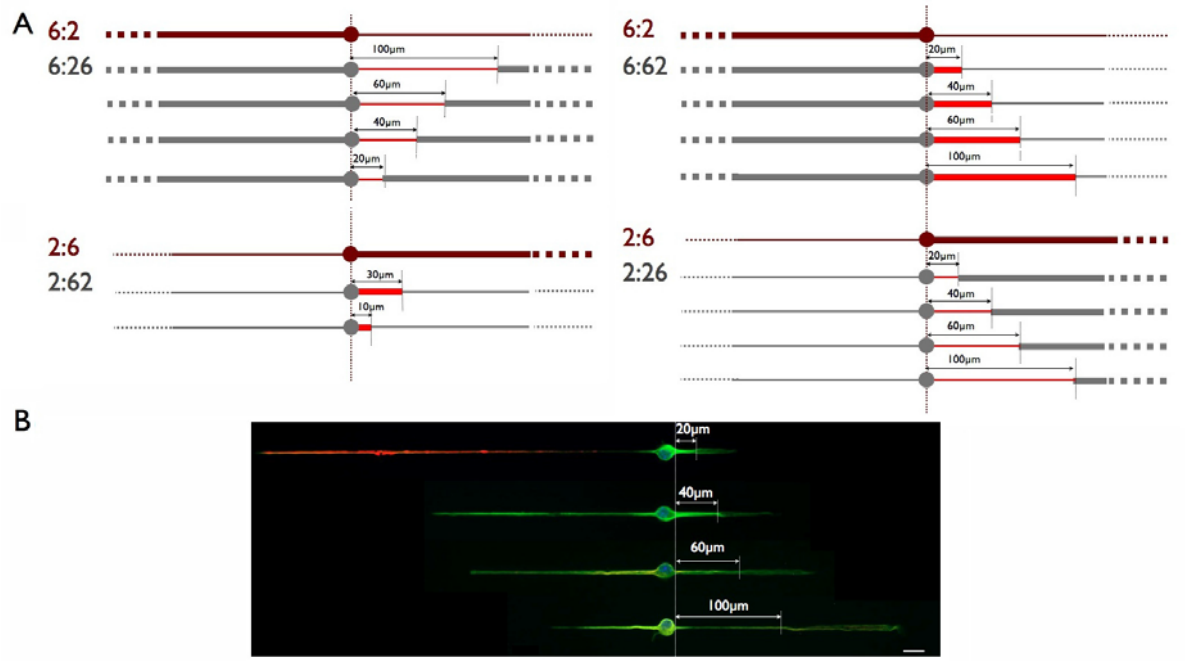

Figure III.6: **Asymmetric micro pattern (2:6) in different modified configurations.** A) In each configuration (6:26, 6:62, 2:62, 2:26) the length of the 2 or 6 μm segment near the central disk varies between 20 and 100 μm. B) Four mouse hippocampal neurons illustrating the four different geometries associated to the 2:26 pattern. The position and length of the various 2 μm wide stumps emerging from the central disk are indicated on each image. Red: tau-1, axons. Green: YL1/2, microtubules. Blue: Hoechst, nuclei. Scale bar: 20 μm.

The model is based on the observations that:

- The growth velocity is affected by the width of the adhesive stripe on which the neurite grows. With the hypothesis that the growth material synthesized at the soma level has to be distributed along the available surface of the neurite, the simplest consideration is that the growth velocity v_{tip} is larger (smaller) when the neurite (i.e. the pattern) width is smaller (wider).

- During the polarization establishment, the future axon increases its growth with a velocity βv_{tip} ($\beta \geq 1$), whereas the other neurites reduce their growth velocity γv_{tip} ($1 \leq \gamma \leq 1$).

- The neuronal polarization event seems to depend on the absolute and critical length of the neurite [17, 18].

By the presence of this critical length that sets the axonal fate, we can define a step–like cumulative probability to polarize $P_{pol}(x)$ (Equation III.2) and its probability distribution function $p_{pol}(x)$ (Equation III.3), represented in Figure III.7. σ_{pol} gives the variance of the probability distribution function around the critical length L_{pol}.

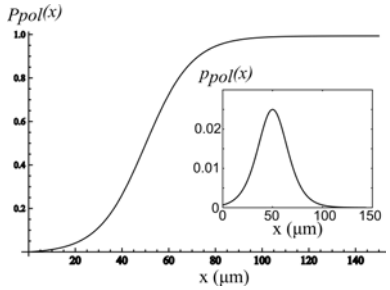

$$P_{pol}(x) = \frac{1}{2}\left(1 + \tanh\left[\frac{x - L_{pol}}{\sigma_{pol}}\right]\right) \quad \text{(III.2)}$$

$$p_{pol}(x) = \frac{dP_{pol}(x)}{dx} = \frac{1}{2\sigma_{pol}}\text{sech}\left[\frac{x - L_{pol}}{\sigma_{pol}}\right]^2 \quad \text{(III.3)}$$

Figure III.7: Polarization cumulative probability $P_{pol}(x)$ (Equation III.2) and the probability distribution function $p_{pol}(x)$ (inset, Equation III.3). The parameters used are $L_{pol} = 50$ μm and $\sigma_{pol} = 20$ μm.

The model requires a set of parameters, namely the culture duration (T), the elongation rates of neurites constrained by either 2 and 6 μm wide stripes, the multiplicative coefficients controlling the change of these elongation rates after axonal specification (β for the axon, γ for the dendrite), and the characteristic lengths of the probability distribution function L_{pol} and σ_{pol}. The three first parameters are fixed by the experiments, with $T = 72$ h (all neurons were fixed and analyzed after 3 DIV), $v_2 = 4$ $\mu m/h$ and $v_6 = 2$ $\mu m/h$, as estimated from the data of the total neurite length of cells grown on symmetric x:x patterns (x = 2 and 6 μm, Table III.2). Values of $L_{pol}, \sigma_{pol}, \gamma$ and β are obtained by fitting the model to the experimental data. Calculations of the neurite lengths and the polarization probabilities are compared to experimental data in Figures III.8, III.9, III.10 and III.11, where the neurite lengths and the observed frequencies of axons identified by immunolabeling are separately represented for each branch of the pattern. Of note, the set of parameters is the same for all cases. Among them, only L_{pol}, σ_{pol}, β and γ were free when running our model.

As remarked previously for the experiments on the patterns with the 2 to 6 branches, neurons plated on the four different x:xy or y:xy sets of patterns were grown in our culture room in Grenoble under slightly different conditions of culture (different serum batch, different mice type, different temperature set–point of the incubator). The lengths obtained from neurons grown on the 2:6 pattern during my stay at the IBENS, in Paris, were too profoundly affected by the changes of experimental conditions to be featured here. Nevertheless, we made the choice to show on the polarization graphs the data coming from all patterns, including the 2:6 geometry (red symbols, positioned at $l = 0$ μm in Figures III.8 and III.9 and arbitrary located at the coordinate $l = 200$ μm in Figures III.10 and III.11), in order to give a complete overview of our results.

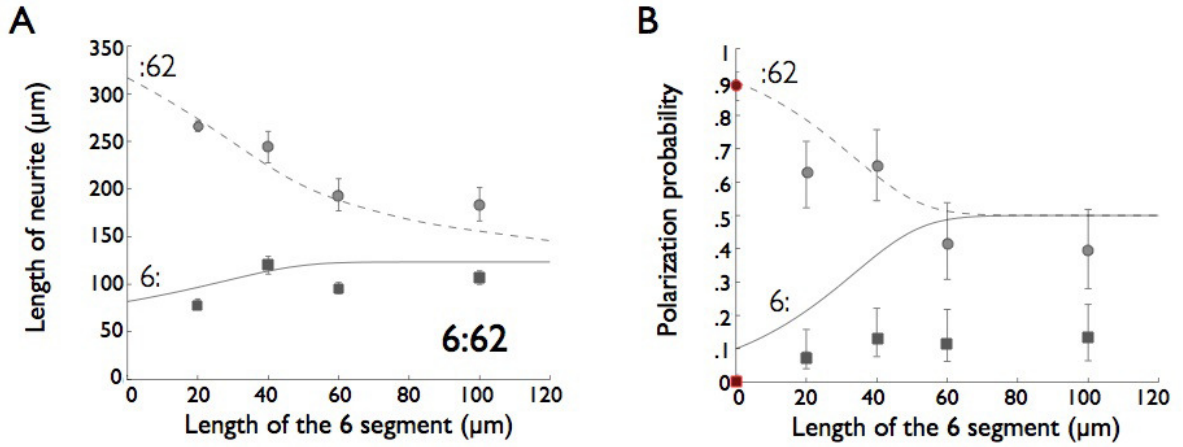

Figure III.8: **Neurite length and polarization on 6:62 patterns at 3 DIV.** A) Lengths of the left and right neurite in the 6:62 pattern. Symbols denote the experimental data and lines the result of the model calculation: Circles (dashed line, L_R) along the right neurite, squares (solid line, L_L) for the left neurite. Error bars denote SD. B) Polarization probabilities of the left and right neurite, in the 6:62 pattern. Symbols denote the experimental data and lines the result of the model calculation: Circles (dashed line, P_R) along the right neurite, squares (solid line, P_L) for the left neurite. Error bars denote the 95% confidence intervals. Red dots correspond to the polarization probability obtained for neurons on the 2:6 pattern and positioned at $l = 0$ μm (experiments performed at the IBENS, in Paris). The parameters used in this calculation are: $T = 72$ h, $\nu_6 = 2$ μm/h, $\nu_2 = 4$ μm/h, $\beta = 1.2$, $\gamma = 0.4$, $L_{pol} = 50$ μm, $\sigma_{pol} = 20$ μm.

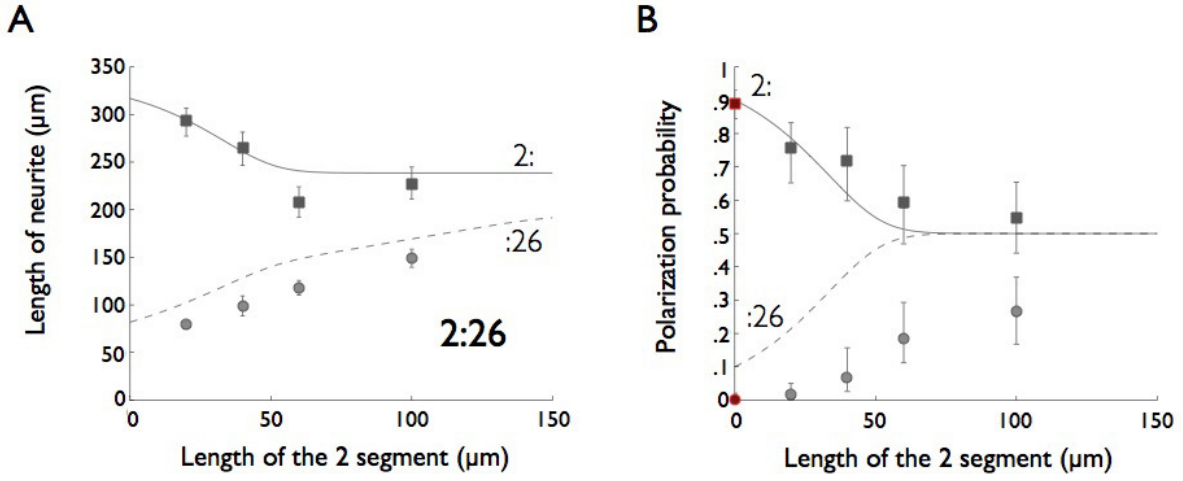

Figure III.9: **Neurite length and polarization on 2:26 patterns at 3 DIV.** A) Lengths of the left and right neurite in the 2:26 pattern. Symbols denote the experimental data and lines the result of the model calculation: Circles (dashed line, L_R) along the right neurite, squares (solid line, L_L) for the left neurite. Error bars denote SD. B) Polarization probabilities of the left and right neurite, in the 2:26 pattern. Symbols denote the experimental data and lines the result of the model calculation: Circles (dashed line, P_R) along the right neurite, squares (solid line, P_L) for the left neurite. Error bars denote the 95% confidence intervals. Red dots correspond to the polarization probability obtained for neurons on the 2:6 pattern and positioned at $l = 0$ μm (experiments performed at the IBENS, in Paris). The parameters used in this calculation are the same as in Figure III.8.

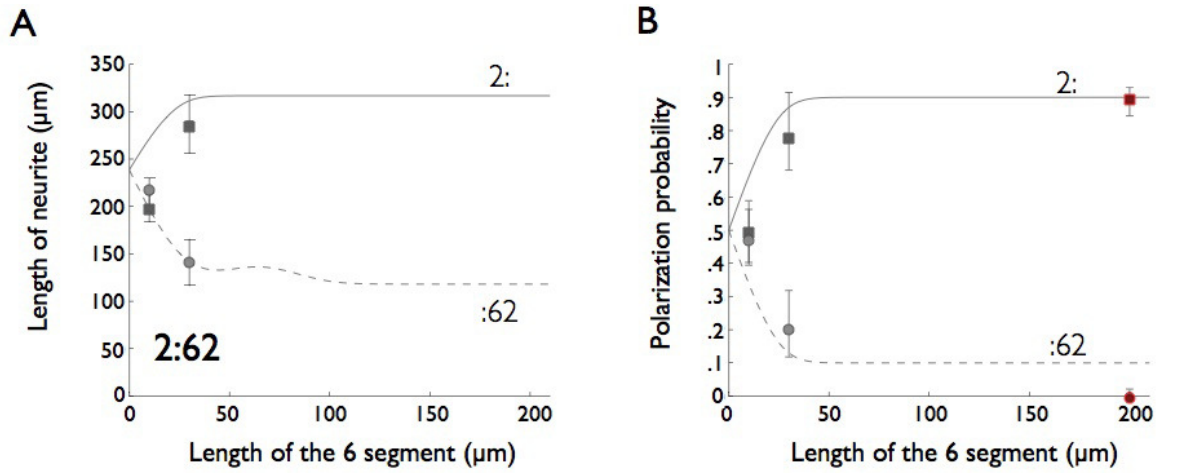

Figure III.10: **Neurite length and polarization on 2:62 patterns at 3 DIV.** A) Lengths of the left and right neurite in the 2:62 pattern. Symbols denote the experimental data and lines the result of the model calculation: Circles (dashed line, L_R) along the right neurite, squares (solid line, L_L) for the left neurite. Error bars denote SD. B) Polarization probabilities of the left and right neurite, in the 2:62 pattern. Symbols denote the experimental data and lines the result of the model calculation: Circles (dashed line, P_R) along the right neurite, squares (solid line, P_L) for the left neurite. Error bars denote the 95% confidence intervals. Red dots correspond to the polarization probability obtained for neurons on the 2:6 pattern and arbitrarily located at the coordinate $l = 200$ μm (experiments performed at the IBENS, in Paris). The parameters used in this calculation are the same as in Figure III.8.

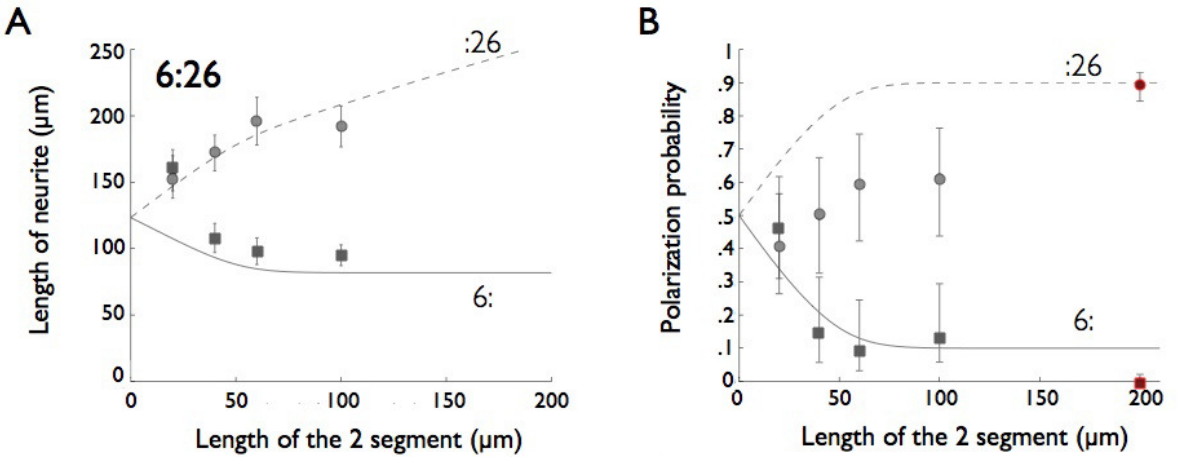

Figure III.11: **Neurite length and polarization on 6:26 patterns at 3 DIV.** A) Lengths of the left and right neurite in the 6:26 pattern. Symbols denote the experimental data and lines the result of the model calculation: Circles (dashed line, L_R) along the right neurite, squares (solid line, L_L) for the left neurite. Error bars denote SD. B) Polarization probabilities of the left and right neurite, in the 6:26 pattern. Symbols denote the experimental data and lines the result of the model calculation: Circles (dashed line, P_R) along the right neurite, squares (solid line, P_L) for the left neurite. Error bars denote the 95% confidence intervals. Red dots correspond to the polarization probability obtained for neurons on the 2:6 pattern and arbitrarily located at the coordinate $l = 200$ μm (experiments performed at the IBENS, in Paris). The parameters used in this calculation are the same as in Figure III.8.

Some conclusions about the model

We note that the length data are very well fitted by our model and that the trend of the polarization rate is also correctly described by the model, although a systematic shift can be observed in certain cases. The fits give for the two parameters L_{pol} and σ_{pol} the following values: $L_{pol} = 50$ μm and $\sigma_{pol} = 20$ μm. The critical polarization length L_{pol} is therefore similar to the length of the axonal initial segment (AIS), i.e. 30 – 40 μm, found experimentally [17, 18], although a little bit higher. Of note, the probability to polarize into an axon has a significant spread around this critical length (see Figure III.7), in coherence with the experimental data reported by Wainrib et al. [19]. Interestingly, it has been shown that a differential neurite elongation obtained using adhesive geometries, where only one neurite among four is allowed to extend beyond a length of $\geq 60\,\mu$m, is highly favorable for the axonal specification of the longest neurite [17]. Our findings are in very good agreement with these recent results, also supporting the existence of a critical length, close to the AIS length, implicated in the establishment of the neuronal polarization. The other parameters used in the model find a biological relevance too. The different elongation rates chosen for the axons (β) and the dendrites (γ) are in coherence with the different growth rates found by Ruthel et al. [20, 21]. Indeed, these authors report that a neurite elongation is mediated by periodic growth spurts produced by propagative growth cone like structures (so–called waves, already introduced in the Section I.3.3) when reaching the neurite tip and that their frequency between the nascent axon and the other minor processes gives a ratio of about $\sim 2 - 4$. This value is in perfect agreement with the value $\beta/\gamma = 3$ that came out of our model.

In conclusion, we have probed the impact of geometry on the neuronal polarization process, putting in relation the neuronal morphology and growth. We have shown that the elongation rate of the neurite tip is width dependent while the critical length for the axonal polarization is width independent. We will discuss in the next section, dedicated to the "waves", some possible mechanisms underlying the control of the neurite growth.

III.2.2 About axonal and dendritic markers

Until here, we have employed the immunostaining technique as a tool to visualize the cell morphology, and consequently to mesure the neurite length and to identify axons by a gradient of tau-1 immunolabeling. Moreover, immunofluorescence, based on the specificity of antibodies to their antigen to target specific molecules inside the cells, is also fundamental to investigate neuron from a molecular point of view.

AnkyrinG and MAP2

We check here if constraining neurons on micropatterns affects the localization of the usual molecular markers of neuronal differentiation. Immunolabeling of MAP2 and ankyrinG (ankG), were performed to identify dendrites and the axonal initial segment (AIS) respectively (see section I.2.4 for more details). Some examples of neurons fixed at 6 DIV on the 6:26 pattern are shown in Figure III.12.

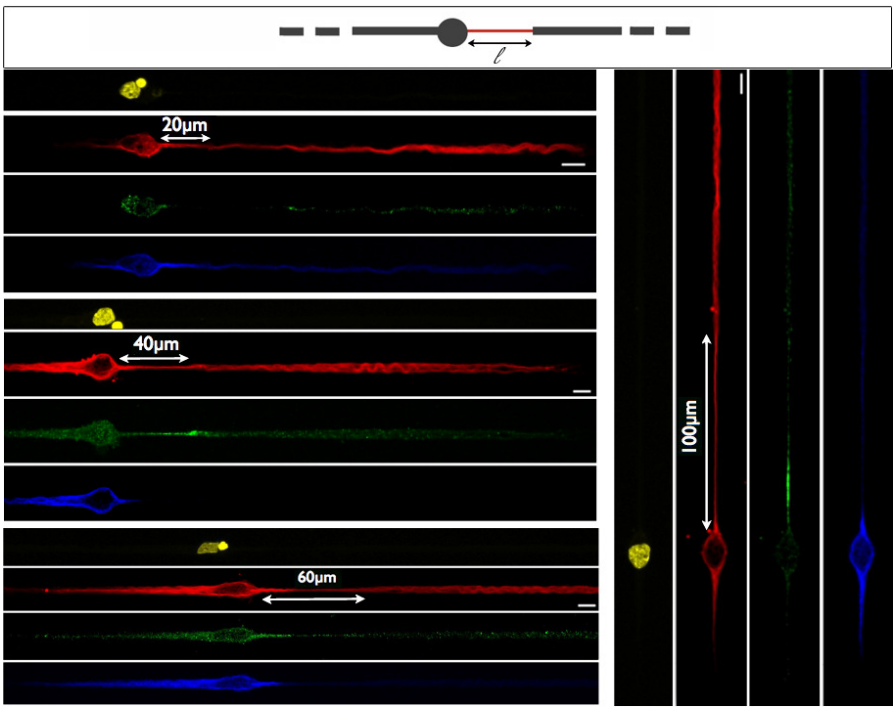

Figure III.12: **Rat hippocampal neurons grown on 6:26 patterns at 6 DIV.** Adhesive pattern (PLO coating) is represented by the grey design, the 2 μm wide segment is shown in red (l = 20, 40, 60, 100 μm). The position and length of the various 2 μm wide stumps emerging from the central disk are indicated on each image of neurons in the four geometries. Yellow: DAPI, nuclei. Red: βIII tubulin, microtubules. Green: AnkyrinG, axonal initial segment. Blue: MAP2, dendrites. Scale bar: 10 μm.

We note that MAP2 is well confined on the shortest neurite, i.e. on the branch on the 6 μm wide branch of the 6:26 pattern, which displays the highest probability to become a dendrite (see Figure III.11). The ankG stained segment seems to be specific of 2 μm wide stumps independently of the length of this section. Moreover, ankG stained segment is 30 – 50 μm long and it appears just after the MAP2 short segment located near the soma, on the :26 side, as expected from observation in non-constrained neurons. Of note, MAP2 staining stops just in the proximal region of the axon near the soma (this area corresponds to begin of the AIS in the neurons in the patterns with l = 40 and 100 μm), while it appears more diffused in the whole neurite in the neuron on the pattern with the shortest l length (l = 20 μm), where the AIS marker is not expressed.

For these experiences, the scarcity of isolated neurons correctly positioned (with their soma on the 15 μm disks) prevented a quantitative analysis of the AIS length and position on varying the parameter l.

More experiences should be performed in order to evaluate from a molecular point of view a possible impact of the pattern shape, i.e. the neurite width close to the soma, on the axon formation. Nevertheless, we have observed that the establishment of the molecular specificities of the AIS and of dendrites was not impaired by morphological constraints.

III.2.3 Summary about our biophysical approach of neuronal polarization

In this second section we have deeper investigated how neurite length critically participates to neuronal polarization. For that, we have combined **experimental and modeling approaches** of neuron growth and polarization under constrained geometries.
Firstly, we have confirmed the existence of a **critical length for neuronal polarization**. Then, we have demonstrated that this length does not depend on the neurite width although the neurite tip elongation rate is dependent on the neurite width.

By immunostaining observations, we have confirmed that **morphological constraints** do not impair the establishment of the molecular specificities of the axonal initial segment nor of the dendrites.

A quantitative analysis of the localization of the axonal initial segment as a function of the neurite width should bring complementary information about the establishment of the axon molecular and morphological properties.

In order to get some clues on the underlying mechanisms at the origin of these observations, in the next section of this chapter we will explore the dynamical properties of propagative growth cone like structures, named "waves" and associated with neurite elongation.

III.3 Growth cone like waves along neurites

III.3.1 Neurite elongation and neuronal polarization: which mechanisms?

The establishment of neuronal polarization relies on the activation of numerous signaling pathways that results in both a morphological and a functional distinction between one axon and several dendrites. In the previous sections we have developed the aspects related to the structural evidence of the polarization event, i.e. the faster elongation of the nascent axon relatively to the other neurites, and how this process is influenced by the width or the number of neurites. It is undoubted that on the observation of fixed cells allow the implementation of statistically relevant analysis of a large number of cells in the same conditions and at the same stage of development. However, an important complement is provided by dynamical observations of living neurons, in order to follow in real time the phenomena associated to neuronal growth. A less known feature of neuronal polarization concerns the properties of propagative growth cone like structures named "waves" by Ruthel and Banker [20].
The fundamental role of these "waves" during development has been assessed by several reports during the last decade, even if not much attention has been paid until now to molecular aspects of these structures. The seminal works of Ruthel and Banker in the late 90' [20, 22] have established several characteristics and functions of these dynamical structures: waves are initiated at the soma level, propagate along neurites at a rate of about 3 μm/min, are two times more frequently directed along the presumptive axon during the stage 2 – 3 transition (Figure I.10), and their arrival at the neurite tip triggers a retraction, whose amplitude is lower in axons than in future dendrites, preceding a growth sprout. A more recent work has also assessed the crucial role of waves in neurite branching and further demonstrated the physiologically relevance of waves by revealing their presence in organotypic hippocampal slices [21].

We have studied the properties of these waves with the purpose to look deeper into their role in neurite growth and in the phenomenology of neuronal polarization. We report in this section the results obtained from our approach of neuronal shapes, i.e. from the control of neurite morphology by micropatterned substrates. We have therefore selected some key micropatterns to study how neurons regulate their wave production.

III.3.2 Neurite width influences wave characteristics

In this section, we will use adhesive stripes to well characterize the wave properties on a minimal and reproducible system of neurons with two diametrically opposed neurites of various widths. Thanks to this configuration, it is possible to (i) accurately measure the contribution of waves in the neurite growth, (ii) to measure the waves characteristics and (iii) to compare these results to the variation of the neurite growth rate we have already observed on different stripe

widths. Indeed, two observations can be put together: the fact that neurite width controls the neurite length (Section III.1) and that waves are associated to neurite growth [22]. We can therefore expect that a link should exist between the neurite width and the wave properties. To collect a convincing amount of data, numerous time–lapse experiments have been necessary. We have selected young neurons (i.e. taken at about 1 DIV) with rather symmetric neurite length (stage 2 of the development of hippocampal neurons *in vitro*, Figure I.10) in order to study the properties of the waves before the process of neuronal polarization (see Section II.4.4 for the modalities of wave identification). The characteristics of waves we are interested in are the velocity, the emission period at the cell level and the allocation of waves along each neurite.

▶ **Waves and neurite growth**

Firstly, we noticed a wave–induced retraction and elongation at the neurite tip on patterned neurons. This feature appears therefore as a generic phenomenon of neuronal growth either in constrained or unconstrained conditions [22]. We have then, similarly to Ruthel and Banker in their seminal works on waves [22], evaluated the proportion of the neurite's growth that is temporally correlated with the arrival of waves at the tip. To assess the relation between neurite growth and waves in morphologically constrained neurons, we have determined separately (i) the transient wave–associated net tip outgrowth, and (ii) the total cell elongation during the full window of observation, computed as the total length increase between the two neurite tips. The wave-associated net tip outgrowth is determined by the difference between the wave–induced neurite elongation and an initial retraction. The initial retraction is computed within the time window of wave propagation (light blue window, Figure III.13.B). Symmetrically, the same duration was used to set the end of the elongation step (red window, Figure III.13.B). To get a direct perception of the effect of a single wave, these two values were computed per wave. For a set of eight neurons plated on 2–2 and 6–6 patterns that display a broad distribution of growth rates, the relation between these two lengths draws a linear variation of slope close to 1 (Figure III.13.A). This reveals the dominant contribution of the transient wave–associated tip growth in neurite elongation.

▶ **Neurite morphology and wave emission frequency**

Then, we focused on the influence of the neurite number and width on the frequency of neuronal waves at the cell level.

We first observed that waves are emitted periodically in all configurations. For the patterns composed of 2 μm wide stripes, we have measured periods that are not significantly different (Figure III.14.A).

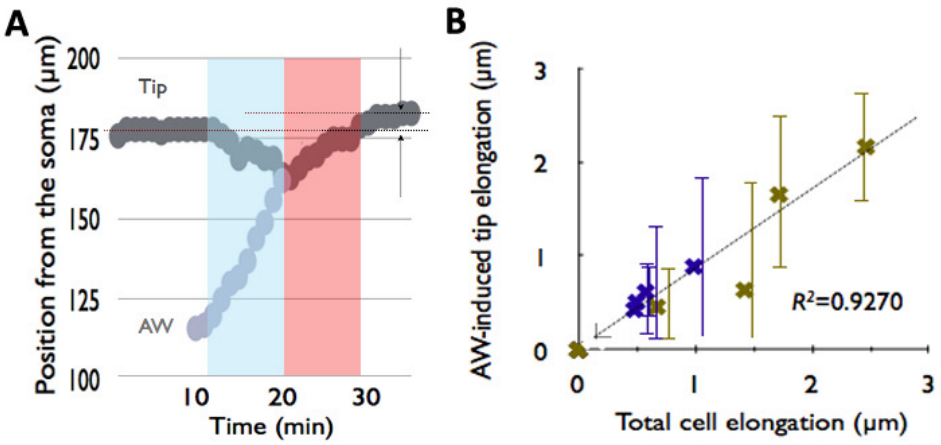

Figure III.13: **Role of waves in cell elongation of mouse hippocampal neurons.** A) Coordinates of a wave (light gray dots) and the corresponding neurite retraction followed by elongation (dark gray dots). The amplitude of the net tip growth is indicated by arrows and results from the sum of the initial tip retraction and the subsequent growth spurt computed within the red and blue windows, respectively. B) The wave–associated elongation versus the total cell elongation. Elongation values are normalized per wave. n (pattern, number of cells) = 191 (2–2 pattern, 4 cells, blue symbols), 57 (6–6 pattern, 4 cells, gold symbols). Error bars indicate SEM. The dashed line is a linear fit of slope 0.84. The goodness of the linear fit is indicated by the R^2 value.

Therefore, varying the number of neurites or forcing the soma to sit on an adhesive disk does not alter the periodicity of wave emission. Then, we have found that the period of waves scaled with the stripe width: the period is multiplied by almost a factor of 3 for stripe widths varying from 2 to 6 μm (Figure III.14.B).

Our results thus demonstrate a simple way to modulate the periodicity of waves in hippocampal neurons by the unique control of the neurite lateral spreading. To check what is the cellular compartment that controls this period, we have analyzed the neuronal growth on the asymmetric 2:6 pattern. Very interestingly, this pattern shows distinct wave periods along each neurite, similar to the values found for the neurites on corresponding symmetric patterns (Figure III.14.C). The production of waves thus appears to be locally tuned by the stripe width, being more frequent along the neurite that elongates on the thinnest adhesive line. In brief, from a variation of the stripe width (i.e. of the neurite width) we have found a method to bias the allocation of waves along neuronal extensions.

We remark that both for neurons on 2–2 (weakly anchored soma configuration) and 2:2 patterns (where the soma is trapped by 15 μm adhesive disks), the emission period (Figure III.14.A) and the alternative rate (70.9% and 71.3% respectively for the 2–2 and the 2:2 pattern) are conserved.

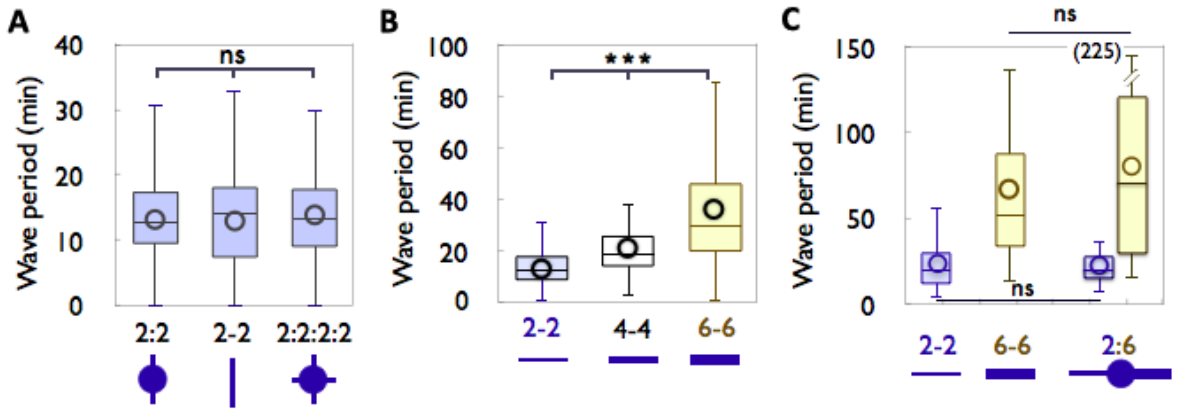

Figure III.14: **Influence of the stripe number and width on the wave emission period.** A) Wave period for the various 2 μm wide stripe patterns. NS: Kruskal–Wallis test. B) Wave period versus the stripe width in the x–x patterns. $p < 0.001$: Kruskal–Wallis test. C) Wave periods measured along a given neurite. For the symmetric x–x patterns, periods are computed neurite by neurite and pooled. All the patterns are sketched in blue below the graphs. Top and bottom of a box indicate 75th and 25th quartiles, respectively; whiskers indicate 10th and 90th percentiles; the middle line is the median. Symbols indicate the mean values. NS: Kruskal–Wallis test. See Table III.10 for relative values and culture conditions.

	Cell level		
Pattern	Wave period (*min*)	Number of waves	Number of cells
2:2	13.2 ± 7.7	136	4
2:2:2:2	13.9 ± 7.0	168	2
2–2	13.0 ± 7.6	186	4
4–4	21.1 ± 12.5	81	4
6–6	36.2 ± 24.2	62	5
	Neurite level		
Pattern	Wave period (*min*)	Number of waves	Number of cells
2–2	23.7 ± 15.6	186	4
6–6	67.1 ± 51.3	62	5
2:6	22.7 ± 9.6 (2:) and 80.5 ± 61.8(:6)	49 (2:) and 16 (:6)	4

Table III.10: **Wave emission period** (mean ± SD). Periods at the cell or the neurite level of cells growing on the selected patterns and observed at 1 DIV. Relative number of waves and of cells for each condition. Period at the neurite level represents the mean between the two neurites of the cell of the period of waves emitted on a single neurite.

Importantly, these results showing that wave emission period does not change between 2:2 and 2–2 patterns and that decreases on wider neurites are consistent with the trends obtained for the neurite length on the same patterns, where not significant differences have been observed between x–x and x:x patterns and where neurites are shorter on wider patterns (see Figure III.2.A). This result reinforces the interplay between the wave production and the neurite growth.

▶ Neurite morphology and wave velocity of propagation

A deeper characterization of waves was performed by measuring their velocity as a function of the neurite width (Figure III.15.A). Along the 6–6 pattern, waves show a significant decrease of their velocity when increasing the neurite width from 2 to 6 μm (3.8 ± 1.6 $\mu m/min$ down to 2.4 ± 0.9 $\mu m/min$). How wider adhesive surface and, probably, across larger neurite section (see Section III.1.3) influence the wave velocity remains an open issue. Conversely, neurite width appears to not influence significantly the alternation of wave emission. Nevertheless, with 29.1% of probability to have two consecutive waves along the same neurite on the 2–2 pattern against 38.7% on the 6–6 pattern (Figure III.15.B), waves on this last pattern seem to follow a tendency to be less alternative.

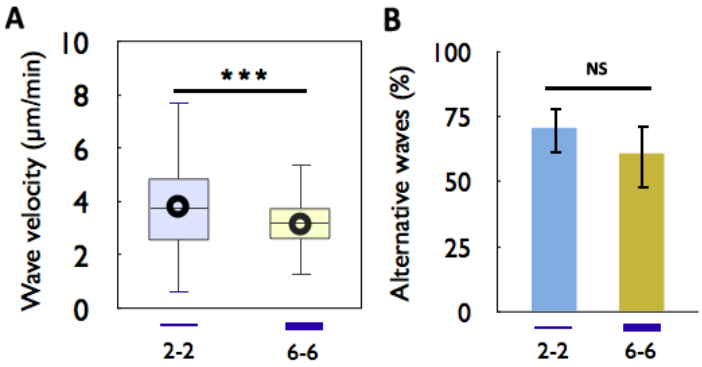

Figure III.15: **Waves dynamics in neurons on 2–2 and 6–6 patterns.** A) Wave velocity along neurites. Top and bottom of a box indicate 75th and 25th quartiles, respectively; whiskers indicate 10th and 90th percentiles; the middle line is the median. Symbols indicate the mean values (8.82 ± 1.65 and 2.36 ± 0.89 are the mean $\pm$ SD on the on the 2–2 and the 6–6 pattern respectively). $p < 0.001$: Mann–Whitney test. B) Alternative waves rate, calculated as the conditional probability to have a wave on a neurite when the previous wave has been emitted on the other one (70.9% on the 2–2 and 61.3% on the 6–6 pattern). NS: Fisher's test. n (pattern, number of cells) = 114 (2–2 pattern, 4 cells) and 67 (6–6 pattern, 5 cells). Error bars denote the 95% confidence intervals. All the patterns are sketched in blue below the graphs.

▶ Influence of the neurite width along wave propagation

Finally, we studied if the wave propagation was influenced by the variation of the neurite width along a given neurite. For that purpose, we have chosen the 2:26 pattern (Figure III.16.A). The analyses of the time–lapse experiments on neurons growing on this kind of pattern have

been performed in the frame of Yohan Lecomte's internship, a student I have co–supervised during my last year of PhD.

Surprisingly, it has been observed that a significant number of waves emitted on the :26 branch stops their propagation where the stripe width changes from 2 to 6 μm (Figure III.16.B). Interestingly, the rate of these "stop" waves increases toward higher values of length of the 2 μm segment (Figure III.16.C). These observations would be interpreted by the existence of critical threshold of concentration of one or several wave's components responsible for the propagation of these structures. Crossing the frontier between 2 and 6 μm wide stripes would correspond to a sudden dilution of some critical components that would further stop the propagation of the wave.

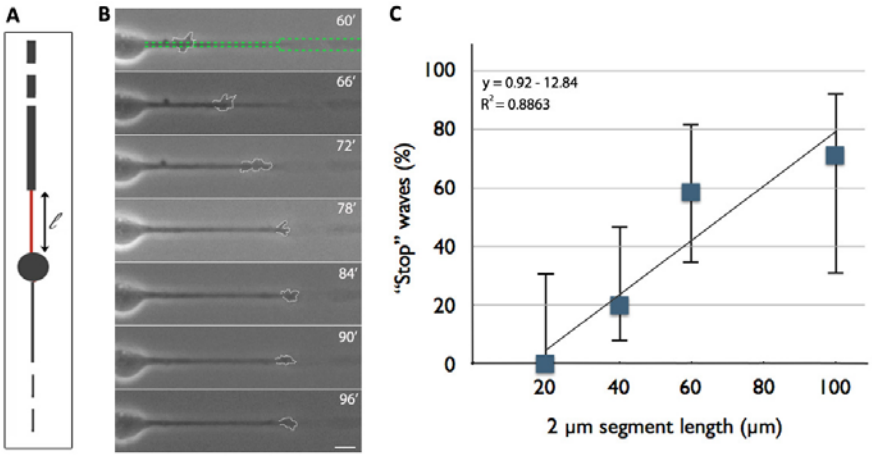

Figure III.16: **Wave characteristics in neurons on the 2:26 pattern.** A) Adhesive pattern represented by the grey design, the 2 μm wide segment is shown in red (l = 20, 40, 60, 100 μm). B) Time–lapse experiment indicated in minutes: 0' is 48 h after plating, l = 60 μm. The frontier of the adhesive region is delimited by two green dashed lines (top image) and waves by white dashed lines. Scale bar: 10 μm. C) Rate of waves stopping at the 2–6 frontier in function of the length of the 2 μm wide segment. n (l, number of cells) = 11 (20 μm, 3 cells), 20 (40 μm, 2 cells), 17 (60 μm, 4 cells) and 7 (100 μm, 3 cells). Error bars denote the 95% confidence intervals. The goodness of the linear fit is indicated by the R^2 value.

To explain why no "stop waves" were observed on the shortest 2 μm stump configuration, we first propose that the 2 μm segment of 20 μm of length is a too short distance from the soma to have an impact on the wave emission and propagation. It may be justified by the observations that (i) this length is of the same order of magnitude of the wave size and that (ii) occasionally waves appear in the proximal part of the neurite rather than strictly at the soma level. We might also hypothesize that the amount of material transported by waves decreases on their way up to the neurite tip. The waves would then have a lowest probability to be maintained, in the long range from the soma, in particular when experiencing a sudden dilution of their constituents at the frontier between 2 and 6 μm wide stripes. To validate this hypothesis, we plan to observe the opposite frontier condition, changing from 6 to 2 μm. The

wave constituents would increase abruptly across this frontier and the "stop" waves phenomena should disappear.

Some conclusions about influence of the neurite width on wave dynamics

We have focused our study on the analysis of the wave dynamics in neurons of controlled widths. We have shown a direct interplay between the characteristics of the wave emission along the neurites and their elongation, with an emission frequency and a velocity of propagation varying inversely to the neurite width. Finally, these results and the observation of the "stop" wave phenomenon in the experiments with neurite width changing along a same neurite suggest that a threshold of wave components might be necessary to allow the wave propagation on wider neurites. This hypothesis is also supported by the preliminary observations reported in the previous section (III.1.3) showing that the neurite volume on wider stripes is similar or greater than for neurites on narrower wide patterns.

In collaboration with B. Friedrich of the Max Planck Institute in Dresden (Germany), we have developed a minimal model of actin wave routing that reconciles our experimental observations of a wave emission dependent on the neurite width (Figure III.17).

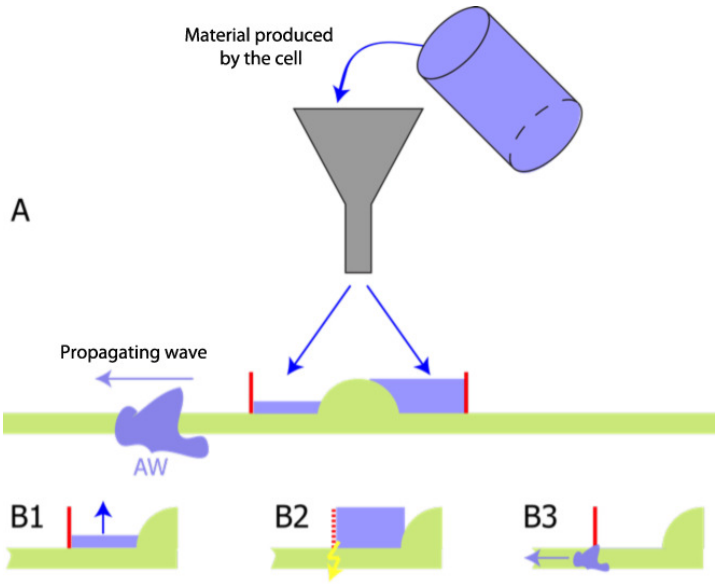

Figure III.17: **"Integrate–and–fire" model of actin wave (AW) routing.** A) A factor critical for AW initiation is produced within the soma at a constant rate and subsequently distributed to the respective neurite bases. B1 – B2) AW initiation along a neurite requires the local concentration of this factor to exceed a threshold. B3) Upon AW routing, the local pool of this factor would be reset.

In this model, we suggest that wave components (excess mass of polymerized actin, and/or critical signaling factor) are produced by the cell at a constant rate and sequentially distributed to the respective neurite bases. When this material reaches a critical neurite-width dependent concentration, wave initiation occurs and the local reservoir of wave components at the neurite

base would be reset.
Although this model does not reflect the complex full biological system, it reconciles the observations of neurite lengths and emission periods on stripes of different widths (Figures III.2.B and III.14B). Moreover, the assumption of a constant rate of material production suffices to predict a emission period independent of the neurite number (in agreement with the graph of Figure III.14.A) and implies a redistribution of waves along the pool of existing neurites. This would give a simple explanation of the conservation of the total neurite length displayed in the graph of Figure III.2. Finally, if we assume that the critical concentration required for actin wave initiations increases with neurite width, the observation of preferential actin wave routing along the thinner neurite on the 2:6 asymmetric pattern is likewise accounted for this model (Figures III.14.C).

Of note, and quite importantly, we have observed waves also in mouse and rat cortical neurons (Figure III.18), suggesting a potentially broader significance of these structures although their association to cortical neuron elongation have still to be demonstrated.

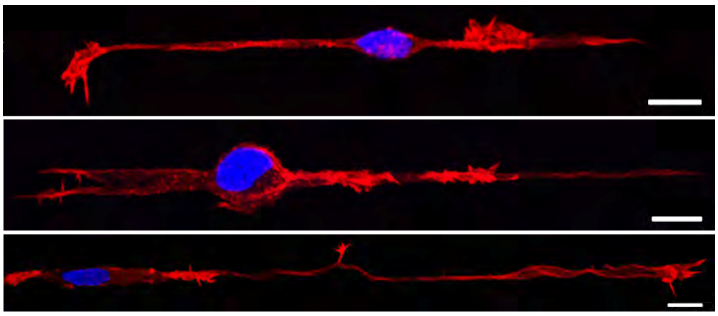

Figure III.18: **Actin waves in rat cortical neurons at 2 DIV.** Neurons on adhesive patterns (from the top: 2:2, 6:6, 6-6). Blue: DAPI, nuclei. Red: actin antibody, actin. Scale bars: 10 μm.

III.3.3 Waves as force generating structures

Previous works in our team have shown that waves are force generating structures. Indeed, the limited surface of adhesion for the soma defined by the micron–wide stripes has revealed that the soma (i) moves concomitantly with the waves and (ii) that it reverses its direction of motion when successive waves are emitted along opposite neurites. All these phenomenological features are represented in Figure III.19, showing an example of a neuron observed during a time–lapse experiment on a 6–6 pattern.

Our group has also previously reported that the neurite with the highest mechanical tension becomes the axon. Furthermore, we suggest that waves may contribute to the neurite tension. Indeed, as shown in Figure III.20, the axonal specification is inhibited in neurites growing

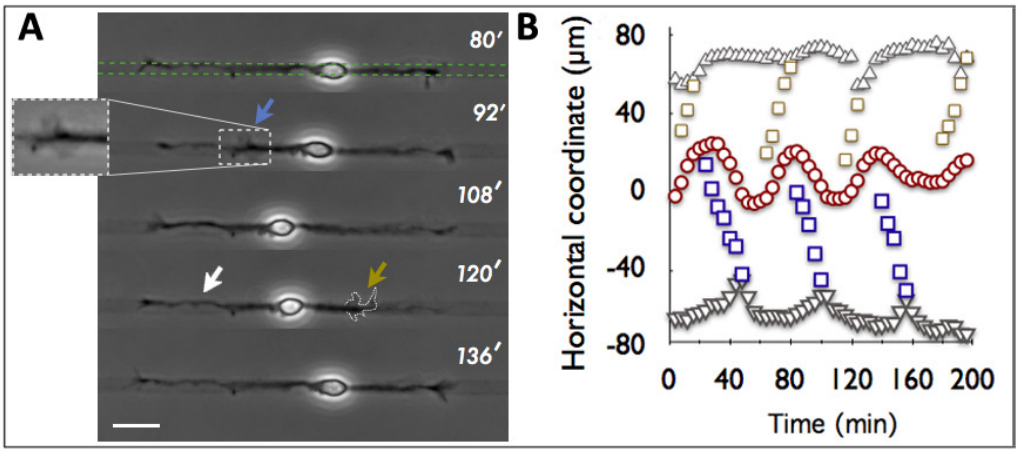

Figure III.19: **Soma and neurite tips dynamics associated to the wave propagation.** A) Time–lapse experiment (indicated in minutes, 0' is 24 h after plating) of a mouse hippocampal neuron developing on a 6–6 pattern. The frontier of the adhesive region is delimited by two green parallel lines (top image) and waves by white dashed lines (the inset displays a wave at higher magnification). Blue and gold arrows point to the waves emitted on the left and on the right of the soma respectively, whose coordinates are represented in (B). White arrow points to instabilities in neurite width near the edges. Scale bar: 20 μm. B) Coordinates of waves (squared gold and blue symbols), neurite tips (triangular grey symbols) and soma center (circular red symbols) versus time for the neuron in (A). They illustrate the oscillatory motion of the soma, in correspondence of the wave arrival and the associated retraction followed by an elongation of the neurite with the wave. The origin of the spatial coordinates is set to the initial soma position.

on curved adhesive micropatterns. This is possibly due to transient and reversible tension–induced unhooking from curved stripes that impairs neuritic elongation within the first stages of development (namely stage 1 and 2, Figure I.10).

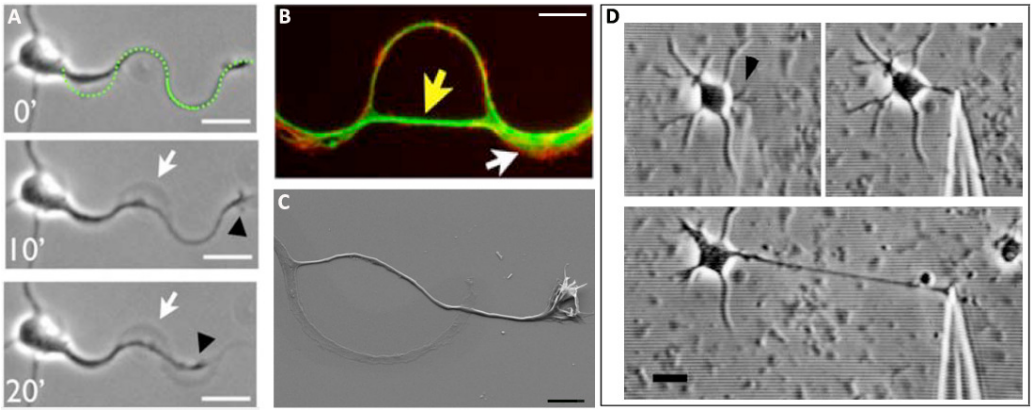

Figure III.20: **Tension in growing neurites.** A, B, C) Neurons growing on curved patterns [23]. A) Time-lapse experiment (indicated in minutes, 0' is 30 h after plating) of a neurite developing on a curved pattern. The adhesive region is marked by the green dashed line (top image). The white arrow points to the region where the neurite partially detaches from the adhesive pattern. The black arrowheads point to the neurite tip. Scale bars: 20 μm. B) Partial (white arrow) and complete (yellow arrow) unhookings observed of a neuron fixed at 3 DIV. Green: YL1/2, microtubules. Red: phalloidin, actin. Scale bar: 10 μm. C) SEM image of an axon crossing the curved pattern. Scale bar: 5 μm. D) Neurite elongation and following axonal specification induced by external tensions [24]. The black arrowhead points to the chosen neurite tip for needle application. Scale bar: 20 μm.

This observation is good in agreement with the experiments performed by Lamoureux et al. where the axonal specification of a given neurite can be induced by its mechanical stretching [24] (Figure III.20.D): by applying a tension between 200 and 1000 pN, undifferentiated neurites become an axon, growing with a rate proportional to the external tension. In addition, we have observed that unhooking events were always associated to the propagation of a wave.

The wave dynamics therefore shows that they are structures involved in the mechanical properties of neurons, e.g. the soma motion, the neurite tension and the neurite tip dynamics associated to the wave propagation. The next step is to try to quantify this contribution and to investigate the mechanisms behind these observations.
We have chosen to approach this issue looking at two possible mechanisms related to wave propagation: the measurement of (i) the membrane tension could provide information about an eventual braking role of neurite membrane and of (ii) the transmitted forces to the substrate at the neurite level could show if wave propagation leans on this kind of forces.
The two following subsections will be dedicated to these problematics.

III.3.3.1 Measurement of the membrane tension

Is there a relationship between the higher frequency of waves in axons reported in the literature and the high tension characterizing the whole axon (including forces coming from the cytoskeleton and the membrane)? Answering this question means to investigate if the wave propagation is associated to an increase of the neurite tension. For that, we have spent a couple of days in the group of Patricia Bassereau at the Curie Institute in Paris (France), where we could use an optical tweezers set–up. This technique (see Section II.4.5 for more details) allows the measurement of the membrane tension, by manipulating microbeads attached to the cell membrane.
Once a microbead is attached up to the neurite membrane, it is possible to form a membrane tether, simply by pulling out the bead at a constant velocity to a known distance from the cell. The diameter of the beads was 2.8 μm and the experimental parameters are represented in Figure III.23.A. Asymmetric patterns have been used in order to induce the breaking of morphology symmetry occurring with neuronal polarization and to probe different neurite widths while keeping a high probability to observe a wave on the thinnest neurite (see Figure III.14.C for results about wave emission periods). The establishment of the membrane tether leads to a quick force peak that decays within a few seconds to reach a force plateau.

Results from optical tweezer measurements

Many measurements have been done to quantify the membrane tension in more than ten neurites of mouse hippocampal neurons growing on our patterned substrates.

Importantly, the force plateau does not seem to depend on the tether length, i.e. the distance x of the bead from the neurite, for the probed tether of lengths up to 20 μm (Figure III.23.B). Similarly, the force values we have obtained from nine neurons do not show a drastic dependence on the distance of the bead from the soma (Figure III.23.C). They seem to have only a weak tendency to increase moving toward the neurite tip, which appears to be in contrast with the inverse tendency of a ~ 2 pN force decrease of tether forces from the soma to the growth cone observed by Dai et al. on embryonic chick DRG neurons [25].

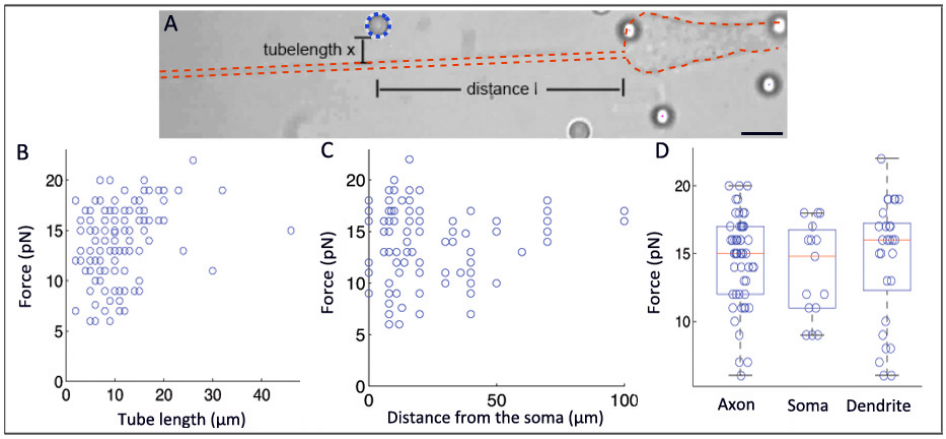

Figure III.21: **Optical tweezers measurements.** A) Experimental parameters: length of the membrane tube between the bead and the neurite (x) and the distance of the bead hook and the the soma (l). The neuron on the asymmetric 2:6 pattern and the hooked bead are marked by the orange and bleu dashed lines, respectively. The other beads are free to move in the culture medium. Scale bar: 10 μm. B) Force plateaus values (pN) in function of the tube length x (μm). C) Force plateaus values (pN) in function of the distance from the soma l (μm). D) Force plateaus values (pN) in function of the bead position relative to the cell regions: axon, soma or dendrite. Cell regions are identified by the "E" marker on the glass surface (see Figure II.5) locating the 2 μm wide stripe (axon), the 15 μm adhesive disk (soma) and the 6 μm wide stripe (dendrite). Top and bottom of a box indicate 75th and 25th quartiles, respectively; whiskers indicate minimum and maximum of the dataset; the middle line is the median. Every force value is the mean over $40 - 60$ s of a force plateau of a single tether with specific length.

More statistics would be necessary to confirm this trend and to better understand the reason of an eventually non uniform tension along the neurites. Associated live imaging experiments would be useful to correlate the measured force values with the neurite dynamics and the growth cone activity. The average value of the observed forces is of 13.9 ± 0.3 pN, a value of the same order of magnitude than the ~ 6.7 pN measured on the growth cone by Dai et al. [26]. On the other hand, the results are probably cell type–dependent, that could justifies that values reported in the literature differ from one another.

We have then analyzed the membrane tension as a function of the specificity of the cell compartment, i.e. the soma, the axon or the dendrite (Figure III.23.D). Our results display that the cell equilibrates its membrane tension after adhering to the substrate, independently of the surface of adhesion.

Finally, we provide one example of measurements in the presence of waves (Figure III.22).

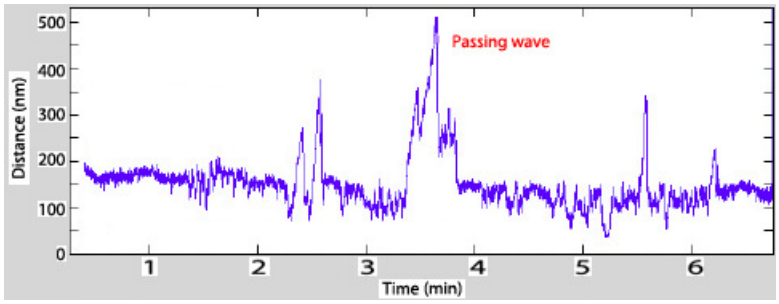

Figure III.22: **Displacement of trapped bead attached to a membrane tether measured with optical tweezers during a passing wave.** The displacement is related to the force acting on the bead via $F = k \cdot x$. The trace shows a force plateau after a tether was pulled from the axon ($t > 0\ min$) and two peaks associated with the wave propagation, due to an active puling of the tether.

The passing wave caused an increase of the measured force, with a force peak similar to the very fast peaks observed during the establishment of the membrane tether. As its duration appears short compared to the order of magnitude of wave propagation velocity ($\sim \mu m/min$), it seems that wave propagation does not lead to an increasing of the membrane tension. This suggests that wave propagation is not braked by a local need of membrane supply. This observation might be explained by an additional contribution of the wave into actin pulling inside the tether and by a local and quite fast reorganization of the cytoskeleton, i.e. between the cylindrical morphology of the neurite and the membrane deformation associated to the wave arrival.
More examples are necessary to quantify the force contribution of a wave and to better correlate this peak of force with the wave propagation.
Actin–fluorescent live imaging experiments might be interesting to access to the interaction between the wave and the membrane tether.

In conclusion, we have shown that the membrane tension equilibrates quite rapidly, on a time scale faster than few seconds, suggesting that if the actin wave increases membrane tension, it would be too short to be responsible for soma motility in response to the wave propagation. We propose the hypothesis that if there is a mechanical reason for the soma movement it is transmitted via microtubules or actin cytoskeleton. More experiments should be done to measure the force values induced by longer tethers and to get more statistics, as well as to quantify the wave contribution to the membrane tension. It might be also interesting if the peaks associated to the establishment of the membrane tethers show a different relaxation time as a function of the neurite width. This would, indirectly probe the levels of the membrane reservoirs associated to these different neurite morphologies.

III.3.3.2 Calculation of the forces transmitted to the substrate

Choice of the methodology

The optical tweezers experiments described above allow an access to the value of the internal membrane tension. Another approach of cellular mechanics is to measure the forces transmitted by the cells to the substrate by quantifying substrate deformations. The capability of these cells to deform their substrate has been largely reported in the literature for several cell types, e.g. fibroblasts, muscle, endothelial or epithelial cells, both in isolated conditions and in cell aggregates [27, 28, 29]. Different techniques have been developed to measure cellular forces, that use different kind of force sensor (Figure III.23).

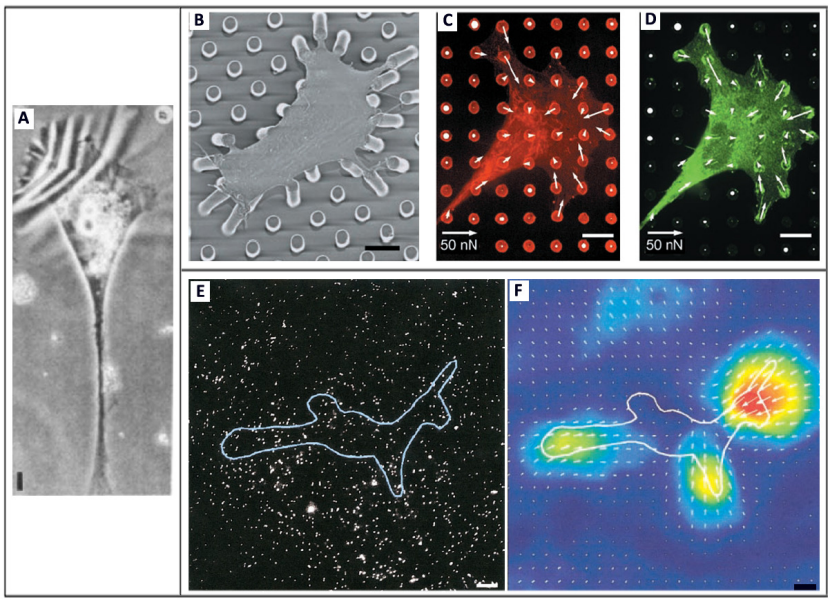

Figure III.23: **Example of substrates deformed by cells.** A) Fibroblast cell on a thin layer of silicone rubber forming some wrinkles at the surface [27]. B) SEM image of a muscle cell on an array of PDMS pillars [29]. C) Confocal image of immunofluorescence staining of a muscle cell on fibronectin (red) coated pillars. White arrows indicate the forces exerted by the cell [29]. D) Confocal image of immunofluorescence staining of the focal adhesion protein vinculin (green) correlated to the force map already shown in (C). E) Fluorescence image of a muscle cell on a polyacrylamide gel where 200 nm beads are embedded (white line represents the outline of the cell) [30]. F) Displacement field of the beads under the adherent muscle cell shown in (E). Arrows represent the relative magnitude of the displacements. Scale bars: 10 μm.

The most employed techniques are presently (i) PDMS micropillars that can be deflected by the cells growing on the top of them, and (ii) polyacrylamide (PA) hydrogels where the substrate deformations are detected by the displacement of fluorescent microbeads that are embedded inside (Traction Force Microscopy technique). In both examples, micropillars and hydrogels, the stiffness of the substrate is controlled by respectively (i) varying the aspect ratio of the pillars and (ii) modulating the polymerization rate of the polyacrylamide or of the PDMS. Importantly, cells adapt the forces they transmit to the extracellular matrix as a func-

tion of its rigidity, as shown by some experiments demonstrating cell capability to adapt their response to the mechanical properties of their microenvironment. For example, it has been shown that fibroblast and epithelial cells linearly increase their force with the substrate rigidity until a saturation plateau of the order of some tens of $nN/\mu\text{m}^2$ [31]. This situation differs in brain cells. For instance, the retrograde flow of actin in neuron growth cones, a quantity that is inversely proportional to the magnitude of the traction forces and is significantly slower on soft substrates than on stiffer ones. This flow reaches a maximum of $\sim 110\ nm/s$ once exceeded a stiffness of $\sim 1.3\ kPa$ [32]. This means that neurons forces transmitted by the growth cone are enhanced on soft substrates. Using micropillars or hydrogels has some implication on cell behavior. Pillar substrates appears microstructured compared to the continuous surface of the hydrogels. Therefore, cell adhesion is constrained to the pillar section and cell behavior is influenced by this discrete adhesive environment (see Section I.5.2 for more details). Additionally, pillars are mechanically independent of each other, meaning that local cellular forces do not transmit through the matrix to some other regions of the cell as it does on a continuous substrate like hydrogels. Forces values are in this case obtained by the measurement of the micropillars deflection, giving access to the shear, tangential forces, but not to the normal, compressive forces. Indeed, micropillars are incompressible in the range of the cellular forces whereas hydrogels have an isotropic elasticity. For these reasons, the micropillar technique is mainly indicated for the study of the mechanics at the micrometric scale of the cellular adhesions. These characteristics, in addition to the low physiological properties of pillars, from a mechanical point of view, make this technique inappropriate for the measurement of the weak forces exerted by so thin cellular processes such as neurites.

Forces associated to neurons

The state-of-the-art on the mechanics of neurons mainly reports experiments that focus on the mechanics of the growth cone. Indeed, this region of the cell is expected to produce the most significant forces due to its role in pathfinding, migration and extension. Nevertheless, it has been shown that growth cones, and other regions of the neuron, exert randomly directed and fluctuating traction forces whereas the main structures responsible for oriented and significant forces are the growth cone filopodia [32]. The growth cone is a very soft structure, that, regarding its function, it is expected to be very sensitive to the mechanical properties of its environment. However, regarding its very low Young's modulus, estimated around a value of 100 Pa [33], the maximal forces that it can transmit are naturally limited by its softness, compared to other stiffer cells such as fibroblasts. By considering the elastic modulus as a force per unit area ($1\ kPa = 1\ nN/\mu m^2$), this result appears also consistent with a neurite tension in the order of magnitude of only some pN (growth cone rigidity: $0.1\ kPa\cdot$ area of the growth cone filopodia of order of $1\ \mu m^2 = 100\ pN$). The same authors have combined the

mechanical properties of the growth cone of NG108-15 cell line to the local measurements of the actin retrograde flow in the direction of the central domain of the growth cone to calculate the internal stresses. Indeed, this retrograde flow, with a centripetal direction, and the pushing actin polymerization toward the edge determines the dynamics of the lamellipodium of the growth cone. In the same study, traction force measurements on PA hydrogels (Young's modulus $\sim 200\ Pa$) have given a independent access to the calculation of the stresses transmitted to the substrate and generated by the internal cellular forces. All these studies show a direct correlation between cell rigidity, internal stresses and traction forces on the substrate (both giving values on the order of $\sim 25 - 30\ Pa$) [33].

Traction force microscopy (TFM) has recently been employed to estimate forces in growth cones of *Aplysia* bag cell neurons on soft silicon gels (Young's modulus $\sim 3\ kPa$, Figure III.24) [34].

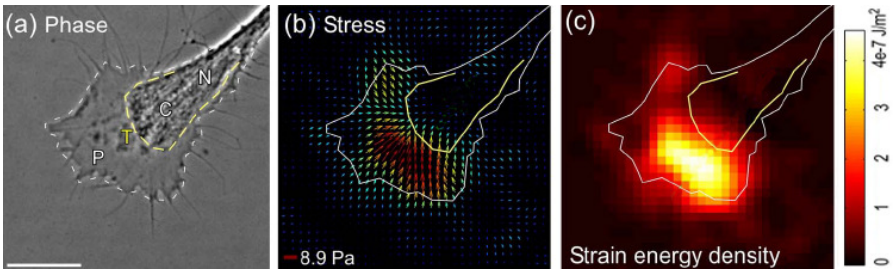

Figure III.24: **Forces in growth cone by traction force microscopy [34].** A) Phase contrast image of *Aplysia* bag cell growth cone. P: peripheral domain, T: transition zone, C: central domain, N: growth cone neck. Scale bar: 20 μm. B) Map of traction stress vectors in growth cone in (A) showing localization of traction force in peripheral domain delimitated by white and yellow outline. C) Map of strain energy density for growth cone in (A).

This work differs from other studies that focused on the forces produced by individual filopodia at the leading edge, showing that the traction stresses applied by the growth cone on the substrate reach the highest values ($\sim 9\ Pa$) in the peripheral domain close to the central domain, i.e. away from the leading edge, following the direction of the actin flow. Forces might then be balanced in other parts of the growth cone or transmitted to the cell in the form of a neurite tension. Moreover, the maximum internal stresses have been measured in the range of kPa, as compared with the few Pa found for the traction forces, suggesting that growth cones are able to accumulate high levels of cytoskeletal stress. Neurite tension was independent of the growth cone size suggesting that growth cone is mechanically isolated from the rest of the cell, possibly in order to independently respond to its environment.

Koch et al. have performed an interesting study in the context of our work, comparing traction forces between peripheral nervous system (PNS) and central nervous system (CNS) cells, i.e. dorsal root ganglion (DRG) and hippocampal neurons [35]. These authors have

reported that neurite outgrowth of hippocampal neurons was independent of the substrate stiffness (PA hydrogels with a Young's modulus in a range between 150 and 5000 Pa) whereas DRG neurons displayed maximal growth rate on substrates with a Young's modulus of $\sim 1\ kPa$. In both cases, the traction force was dependent on the substrate stiffness: from 23 to 31 Pa (with a peak of 39 Pa on 1.1 kPa substrates) for DRG growth cones at $3-10\ h$ after plating in the range $500-1700\ Pa$ substrates and from 26 to 29 Pa (with a peak of 44 Pa on 1 kPa substrates) at $20-30\ h$ after plating; from 5 to 9 Pa for hippocampal neurons at $20-30\ h$ after plating on the substrates within the range $200-430\ Pa$ (pay attention to the different stress scale bars in Figure III.25). Deformations on stiffer gels were not larger than the measurement noise for this kind of cells, showing a remarkable low capability of hippocampal neurons to generate traction forces. This observation might be explained by (i) the three times faster retrograde flow of actin and (ii) a significantly lower concentration of paxillin in these neurons in comparison with the DRG ones (Figure III.25).

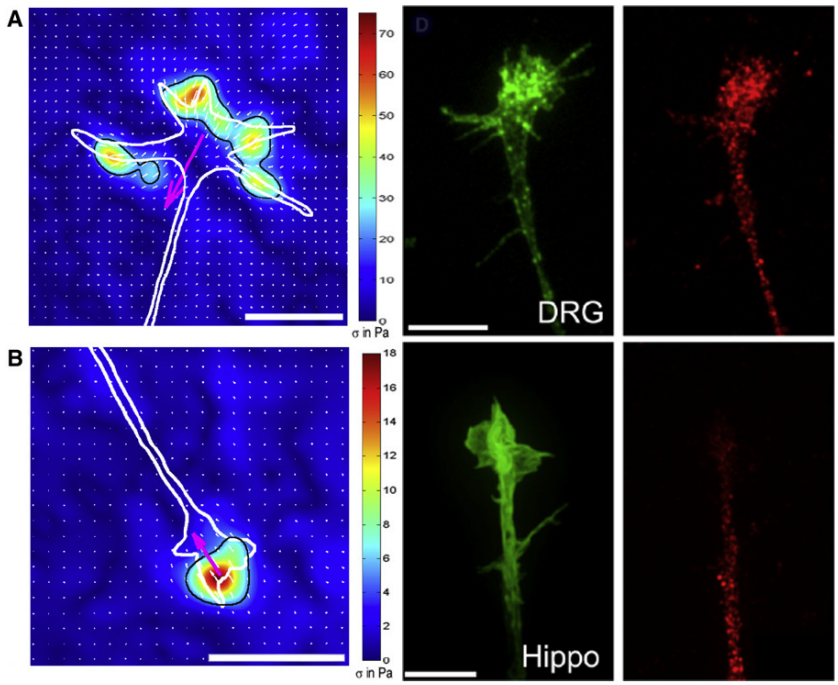

Figure III.25: **Comparison between PNS and CNS growth cones [35].** A) Growth cone of a dorsal root ganglion neuron (PNS). From the left to the right: traction stress fields on a 1 kPa substrate, actin (green) and paxillin (red) distribution. B) Growth cone of an hippocampal neuron (CNS). From the left to the right: traction stress fields on a 300 Pa substrate, actin (green) and paxillin (red) distribution. Growth cone shapes are indicated by the white outline. The white arrows give the direction and magnitude of traction stress. The magenta arrow shows the direction of the net traction force (calculated in the area surrounded by the black line). Scale bars: 10 μm.

Indeed, in DRG neurons paxillin is concentrated in the growth cone periphery and along filopodia while it is almost absent of the growth-cone of hippocampal neurons where it concentrates within neurites. Interestingly, the higher traction stresses of DRG growth cones after 1 DIV, a stage of development characterized by substantial rearrangement of neuronal pro-

cesses associated to the formation of interconnected networks, are associated with a significant level of internal tension.

In DRG growth cones, the highest traction stresses are located around the peripheral region, in particular at the filopodia level, and the traction they generate is quite stable in time. This is in contrast with the properties of hippocampal growth cones that display short periods of high stress with long phases of low stress, expressing a highly dynamic behavior. These rapid changes of the traction stresses are also in agreement with the quasi absence of focal adhesions observed by paxillin immunostainings (Figure III.25.B).

These findings contribute to reveal the different properties of PNS and CNS neurons related to their different behaviors and functions. First, PNS and CNS neurons live in mechanically distinct environments. Both of them find their way through growth cones exploration. Consequently, they involve a different distribution of paxillin in the focal adhesion regulation. From a mechanical point of view, the PNS neurons, unlike most other cell types, do not prefer substrate stiffnesses on the order of the kPa. Moreover, they show a relatively narrow maximum in outgrowth and traction force versus stiffness. This high degree of mechanosensitivity might be useful considering the extended range of substrate stiffness encountered by these cells in the PNS (see Section I.1). In contrast, the CNS neurons grow indifferently from stiff to extremely soft substrates with a non measurable mechanosensitivity, possibly in response to their very soft environment of the whole developing brain. Moreover, neurite extension takes place also with very low traction stresses, indicates that CNS neurons are less dependent on the adhesion to modulate their growth and guidance. However, traction forces produced by growth cones may play an important role in the establishment of neuritic tension and consequently, as exposed above by works about neurite tension, in axonal specification. Consistent with this hypothesis, it has been shown in Figure III.25 that the traction stress field of hippocampal growth cones is often highly localized and aligned with the net force toward the axon.

These works highlight the importance of considering cell interaction with the mechanical environment to better understand cell functions, as well as the complexity of this relationship. In the same line, the different behaviors and properties depending of the specific cell type, and even more specifically among neurons, express the importance to be consistent between the choice of a cell type and of the experimental method when addressing a scientific issue. Last, but not least, these reports on the mechanical aspects of neurons further support our interest for the force–generating properties of waves despite the extreme difficulty to measure forces in hippocampal neurons. We have therefore chosen to try to investigate the interplay between waves and the force generation, as exposed in the next section.

Traction Force Microscopy to investigate wave contribution to neurite forces

We have used PA hydrogel substrates, loaded with fluorescent microbeads to characterize the forces produced by developing neurons by Traction Force Microscopy (see Section III.3.3.2). Image analysis and mathematical algorithms of microbead tracking have been developed in the context of Michel Moussus's PhD on the characterization of the mechanical forces within the endothelium [36].

The main difference between neurons and endothelial cells is the order of magnitude of the expected forces: lower than 50 Pa for neurons, and in the range of few hundreds Pa for endothelial cells. This aspect sets a critical constraint for the substrate fabrication, whose elastic modulus has to be of the order of a few Pa. The narrow range between the lowest stiffness limit (the hydrogel must be polymerized everywhere, so to be elastic but not viscous) and the highest one (forces transmitted by neurons must be detectable) imposes to achieve a high uniformity of the substrate stiffness using substrates with few hundreds Pa. For this reason, we have mainly employed the photopolymerization technique developed in our laboratory [37], as described in Section II.1.2.2.

There are two methods to obtain the displacement field: Particle Imaging Velocimetry (PIV) and Particle Tracking Velocimetry (PTV). PIV averages the displacements on fixed windows of the field of view, giving a regular field of displacements. It is quite fast and it has indeed given more accurate results. PTV technique is based on the tracking of single bead trajectories, giving a displacement field that depends on the local density of the particles. The thinness of the neurites (few microns wide) makes this constraint difficult to achieve. Therefore, the PIV method seems to be more adapted for our problematic.

First, it is necessary to compensate the thermal drift and the hysteresis of the microscope stage: the image sequences of the time–lapse experiments are realigned using the regions of the gel that are free of cells. Indeed, during the acquisition, the microscope stage is not absolutely stable, producing some variations in the position of the field of view. This problem is caused by (i) the microscope precision to come back to the same position during a multi–position acquisition and (ii) the thermal stability of the set-up. The PIV technique provides the corrections of the beads positions in the x and y directions, with a precision of $\sim 70\ nm$ (Figure III.26). Then, the PIV method is employed a second time to define the field of the deformation of the substrate. For this purpose, the field of view is divided in windows of 16 x 16 $pixels$. The little size of the windows (compared with the other values also commonly employed of 32 x 32 or 64 x 64 $pixels$) is justified by the small displacements expected for the weak forces exerted by the neurons. This point also explains why we took the first (or the last) image of the image sequence as a reference for this calculation in order to measure the displacements relatively to a fixed position. Indeed, the displacements calculated using consecutive images are too small

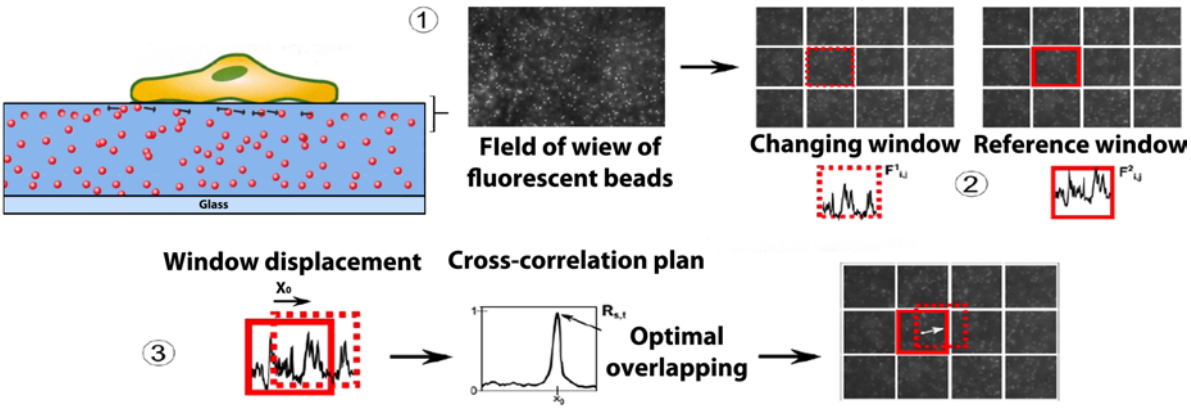

Figure III.26: **Particle imaging velocimetry (PIV) principle.** Side view (sketch on the left) and top views (fluorescent images) of an hydrogel substrate for PIV measurements. 1) Fluorescent microbeads (in red) are uniformly distributed in the hydrogel (in blue, over the glass coverslip). Cells (in yellow) are deposited on the surface, where their forces transmitted to the substrate induce a displacement of the beads (black arrows). The fluorescent image reports an example of field of view of fluorescent beads. 2) The field of view with the fluorescent beads is divided in small windows (16 x 16 *pixels*). 3) The changing windows are compared with the reference window. The peak in the cross-correlation plan corresponds to the optimal overlapping between the windows. The PIV provides the final displacement field of the beads. Adapted from [36]

to be detected. The algorithms of correlation between consecutive images were implemented in Matlab software and allowed a sub-micrometric resolution in particle tracking. The total resolution of these calculations can be estimated around 50 – 100 nm.

Results from traction force microscopy measurements

The technique of photopolymerization employed for the hydrogel fabrication leads either to uniform or patterned stiffnesses depending on the design of the mask used for the UV light illumination. In the range of stiffness of interest for our study, we were quite limited by the situations of instability of the microbeads within ultra–soft gels or of inhomogeneous unmolding of the gel from the mask giving irregular surfaces. Both situations mean that the field of spatial bead distribution do not have the necessary properties to be used for the TFM. Initially, we have employed hydrogel substrates with alternative submillimetric stripes of low and high stiffnesses. In this configuration we have obtained ∼10 kPa stripes surrounded by larger ones of much lower stiffness (∼100 Pa). Hippocampal neuronal cultures have been observed on this kind of gels, giving qualitatively results that support the hypothesis of an interplay between wave propagation and neurite forces (Figure III.27). However, this example has been an exception and the inhomogeneity of the hydrogel stiffness has not made possible to provide quantifications of the forces observed on this hydrogel. After some experiments without significant results, also changing the exposure time, we have concluded that the stiffness gradient between two hard stripes was too important to obtain very soft regions sufficiently homogeneous at the cell level.

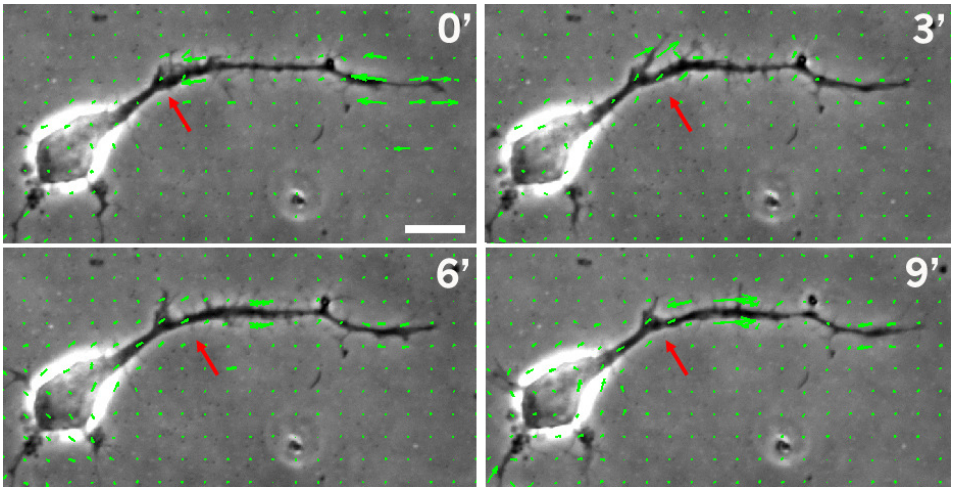

Figure III.27: **TRM of mouse hippocampal neurons on a PA hydrogel at 1 DIV (photopolymerization method).** PA gel fabricated with the photopolymerization method with a mask giving alternative stripes of Young's modulus of ~ 10 and 0.1 kPa. Phase image of a wave (pointed by the red arrow) propagating along a neurite on the softest region and the associated field of forces (green arrows) obtained from the displacements of fluorescent microbeads (infrared, 200 nm in diameter, 60 $\mu l/ml$, i.e. 0.12% v/v) embedded into the hydrogel. Scale bar: 10 μm

Technical problems have played a crucial role in these already challenging experiments, also on uniform gels: absence of visible neuronal waves, lost of focus during the time–lapse imaging, changes of some components of the UV lamp and of the experimental set-up influencing the reproducibility of the calibrated exposure times versus stiffness, replacement of the microscope set-ups. Some combinations of these problems were also associated to the difficulty to perform these experiments a great number of time, due to the scarcity of primary neuronal cells we had access to.

Finally, we have compared both photopolymerization and chemical techniques of hydrogels fabrication. In this case the Young's modulus measured for the photopolymerized gels was of $\sim 1.4 \pm 0.6$ kPa with 4.4 s of UV light exposure and a nominal stiffness of $\sim 0.5 \pm 0.2$ kPa for the PA gels with the chemical method (acrylamide – bis-acrylamide concentration: 3%–0.06%) [38].

We summarize the results obtained with the PIV technique described above through some examples. We display in Figure III.28.A a typical distribution of microbeads in a very soft gel and a field of displacements in PA gels in response to the growth of hippocampal neurons (Figure III.28.B). The cell density employed is 100 $cells/mm^2$ in order to ensure both a sufficient number of cells to obtain good conditions of survival and a sufficient number of isolated cells. From the displacement values in the x and y directions we can obtain the displacement modulus ($\sqrt{x^2+y^2} = \mid u \mid$) and analyze its distribution (Figure III.28.C). In this way, a direct and approximate information of the noise in our calculations is provided, by means of the statistical distribution giving the most probable value, i.e. the first peak value. We obtained $\sim 22 \pm 8$ nm for the gel fabricated with the chemical method (Young's modulus:

$\sim 0.5 \pm 0.2\ kPa$) and $\sim 27 \pm 9\ nm$ using the phopolimerization method (Young's modulus: $\sim 1.4 \pm 0.6\ kPa$, exposure time: 4.4 s, gel in Figure III.30). In order to check if the second peak that appears in histograms such as the one displayed in Figure III.28.C corresponds to specific areas occupied by neurons, we have reported their localization on the respective field of view of the hydrogel. However, the noise dispersion is unfortunately too important to allow any consistent conclusions (Figure III.28.D).

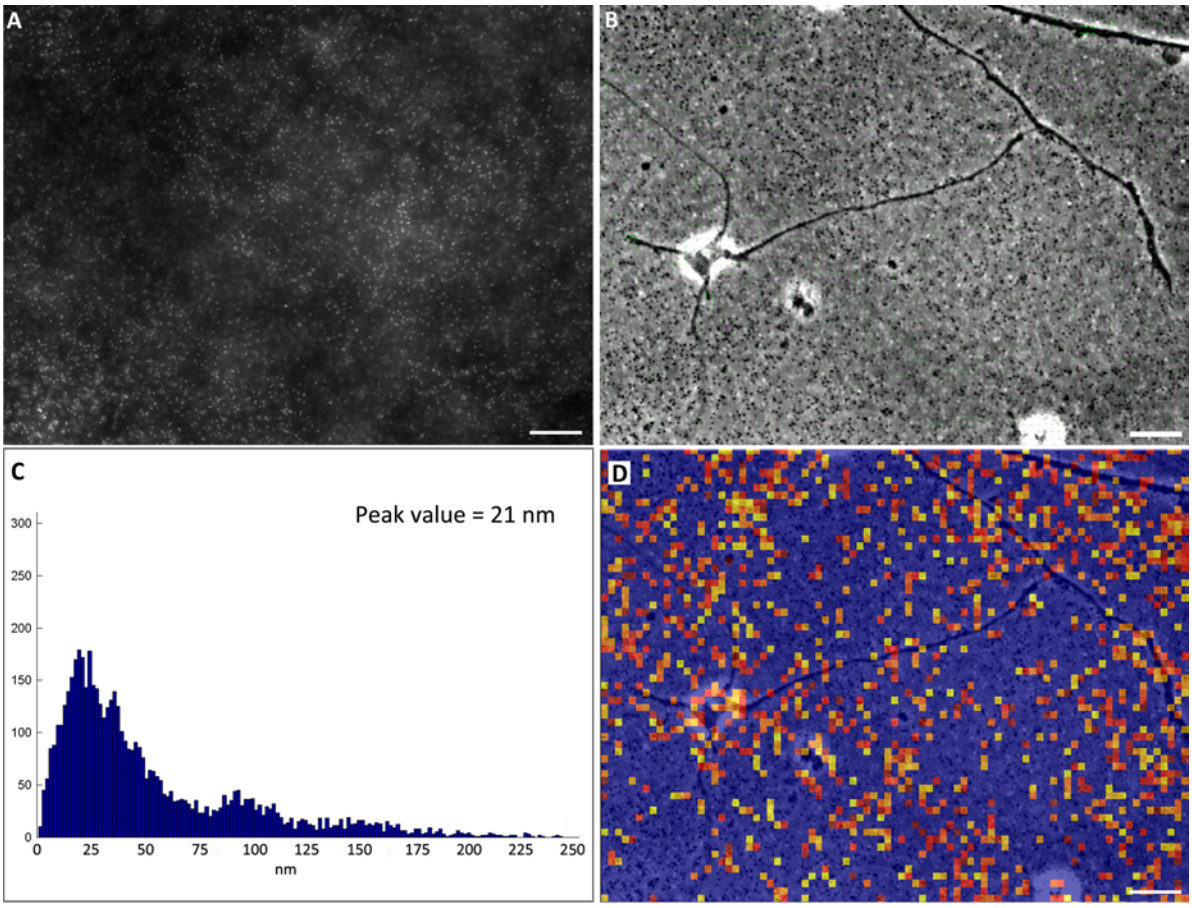

Figure III.28: **TRM of mouse hippocampal neurons on a PA hydrogel at 3 DIV (chemical method).** PA gel fabricated with the chemical method and with a Young's modulus of $\sim 0.5 \pm 0.2\ kPa$. A) Field of fluorescent microbeads (infrared, 500 nm in diameter, 100 $\mu l/ml$, i.e. 0.22% v/v). B) Phase image and displacements field (green arrows) of the field of view in (A). C) Histogram of the displacement modulus values expressed in nm. D) Localization of the values of the displacement modulus belonging to the second peak of the histogram in (C), i.e. fixed between 80 and 113 nm, and superposed to the field of view of (B). Scale bars: 20 μm.

Indeed, in general, there are no values exceeding the noise level. This is not surprising if we take into account the displacement values measured by Odde et al. [32] (~ 10 – $20\ nm$) and the force values reported by Koch et al. [35] ($\sim 10\ Pa$) for hippocampal neurons.
We can nevertheless provide an approximate information of the force value corresponding to the measured noise as an estimation of the upper limit of the forces exerted by hippocampal neurons. We consider the hydrogel, whose thickness is of ~ 80 – $100\ \mu$m, as an elastic and

half–space medium with an uniform stiffness. The hypothesis of a "semi–infinite" medium is justified by the presence of only one limit represented by the interface in contact with the cells whereas the coverslip supporting the gel is relatively far to not have a significant contribution. The force distribution $\vec{f}$ acting on the surface of the elastic medium with a displacement field $\vec{u}$ is represented by the following equation [39]:

$$\vec{u}(x,y) = \int \vec{\vec{G}}(x-x', y-y')\vec{f}(x',y')dx'dy' \tag{III.4}$$

where $\vec{\vec{G}}$ is the Green's tensor, x and y the coordinates of the bead displacements on the plane at the surface. The relation between the displacement u of the 16 x 16 *pixels* windows given by PIV and the force F can be approximate by the following relation:

$$u \sim \frac{F}{E} \tag{III.5}$$

with E the Young's modulus of the hydrogel. By this approximation of the elastic problem we firstly obtain the stress value σ corresponding to the displacement u by:

$$\sigma \sim \frac{E \cdot u}{L_{window}} \tag{III.6}$$

with L_{window} the side of the window obtained by PIV. With the hypothesis that the stress is uniformly distributed on the PIV window, we can finally obtain an estimation of the local force on one bead:

$$F_{bead} \sim \sigma \cdot R_{bead}^2 \tag{III.7}$$

with R_{bead} the bead radius. Using approximated values of the parameters just described ($E \sim 1\,kPa$, $u \sim 25\,nm$, $L_{window} \sim 2.5\,\mu m$ and $R_{bead} \sim 0.25\,\mu m$), we obtain a noise value (i.e. corresponding to the first peak value of the histogram) of the order of 0.1 – $1pN$.

Then, we have compared the results obtained on the gels fabricated with the two methods mentioned above (Figures III.29 and III.30). They reveal that some forces seem to be exerted at the level of the growth cone, in particular during the retraction of a neurite (red inset in Figure III.29) but not significant results have been observed in the presence of the waves.

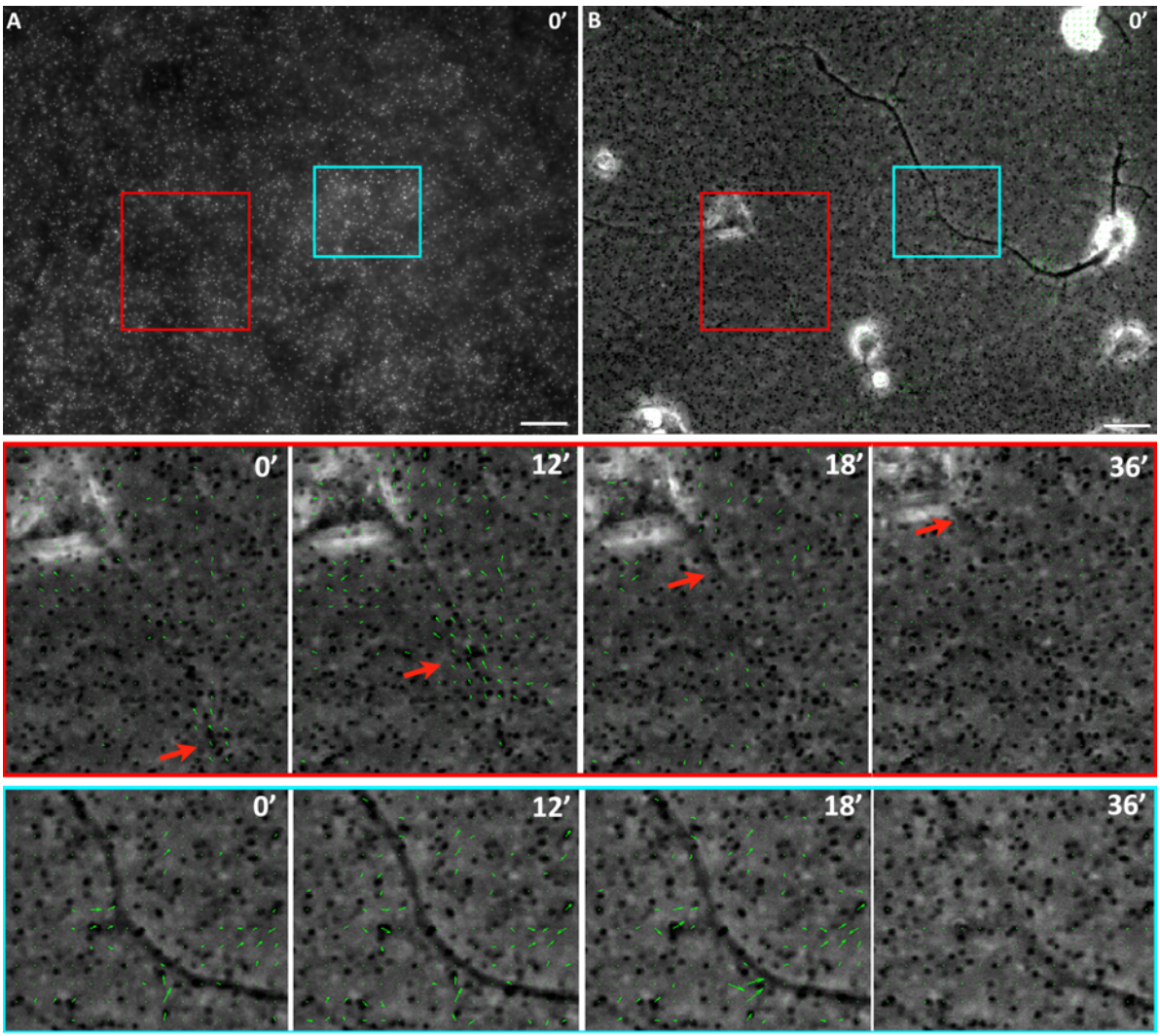

Figure III.29: **TRM of mouse hippocampal neurons on a PA hydrogel at 2 DIV (chemical method).** PA gel with a Young's modulus of $\sim 0.5 \pm 0.2\ kPa$. A) Field of fluorescent microbeads (infrared, 500 nm in diameter, 100 $\mu l/ml$, i.e. 0.22% v/v). B) Phase image and displacements field (green arrows) of the field of view in (A). Scale bars: 20 μm. Time–lapse experiments of the selected areas in red and light blue are reported below. Time is indicated in minutes: 0' is 48 h after plating. The orange arrows in the red square point to the neurite tip during its retraction.

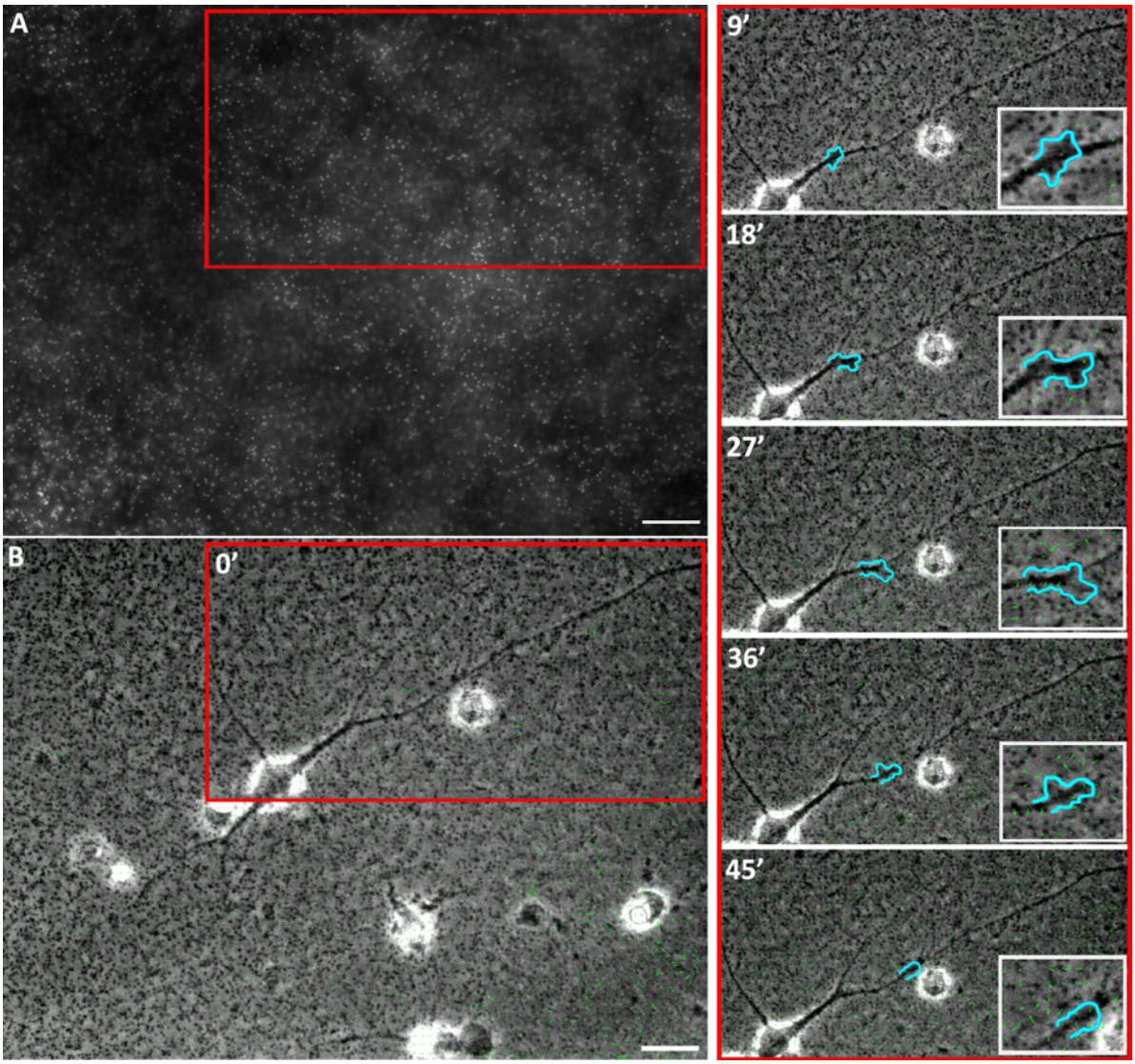

Figure III.30: **TRM of mouse hippocampal neurons on a PA hydrogel at 3 DIV (photopolymerization method).** PA gel with a Young's modulus of $\sim 1.4 \pm 0.6\ kPa$. A) Field of fluorescent microbeads (infrared, 500 nm in diameter, 100 $\mu l/ml$, i.e. 0.22% v/v). B) Phase image and displacements field (green arrows) of the field of view in (A). Scale bars: 20 μm. Time–lapse experiment of the selected area in red is reported on the right. Time is indicated in minutes: 0' is 72 h after plating. The wave localization and propagation along the neurite is delimited by the blue line and reported in the insets. No significant displacements are detected.

Some conclusions and perspectives to improve the experimental system

It seems that neurites are not strongly adherent to the surface, which could explain the quite absence of forces transmitted to the substrate. See as an example the blue inset in Figure III.29 where the curved region of the neurite gradually moves out of the focus. Considering the number of experiments where the right conditions of softness and surface chemistry were gathered, we can conclude this method is not adapted to measure forces within waves.
Experiments with softer gels may still reduce the noise and improve the resolution to better evaluate the threshold corresponding to the maximal forces transmitted to the surface. However, these experiments reveal that these forces are very low or absent and this suggests that waves have no impact on the mechanical properties surrounding the neurite.

We propose some methodological aspects that could be improved.
First, we need an improvement of microscope setup with a better stability and objectives with an higher magnification and resolution (60x instead of 40x and an oil objective instead of the available air one), the use of smaller fluorescent microbeads (200 nm-diameter beads) and the achievement of z–stacks time–lapse experiments in order to not loose the information about the bead displacements in the perpendicular direction. Moreover, as we have observed that waves were very sensitive to the cellular stresses, eventually stopping or vanishing much below the level of stress leading to neuronal death, we might also achieve less toxic conditions of observations by increasing the exposure time while reducing the laser intensity. A fine control of the adhesive coating might be improve the neuronal adhesion, and thus the interaction with the hydrogel structure.

III.3.4 Summary about wave dynamics

This third section has focused on the properties of waves on geometrically constrained neurons.

We have observed that:

- it exists a direct interplay between **wave arrival** at the neurite tip and the total **elongation of the neurite**;
- the frequency of wave production is independent on the **neurite number**;
- enlarging the **neurite width** decreases the frequency of wave emission;
- the frequency of wave emission on the **asymmetric adhesive patterns** seems to be controlled at the single neurite;
- the **wave velocity** decreases on larger neurites.

Our works has shown that neurite width was controlling the wave period, as it controls the neurite length. Moreover, the periodicity of waves in asymmetric patterns has suggested that this control was performed at the neurite level (rather than at the soma level). Consistent with these results, we have proposed a minimal model suggesting that wave components (excess mass of polymerized actin, and/or critical signaling factor) are produced by the cell at a constant rate and that a critical neurite–width dependent concentration has to be reached to initiate wave emission.

Together, our work reinforces the association between neurite elongation and waves and gives a phenomenological framework of waves as a basis for future molecular studies. The exploration of a possible mechanism of neuronal polarization through a preferential allocation of waves in the future axon will be the object of further studies in our team.

As various lines of evidence suggest that axons are the neurite under the highest tensile stress and as waves might contribute to the establishment of this tension, we have reported some results about the calculation of **membrane tension** as function of the neurite nature (axon ans dendrite) and width and of **transmitted forces** associated to wave propagation.

We have shown that the neurite width does not influence the membrane tension and that this tension equilibrates fast. Additionally, we have shown that wave propagation only induces a transient resistance of the membrane, that we suspect to be associated to the remodelling of the membrane cortex as the wave forms. In the same line, traction force microscopy experiments have provided that forces directly transmitted to the substrate by waves were absent or very weak (lower than $\sim pN$). However, we could show that wave propagation does not result in stress transmission to the extracellular matrix, suggesting that wave propagation relies on internal tension. Some technical suggestions have been made to improve further experiments, although neuronal adhesions seem to be too low to measure with this method eventual forces exerted by waves.

In conclusion, wave propagation seems to not strongly involve mechanical mechanisms, at least at level neither of neurite membrane nor of forces transmitted to the substrate. A study of this process from a molecular point of view is therefore addressed in the next section.

III.4 Molecular high resolution investigation

In the previous section we have exposed our results about the dynamical and mechanical characteristics of waves during neurite elongation. A better understanding of the mechanisms behind their propagation would require to investigate these structures from a molecular point of view.

The investigation of the actin dynamics and of the proteins involved in the cytoskeleton organization can contribute to clarify the role of waves in the neuronal growth and polarization. For that purpose, we have performed preliminary studies on the wave components potentially involved in the mechanisms of propagation of these structures.

During my PhD, I had the opportunity to spend two weeks in the Giorgio Scita's group at the IFOM in Milan (FIRC Institute of Molecular Oncology, Italy) and three weeks in the Casper Hoogenraad's group at the Utrecht University (The Netherlands). These labs are among the best places in Europe for their recognized expertise respectively in cellular dynamics of actin structures and microtubules dynamics in neurons.

A fundamental contribution to the cellular understanding results from dynamical observations. This consideration is particularly true for waves, that are quite compact and very dynamical structures. However, several aspects make the tracking of waves a challenging purpose. First, our attention must be focused on isolated neurons in order to ensure that the wave dynamics is not affected by the interaction with other neurites. To increase the number of isolated cells growing on the patterns we have to plate cells at low densities. Live imaging on single cells and low density cultures are two conditions that make cells, and even more patterned cells, very sensitive to the stress of their environment, especially to the phototoxicity. Importantly, waves emission drastically decreases in cells submitted to stress. Moreover, the time window with the highest wave emission is quite short (1 – 3 DIV) and it coincides with the early steps of cell growth, where neurons are very fragile. Finally, virus infections or transfections techniques are required to selectively observe the molecular constituent of waves, but are known to stress cells. Furthermore, this means that fluorescent microscopy has to be employed, that involves an additional phototoxicity effect.

Both techniques, i.e. lentivirus infections and transfection by electroporation, have been tested and the first one has given the best results. Efficient live imaging experiences have been performed at 2 DIV for two main reasons:

- at 1 DIV cells are too much fragile, leading to a high rate of cell death
- and at 3 DIV the higher expression level of fluorescent proteins compromised the cells survival in these particular conditions of culture.

III.4.1 Actin structure and effectors

Live imaging with GFP–Lifeact has allowed to observe actin concentration and propagation within waves, that is usually not accessible by common bright field imaging. Some examples of these waves are shown in Figure III.31, confirming the high concentration of actin in the waves. We have also checked that actin immunostainings (from the phalloidin marker) and the Lifeact signal show a good colocalization (Figure III.32).

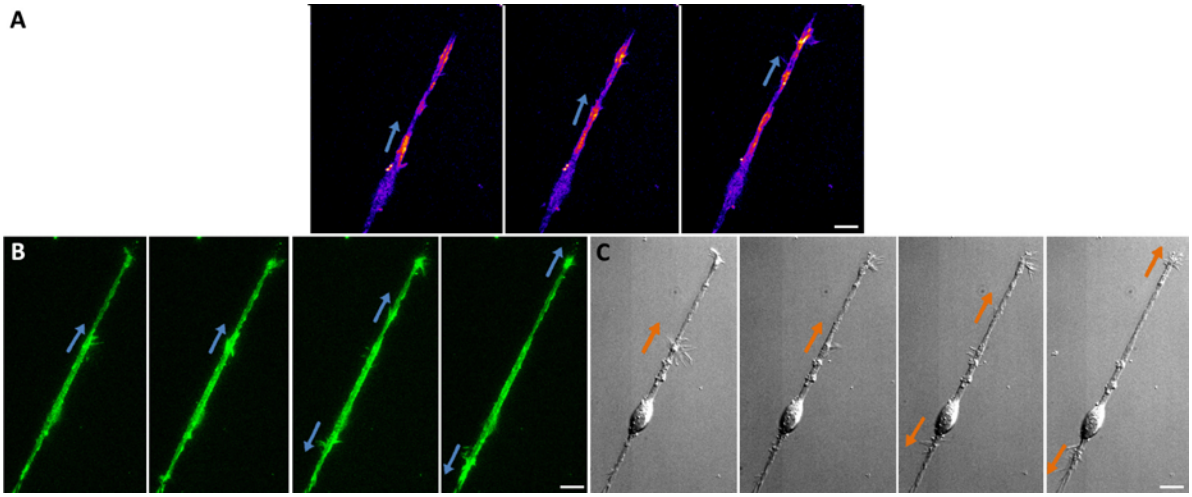

Figure III.31: **Live imaging of a GFP–LifeAct infected neurons at 2 DIV.** Mouse hippocampal neurons on 2 μm adhesive pattern, PLO coating. A) Spinning Disk microscope. Acquisition interval: 15 s. Times of shown stacks (from the left to the right): 51, 54 and 78 min. B, C) TIRF microscope: GFP–Lifeact (B) and bright field (C). Acquisition interval: 15 s. Times of shown stacks (from the left to the right): 0.5, 2, 3 and 5 min. Arrows show actin wave position and its propagation way. GFP–LifeAct infection conditions: 20 μl, overday (A) and overday / overnight (B). Scale bars: 10 μm.

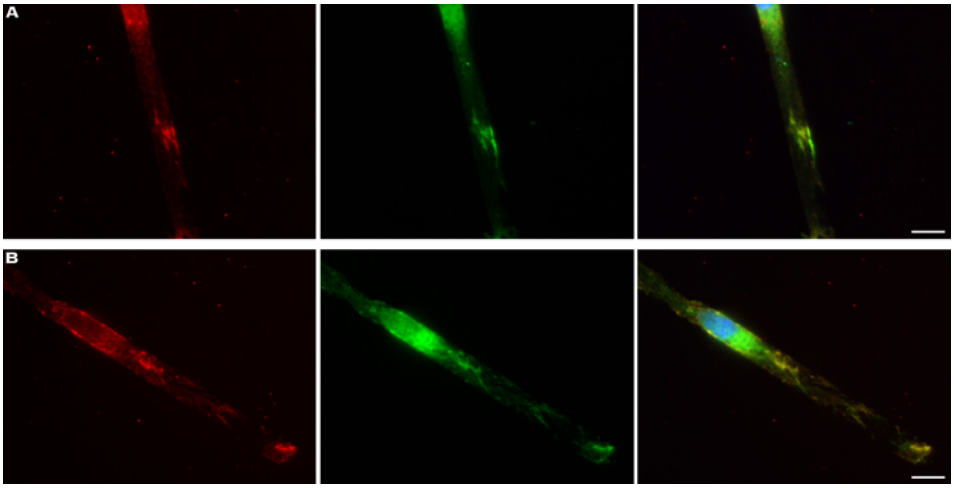

Figure III.32: **GFP–LifeAct infected neurons at 2 DIV.** Mouse hippocampal neurons on 6 μm adhesive pattern, PLO coating. A) Actin localization in a wave. B) Actin localization in a growth cone. Blue: DAPI, nuclei. Green: GFP antibody, Lifeact. Red: pholloidin, actin. GFP–LifeAct infection conditions: 20 and 10 μl respectively, overday / overnight. Scale bar: 10 μm.

Then, we have investigated actin regulatory proteins like VASP end Eps8 (see section I.2.2 for more details). Both appear highly concentrated within waves of living neurons.
Unfortunately, it was not possible to resolve their fine structure inside the waves, that where unusually narrow possibly due to the stress induced by infection and imaging (Figures III.33 and III.35).
We have nevertheless confirmed some known characteristics of these proteins, e.g. their presence in the lamellipodia and the filopodia tips (Figures III.36 and III.34.A). VASP colocalizes with focal adhesions, observed here in glial cells (Figure III.34.B). Interestingly, the growth cone shown in Figure III.34.C has adapted its morphology to the 15 μm adhesive disk, allowing the observations of clear spots of VASP staining along all the growth cone edges. Of note, the Eps8 overexpression might be explain the unusual morphology and slow time of propagation of the wave observed in Figure III.35.

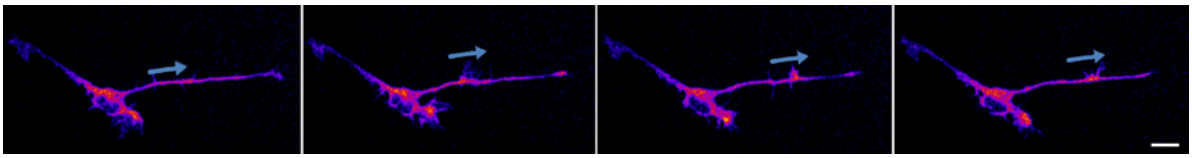

Figure III.33: **Live imaging of a GFP–VASP electroporated neuron at 1 DIV.** Mouse hippocampal neuron partially positioned on 2 μm adhesive pattern, PLO coating. Spinning Disk microscope. Acquisition interval: 15 s. Times of shown stacks (from the left to the right): 4, 6, 8 and 9 min. Arrows show actin wave position and its propagation way. GFP–VASP electroporation conditions: 1 pulse, 20 ms, 1600 V, 0.5 μg of DNA. Scale bar: 10 μm.

III.4.2 Microtubules organization and associated proteins

The organization of microtubules, the other key element of the cytoskeleton, has been investigated by immunostaining of microtubule end–binding proteins (see section I.2.1 for more details). We have observed that (i) microtubule plus–ends (EB1 and 3, in green) are excluded from the waves like in growth cones (Figure III.37.A, B), (ii) they seem to be lengthwise aligned with patterns both in 8 μm (Figure III.37.C) and in 2 μm (Figure III.37.D) wide stripes and to localize preferentially near the neurite edges, whereas (iii) microtubule minus–ends (CAMSAP2, in red) seem to have a more compact distribution, mainly in the middle of the neurites. Of note, the immunostainings for microtubules in large patterns have not revealed individual microtubules, since they seem to bundle also in these wide patterns, at least in these few examples.

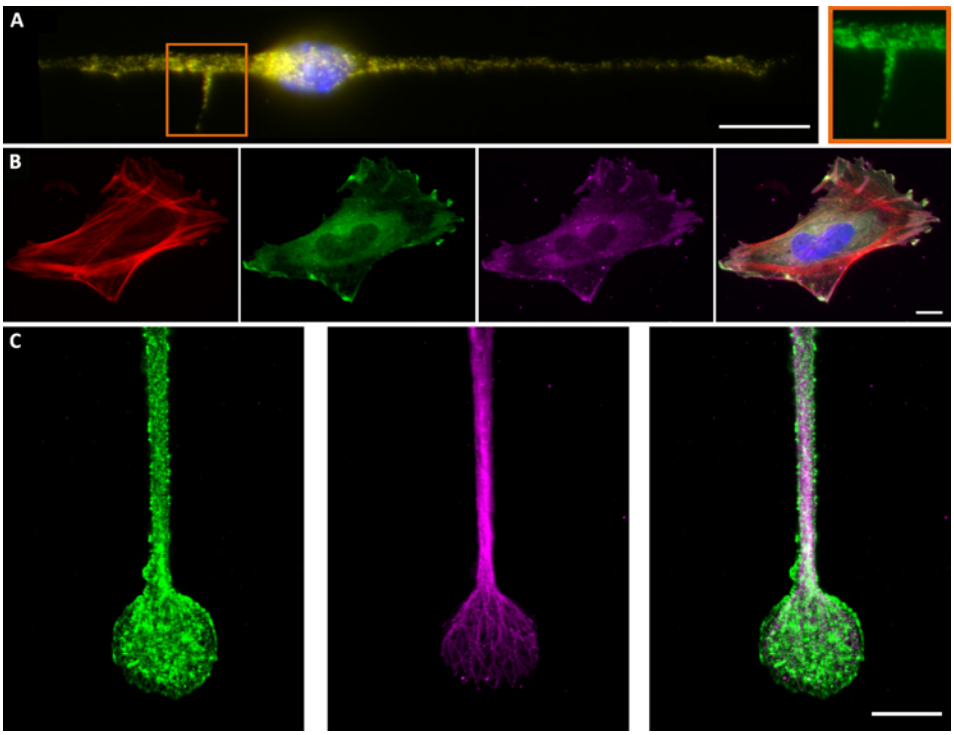

Figure III.34: **VASP localization in brain cells at 2 DIV.** Mouse hippocampal neurons and glial cell, PLO coating. A) Neuron grown on a 2–2 pattern. Blue: DAPI, nuclei. Red: phalloidin, actin. Green: GFP antibody, VASP. Inset: zoom of the orange rectangle showing the VASP staining in a filopodium along a neurite. B) Glial cell grown on a uniform adhesive area. Blue: DAPI, nuclei. Red: phalloidin, actin. Green: GFP antibody, VASP. Magenta: vinculin antibody, focal adhesions. C) Confocal microscope image of a neuron (cell body out–field) grown on a 2 μm wide pattern and the 15 μm adhesive disk. Green: GFP antibody, VASP. Magenta: microtubules. GFP–VASP electroporation conditions: 1 pulse, 20 ms, 1600 V, 0.5 μg DNA. Scale bars: 10 μm.

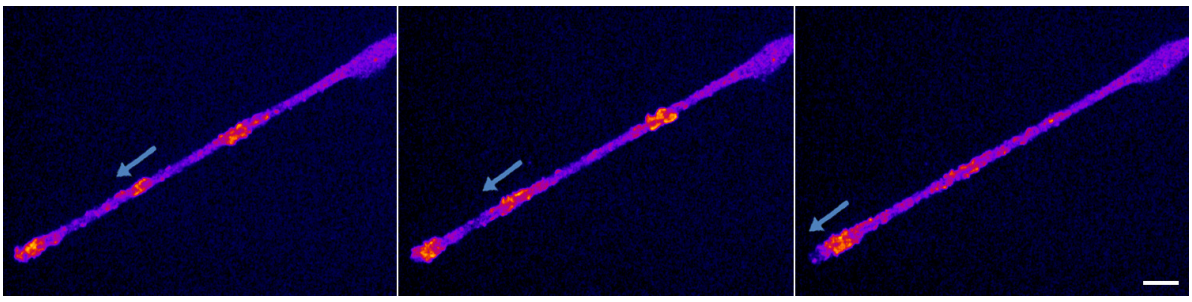

Figure III.35: **Live imaging of a GFP–Eps8 infected neuron at 2 DIV.** Mouse hippocampal neuron on 2 μm adhesive pattern, PLO coating. Spinning Disk microscope. Acquisition interval: 15 s. Times of shown stacks (from the left to the right): 0, 23 and 44 min. Arrows show actin wave position and its propagation way. GFP–Eps8 infection conditions: 20 μl, overday. Scale bar: 10 μm.

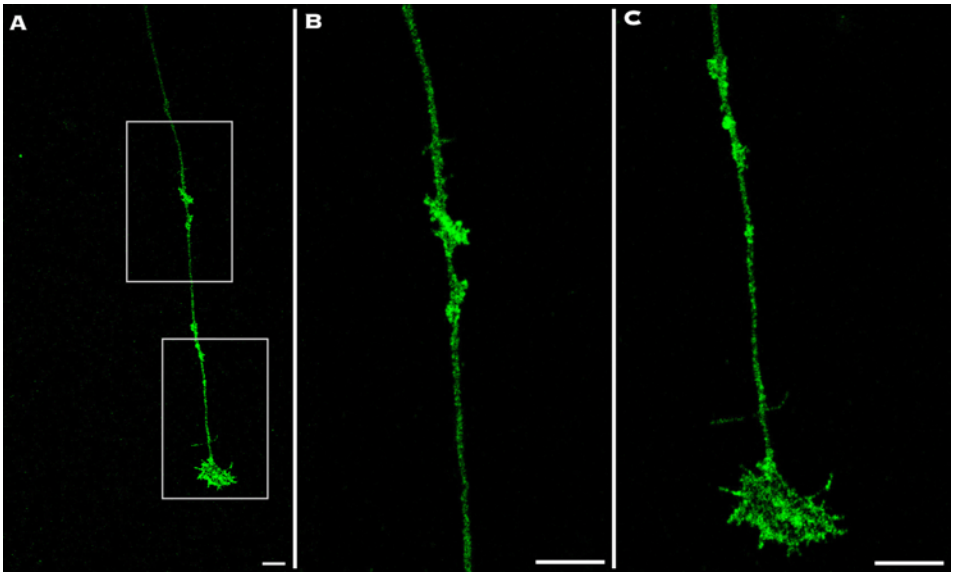

Figure III.36: **Eps8 localization in neurons at 2 DIV.** A) Confocal microscope image of a mouse hippocampal neuron (cell body out–field) grown on uniform adhesive area, PLO coating. Green: GFP antibody, Eps8. GFP–Eps8 electroporation conditions: 1 pulse, 20 ms, 1600 V, 0.5 μg DNA. Grey rectangle corresponds to the zoom shown in (B) and (C). Scale bars: 10 μm.

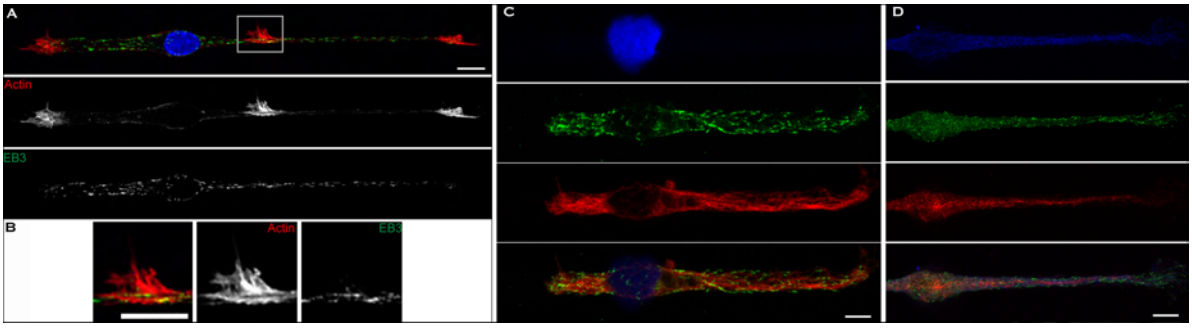

Figure III.37: **Microtubules organization in neurons on patterns of different widths.** Rat hippocampal neuron, PLO coating. A) Neuron on a 2:6 pattern at 2 DIV. Blue: DAPI, nuclei. Red: actin–antibody, actin. Green: EB3, end–binding protein of microtubules. Grey rectangle corresponds to the zoom shown in (B). B) Zoom of (A) showing an actin wave. C) Neuron on a 8–8 pattern at 2 DIV. Blue: DAPI, nuclei. Green: EB3, end–binding protein of microtubules. Red: βIII–tubulin, microtubules. D) Neuron on a 6:6 pattern at 6 DIV. Blue: βIII–tubulin, microtubules. Green: EB1, end–binding protein of microtubules. Red: CAMSAP2, minus–end binding protein of microtubules. Scale bars: 10 μm.

III.4.3 Summary about waves and molecular aspects

With the few results obtained until now, we can conclude that waves display an actin rich organization similar to growth cone. For the first time, actin dynamics has been observed by time-lapse experiments showing high actin concentrations within waves, propagating along neurites toward the growth cone. Moreover, the wave velocity of propagation on the order of a few $\mu m/min$ is compatible with a few tens of nm/s characterizing both the rate of actin polymerization of F-actin filaments and molecular motors dynamics along microtubules [40].

Some regulatory proteins for the branching (VASP) or the bundling (Eps8) of actin filaments have been observed in fixed and living neurons. These proteins are involved in axonal guidance, showing an enriched localization at the leading edge of the growth cone lamellipodia, at the tips of filopodia [41, 42, 43] or in dendritic spines [44]. Here, we have confirmed a similar localization in hippocampal neurons and show in addition that these proteins accumulate.

Microtubules end-binding proteins have been also observed. Our initial aim was to take advantage of the de-bundling of microtubules sometimes observed in neurite growing on the largest stripes to follow the dynamics of individual filaments, eventually in interaction with F-actin. These preliminary experiments have shown their exclusion from the membrane deformations produced by waves and their spatial organization was not qualitatively different in waves compared to the rest of the neurite shaft. An interaction of F-actin filament of waves with the central structure of microtubules in neurites is however not excluded. It would require to search for actin-microtubule linkers, as formins.

Two hypothesis at the basis of wave propagation seem thus to be consistent, or not excluded by with these exploratory experiments. Of note, both of them have not to be seen as exclusive: (i) the wave propagation might be associated to an actin polymerization along the neurites and (ii) it could be supported by an actif transport managed by molecular motors along microtubules, such as kinesins.

To achieve a deep understanding of these high dynamic structures it will be necessary to perform more experiments on living cells, interfering with the expression of specific genes that could be involved in wave propagation.

III.5 Toward controlled neuronal networks

The possibility to master the axonal specification process can be seen as a strategy to control of mature neuronal networks *in vitro* in terms of polarity and connectivity.
In this section, we will show some analysis on neurons at a later stage of development than that previously exposed. The idea was to investigate the molecular aspects related to the functional properties of neuronal networks grown on our microstructured substrates and to present a few examples of patterned neuronal networks as a first step toward functional organized neuron architectures.

Neurons fixed at 6 DIV showing dendrites and axons stainings (MAP2 and ankyrinG respectively, Figure III.12) represent already an encouraging result showing that neuronal development is not compromised morphological constraints, at least until this stage.
Neurons fixed at 16 DIV have been immunostained with synapsin I, a synaptic vesicle protein. In mature cultures of hippocampal neurons (i.e. starting from around 10 DIV), this pre–synaptic protein has been observed in concentrated spots corresponding on the sites where axons contact neuronal cell bodies and dendrites [45]. In early stage, synapsin I is primarily concentrated in the soma and it can also be present along the neurites. Then its distribution into the axon occurs even in isolated cells, independently of interactions with other cells. More generally, its expression increases throughout the course of development. Importantly, authors highlight that spots of synapsin I staining were seen even also along isolated axons, but forming smaller spots than at the level of the presynaptic points of contact with dendrites or somas. These results have been confirmed by our observations: a growth cone of a neuron fixed at 2 DIV (Figure I.9) displays a quite uniform distribution of synapsin I, and synapsin I spots are clearly visible on neurons at a later stage of development (Figure III.38).

In contrast with the Fletcher's observations, in our cultures all branches of isolated cells (axon and dendrites) present spots of synapsin I staining. There is little doubt that the longest and weakly branched neurite of the neuron in Figure III.38.A is the axon. This assumption is also in agreement with the weaker presence of visible spots of synapsin I staining, as described by [45]. This condition might suggest that a dense network of other very thin extensions cross dendrites giving the bright synapsin I spots. This hypothesis should be confirmed by microscopy technique with an higher resolution, as SEM (scanning electron microscopy).

As clearly evidenced by the morphology of neurons in Figure III.38 that does not follow anymore the initial 2:2 pattern, the patterning technique employed here is therefore not adapted for long term cultures. Other solutions are exposed in the Section II.1.1.4.

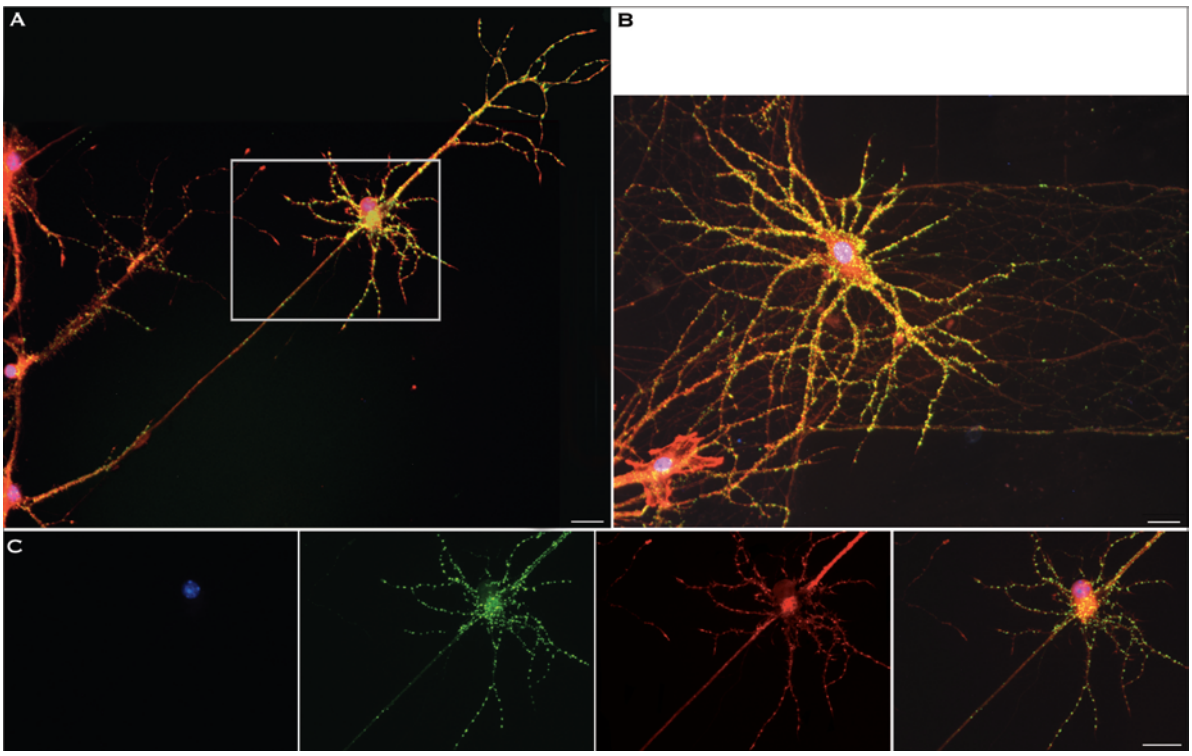

Figure III.38: **Mouse hippocampal neurons at 16 DIV.** A) Neuron on adhesive 2 μm wide pattern. Grey rectangle corresponds to the zoom shown in (C). B) Neuron on uniform adhesive area. C) Zoom of (A). Blue: Hoechst, nuclei. Green: synapsin I, synaptic vesicles. Red: Phalloidin, actin. PLO coating. Scale bars: 20 μm.

Finally, an example of design of connected neuronal architectures is shown in Figure III.39. Our goal was to recreate *in vitro* the conditions for a deterministic axonal localization. We refer to the section I.6 and to the several examples of only a partial control of the axo–dendritic process achieved until now in the literature (obtained by playing with the molecular specificities of the extra–cellular matrix [46, 47, 48] or by employing adhesive micropatterns [49] inspired by the axonal preference to low adhesive conditions reported by Prochiantz et al. [14]) to illustrate the purpose of such a goal. Our results on the control of the localization of axonal specification achieved on isolated cells have been applied here to iinterconnected neurons. In addition, curvatures at the tip of the thinnest branch (presumably the axon) have been designed to increase the probability to form synaptic connections through axonal branching. Three connected neurons fixed at 3 DIV with their soma correctly positioned on the 15 μm disk are shown in Figure III.39. The same pattern fabricated with the methods described in the Section II.1.1.4 (i.e. combining the grafting of repulsive and adhesive areas) might allow a good cellular confinement to grow controlled neuronal networks until a more mature stage.

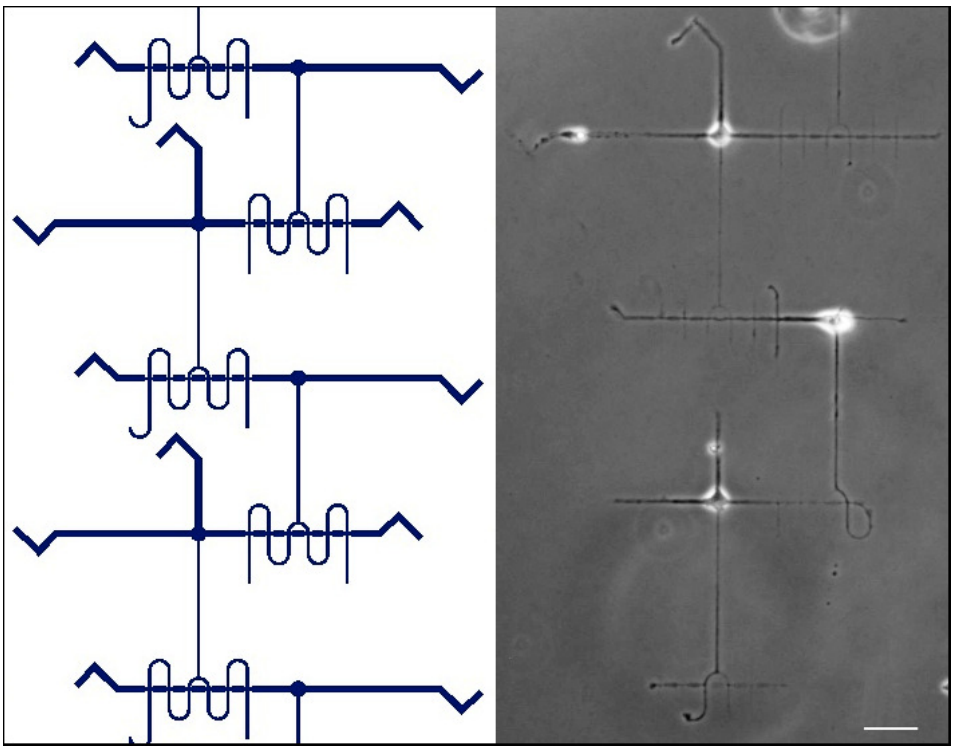

Figure III.39: **Controlled network of mouse hippocampal neurons at 3 DIV.** Adhesive pattern (left) and phase contrast image of three connected neurons (right). PLO coating. Scale bar: 50 μm.

III.6 Conclusion

In this chapter we have investigated the question of how **geometrical constraints** at the cell level can influence **neuronal growth and differentiation**. For that, we have mainly observed hippocampal neurons in a time window around 1 – 3 days *in vitro*, in order to follow the first steps of growth, until the axonal differentiation phase. We have adapted the size of the adhesive patterns to the order of magnitude of mouse neurons at this stage of development *in vitro*, i.e. around 1 – 2 μm of width and until few hundreds of μm of length. We have made the choice to employ pattern designs characterized by minimal straight stripes, varying their number or width. In this way, cell responses to adhesive 2D properties could be analyzed separately and quantified (see Section III.1.4).

In a second part of this chapter, we have investigated the existence of a **neurite critical length** in the process of neuronal polarization. Experimental and theoretical approaches have been employed, as described in the summary of the Section III.2.3.

Then, we have reported in the Section III.3.4 the conclusions about our study of the **wave dynamics**, including the influence of the neurite width and the forces associated to their propagation.

In the fourth section we have explored the **molecular aspects** associated to wave propagation, looking for the actin effectors and microtubule associated proteins. The summary of these explorative experiments about possible mechanisms at the basis of wave propagation along the neurites is reported in Section III.4.3.

Of note, and quite importantly, we observed waves in **cortical neurons**, suggesting a potentially broader significance of these structures although their association to cortical neuron elongation is still to be demonstrated (Figure III.18).

Finally, we have shown as our results might provide practical implications for the manipulation of *in vitro* neurons and the design of **controlled neuronal micro–circuits**. These kinds of architectures would be also interesting to study synaptic formation in different and controlled configurations, like for example in tip to tip connections.

Bibliography

[1] DL Benson, FH Watkins, O Steward, and G Banker. Characterization of gabaergic neurons in hippocampal cell cultures. *Journal of neurocytology*, 23(5):279–295, 1994. 17, 110

[2] Nobutaka Hirokawa, Takeshi Funakoshi, Reiko Sato-Harada, and Yoshimitsu Kanai. Selective stabilization of tau in axons and microtubule-associated protein 2c in cell bodies and dendrites contributes to polarized localization of cytoskeletal proteins in mature neurons. *The Journal of cell biology*, 132(4):667–679, 1996. 114

[3] Ling-Qiang Zhu, Hong-Yun Zheng, Cai-Xia Peng, Dan Liu, Hong-Lian Li, Qun Wang, and Jian-Zhi Wang. Protein phosphatase 2a facilitates axonogenesis by dephosphorylating crmp2. *The Journal of Neuroscience*, 30(10):3839–3848, 2010. 116

[4] Susana Gomis-Rüth, Corette J Wierenga, and Frank Bradke. Plasticity of polarization: changing dendrites into axons in neurons integrated in neuronal circuits. *Current Biology*, 18(13):992–1000, 2008. 21, 22, 116

[5] Etienne Delain, Alain Fourcade, Jean-Claude Poulin, Agnès Barbin, Dominique Coulaud, Eric Le Cam, and Emmanuel Paris. Comparative observations of biological specimens, especially dna and filamentous actin molecules in atomic force, tunnelling and electron microscopes. *Microscopy Microanalysis Microstructures*, 3(6):457–470, 1992. 119

[6] Matthias Rief, Jaime Pascual, Matti Saraste, and Hermann E Gaub. Single molecule force spectroscopy of spectrin repeats: low unfolding forces in helix bundles. *Journal of molecular biology*, 286(2):553–561, 1999. 119

[7] Jonne Helenius, Carl-Philipp Heisenberg, Hermann E Gaub, and Daniel J Muller. Single-cell force spectroscopy. *Journal of Cell Science*, 121(11):1785–1791, 2008. 119

[8] Pierre-Henri Puech, Kate Poole, Detlef Knebel, and Daniel J Muller. A new technical approach to quantify cell–cell adhesion forces by afm. *Ultramicroscopy*, 106(8):637–644, 2006. 119

[9] Valérie M Laurent, Alain Duperray, Vinoth Sundar Rajan, and Claude Verdier. Atomic force microscopy reveals a role for endothelial cell icam-1 expression in bladder cancer cell adherence. *PloS one*, 9(5):e98034, 2014. 119

[10] Benjamin Rappaz, Alexander Barbul, Yves Emery, Rafi Korenstein, Christian Depeursinge, Pierre J Magistretti, and Pierre Marquet. Comparative study of human erythrocytes by digital holographic microscopy, confocal microscopy, and impedance volume analyzer. *Cytometry Part A*, 73(10):895–903, 2008. 119

[11] Yves Emery, Etienne Cuche, Francois Marquet, Nicolas Aspert, Pierre Marquet, Jonas Kuhn, Mikhail Botkine, Tristan Colomb, Frederic Montfort, Florian Charriere, et al. Digital holography microscopy (dhm): fast and robust systems for industrial inspection with interferometer resolution. In *Optical Metrology*, pages 930–937. International Society for Optics and Photonics, 2005. 119

[12] Pascal Jourdain, Nicolas Pavillon, Corinne Moratal, Daniel Boss, Benjamin Rappaz, Christian Depeursinge, Pierre Marquet, and Pierre J Magistretti. Determination of transmembrane water fluxes in neurons elicited by glutamate ionotropic receptors and by the cotransporters kcc2 and nkcc1: a digital holographic microscopy study. *The Journal of Neuroscience*, 31(33):11846–11854, 2011. 119

[13] William P Bartlett and Gary A Banker. An electron microscopic study of the development of axons and dendrites by hippocampal neurons in culture. i. cells which develop without intercellular contacts. *The Journal of neuroscience*, 4(8):1944–1953, 1984. 121

[14] A Prochiantz, A Rousselet, and B Chamak. Adhesion and the in vitro development of axons and dendrites. *Progress in brain research*, 86:331–336, 1989. 121, 167

[15] Benjamin Rappaz, Pierre Marquet, Etienne Cuche, Yves Emery, Christian Depeursinge, and Pierre Magistretti. Measurement of the integral refractive index and dynamic cell morphometry of living cells with digital holographic microscopy. *Optics express*, 13(23):9361–9373, 2005. 122

[16] Céline Bottier, Chiara Gabella, Benoît Vianay, Lara Buscemi, Ivo F Sbalzarini, Jean-Jacques Meister, and Alexander B Verkhovsky. Dynamic measurement of the height and volume of migrating cells by a novel fluorescence microscopy technique. *Lab on a Chip*, 11(22):3855–3863, 2011. 122

[17] Hideaki Yamamoto, Takanori Demura, Mayu Morita, Gary A Banker, Takashi Tanii, and Shun Nakamura. Differential neurite outgrowth is required for axon specification by cultured hippocampal neurons. *Journal of neurochemistry*, 123(6):904–910, 2012. 21, 125, 129

[18] Dominique Seetapun and David J Odde. Cell-length-dependent microtubule accumulation during polarization. *Current Biology*, 20(11):979–988, 2010. 125, 129

[19] Wainrib Gilles, Thieullen Michèle, and Pakdaman Khashayar. Intrinsic variability of latency to first-spike. *Biological cybernetics*, 103(1):43–56, 2010. 129

[20] Gordon Ruthel and Gary Banker. Actin-dependent anterograde movement of growth-cone-like structures along growing hippocampal axons: A novel form of axonal transport? *Cell motility and the cytoskeleton*, 40(2):160–173, 1998. 26, 27, 129, 133

[21] Kevin C Flynn, Chi W Pak, Alisa E Shaw, Frank Bradke, and James R Bamburg. Growth cone-like waves transport actin and promote axonogenesis and neurite branching. *Developmental neurobiology*, 69(12):761–779, 2009. 26, 27, 129, 133

[22] Gordon Ruthel and Gary Banker. Role of moving growth cone–like "wave" structures in the outgrowth of cultured hippocampal axons and dendrites. *Journal of neurobiology*, 39(1):97–106, 1999. 27, 95, 133, 134

[23] Sophie Roth, Mariano Bisbal, Jacques Brocard, Ghislain Bugnicourt, Yasmina Saoudi, Annie Andrieux, Sylvie Gory-Fauré, and Catherine Villard. How morphological constraints affect axonal polarity in mouse neurons. *PloS one*, 7(3):e33623, 2012. 37, 38, 141

[24] Phillip Lamoureux, Gordon Ruthel, Robert E Buxbaum, and Steven R Heidemann. Mechanical tension can specify axonal fate in hippocampal neurons. *The Journal of cell biology*, 159(3):499–508, 2002. 38, 141, 142

[25] Jianwu Dai and Michael P Sheetz. Axon membrane flows from the growth cone to the cell body. *Cell*, 83(5):693–701, 1995. 143

[26] Jianwu Dai and Michael P Sheetz. Mechanical properties of neuronal growth cone membranes studied by tether formation with laser optical tweezers. *Biophysical journal*, 68(3):988–996, 1995. 143

[27] Albert K Harris, David Stopak, and Patricia Wild. Fibroblast traction as a mechanism for collagen morphogenesis. *Nature*, 290(5803):249–251, 1981. 145

[28] Sung Sik Hur, Yihua Zhao, Yi-Shuan Li, Elliot Botvinick, and Shu Chien. Live cells exert 3-dimensional traction forces on their substrata. *Cellular and molecular bioengineering*, 2(3):425–436, 2009. 145

[29] John L Tan, Joe Tien, Dana M Pirone, Darren S Gray, Kiran Bhadriraju, and Christopher S Chen. Cells lying on a bed of microneedles: an approach to isolate mechanical force. *Proceedings of the National Academy of Sciences*, 100(4):1484–1489, 2003. 145

[30] James P Butler, Iva Marija Tolić-Nørrelykke, Ben Fabry, and Jeffrey J Fredberg. Traction fields, moments, and strain energy that cells exert on their surroundings. *American Journal of Physiology-Cell Physiology*, 282(3):C595–C605, 2002. 145

[31] Marion Ghibaudo, Alexandre Saez, Léa Trichet, Alain Xayaphoummine, Julien Browaeys, Pascal Silberzan, Axel Buguin, and Benoît Ladoux. Traction forces and rigidity sensing regulate cell functions. *Soft Matter*, 4(9):1836–1843, 2008. 146

[32] Clarence E Chan and David J Odde. Traction dynamics of filopodia on compliant substrates. *Science*, 322(5908):1687–1691, 2008. 146, 153

[33] Timo Betz, Daniel Koch, Yun-Bi Lu, Kristian Franze, and Josef A Käs. Growth cones as soft and weak force generators. *Proceedings of the National Academy of Sciences*, 108(33):13420–13425, 2011. 34, 37, 146, 147

[34] Callen Hyland, Aaron F Mertz, Paul Forscher, and Eric Dufresne. Dynamic peripheral traction forces balance stable neurite tension in regenerating aplysia bag cell neurons. *Scientific reports*, 4, 2014. 147

[35] Daniel Koch, William J Rosoff, Jiji Jiang, Herbert M Geller, and Jeffrey S Urbach. Strength in the periphery: growth cone biomechanics and substrate rigidity response in peripheral and central nervous system neurons. *Biophysical journal*, 102(3):452–460, 2012. 147, 148, 153, 180

[36] Michel Moussus. *Forces mécaniques au sein de l'endothélium*. PhD thesis, Grenoble, 2014. 150, 151

[37] Danielle Gulino, Abbas Mgharbel, and Alice Nicolas. Procédé de preparation d'une matrice en hydrogel par photopolymerisation, June 6 2013. WO Patent App. PCT/EP2012/066,781. 76, 150

[38] Justin R Tse and Adam J Engler. Preparation of hydrogel substrates with tunable mechanical properties. *Current protocols in cell biology*, pages 10–16, 2010. 78, 152

[39] L. Landau and E. Lifchitz. *Theory of elasticity*. Mir Ed., 1967. 154

[40] Jonathon Howard et al. *Mechanics of motor proteins and the cytoskeleton*. Sinauer Associates Sunderland, MA, 2001. 165

[41] Lorene M Lanier and Frank B Gertler. From abl to actin: Abl tyrosine kinase and associated proteins in growth cone motility. *Current opinion in neurobiology*, 10(1):80–87, 2000. 165

[42] Matthias Krause, Erik W Dent, James E Bear, Joseph J Loureiro, and Frank B Gertler. Ena/vasp proteins: regulators of the actin cytoskeleton and cell migration. *Annual review of cell and developmental biology*, 19(1):541–564, 2003. 165

[43] Elisabetta Menna, Andrea Disanza, Cinzia Cagnoli, Ursula Schenk, Giuliana Gelsomino, Emanuela Frittoli, Maud Hertzog, Nina Offenhauser, Corinna Sawallisch, Hans-Jürgen Kreienkamp, et al. Eps8 regulates axonal filopodia in hippocampal neurons in response to brain-derived neurotrophic factor (bdnf). *PLoS biology*, 7(6):e1000138, 2009. 19, 165

[44] Eleanna Stamatakou, Aude Marzo, Alasdair Gibb, and Patricia C Salinas. Activity-dependent spine morphogenesis: a role for the actin-capping protein eps8. *The Journal of Neuroscience*, 33(6):2661–2670, 2013. 165

[45] Tara L Fletcher, Patricia Cameron, Pietro De Camilli, and Gary Banker. The distribution of synapsin i and synaptophysin in hippocampal neurons developing in culture. *The Journal of neuroscience*, 11(6):1617–1626, 1991. 166

[46] Teresa Esch, Vance Lemmon, and Gary Banker. Local presentation of substrate molecules directs axon specification by cultured hippocampal neurons. *The Journal of neuroscience*, 19(15):6417–6426, 1999. 28, 41, 67, 167

[47] Stephan KW Dertinger, Xingyu Jiang, Zhiying Li, Venkatesh N Murthy, and George M Whitesides. Gradients of substrate-bound laminin orient axonal specification of neurons. *Proceedings of the National Academy of Sciences*, 99(20):12542–12547, 2002. 32, 167

[48] Anthony A Oliva Jr, Conrad D James, Caroline E Kingman, Harold G Craighead, and Gary A Banker. Patterning axonal guidance molecules using a novel strategy for microcontact printing. *Neurochemical research*, 28(11):1639–1648, 2003. 41, 167

[49] Rita Fricke, Peter D Zentis, Lionel T Rajappa, Boris Hofmann, Marko Banzet, Andreas Offenhäusser, and Simone H Meffert. Axon guidance of rat cortical neurons by microcontact printed gradients. *Biomaterials*, 32(8):2070–2076, 2011. 41, 167

Chapter IV

Glial cells under physical constraints

Contents

Chapitre IV : résumé

Dans ce chapitre nous présentons des résultats expérimentaux portant sur la sensibilité des cellules du cerveau aux propriétés mécaniques de leur environnement. Les cellules gliales, qui sont actuellement un sujet d'étude en forte expansion, jouent un rôle important dans la formation et la réparation des réseaux neuronaux. Nous analysons, par une étude systématique et quantitative, l'effet de la rigidité du substrat et de ces propriétés chimiques ainsi que la contribution du milieu de culture, sur l'adhérence et la prolifération cellulaire. Nous montrons que contrairement aux neurones, les gliales sont influencées de manière significative par ces paramètres. Pour la première fois, nous montrons que l'adhérence et la prolifération des gliales sont augmentées dans un environnement rigide mais que ce résultat est conditionné par la chimie de surface, ouvrant des questions sur les mécanismes d'adhésion de ces cellules du cerveau.

Ce chapitre se termine par une exploration de la sensibilité des cellules gliales à la topographie du substrat, à l'échelle de quelques centaines de nanomètres, qui conclut à l'absence d'influence significative de cette échelle de topographie sur la morphologie cellulaire.

List of abbreviations and nomenclatures

AFM ..... Atomic Force Microscope

CNS ..... Central Nervous System

DHM ..... Digital Holographic Microscope

DIV ..... Days In Vitro

DMEMs ..... Dulbecco's Modified Eagle Medium ("s" is for "supplemented")

ECM ..... Extra Cellular Matrix

FAs ..... Focal Adhesions

FN ..... Fibronectin

GFAP ..... Glial Fibrillary Acid Protein

LN ..... Laminin

MEMs ..... Minimum Essential Medium ("s" is for "supplemented")

NBs ..... NeuroBasal ("s" is for "supplemented")

PA ..... PolyAcrylamide

PLL ..... Poly-L-lysine

PLO ..... Poly-ornithine

SD ..... Standard Deviation

IV.1 Glial cells sensitivity to the substrate stiffness

Most cells are sensitive to their environment in the sense that they adapt their characteristics to the properties of this environment [1, 2]. Among these properties, stiffness plays an important role in the regulation of cell behavior. The aim of *in vitro* studies is, by reproducing a large range of physiological *in vivo* ECM stiffnesses, to highlight the cellular responses to this physical parameter. The further challenge is then to find and understand the correlations between the *in vitro* and the *in vivo* behaviors.
Although several studies have confirmed that the brain is the softest tissue in mammals, in the order of few hundreds Pa [3], the brain cell mechanosensitivity is still poorly understood. Moreover, the brain global stiffness is not uniform, also over time. For example, similarly to the organization and the concentrations of the different brain cell types, brain stiffness changes during its development and in pathological conditions, showing that mechanical properties are quite intrinsically linked to brain functions [3, 4, 5].

The interest for glial cells is in part motivated by their involvement in injuries or cancers. For example, it has been demonstrated that soft hydrogel implants prevent the formation of glial scars, favouring neuronal regrowth [1]. Glial cells seem to respond to a larger range of stiffness values than the central nervous system (CNS) neurons [6, 7, 8]. Some studies have shown that glial cells survive better and spread more on stiff substrates [9, 10, 11]. The scarcity of studies giving a complete analysis of the brain cells mechanosensitivity may be explained by the complexity of the brain and especially by the difficulty to manipulate brain cells.

In this context, we have made the choice to deeper investigate this issue. Thus, in this chapter we will focus on the mechanosensitivity of glial cells. In particular, we will provide some exploratory experiments leading to systematic quantifications of glial cell density, in the context of adhesion and proliferation, as a function of the substrate stiffness. Although our conclusions are for the moment based on only few cell cultures, some key cell responses come to light rather coherently. We will report these experimental results with the purpose to highlight the glial cell sensitivity to mechanical stimuli and how this clear mechanosensitivity is influenced by the cell chemical environment, e.g. the culture medium, the molecules of adhesion and the presence of neurons.

IV.1.1 Methodology

We have employed microstructured hydrogels of polyacrylamide (PA) to elucidate the contribution of precise conditions of *in vitro* cultures such as the stiffness and the topography of the ECM, the composition of the medium and the nature of the adhesive ligands on the ECM. As the glial cell response is influenced by the presence of neurons, we will discuss the two cases of mixed glial/neurons and pure glia cultures in two separate sections.
The photopolymerization technique used for the fabrication of PA gels has already been discussed in the section III.3.3.2 dedicated to the study of the forces exerted by neurons. It is here employed to create rigidity patterns of various geometries. This technique allows to create elastic patterns with tunable geometries and mechanical properties. We have chosen for this study to probe the response of glial cells on mechanically uniform substrates within a panel of stiffnesses, and on mechanically non uniform substrates consisting of two apposed, significantly distinct values of stiffnesses with three kinds of geometrical designs. With this latter configuration, we explored the role of high stiffness gradient, at various scales in comparison with cell size, as presented in the Table IV.1.

Pattern	Characteristics	Aim	Pattern	Characteristics	Aim
 Uniform	Uniform stiffness depending on the exposure time	Comparison of cell behavior as a function of stiffness	 Double stiffness	Two stiffnesses characterized by a difference of several tens of kPa	Analysis of the response to both sharp gradient and uniform stiffness
 Stripes	Stripes of different widths, between 5 to 75 μm	Analysis of the response to high stiffness gradients at the cell level	 Target	Circular areas with a delta of several tens of kPa	Multiply the number of high stiffness gradients at a larger scale than the cell level

Table IV.1: **Designs of stiffness patterns projected on polyacrylamide (PA) hydrogels.** Substrates are transferred on round coverslips ($\phi = 30\ mm$). The orange regions correspond to the soft parts of the gel, the blue ones are the rigid regions. The "Characteristics" and the "Aim" columns express the interest of the corresponding pattern.

We have exposed in Section II.2 the techniques employed to *in vitro* manipulate glial cells to obtain mixed or pure cultures. For all experiments with mixed or pure glial cell cultures we have used mouse cortical cells from embryos of 18 days of gestation.

In the next section we analyze how glial cell proliferation is influenced by the mechanical properties of their ECM, in the presence of neighboring neuronal cells in mixed culture conditions. Therefore, the exploration of their mechanosensitivity with this method is closer to the *in vivo* situation than with pure cultures. Of note, in *in vitro* mixed cultures glial cells are usually observed in direct contact with the substrate (neurons are located on top of glial cells). For this reason, glial cells interaction with the substrate stiffness is not impaired by neurons.
Pure culture has been used to investigate the response of primary glial cells both in terms of adhesion and proliferation as a function of the substrate stiffness. As it will be discussed, this technique presents also the advantage to get a more controlled condition in terms of initial cell concentration. These results will be presented in the Section IV.1.3.
For each experiment, we will report in the footnotes information about hydrogels, including parameters of fabrication, concentration of molecules of adhesion, medium employed for the culture and cell seeding concentration. See footnotes in the Section II.2 for information about the composition of the culture media.

IV.1.2 Mixed neuronal–glial cell cultures

We first describe preliminary experiments, that give a first insight of glial cell response to stiffness. We then report more systematic analysis.

Qualitative explorations of glial cells mechanosensitivity on mixed cultures

Some different culture conditions, including adhesive coating and culture medium, are explored.

◊ Poly-L-lysine and laminin (PLL/LN) coating and serum free culture medium

To investigate the glial cells behavior in presence of neurons, an important component of their static mechanical environment, we have chosen the "double stiffness" substrates (see the Table IV.1 for the nomenclature) functionalized with PLL/LN proteins and cultured in a medium adapted to neuronal development. We observed that glial cells proliferate on the stiff side and stop at the frontier with the soft region, whereas neurons extend branches on both surfaces (Figure IV.1)[1].

◊ Fibronectin (FN) coating and culture medium supplemented with serum

Then, the experience has been repeated on "uniform" and "double stiffness" hydrogels, functionalized with FN protein and cultured in a medium adapted for glial cells proliferation. This

[1] **Details of fabrication, functionalization and culture of the hydrogel.** 3 equivalent samples. Exposure time: 100 s; chrome thickness: 40 nm; fluorescent microbeads: $\phi = 200\ nm$, 30 $\mu l/ml$, i.e. 0.06% v/v; PLL 105 $\mu g/cm^2$ during 1 h, LN 1.1 $\mu g/cm^2$ during 1 h. Seeding conditions: $\sim$ 100 $cells/mm^2$ in MEMs culture medium, replaced after 3 h by NBs. Young's moduli: $\sim$ 100 kPa (transparent region) and $\sim$ 25 kPa (chromed region).

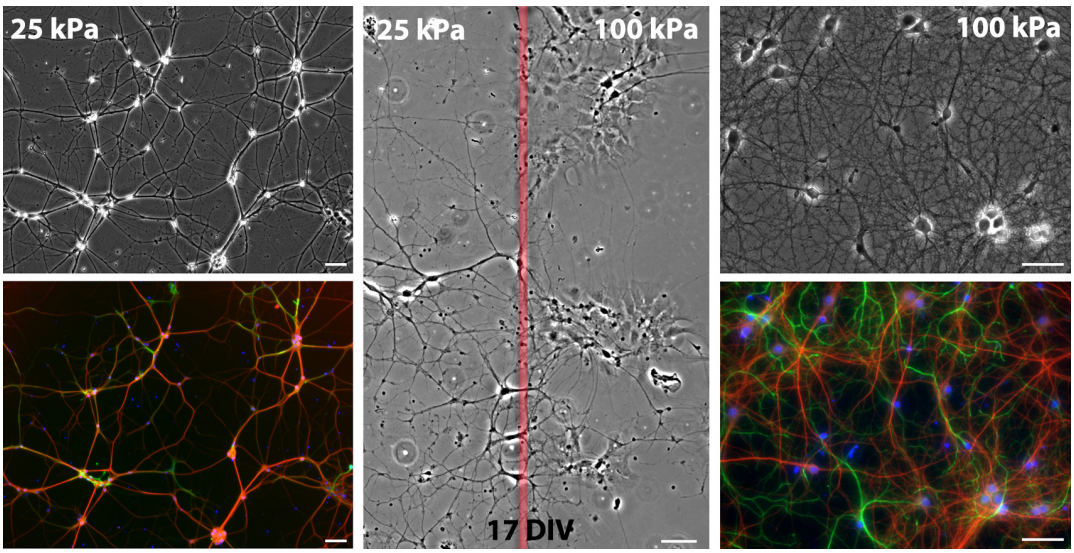

Figure IV.1: **Cortical mixed culture on a "double stiffness" hydrogel using PLL/LN surface coating and NBs as culture medium.** Phase contrast (top) and fluorescence (bottom) images of mixed neuronal–glial cell culture on a "double stiffness" gel of 25 kPa (left) and 100 kPa (right). Green: α–GFAP, glial cells. Red: MAP2, neurons. Blue: Hoechst, nuclei. Central picture shows the frontier between the stiff and soft regions (red line). Glial cells only grew on the stiff side and their proliferation stopped at the border, while neurons crossed it freely. Cells are fixed at 17 Days In Vitro (DIV). Scale bars: 50 μm.

time glial cells grew on both sides but achieved confluence faster on the stiff region.

Interestingly, after reaching confluence at 7 and 10 DIV on the stiff and the soft region respectively, cells tend to gather together and to detach themselves from the surface (Figure IV.2)[2], a phenomenon that is never observed when glial cells are cultivated at the bottom of a Petri dish.

The tendency of glial cells to preferentially proliferate on stiff substrates that emerges from these experiments needs now a deeper analysis of the impact of the medium and the proteins of adhesion on the cells behavior, as developed below.

◊ Four different conditions of molecules of adhesion and culture medium

Some experiments have been conducted on "double stiffness" hydrogels, where we have tracked glial cell development in four different configurations of medium and coatings (Table IV.2)[3].

[2]**Details of fabrication, functionalization and culture of the hydrogels.** Exposure time: 15 and 150 s (homogenous gels), 55 s ("double stiffness" gel, chrome thickness: 20 nm); protocol with dehydration; FN 3.5 $\mu g/cm^2$ during 1 h. Seeding conditions: $\sim$ 400 $cells/mm^2$ in DMEMs culture medium. Young's moduli: $\sim$ 25 kPa and $\sim$ 60 kPa (homogenous gels), 100 kPa and 25 kPa (transparent and chromed regions of the "double stiffness" gel).

[3]**Details of fabrication, functionalization and culture of the hydrogels.** Exposure time: 44 s; chrome thickness: 20 nm; fluorescent microbeads: ϕ = 500 nm, 100 $\mu l/ml$, i.e. 0.22% v/v; protocol with dehydration; FN 3.5 $\mu g/cm^2$ during 1 h; PLL 110 $\mu g/cm^2$ during 1 h, LN 1.1 $\mu g/cm^2$ during 1 h. Seeding conditions: $\sim$ 200 $cells/mm^2$ in DMEMs culture medium, eventually replaced after 3 h by NBs. Young's moduli: 60 kPa (transparent region) and 30 kPa (chromed region).

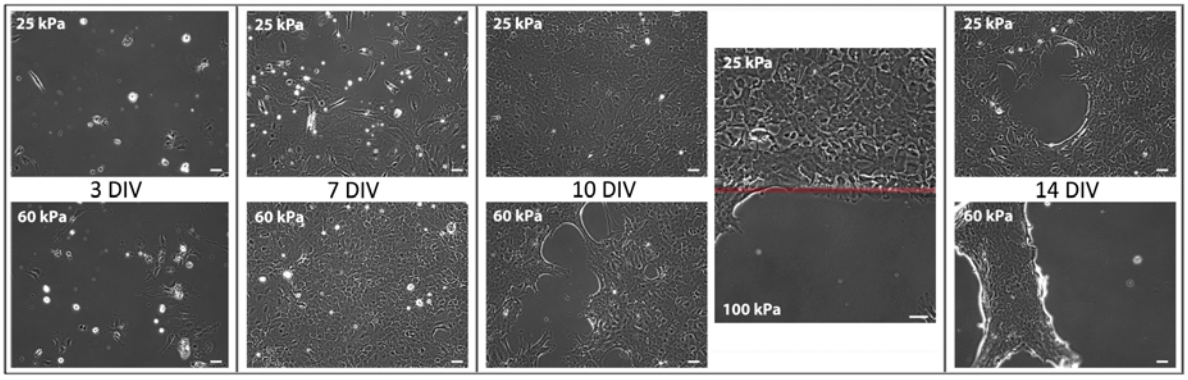

Figure IV.2: **Cortical mixed culture on "uniform" and "double stiffness" hydrogels with FN as adhesion ligand and DMEMs as culture medium.** Phase contrast images of a neuronal–glial cell culture on soft (25 kPa, top) and stiff (60 – 100kPa, bottom) "uniform" gels during development. The picture on the right of 10 DIV shows the frontier area at similar ageing of a mixed culture on a "double stiffness" gel, delimited by the red line. Images show the gradually achievement of the confluence stage and the consequently detachment of the cell layer. This phenomenon occurs firstly on the stiff gels (bottom, 10 DIV) then on the soft ones (top, 14 DIV). FN coating, DMEMs culture medium. Scale bars: 50 μm.

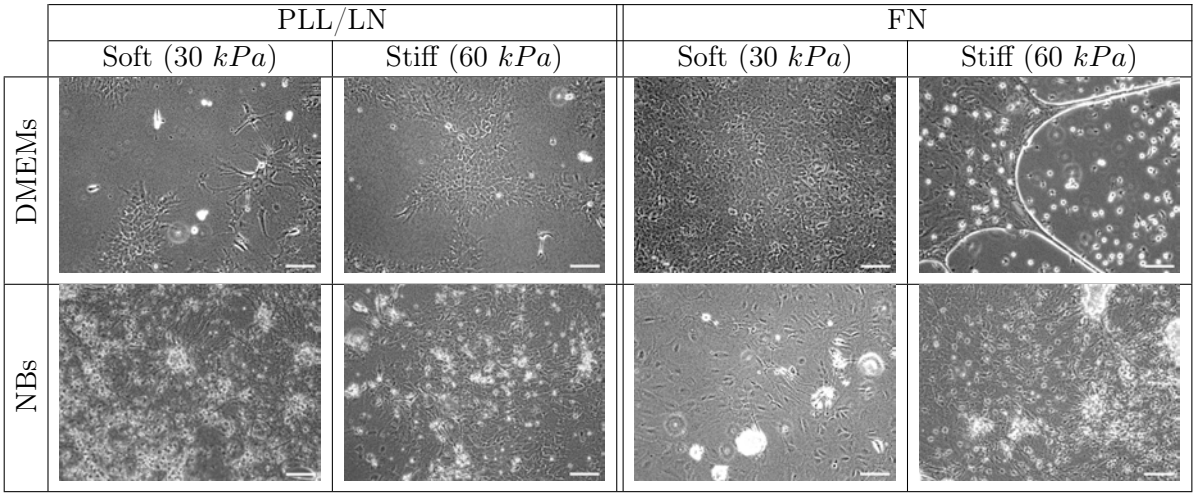

Table IV.2: **Influence of the culture conditions on cortical mixed cultures on "double stiffness" hydrogels.** Phase contrast images of a neuronal–glial cell culture on the soft (30 kPa) and the stiff (60 kPa) side of "double stiffness" gels in different conditions of medium and proteins of adhesion: PLL/LN coating or FN coating with NBs or DMEMs culture medium. Cells are fixed at **14 DIV**. Scale bars: 100 μm.

These experiments confirmed a higher rate of glial cell proliferation in presence of both FN coating and DMEMs medium, with the highest rate on the stiff regions. While neurons are never observed directly on the FN as adhesion ligand, we observed neuronal growth on top of glial cells. The PLL/LN–DMEMs condition led to similar observations, although the initial neuron concentration after plating was higher. In both cases, the DMEMs medium progressively kills neurons, independently of the surface chemistry. Conversely, a combination

of PLL/LN surface chemistry and NBs culture medium led to dense neuron network both on the soft and stiff regions. On the contrary, for both adhesive coatings in NBs medium glial cell proliferation is delayed on the soft substrate, although higher with FN. In brief, these exploratory experiments concerning glial cells seem display that the effect of stiffness can be modulated by the conditions of culture (DMEMs versus NBs and FN versus PLL/LN).

Quantitative results of glial cells mechanosensitivity on mixed cultures

The culture conditions just discussed in the preliminary experiments, associated to a larger panel of stiffnesses, should give a better understanding of the mechanosensitivity of the glial cells. Therefore, we have designed "target" patterns to:

- multiply the number of different stiffnesses available on a single substrate, and to highlight cell responses at the frontiers between two different stiffnesses;
- analyze different conditions without duplicating the number of samples, as it should be necessary with elastically uniform substrates.

The thickness of the chrome layer on the mask has been adapted to observe on the same substrate glial cells behavior on highly contrasted values of stiffness (some tens of kPa) and the stiffness of the soft regions has been reduced to values close or lower than 1 kPa, in order to approach the order of magnitude of the whole brain stiffness.

Let us remark that for the "target" pattern the two soft regions do not have the same rigidity, with the inner area surrounded by the stiff disk slightly stiffer than the external one. We refer to the paragraph "Hydrogel stiffness characterization by atomic force microscopy (AFM)" of Section II.1.2.2 for the reason of this feature. A similar difference should be obtained between the two stiff regions but the external one was too close to the Petri dish edges to be correctly analyzed. We will use the nomenclature "soft 1" for the inner region and "soft 2" for the external one. The "stiff" will correspond to the region between the two soft disks (see Table IV.1 for the "target" design).

◊ Long mixed cultures under four different conditions of molecules of adhesion and culture medium

We have quantified glial cell proliferation from the first days of culture up to three weeks, in mixed cell populations as a function of the culture conditions (see Tables A.1 and A.2 for respectively the glial and the neuronal cell densities)[4].

[4]**Details of fabrication, functionalization and culture of the hydrogels.** Exposure time: 20 s; chrome thickness: 30 nm); protocol with dehydration; FN 1.1 $\mu g/cm^2$ during 1 h (nominal value 3.5 $\mu g/cm^2$); PLL 110 $\mu g/cm^2$ during 1 h, LN 1.1 $\mu g/cm^2$ during 1 h. Seeding conditions: $\sim$ 150 $cells/mm^2$ in DMEMs culture medium, eventually replaced after 3 h by NBs. Young's moduli: 45 kPa (transparent regions), $\sim$ 1 kPa and $<$ 0.5 kPa (chromed regions, "soft 1" and "soft 2" respectively).

▶ Glial cell proliferation is influenced by the culture medium

We focused our analysis on the proliferation of the glial cells and their sensitivity to the stiffness of the substrate. For that, we plotted the glial cell density versus time, showing the behavior for each culture condition on the different regions of stiffness (Figure IV.3).

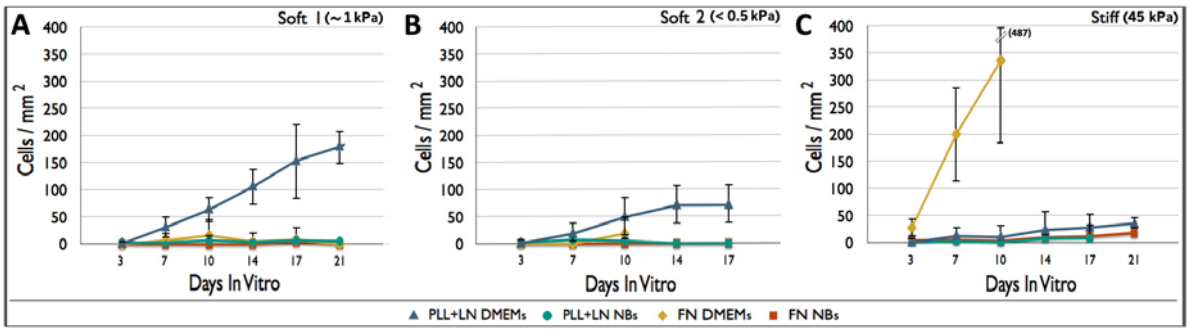

Figure IV.3: **Glial cell density ($cells/mm^2$) in different culture conditions**: PLL/LN or FN coating, DMEMs or NBs culture medium. Cells were observed between 3 and 21 DIV. Evolution over time on the "soft 1" substrate (A, $\sim 1\ kPa$), on the "soft 2" substrate (B, $< 0.5\ kPa$) and on the stiff substrate (C, 45 kPa). Error bars denote SD.

We first note that the impact of the medium is the highest. In the serum free NBs, the concentration of glial cells is not significantly different from zero, independent of the stiffness and of the adhesive coating of the substrate. In DMEMs, the observation differs depending whether the cells grow on PLL/LN or on FN.

▶ Glial cell mechanosensitivity is influenced by the adhesive coating

We report in separate graphs the evolution of cell density under the two coating conditions for an easy comparison of the response of glial cells to the mechanical properties of the substrate in proliferation medium (DMEMs, Figure IV.4).

In the case of PLL/LN coating, a high proliferation rate is favoured by the soft conditions.

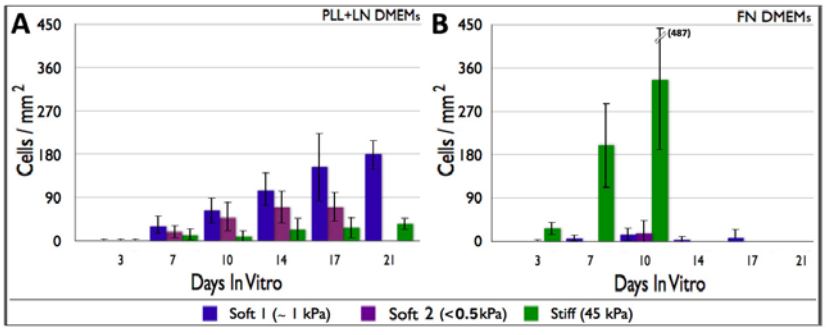

Figure IV.4: **Glial cell density ($cells/mm^2$) with different functionalizations**: PLL/LN (A) or FN (B) coating, DMEMs culture medium. Cells were observed between 3 and 21 DIV. Evolution over time on the "soft 1" substrate ($\sim 1\ kPa$), on the "soft 2" substrate ($< 0.5\ kPa$) and on the stiff substrate (45 kPa). Error bars denote SD.

The proliferation on the soft region at different stages is illustrated in Figure IV.5.

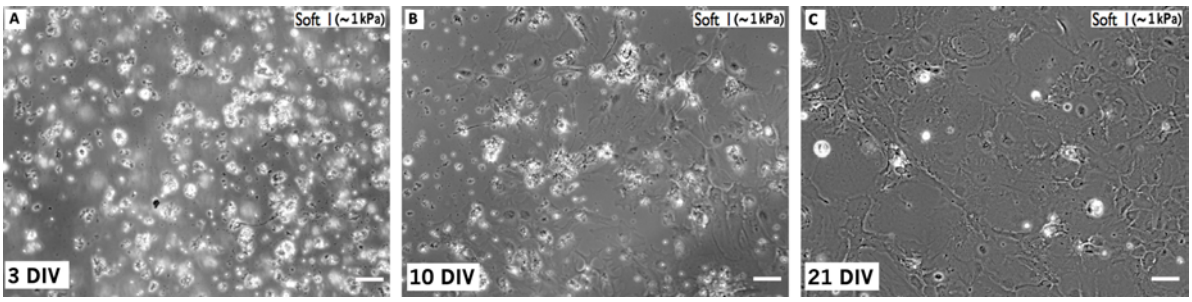

Figure IV.5: **Neuronal–glial cell culture on a PLL/LN coated hydrogel and maintained in the DMEMs culture medium.** Phase contrast images of the "soft 1" area ($\sim 1\ kPa$) at 3 (A), 10 (B) and 21 (C) DIV showing the gradual proliferation of glial cells. Scale bars: 60 μm.

Of note, the highest values of cell density were surprisingly obtained on the "soft 1" area, that is the less soft area among the two soft regions of the "target" hydrogel.
This result could arise from the fact that ultra-soft gels like in the "soft 2" region often show inhomogeneities in terms of thickness (close to the polymerization limit, hydrogel incorrectly demould from the mask). This would in turn decrease locally the gel stiffness and thus increase the effective stiffness of the substrate felt by cells.

Another hypothesis is that glial cells display a maximum of proliferation for the stiffness corresponding to the soft 1" region. This point remains an open question and these results obtained from one cell culture should be certainly confirmed with more experiments.
Another unexpected result is the inversion of the mechanosensitivity phenomenon by the nature of the gel coating. To understand why the PLL/LN functionalization gives a higher rate of proliferation on soft rather than on stiff substrates, we first refer the reader to the paragraphs "Hydrogels functionalization and characterization" of Section II.1.2.2 for a discussion about the differences of protocol for the FN and the PLL coatings. Indeed, they currently leads to a less controlled distribution of the molecules of adhesion for the PLL coating condition in presence of a high stiffness gradient between the soft and the stiff regions. As it appears that the PLL/LN coating is less uniform on soft gels, where it is enriched close to glial cells, we could hypothesize that low stiffness might influences their capacity to secrete LN and therefore to adapt their proliferation rate as a function of the rigidity of the substrate. These hypothesis are both supported (i) by some confocal images of the hydrogels surface recorded at the end of the experience, showing a higher and non uniform surface density of LN on the soft than on the stiff region (Figure IV.6) and (ii) by the observations reporting that glial cells are able to secrete LN (Figure IV.7).

An opposite behavior is observed with the FN coating: the stiff region induces a rate of proliferation that is more than a factor of ten higher than on the soft regions. Strikingly, this is the highest absolute rate observed for all culture conditions. Some views of these samples are reported in Figure IV.8.

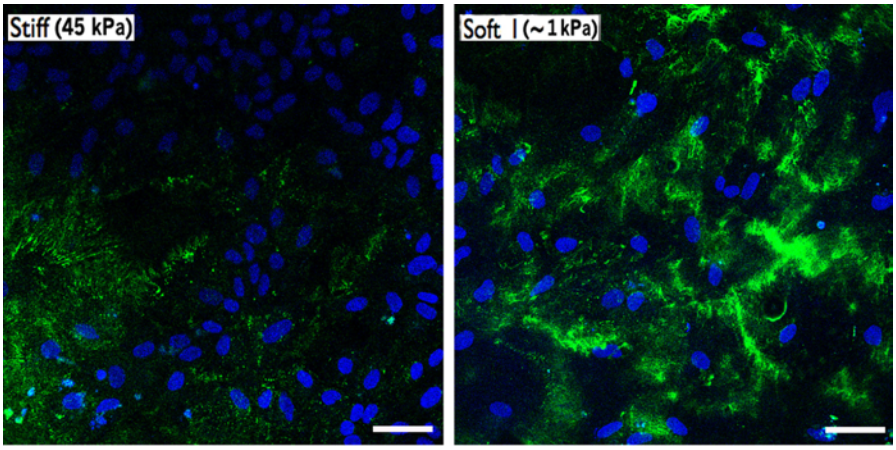

Figure IV.6: **Glial cells growing on a PLL/LN coated "target" hydrogel and maintained in the DMEMs culture medium.** Neuronal–glial cell culture fixed at **21 DIV**. Confocal images of the stiff (45 kPa, left) and the "soft 1" area ($\sim$ 1 kPa, right) of a "target" hydrogel showing an irregular distribution of the proteins of adhesion and a higher concentration around cells on the soft region. Green: α–LN. Blue: Hoechst, nuclei. Scale bars: 50 μm.

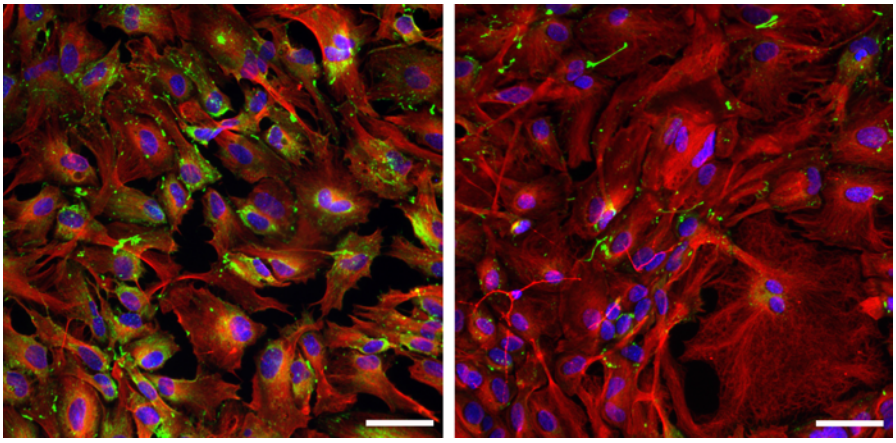

Figure IV.7: **Exploration of LN and FN secretion by glial cells.** Pure glial cell culture on PLO coated coverslips and maintained in the DMEMs culture medium, showing both LN and FN on the cells. Cells are fixed at **11 DIV**. Green: α–LN (left) and α–FN (right). Red: Phalloidin, actin. Blue: Hoechst, nuclei. Scale bars: 50 μm.

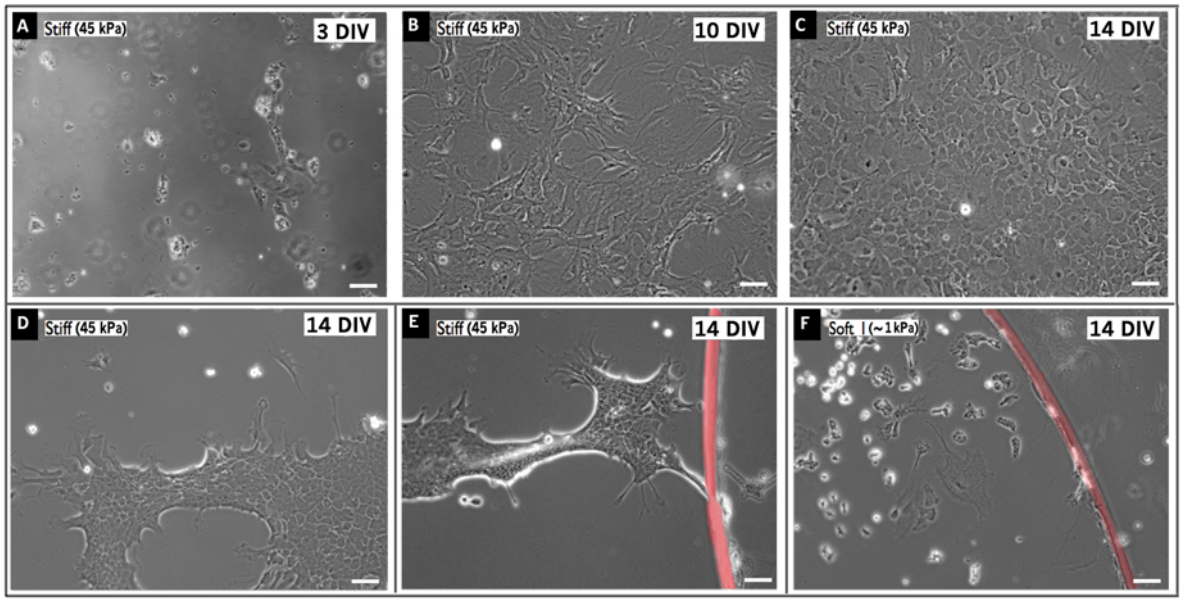

Figure IV.8: **Neuronal–glial cell culture on a FN coated "target" hydrogel and maintained in the DMEMs culture medium.** Phase contrast images of: A – B – C) glial cell proliferation between 3 and 14 DIV, until the confluence stage, on the stiff area (45 kPa); D – E) stiff areas (45 Pa) at 14 DIV showing cells detachment from the surface after the confluence stage. F) "soft 1" area ($\sim$ 1 kPa) at 14 DIV showing mainly rounded or small cells. In (E) and (F) the stiff region is not in focus. Scale bars: 60 μm.

This such high rate of proliferation leads to the already described effect of detachment of layers of confluent cells (see Figure IV.2 and Table IV.2) causing the impossibility to count the cells at 14 DIV and later (Figure IV.8.D–E). This effect will be discussed in more details further in this manuscript, in order to give a complete overview of this phenomenon for both mixed and pure glial cell cultures (Section IV.1.4).

► **Neuronal cell density is influenced by the adhesive coating and the culture medium**

As observed previously, the only favourable condition of culture for neurons are substrate functionalization with PLL/LN coating and culture in the NBs medium (Figure IV.9). In this case, the number of neurons is slightly larger on the soft substrates than on the stiff one. Moreover, neuron density is statistically constant over time, showing a good survival in this culture condition.

The fluctuations observed in the number of neurons over time are related to the difficulty to count them in bright field images, especially after two weeks of culture when neurons are organized in mature networks and where individual soma are quite difficult to identify. Some pictures of the condition of PLL/LN coating in NBs medium are reported in Figure IV.10 as examples.

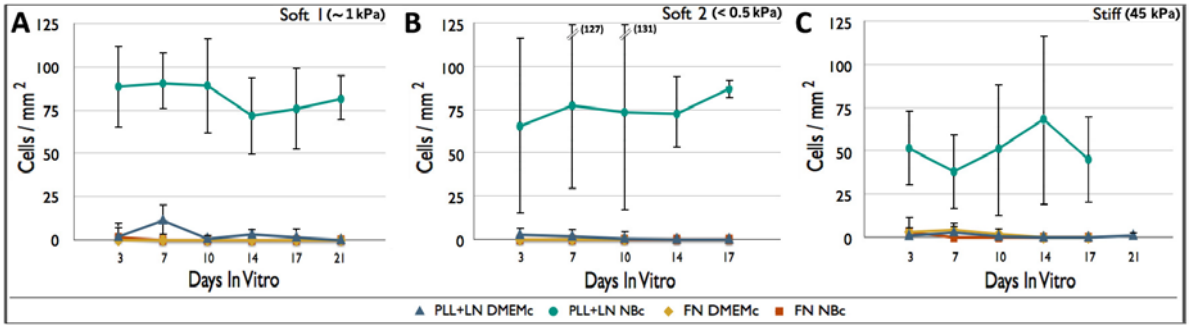

Figure IV.9: **Neuron density ($cells/mm^2$) in different culture conditions**: PLL/LN or FN coating, DMEMs or NBs culture medium. Cells were observed between 3 and 21 DIV. Evolution over time on the "soft 1" substrate (A, $\sim 1\ kPa$), on the "soft 2" substrate (B, $< 0.5\ kPa$) and on the stiff substrate (C, 45 kPa). Error bars denote SD. See Figure IV.3 for a direct comparison with the glial cell density in the same culture conditions.

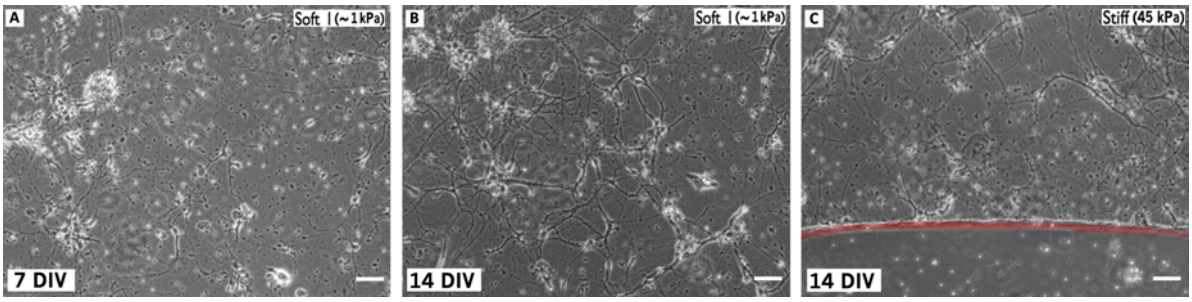

Figure IV.10: **Neuronal–glial cell culture on a PLL/LN coated "target" hydrogel and maintained in the NBs culture medium.** Phase contrast images of the "soft 1" area ($\sim 1\ kPa$) at 7 (A) and 14 (B) DIV and of the frontier (red line) with the stiff area (45 kPa) at 14 DIV (C) showing mature and dense neuronal networks both on soft and stiff regions. The soft region is not in focus. Scale bar: 60 μm.

The NBs culture medium is therefore essential for neuron survival but cannot compensate for a non suitable coating like FN. In this case, the adhesion of neurons is strongly impaired. Indeed, in Figure IV.11 (FN–NBs conditions) we initially observe neurons almost exclusively on top of glial cells and progressively making compact clusters, at the level of the very low number of the glial cells. Indeed their absence of proliferation is caused by NBs medium. This neuron morphology is typically observed in situations of inadequate conditions of adhesion.

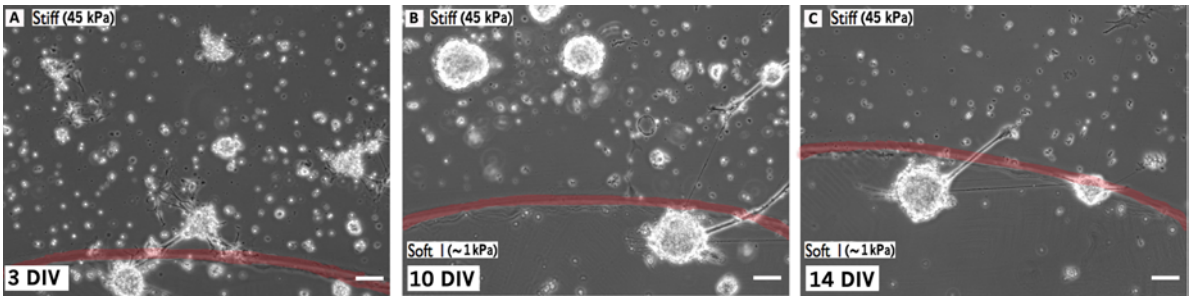

Figure IV.11: **Neuronal–glial cell culture on a FN coated "target" hydrogel and maintained in the NBs culture medium.** Phase contrast images of the frontier (red line) between the "soft 1" area ($\sim 1\ kPa$, bottom of the frontier) and the stiff area ($45\ kPa$, top of the frontier) at 3 (A), 10 (B) and 14 (C) DIV showing neurons growing on the glial cells and gradually gather together in spheric aggregates. Scale bar: 60 μm.

The results obtained in this section are now compared to those of similar experiments performed with pure cultures. This comparison is crucial to elucidate the role of neurons in the glial cell sensitivity to the mechanical and chemical properties of their environment. The results of this study are presented in the next section.

IV.1.3 Pure glial cell cultures

The purpose of this section is to decouple the possible effect of glial cells interaction with neurons on glial cell response to mechanical cues. We have employed the same methodology as described above to analyze the glial cell response to the stiffness as a function of different growth conditions.

The fundamental difference for this set of experiences is that pure cultures are obtained at least one week after brain dissection. This means that cells are plated on the hydrogel substrates once they have sufficiently proliferated inside PLO coated rigid Petri dishes in DMEMs medium. This point is of importance for its potential influence on the results, in addition to the absence of neurons. On the other hand, this two–step protocol offers two advantages: (i) to control the initial number of glial cells in contrast to experiments performed on mixed cultures, just after dissection (usually polluted with tissue fragments) and (ii) to quantify the percentage of adhesive cells to integrate our previous study on glial cell proliferation in mixed cultures.

Of note, the initial cell density of seeding for pure cultures is reduced to $\sim$30 $cells/mm^2$

(∼150 $cells/mm^2$ for mixed cultures). We tried to work with a similar glial cell density in the two conditions. For that, we took into account that (i) the glial–neuronal cell ratio is close to 2 in the mature brain, and (ii) glial cells represent about the 20% of the cells in the cerebral cortex at 18 days of gestation. This proportion was deduced from the final density of glial cells (after one week of culture) compared to the seeding density of cortical cells and the proliferation rate estimated from Figure IV.3 (i.e. $\sim$ 1.4 per day). This weak proportion of glial cells is coherent with the fact that the burst of glial cell proliferation *in vivo* occurs only after birth.

As for experiments with mixed cultures, we first describe preliminary experiments, that give a first insight of the response to stiffness of glial cells coming from pure cultures. We then further report more systematic quantitative analysis.

Qualitative explorations of glial cells mechanosensitivity on pure cultures

On the basis of the results obtained with mixed cultures (see Figure IV.3), we firstly focused on the conditions of surface functionalization and culture medium that had given the higher rate of proliferation (i.e. FN and DMEMs respectively), to insure good conditions for glial cells to adhere and proliferate.

◊ Fibronectin (FN) coating and culture medium supplemented with serum

First experiments have been performed on "uniform" hydrogels (see Table IV.1 for the nomenclature), as preliminary tests of adhesion to investigate the impact of substrate stiffness on glial cell behavior. These experiments have confirmed the tendency for glial cells to adhere and proliferate preferentially on stiff substrates (Figure IV.12)[5].

▶ Glial cell adhesion and proliferation are influenced by the substrate stiffness

Then, experiments were performed to analyze the mechanosensitivity of glial cells within different chemical environments, using the "target "pattern, as for the study with mixed cultures. The choice to observe glial cell behavior by live–imaging just after cell seeding gave us the possibility to follow step-by-step the evolution of single cells on our substrates. Videomicroscopy observations of the border between a soft and a stiff region suggested that processes of mitosis mainly occur on the stiff side, as illustrated in Figure IV.13[6].

[5] **Details of fabrication, functionalization and culture of the hydrogel.** Exposure time: 10 and 150 s; protocol with dehydration; FN 3.5 $\mu g/cm^2$ during 1 h. Seeding conditions: $\sim$ 15 $cells/mm^2$ in DMEMs culture medium. Young's moduli: $\sim$ 20 and 60 kPa.

[6] **Details of fabrication, functionalization and culture of the hydrogel.** Exposure time: 19.3 s; chrome thickness: 30 nm; protocol with dehydration; FN 3.5 $\mu g/cm^2$ during 1 h. Seeding conditions: $\sim$ 30 $cells/mm^2$ in DMEMs culture medium. Young's moduli: 45 kPa (transparent regions), $\sim$ 1 kPa and $<$ 0.5 kPa (chromed regions, "soft 1" and "soft 2" respectively).

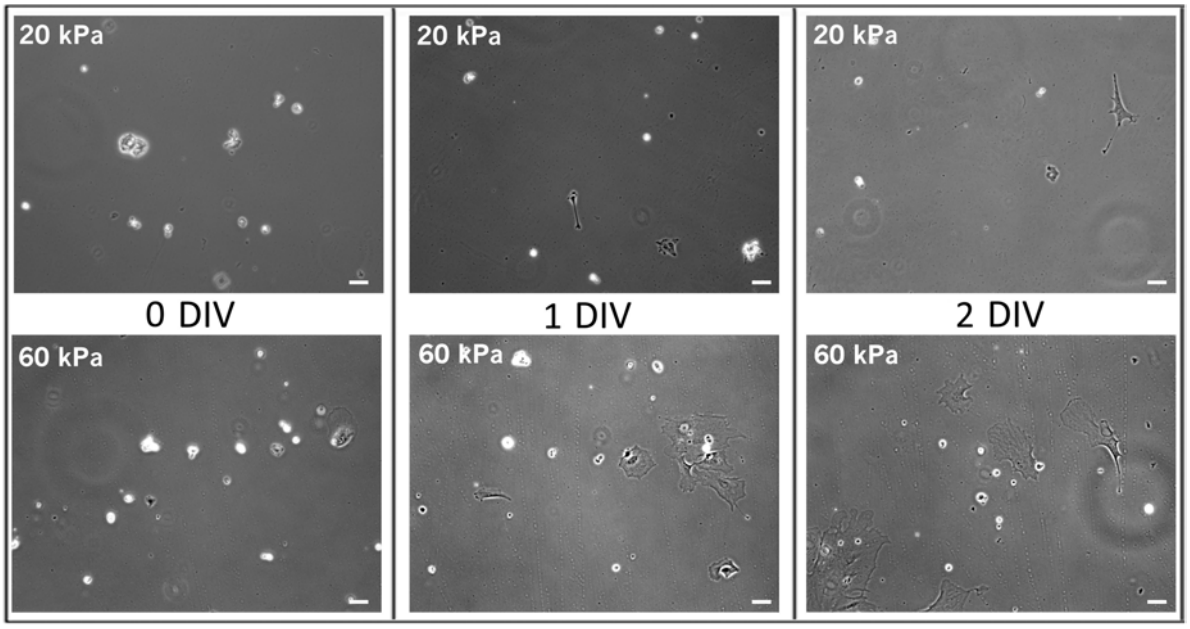

Figure IV.12: **Cortical pure culture on a FN coated "uniform" hydrogels and maintained in the DMEMs culture medium.** Phase contrast images of a glial cell culture on "uniform" gels of 20 kPa (top) and 60 kPa (bottom), showing the tendency to adhere and proliferate more on the stiff substrate. Cells are observed 4 h after seeding, at 1 and 2 DIV (from the left to the right). Scale bars: 50 μm.

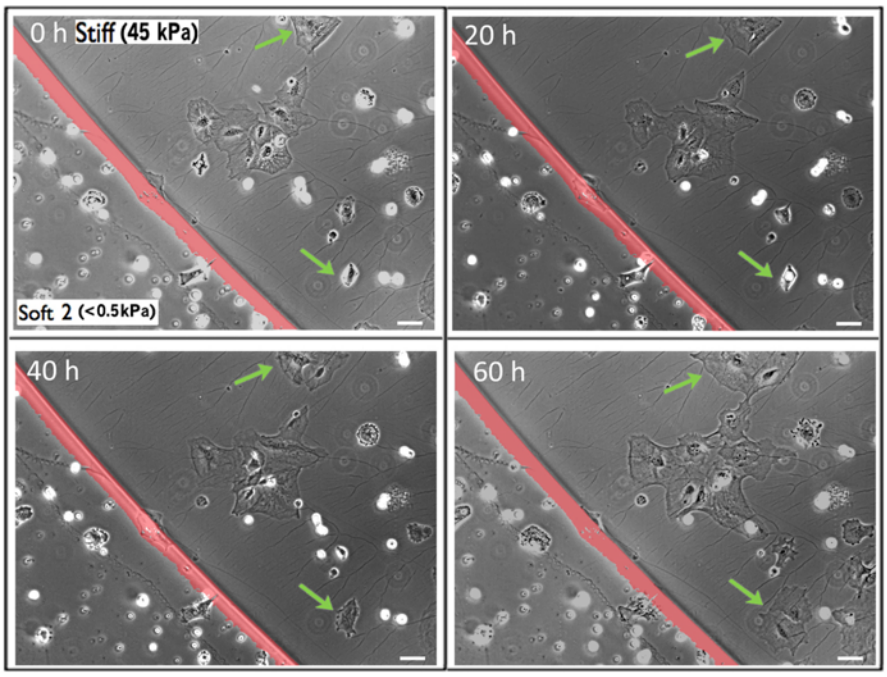

Figure IV.13: **Cortical pure culture on a FN coated "target" hydrogels and maintained in the DMEMs culture medium.** Time–lapse experiment (indicated in hours, "0 h" is 24 hrs after plating) of a glial cell culture at the frontier (red line) between the "soft 2" area (< 0.5 kPa, left of the frontier) and the stiff area (45 kPa, right of the frontier). Green arrows point to cells in phase of mitosis on the stiff region. Mainly rounded cells are present on the soft region. Scale bars: 50 μm.

During two days and a half of observations, very different behaviors have been observed on the two rigidities: glial cells display roundish shapes on soft regions whereas on the stiff areas they spread and can divide. These cellular processes being slow and repetitive, we found more informative to resume our observations at several days interval outside the videomicroscope set–up, typically taking pictures at 7 and 12 DIV (Figures IV.14 and IV.15).

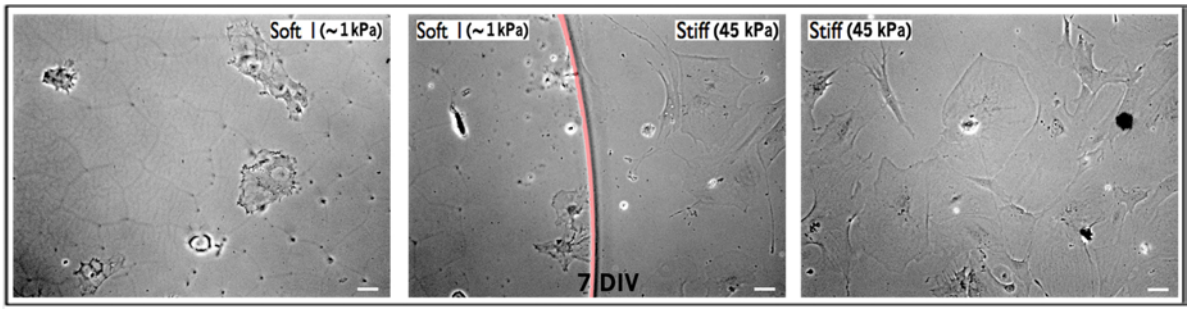

Figure IV.14: **Cortical pure culture on FN coated "target" hydrogels and maintained in the DMEMs culture medium.** Phase contrast images of a glial cell culture at the frontier (red line) between the "soft 1" area ($\sim 1\ kPa$, left of the frontier) and the stiff area (45 kPa, right of the frontier), on the "soft 1" region (left) and the stiff region (right). A higher number of spread cells is present on the stiff regions. Cells are aged of **7 DIV**. Scale bars: 50 μm.

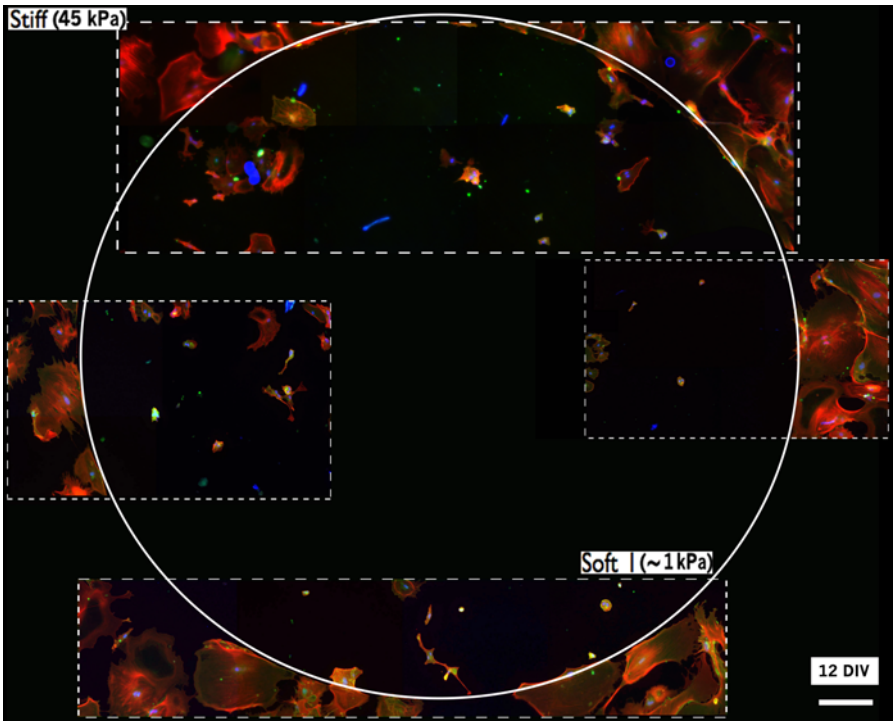

Figure IV.15: **Cortical pure culture on a FN coated "target" hydrogel and maintained in the DMEMs culture medium.** Immunofluorescence images of a glial cell culture at the frontier (solid white line) between the "soft 1" area ($\sim 1\ kPa$, inner region) and the stiff area (45 kPa, external region). Images are delimited by dashed white lines in the corresponding position on a reconstruction of the inner soft region and the surrounding stiff region of the "target" pattern. Few and small cells adhere on the soft region as compared to the numerous and spread cells on the stiff one. Red: phalloidin, actin. Green: N-Cadherin, cell-cell adhesions. Blue: Hoechst, nuclei. Cells are fixed of **12 DIV**. Scale bars: 300 μm.

► **Cytoskeletal organization of glial cell is influenced by the substrate stiffness**

Such a significant difference in terms of adhesion and morphology of the glial cells as a function of the substrate stiffness leads to some inevitable questions about the structure and adhesion of glial cells. Figure IV.15 shows that immunolabeled cells are very spread on the stiff region with respect to the soft one.

A deeper investigation at higher magnification displays that on the soft substrate cells appear generally smaller and isolated, with a disorganized network of actin and a surrounding lamellipodium where focal adhesions (FAs) staining is associated to actin filaments (vinculin labeling, Figure IV.16.A). On the stiff substrate stress fibers are long and cover large portions of the surface, where FAs staining occurs as short segments along the actin filaments (vinculin labeling, Figure IV.16.B). However, no significant differences characterize the intercellular adhesions on the soft (in the rare case where cells are in contact) and the stiff regions (N–cadherin labeling, Figures IV.16.C–D).

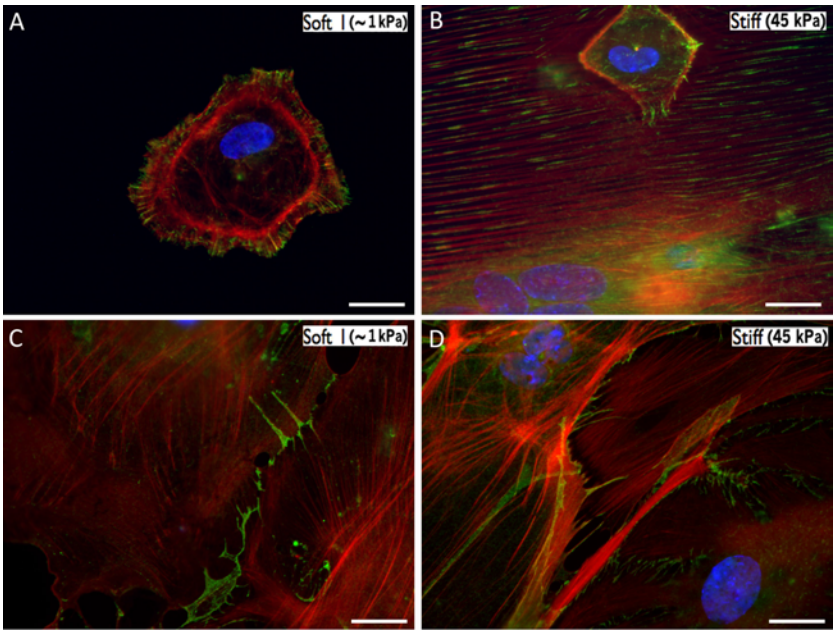

Figure IV.16: **Comparison of the structure and the FAs localization on cortical glial cells on soft and stiff substrates.** Immunofluorescence images of a pure culture at 12 DIV on the "soft 1" area ($\sim 1\ kPa$, A – C) and the stiff area ($45\ kPa$, B – D) of a "target" hydrogel. Red: phalloidin, actin. Green (A – B): Vinculin, FAs. Green (C – D): N-Cadherin, cell-cell adhesions. Blue: Hoechst, nuclei. "target" hydrogel, FN coating, DMEMs culture medium. Scale bars: 20 μm.

These experiments have qualitatively shown that in conditions well-adapted to glial cell development, i.e. a FN coating and DMEMs as a culture medium, stiff substrates promote both glial cell adhesion and proliferation. Moreover, glial cells on the stiff regions display a larger

area of adhesion and significant stress fibers associated to dashed localizations of adhesions to the substrate. To obtain a quantitative description of the cytoskeleton organization and the adhesion site localization as a function of the substrate stiffness, it is necessary to analyse a greater number of images. For that, a combination of rigidity and chemical patterns at the cell level might provide an interesting experimental support. We report now some results about the impact of the chemical environment on the mechanical sensitivity of the glial cells.

◊ **Long pure cultures under four different conditions of molecules of adhesion and culture medium**

Similarly to the experimental procedure followed for the mixed cultures, we perform a quantitative study of the glial cell mechanosensitivity by analyzing the evolution of cell density with time in different cell culture conditions.

For that, we have selected the "target" pattern and we have followed the glial cell adhesion and proliferation during a couple of weeks in different conditions of medium and proteins of adhesion (Table A.3)[7].

We report in Figure IV.17 the cell density over time for different culture conditions and in separate graphs as a function of the substrate stiffness.

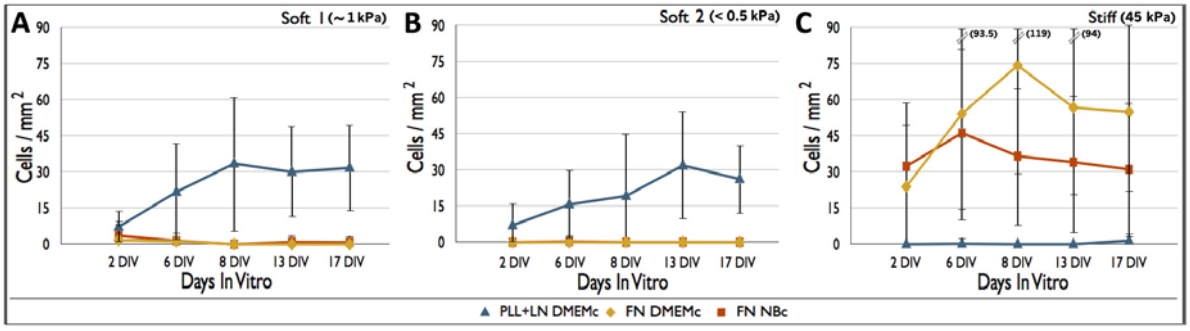

Figure IV.17: **Glial cell density ($cells/mm^2$) in different culture conditions**: PLL/LN or FN coating, DMEMs or NBs culture medium. Cells were observed between 2 and 17 DIV. Evolution over time on the "soft 1" substrate (A, $\sim 1\ kPa$), on the "soft 2" substrate (B, $< 0.5\ kPa$) and on the stiff substrate (C, 45 kPa). Error bars denote SD.

► **Glial cell adhesion is influenced by the substrate stiffness and the adhesive coating**

We first note that at 2 DIV the two soft regions displays equivalent results, showing for all the culture conditions a very low rate of adhesion: this is slightly higher on the PLL/LN coating

[7]**Details of fabrication, functionalization and culture of the hydrogels.** Exposure time: 20 s; chrome thickness: 30 nm; fluorescent microbeads: $\phi = 500\ nm$, 5 $\mu l/ml$, i.e. 0.01% v/v; protocol with dehydration; FN 3.5 $\mu g/cm^2$ (nominal value) during 1 h; PLL 145 $\mu g/cm^2$ during 1 h, LN 1.1 $\mu g/cm^2$ during 1 h. Seeding conditions: $\sim 30\ cells/mm^2$ in DMEMs culture medium, eventually replaced after 24 hrs by NBs. Young's moduli: 45 kPa (transparent regions), $\sim 1\ kPa$ and $< 0.5\ kPa$ (chromed regions, "soft 1" and "soft 2" respectively).

than on the FN one (Figure IV.17.A, B). On the stiff region, the density of adherent cells is equivalent to the initial cell density plated on each hydrogel ($\sim 30\ cells/mm^2$, Figure IV.17.C).

▶ **Glial cell proliferation is influenced by the substrate stiffness and the culture medium**

The culture medium appears crucial to obtain a significant rate of proliferation. Indeed, the Figure IV.17.C shows a constant cell density for the NBs medium condition. The initial concentration is due to the first hours of incubation in the DMEMs culture medium that are required to allow the glial cell adhesion. We thus note that glial cells survive in the NBs culture medium but their proliferation is quite null. Some pictures of glial cells growing in this condition are reported in Figure IV.18 as example.

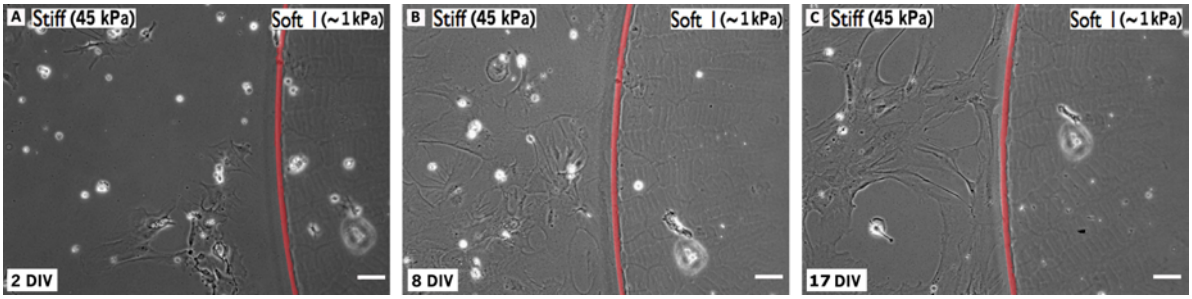

Figure IV.18: **Glial cell culture on a FN coated "target" hydrogel and maintained in the NBs culture medium.** Phase contrast images of the frontier (red line) between the "soft 1" ($\sim 1\ kPa$, right of the frontier) and the stiff (45 kPa, left of the frontier) area at 2 (A), 8 (B), and 17 (C) DIV. Images show the proliferation of glial cells on the stiff side and an apparent saturation of the cell density induced by the getting in touch with very spread cells. Scale bars: 60 μm.

We observe on these pictures that glial cells preferentially attached and then spread on the stiff part of the gel.

▶ **Glial cell mechnosensitivity is influenced by the adhesive coating**

Interestingly, with the DMEMs medium, opposite behaviors are observed depending of the proteins of adhesion, similarly to the results obtained for mixed cultures. On the PLL/LN functionalized hydrogels glial cells slowly proliferate on the soft regions and they do not adhere nor proliferate on the stiff ones (Figure IV.19).

Inversely, on the FN coated substrates glial cells strongly proliferate on the stiff regions whereas soft areas impair both cell adhesion and proliferation (Figure IV.20).

From these observations, we have made the choice to not perform the condition that couples PLL/LN coating with the NBs medium. A nearly null cell adhesion would be expected, as would be the cell proliferation rate.

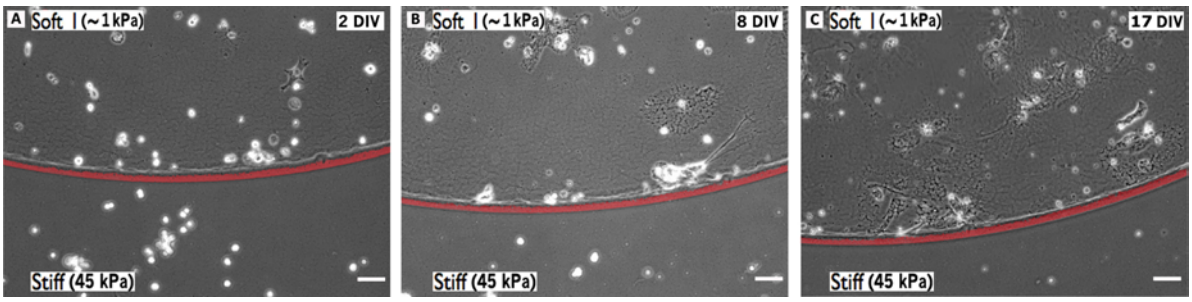

Figure IV.19: **Glial cell culture on a PLL/LN coated "target" hydrogel and maintained in the DMEMs culture medium.** Phase contrast images of the frontier (red line) between the "soft 1" ($\sim 1\ kPa$, top of the frontier) and the stiff (45 kPa, bottom of the frontier) area at 2 (A), 8 (B), and 17 (C) DIV, showing the glial cell proliferation on the soft side. Scale bars: 60 μm.

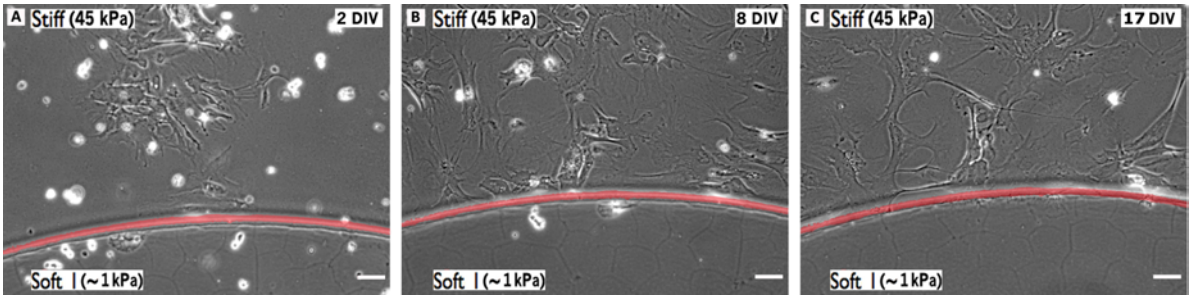

Figure IV.20: **Glial cell culture on a FN coated "target" hydrogel and maintained in the DMEMs culture medium.** Phase contrast images of the frontier (red line) between the "soft 1" ($\sim 1\ kPa$, bottom of the frontier) and the stiff (45 kPa, top of the frontier) area at 2 (A), 8 (B), and 17 (C) DIV, showing the glial cell proliferation on the stiff side. Scale bars: 60 μm.

IV.1.4 Discussion about glial cell mechanosensitivity in mixed and pure cultures

Let us remark that the main difference between the experiments employing mixed and pure cultures is a lower rate of proliferation in the second case. This point is highlighted both quantitatively by the graphs showing the cell density (Figure IV.3 and IV.17) and qualitatively by the absence of detachment from the surface of the layer of confluent cells, that was observed in the experiences with mixed cultures (Figure IV.2 and Table IV.2). We compare the behavior of cells growing on the stiff regions coated with FN and cultured in the DMEMs medium in the two experimental conditions. Interestingly, the cell density in the experiments with mixed cultures achieves a saturation level of confluence around a value of 350 $cells/mm^2$ followed by a cell detachment from the surface (Figure IV.3). In the case of pure cultures, cells are very spread and can therefore approach a confluence stage where cells cover almost the entire surface with a density of only $\sim$ 100 $cells/mm^2$ (Figure IV.17). This high spreading seems to be associated within an inhibition of cell proliferation, coupled to a rearrangement on the surface without significant change in the total number of cells, as suggested by the observations of the same regions over the time where the cell density can locally decrease without that the total cell density measured on the hydrogel changes (Figure IV.20.B–C). Therefore, is the

detachment phenomenon caused by a cell density at confluence above a certain threshold? We have investigated this phenomenon by confocal imaging but deeper analyses are required to give a definitive explanation for the detachment occurring after at least one week of culture. We display some examples recorded with a confocal microscopy of samples where this phenomenon has occurred or not (Figure IV.21).

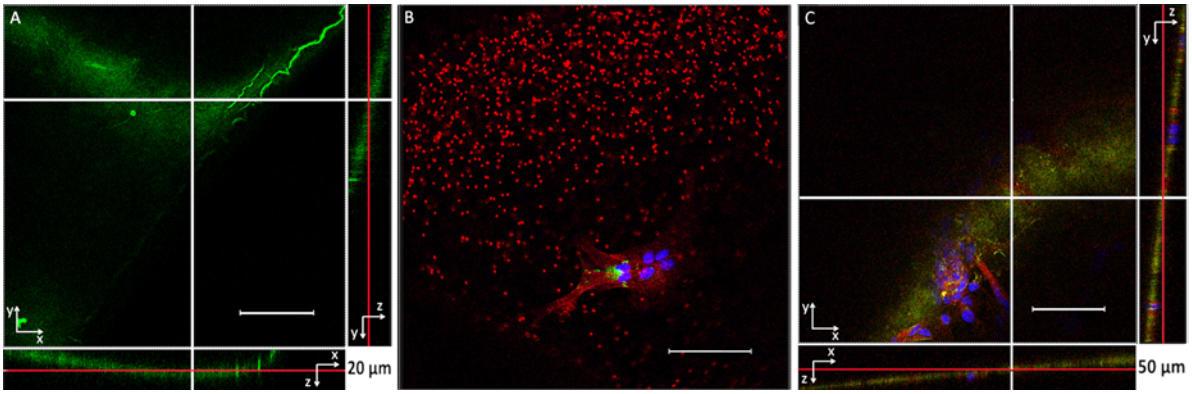

Figure IV.21: **Confocal images of hydrogels functionalized with FN and kept in culture during 21 DIV in the DMEMs medium.** The images represent the plan xy and the relative projections yz (right) and xz (bottom). A) Portion of a stiff region showing a typical inclination in the case of cell detachment, suggesting an upthrust of the entire gel surface. B) Portion of a stiff curved surface showing a cell on a different plane than the close gel surface. The surface of the gel is represented by the layer of fluorescent red microbeads. C) Glial cells on a sloping but flat portion of a stiff region showing the case of a entire tilted sample without the detachment phenomenon. Green: α–FN, surface coating. Red: phalloidin, actin. Blue: Hoechst, nuclei. Step between two consecutively z slices: 0.8 μm. Scale bars: 80 μm.

By the observation of the fluorescence of the proteins of adhesion coating the hydrogel surface (IV.21.A, C) and of microbeads embedded into the hydrogel (IV.21.B), the cell detachment phenomenon does not seem be a local phenomenon: an entire upper portion of the hydrogel detaches with the cell layer. These observations might suggest that, when cell confluence occurs, the cell layer deforms sufficiently the gel so that it comes off with the cells, inducing its detachment from the glass coverslip. However, this detachment might be a result of an association of different effects still not completely understood and the very high deformations observed by phase contrast imaging are too important to be deeply analyzed by confocal microscopy.

On the same gel, the cell detachment has always been observed to start on the stiff regions where the cells are the first to reach confluence. Rather, as detachment was observed in all experiences performed with mixed cultures[8] but only in one sample in pure culture conditions[9],

[8]Phenomenon observed on a total of six samples functionalized with FN and maintained in DMEMs culture medium, with different patterns (homogenous, double stiffness and circular) and fabricated for three different cultures performed in a window of time of eight months.

[9]Total of four samples with the circular pattern functionalized with FN and maintained in DMEMs culture medium, fabricated for two different cultures performed in a window of time of four months. The detachment

although the same protocol and the same culture duration were performed[10], the nature of cell-cell interactions might be involved.

The medium has been identified as the necessary element for glial cell proliferation. Glial cell favorable medium (DMEMs, a medium supplemented with serum) concomitantly suppresses neuronal cell growth. For this reason, the higher proliferation rate observed in the mixed cultures compared to the pure ones,might be more justified by the difference in steps of glial cell plating in the two situations than by the presence of neurons. Indeed, the cultivation during a week of glial cells in Petri dishes to promote their growth and to suppress neurons, might reduce their capability to proliferate. Of note, technical problems linked to the effective concentration of FN that is grafted to the surface have not allowed to achieve parallel (i.e. in identical conditions) experiments with mixed and pure cultures In DMEMs medium. This experiment should be repeated again to get a finer quantitative comparison between the results obtained on pure and mixed glial cell cultures with identical FN coating.

The interaction between glial and neuronal cells therefore needs more investigations in order to elucidate if the presence of neurons plays a role in the functions supplied by glial cells, and in association, if it changes the mechanosensitivity of glial cells.

An alternative solution to analyze the influence of neurons on the glial cell proliferation might be to use two different substrates, one with neurons alone and another without, and to plate glial cells on both. The comparison of the glial cell proliferation in both cases would be very informative. To keep neurons alive, it could be useful to cultivate cells in the MEMs medium, a medium observed to be less harmful for neurons (also less adapted for glial cells) supplemented with the serum necessary for the glial cell proliferation. We have also observed that the PLL/LN coating is more adapted to neurons as compared with the FN functionalization, that is better for glial cells. Thus, mixing FN and LN as surface coating might be a compromise to achieve acceptable culture conditions for both neurons and glial cells.

Nevertheless, despite their limitations, these experiments showed that glial cells maintain their mechanosensitive properties independently of their history after dissection, i.e. for mixed cultures directly extracted from the brain or for pure cultures obtained after a step of preliminary *in vitro* culture.

phenomenon has been observed on only one sample, not shown in the results because failed from a point of view of cell adhesion. We consider important to report this unique case, even if probably fabrication problems (silanization, polymerization, ...) have occurred for this sample.

[10]Phenomenon never observed for a total of sixteen samples (double stiffness and circular patterns, five cultures on a window of time of eleven months), cultured for the same time duration of the sample in the condition of DMEMs culture medium with FN coating but in NBs and functionalized with PLL/LN or FN coatings or in DMEMs functionalized with PLL/LN.

IV.1.5 Mechanical constraints at the cell level

In the previous sections we have demonstrated that the sensitivity of glial cells to the mechanical properties of their environment is strongly influenced by the chemical culture conditions. We have reported a significant change of adhesion and proliferation between stiff substrates (Young's modulus of several tens kPa) and soft substrates below a threshold of stiffness (i.e. below a Young's modulus $\sim$ 1 kPa). We have also observed that above this approximate threshold of 1 kPa, cell response keeps similar whatever the rigidity, but is accelerated by increased rigidity (from few tens of kPa to 100 kPa). This raises the following issue: are these behaviors maintained also when cells are forced to encounter a stiffness gradient at the scale similar to their size? To answer to this question, we analyze now the glial cells behavior on the "stripes" pattern, i.e. on hydrogels where the alternation of soft and stiff regions takes place on the spatial scale of the cell size.
Some preliminary experiments have been necessary to optimize the chemical functionalization on this kind of pattern in order to obtain a concentration of adhesive molecules independent of the rigidity and, consequently, to keep the substrate stiffness as the only control parameter. We report in Figure IV.22 the most significant results of glial cells growing on this pattern during the first hours after plating[11].

► **Glial cell mechanosensitivity revealed at cell level in pure cultures**

We note that glial cells adapt their morphology to follow and to find contacts with the stiff stripes, confirming the previous results obtained on larger stiff and soft regions. Different shapes are observed as a function of the width of the stripes. Interestingly, glial cells are able to proliferate on this kind of substrate. Performing other experiments on stripes with higher gradients of stiffness, i.e. stripes with a greater difference between the stiff and the soft values, might give the possibility to explore some issues: (i) could a total confinement be obtained within a stiff stripe? (ii) Is there a threshold of width above which glial cell adhesion is suppressed on soft stripes? (iii) Could glial cells proliferation occur on constrained adhesion conditions given by stiff stripes? More experiments should be also performed to investigate the localization of the adhesive contacts of glial cells on this kind of substrate and to deeper investigate the dependence of the cellular shape with the width of the stripes.

► **Investigation of the hydrogel topography**

Finally, some observations using a confocal and a digital holographic microscopes have been made in order to investigate if the variation of rigidity was associated to a difference of topography. This might have some eventual impacts on the results just discussed above (Figure IV.23).

[11] **Details of fabrication, functionalization and culture of the hydrogels.** Exposure time: 20 s; chrome thickness: 15 nm; protocol with dehydration; FN 3.5 $\mu g/cm^2$ during 1 h. Seeding conditions: $\sim$ 30 $cells/mm^2$ in DMEMs culture medium. Young's moduli: $\sim$ 40 kPa (transparent stripes), $\sim$ 10 – 20 kPa (chromed stripes).

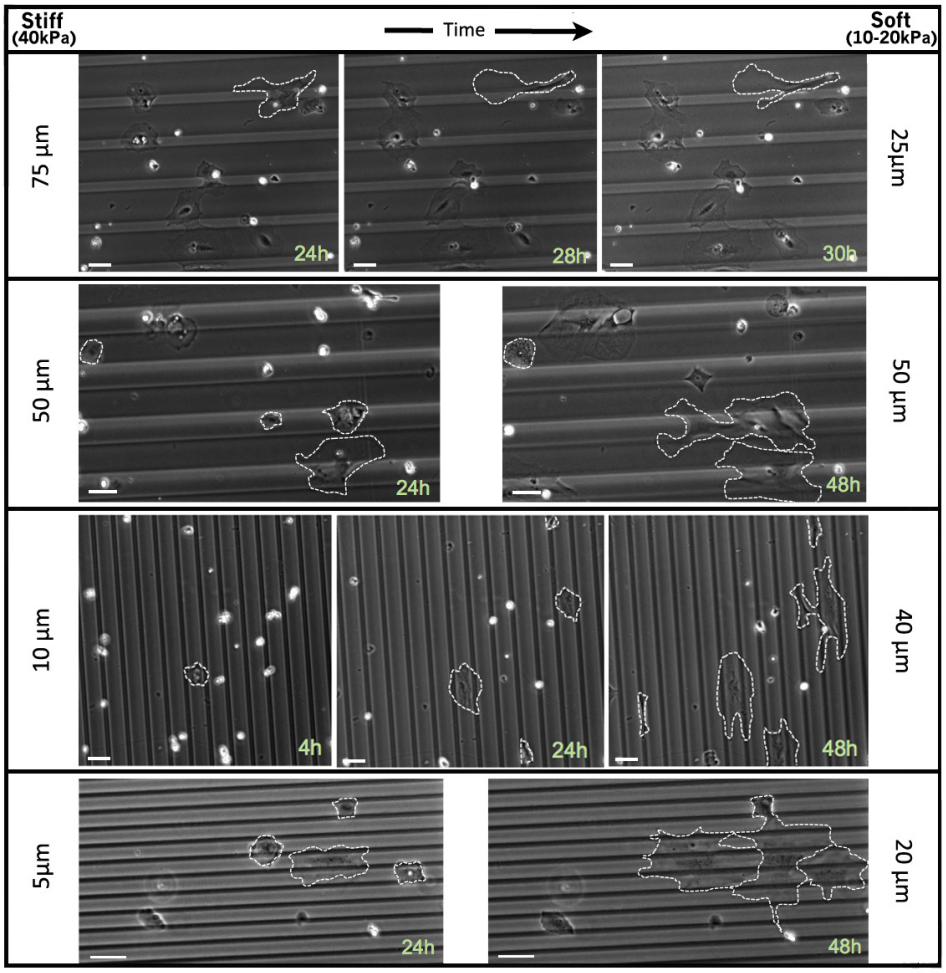

Figure IV.22: **Pure cortical culture on FN coated stiff/soft alternate "stripes" in hydrogels and maintained in DMEMs culture medium.** Time–lapse experiment (indicated in hours, 0 h being the seeding time) of a glial cell culture on stripes of different rigidities and widths. Widths of stiff (darker stripes, $\sim$ 40 kPa depending on the size) and soft ($\sim$10 – 20 kPa depending on the size) areas are reported respectively on the left and on the right of the images. The images selected here show the cell alignment with the stiff stripes. Scale bars: 50 μm.

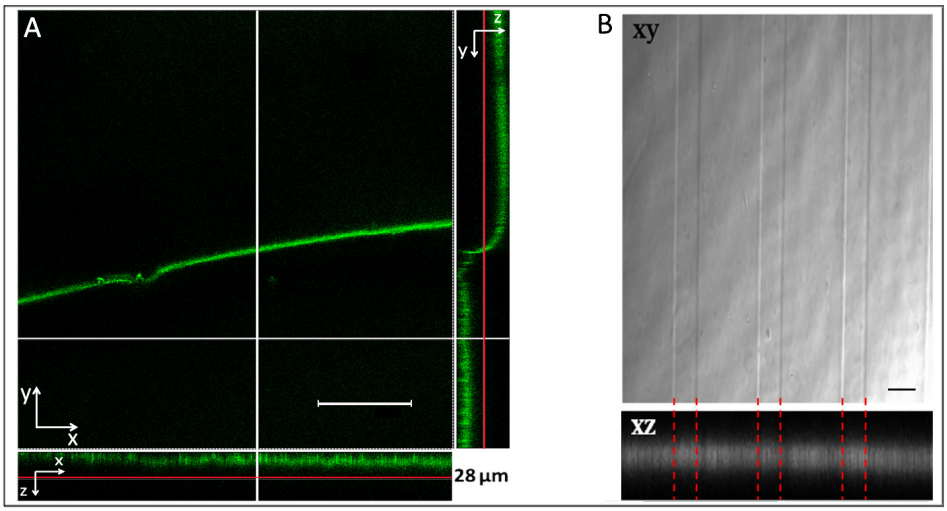

Figure IV.23: **Analysis of the topography of "target" and stiff/soft alternate "stripes" hydrogels by confocal microscope.** A) Confocal image of a "target" hydrogel functionalized with FN and kept in culture during 21 DIV in the NBs medium. The images represent the xy view and the relative projections yz (right) and xz (bottom), showing the frontier between the stiff (45 kPa, top of the frontier) and soft ($\sim$ 1 kPa, bottom of the frontier) region of a "target" pattern. Green: α–FN, surface coating. Step between two consecutively z slices: 0.3 μm. Scale bar: 80 μm. B) Differential interference contrast (DIC, top, xy view) and confocal (bottom, xz view) images of a "stripes" hydrogel functionalized with FN. The dashed red lines delimit the frontier between stiff (40 kPa, narrow stripes) and soft ($\sim$ 12 kPa, wide stripes) showing the absence of topography at the surface of this hydrogel. Scale bar: 30 μm.

These images show that during the hydrogel fabrication variation of stiffness can be associated to variation of gel thickness. We have observed that the difference of height between areas of different rigidities could be reduced by a slow demolding of the mask (Figure IV.23.B). Therefore, the amplitude of the topographical effect can slightly change from one sample to another. However, in particular when the difference of stiffness from two regions is quite high, it is very difficult to completely eliminate topography (Figure IV.23.A).

Cells can be observed to align their morphology along the frontiers, suggesting a sensitivity to high gradients of rigidity or maybe to the topography. Gel topography scales either at the nanoscale (gels are porous materials) and at the micrometer scale when mechanically patterned. In order to get preliminary insights on the impact of topography on glial cell adhesion, we addressed this issue by looking at the effect of a topography at a sub-micrometric scale on an infinitely rigid surface. We will discuss some exploratory experiments concerning this last aspect in the next section.

IV.2 Glial cells sensitivity to the substrate topography

We have reported in the previous sections different approaches and configurations in order to shed light on the sensitivity of glial cells to the stiffness of their environment. Cells can be observed to align their morphology along the frontiers, suggesting a sensitivity to high gradients of rigidity or to the topography. We present here some preliminary experiments to approach this issue.

We have adopted a micropatterning technique by photolithography to obtain topographical patterns (i.e. grooves) on glass coverslips in controlled conditions (see Figure II.14). The parameters taken into account were the influence of the topography alone or coupled with the surface chemistry, i.e. within uniform coating conditions or a chemical functionalization restricted to the bottom and edges of the grooves (i.e. "in-groove patterning"). Firstly, we have not observed any differences on the glial cells response to the topography in a range of PLO concentration between 2 to 12 $\mu g/cm^2$. Thus, we have chosen a concentration of 3.6 $\mu g/cm^2$ for the ensemble of the experiments and the Table IV.3 illustrates some representative exemplars for the most significant experimental conditions.

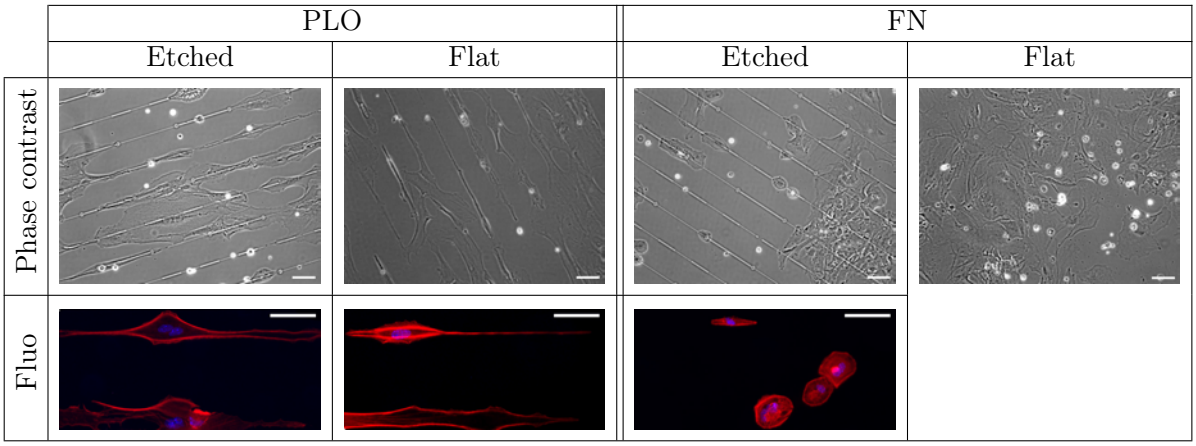

Table IV.3: **Glial cell response to the surface topography compared to flat substrates.** Phase contrast and fluorescence images of cortical pure glial cell cultures on chemical and physical patterns (i.e. "in-groove patterning" condition, 90 nm, "Etched" column) or chemical patterns alone ("Flat" column) of different proteins of adhesion: PLO coating (3.6 $\mu g/cm^2$) or FN coating (0.3 $\mu g/cm^2$) in DMEMs culture medium. Cells are fixed at 4 DIV. Etched patterns are represented by the light grey regions in phase contrast images. The same pattern design has been employed for chemical patterns on "Flat" substrates and the stripe geometry is recognizable by the glial cell shape in parallel lines. Red: Phalloidin, actin. Blue: Hoechst, nuclei. Scale bars: 50 μm.

▶ Morphology of glial cells from pure cultures is more influenced by the adhesive coating than by topography

We observed no significant difference between flat or etched substrates ("in-groove patterning" condition): in both cases, glial cells are only partially restrained into the PLO patterns. Differently, on FN patterns, glial cells are not at all restrained by the chemical contrast of adhesion

and are only slightly sensitive to the etched patterns. For this reason, we adopted the PLO coating in the following experiments.

Then, we have investigated the influence of the pattern depth, with or without the coupling with the chemical confinement. Again, the Table IV.4 illustrates some representative exemplars for the most significant experimental conditions.

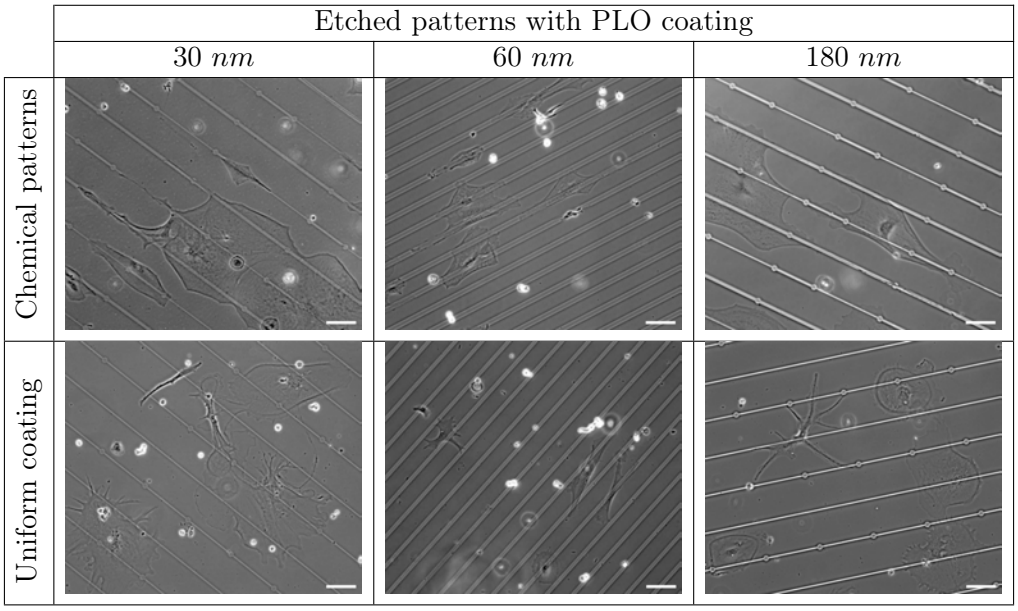

Table IV.4: **Glial cell response to the surface topography coupled or not with chemical patterns.** Phase contrast images of cortical pure glial cell cultures on physical coupled chemical patterns ("Chemical patterns" row) or physical patterns with uniform chemical coating ("Uniform coating" row) of different depths. PLO coating in DMEMs culture medium (cell passaging 1 for 60 nm patterns and cell passaging 3 for 30 and 180 nm, 2 coverslips for each condition). Cells are fixed at 2 DIV. Etched patterns are represented by the light grey regions. Scale bars: 50 μm.

The comparison between patterns of different depths between a few tens to a few hundreds of nm has not given significantly different cell responses ("Chemical patterns" condition, Table IV.4). The comparison between uniform or patterned adhesive coatings has shown that chemistry plays the highest role in the cell sensitivity to the microstructuration of the surface. Indeed, cells grow almost completely unrestrained on uniform grooved functionalized substrates ("Uniform coating" condition, Table IV.4).

To conclude concerning the glial cell sensitivity, these experiments have shown that in the range of pattern depths observed (between some tens to some hundreds of nm) the chemical confinement is more effective than the topographical one.

These experiments are far to be complete and would require complementary observations, e.g. increasing the depth of the patterns and checking by immunofluorescence that the adhesive molecules do not concentrate on the edges of the grooves. However, microfabrication techniques applied to hard substrates, like glass, are time consuming and the etching profiles are less

controlled, as we have discussed in the dedicated section on the second chapter (II.1.2.1). It would be interesting to switch to PDMS substrates to study the effects of topography.

IV.3 Discussion

In this chapter we have reported our results about glial cells sensitivity to the mechanical properties of their environment. In particular, we have analyzed their response to stiffness on polyacrylamide hydrogels. The employed technique is based on hydrogel photopolymerization that gives the possibility to create elastic patterns with a micron–scale resolution.
This set of experiments has highlighted the potential of the photopolymerization technique for the hydrogels fabrication, giving the possibility to simultaneously observe cell behavior on stiff and soft regions, under identical culture conditions. Moreover, we have shown that the number of frontiers between two regions can be increase by the geometrical design in order to obtain statistically robust results. Doing so, the reduction of the number of required samples is an advantage to take into account.
We have investigated cell adhesion and proliferation on different configurations of pattern size and design as well as on different culture conditions.

These experiments have allowed to quantify glial cell response to the stiffness as a function of the culture medium and the molecules of adhesion bound to the surface.

▶ **Glial cell mechanosensitivity and culture medium**

In both situations of mixed and pure cultures, the proliferation rate is enhanced on stiff substrates and favored by the DMEMs medium, that proved to constitute the major element required for glial cell proliferation. Glial cell proliferation has been observed in NBs culture medium only on substrates of several tens of kPa. The most evident difference between NBs and DMEMs medium is the presence of the serum. Therefore, it should be interesting to repeat the experience with NBs supplemented with serum in order to confirm the critical role played by the serum in the glial cell proliferation. Doing so, the serum influence on neuron survival would be also tested.

▶ **Glial cell mechanosensitivity and molecules of adhesion**

It has been confirmed by several experiments that the strongest rate of proliferation occurs with the combination of the following conditions: stiff substrate, fibronectin (FN) coating and DMEMs medium. Contrarily, still in DMEMs medium, poly–L–lysine and laminin (PLL/LN) coating seems to promote glial cell proliferation on soft regions. In this case, the proliferation rate was lower compared to the rate observed on stiff regions functionalized with FN.

Importantly, these results need to be confirmed after an optimization of the protocol of functionalization in order to guarantee a uniform distribution of the bound molecules of adhesion on the surface, as already done for FN. Indeed, if our current protocol leads to a higher density PLL/LN molecules on soft regions, it may explain the glial cell proliferation on these regions compared to the absence of cells on stiff ones in pure cultures. However, in mixed cultures we have observed a lower, but not nul, concentration of glial cells on stiff regions than on soft ones. This confirms the glial cell tendency in these culture conditions to proliferate more on soft regions. On the other hand, it expresses a certain variability in the results that would support the hypothesis of a not well reproducible functionalization with the PLL/LN coating. An other explanation is that the irregular density of LN that we observed locally at the cell level occurs independently of the mechanical properties of the hydrogel, this may means that on soft region glial cells are able to secrete the necessary proteins to supply the irregular chemical environment. This could explain the cell behavior that we have observed. Moreover, analyses by confocal microscope showing high and irregular concentration of LN on soft regions close to cells seem to confirm this hypothesis. More analysis of the secretion of LN and FN from glial cells on these coatings and in according to the substrate stiffness might contribute to the understanding of this issue. In experiments with pure cultures, we have observed a higher rate of adherent cells at 2 days *in vitro* on soft regions compared to the quasi absence of adhesion on stiff ones, that might be an element in favor of a higher concentration of adhesive molecules on soft areas since the cell seeding step. However, the two hypothesis are still an open question to explore.

A factor to investigate in order to better elucidate the results obtained with the PLL/LN coating, is the role of the PLL and the LN interaction with the glial cells. Some experiments with the only PLL functionalization might confirm that (i) PLL alone is not a good candidate for the glial cell adhesion and proliferation and that (ii) a PLL (or poly–ornithine) uniform coating is necessary to guarantee a consequent homogeneous binding of the proteins of adhesion, such as LN.

All these observations also suggest that the glial cell adhesion and proliferation, and thus the sensitivity to the substrate stiffness, might be dependent on the concentration of the proteins of adhesion. To verify this hypothesis, some supplementary experiments should be performed to probe the effect of the density of proteins grafted at the surface. If this assumption is confirmed, an analysis from a molecular point of view would be required in order to highlight the mechanisms at the basis of cell response to the mechanical-chemical properties of the ECM.

▶ Glial cell mechanosensitivity and neurons

An important factor to keep into account when analyzing the glial cell interaction with its ECM is the presence of neurons. From this study, it seems that neurons do not play a significant

role in glial mechanosensitivity. Similar results have been obtained both in mixed and pure cultures of glial cells, apart from the only condition where neurons were significantly maintained in culture (PLL/LN coating in NBs medium, i.e. the worst environment for glial cells). In this culture condition let us note that neurons have displayed only a slightly higher cell density on the soft regions than on the stiff ones. For chemical environments scarcely adapted for neuronal survival, glial cells seem thus to play a role of physical support for neuron growth. This was not the case for glial cells, which behavior follows the same tendency in presence or not of neurons.

These observations suggest the existence of a bi-univocal interaction between neurons and glial cells that might mainly depend on chemical rather than on mechanical environment.

By performing some co–cultures of neurons and glial cells, it would be possible to deeper explore this issue. For example, neurons could be added in high concentrations once glial cells are already adherent, in order to not compromise the neuron survival if the substrate coating is not adapted for neurons. Inversely, glial cells could be plated on a neuronal cell culture where neurons have been isolated in a given region: will glial cells adhere more on soft, stiff areas or in the area in presence of neurons?

These configurations just proposed might be more pertinent considering the 3D *in vivo* glial/neuron organization within brain. With this point of view, it would be interesting to investigate if the proliferation of glial cells depends on their localization in brain, according to their local specific functions.

▶ **Glial cells and topography**

Finally, our study has been completed with some preliminary results about glial cell sensitivity to the substrate topography. Grooves in the order of some hundreds of nanometers have displayed no significant influence on glial cell growth. Nevertheless, cultures on deeper topography should be performed to explore the possible existence of a threshold of sensitivity to substrate topography.

▶ **Isolated glial cells and aggregates**

Finally, a fine analysis of the response of glial cells to the properties of their environment should also require to study the influence of cell concentration, in order to distinguish between the behavior of isolated cells and of aggregates. Indeed, the intracellular interactions in aggregates could interfere in the interpretation of results.

Bibliography

[1] Penelope C Georges and Paul A Janmey. Cell type-specific response to growth on soft materials. *Journal of Applied Physiology*, 98(4):1547–1553, 2005. 76, 180

[2] Benoit Ladoux and Alice Nicolas. Physically based principles of cell adhesion mechanosensitivity in tissues. *Reports on Progress in Physics*, 75(11):116601, 2012. 180

[3] Amit Gefen and Susan S Margulies. Are in vivo and in situ brain tissues mechanically similar? *Journal of biomechanics*, 37(9):1339–1352, 2004. 32, 180

[4] Frank Xue Jiang, Bernard Yurke, Rene S Schloss, Bonnie L Firestein, and Noshir A Langrana. Effect of dynamic stiffness of the substrates on neurite outgrowth by using a dna-crosslinked hydrogel. *Tissue Engineering Part A*, 16(6):1873–1889, 2010. 180

[5] Yun-Bi Lu, Ianors Iandiev, Margrit Hollborn, Nicole Körber, Elke Ulbricht, Petra G Hirrlinger, Thomas Pannicke, Er-Qing Wei, Andreas Bringmann, Hartwig Wolburg, et al. Reactive glial cells: increased stiffness correlates with increased intermediate filament expression. *The FASEB Journal*, 25(2):624–631, 2011. 33, 180

[6] Daniel Koch, William J Rosoff, Jiji Jiang, Herbert M Geller, and Jeffrey S Urbach. Strength in the periphery: growth cone biomechanics and substrate rigidity response in peripheral and central nervous system neurons. *Biophysical journal*, 102(3):452–460, 2012. 147, 148, 153, 180

[7] Penelope C Georges, William J Miller, David F Meaney, Evelyn S Sawyer, and Paul A Janmey. Matrices with compliance comparable to that of brain tissue select neuronal over glial growth in mixed cortical cultures. *Biophysical journal*, 90(8):3012–3018, 2006. 33, 34, 76, 180

[8] Shantanu Sur, Christina J Newcomb, Matthew J Webber, and Samuel I Stupp. Tuning supramolecular mechanics to guide neuron development. *Biomaterials*, 34(20):4749–4757, 2013. 33, 34, 180

[9] Lisa A Flanagan, Yo-El Ju, Beatrice Marg, Miriam Osterfield, and Paul A Janmey. Neurite branching on deformable substrates. *Neuroreport*, 13(18):2411, 2002. 33, 180

[10] Pouria Moshayedi, Luciano da F Costa, Andreas Christ, Stephanie P Lacour, James Fawcett, Jochen Guck, and Kristian Franze. Mechanosensitivity of astrocytes on optimized polyacrylamide gels analyzed by quantitative morphometry. *Journal of Physics: Condensed Matter*, 22(19):194114, 2010. 34, 180

[11] Chao-Min Cheng, Philip R LeDuc, and Yi-Wen Lin. Localized bimodal response of neurite extensions and structural proteins in dorsal-root ganglion neurons with controlled polydimethylsiloxane substrate stiffness. *Journal of biomechanics*, 44(5):856–862, 2011. 33, 180

Conclusions and perspectives

The research work of this PhD thesis has focused on the study of the response of primary brain cells to chemical and physical cues of their *in vitro* microenvironment.

This work has been achieved in a context where high technological tools from microelectronics field were available. In parallel, various collaborations with cell biologists have nourished our work and have provided the fundamental competences required to conduct this study.

Brain cells exhibit a large variety of morphologies according to their localization, their function in the brain and eventually their pathologies. The purpose of this PhD thesis was therefore to investigate the interplay between shapes and functions.

We have explored neuronal and glial cell growth in *in vitro* controlled microenvironments with the aim to investigate how chemical and physical constraints can modify cell development. Employing technologies from the microelectronics, such as lithography, we have achieved the fabrication of chemical, structural or elastic patterns at the micron scale of cells. In this way, we have reached a reliable and reproducible control of some properties of the *in vitro* environment, like chemistry, rigidity or topography, giving access to the analysis of specific aspects of cell growth. For example, elongation and polarization in the case of neurons, and adhesion and proliferation in the case of glial cells.

Isolated neurons under chemical constraints

Well-reproducible experiments have been performed with hippocampal neurons of mouse embryos. Robust results have been obtained on isolated cells growing on chemical patterns, giving the possibility to quantify the neuronal response to morphological contraints. Our geometrical approach has revealed that a single morphological parameter like the neurite width can direct the complex process of neuronal polarization. Indeed, the control of the neurite width results in the modulation of the neurite length, leading to a modulation of the polarization rate and of the localization of axonal specification. This study has also showed that the kinetic of neuronal polarization is accelerated when providing to the cell an initial morphological asymmetry and that, unlike to what occurs in conventional *in vitro* preparations, a deterministic and not a probabilistic localization of the axon could be achieved. Moreover, this

study has shown that changing the neurite elongation is not associated to a conservation of the adhesive surface. Some explorative experiments have been conducted to investigate volume conservation, showing that this 3D parameter in neurites is not systematically controlled by the neurite width. Further quantitative analyses of the dependence of the neuronal volume in association to 2D morphological constraints will be the object of forthcoming researches in our group.

Some mechanisms at the origin of these results have been addressed. For instance, the dynamical properties of propagative growth cone like structures named waves and produced during neuronal growth and polarization stages have been investigated. These structures, previously reported in the literature, were still poorly analyzed. This work have allowed to reinforce the association between waves and neurite elongation. The influence of the neurite width on the dynamical properties of waves, such as frequency of emission and their velocity, has been showed.

Our studies have led to a few models supporting the dependence of neuronal elongation and wave emission on neurite width. We have provided a phenomenological framework of waves as a basis for future molecular studies. Some preliminary investigation of the elements constituting the cytoskeleton, such as actin, microtubules and associated proteins, have showed some similarities between the molecular composition of waves and growth cones. A mechanism involving both molecular motors along microtubules and actin polymerization at the basis of the wave propagation is not excluded. Eventually, we propose some new perspectives to investigate this issue:

- ▷ The elucidation of the role played by centrosome in microtubules polarization related to wave emission.
- ▷ Observations at high resolution of actin filaments in waves. This might give important information about their dynamics and structure.
- ▷ Deeper molecular analyses employing some drug treatments might highlight which components are essential for wave formation and propagation. Examples of drugs: blebbistatin, a myosin II inhibitor, latrunculin B or nocodazole, that respectively depolymerize actin and microtubules, taxol, a microtubule stabilizer, or formin, a molecular motor inhibitor (for example, it has been reported in the literature that nocodazole occasionally induces a reversal of the direction of wave propagation before a systematic disorganization of wave structure and its collapse (Ruthel et al., 1998)).

Finally, a possible role of wave in axonal branching is suggested by the observation reported in literature that the inhibition of doublecortin, a protein that colocalizes with microtubules and observed within waves, delays collateral branching in hippocampal neurons and also decreases the wave frequency (Tint et al., 2010).

The combination of these molecular approaches with our control of the neuronal morphology

might enrich and promote the understanding of these complex issues related to neuronal growth and polarization.

Neuronal and glial cells under mechanical constraints

Little is currently known about the mechanical properties of the physiological environment of brain cells.

We have focused our study on glial cell response to mechanical stimuli. We have shown that mechanosensitivity of glial cells depends on the chemistry of their environment. We have employed elastic patterns to achieve a systematic analysis of their adhesion and proliferation according to the chemical properties of their substrate and of the medium employed to maintain them in *in vitro* culture. Chemistry represents a critical element for neuron growth too, but no remarkable mechanosensitive response has been observed. The presence of neurons does not seem to have a significant influence on glial cell mechanosensitivity.
Varying the sizes of rigidity patterns has given access to a multiscale analysis, from isolated cells to more collective configurations (both with glial cells alone and in interaction with neurons). As the best chemical conditions were not the same for neuronal and glial cells, some possible ways to deeper investigate how the mechanosensitive response of glial cells is influenced by the interplay between these two kind of cells in mechanosensitivity has been discussed.

This study represents a first step toward a quantitative investigation and dissection of the different elements attending glial cell dependence on the mechanical properties of their environment.

In conclusion, we have probed neuronal and glial cell growth with novel experimental set-ups that allow to select specific cell behaviors in controlled microenvironments and to emphasize key elements having a major role in their growth. These insights might also contribute to envision new experimental systems to study brain cell behavior, for example, leading to controlled *in vitro* colocalizations of glial and neuronal architectures.

An approach towards 3D systems, in particular for glial cells, should be considered in the future to get closer the heterogeneous 3D microenvironment of cell *in vivo*. Some methods to achieve 3D environments have been very recently developed (Tian et al. 2012, Dana et al. 2014) but they are still scarcely mastered. When mature, these techniques, coupled to the outcomes of 2D studies, appear as promising tools to meet the needs in the field of neuroscience that take place at different levels, from the most fundamental basics of neurobiology to medical applications.

Conclusions et perspectives

Les travaux de recherche de cette thèse ont porté sur l'étude de la réponse des cellules primaires du cerveau à des signaux chimiques et physiques de leur microenvironnement *in vitro*. Ce travail a été réalisé dans un contexte où des outils technologiques issus de la microélectronique étaient disponibles. En parallèle, diverses collaborations avec des biologistes cellulaires ont nourri notre travail et ont fourni les compétences fondamentales nécessaires pour mener cette étude.

Les cellules du cerveau présentent une grande variété de morphologies en fonction de leur localisation, leur fonction dans le cerveau et, éventuellement, leurs pathologies. L'objectif de cette thèse était donc d'étudier l'interaction entre ces formes et ces fonctions.

Nous avons étudié la croissance des cellules neuronales et gliales *in vitro* dans des microenvironnements contrôlés dans le but d'étudier la façon dont les contraintes chimiques et physiques peuvent modifier le développement des cellules. Employant des technologies de la microélectronique, comme la lithographie, nous avons réalisé la fabrication de motifs chimiques, structurels ou élastiques à l'échelle micrométrique. De cette façon, nous avons atteint un contrôle fiable et reproductible de certaines propriétés de l'environnement *in vitro*, comme la chimie, la rigidité ou la topographie, donnant accès à l'analyse d'aspects spécifiques de la croissance cellulaire. Par exemple, l'élongation et la polarisation dans le cas des neurones, et l'adhésion et la prolifération dans le cas de cellules gliales.

Neurones isolés sous contraintes chimiques

Des expériences reproductibles ont été réalisées avec des neurones d'hippocampe d'embryons de souris. Des résultats solides ont été obtenus sur des cellules isolées sur des motifs chimiques, donnant la possibilité de quantifier la réponse neuronale à des contraintes morphologiques. Notre approche géométrique a révélé qu'un seul paramètre morphologique comme la largeur des neurites pouvait diriger le processus complexe de polarisation neuronale. En effet, le contrôle de la largeur des neurites amène à une modulation de la longueur, du taux de polarisation axonale ainsi que de la localisation de l'axone. Cette étude a également montré que la cinétique de polarisation neuronale est accélérée lorsqu'une asymétrie morphologique initiale est imposée et que, contrairement à ce qui se passe dans les préparations classiques *in*

vitro, une localisation déterministe et non probabiliste de l'axone peut être obtenue. En outre, cette étude a montré que la modification de l'élongation neuritique n'est pas associée à une conservation de la surface d'adhésion. Certaines expériences exploratoires ont été menées pour étudier la conservation du volume, montrant que ce paramètre en 3D dans les neurites n'est pas systématiquement contrôlé par la largeur des neurites. D'autres analyses quantitatives de la dépendance du volume neuronale en association aux contraintes morphologiques en 2D feront l'objet de recherches à venir dans notre groupe.

Certains mécanismes à l'origine de ces résultats ont été pris en compte. Par exemple, les propriétés dynamiques de structures appelées vagues et similaires au cône de croissance qui sont produites pendant les phases de croissance et de polarisation de neurones ont été étudiées. Ces structures, déjà rapportés dans la littérature, étaient encore peu analysées. Ce travail a permis de renforcer l'association entre les vagues et l'élongation des neurites. L'influence de la largeur des neurites sur les propriétés dynamiques de vagues, telles que la fréquence d'émission et leur vitesse, a été montrée.

Nos études renforcent l'existence d'un lien entre l'élongation neuronale et l'émission des vagues. Nous avons fourni un cadre phénoménologique d'analyse des vagues pour des études moléculaires futures. Quelques études préliminaires des éléments constituants le cytosquelette, tel que l'actine, les microtubules et quelques unes de leurs protéines associées, ont montré des similitudes entre la composition moléculaire des vagues et celle du cône de croissance. Un mécanisme de propagation des vagues impliquant à la fois des moteurs moléculaires le long des microtubules et une polymérisation de l'actine n'est pas exclu. Finalement, nous proposons de nouvelles perspectives pour étudier cette question :

- ▷ L'élucidation du rôle joué par le centrosome dans la polarisation des microtubules liée à l'émission des vagues.
- ▷ Des observations à haute résolution des filaments d'actine dans les vagues. Cela pourrait donner des informations importantes sur leur dynamique et leur structure.
- ▷ Des analyses des aspects moléculaires plus approfondies employant des traitements pharmacologiques pourraient mettre en évidence les composants essentiels pour la formation et la propagation des vagues.
- ▷ L'utilisation de drogues : la blebbistatine, un inhibiteur de la myosine II, la latrunculine B ou le nocodazole, qui dépolymérisent respectivement l'actine et les microtubules, le taxol, un stabilisateur des microtubules, ou la formin, un inhibiteur des moteurs moléculaires (par exemple, il a été rapporté dans la littérature que le nocodazole induit parfois une inversion de la direction de propagation des vagues avant une désorganisation systématique de leur structure et son effondrement (Ruthel et al., 1998)).

Enfin, un rôle possible des vagues dans la ramification axonale est suggéré par l'observation rapportée dans la littérature que l'inhibition de la doublecortine, une protéine qui est coloca-

lisée avec les microtubules et observée dans les vagues, retarde le branchement des axones hippocampiques tout en diminuant la fréquence des vagues (Tint et al., 2010).

La combinaison de ces approches moléculaires avec notre contrôle de la morphologie neuronale pourrait enrichir et promouvoir la compréhension de ces questions complexes liées à la croissance neuronale et la polarisation.

Cellules neuronales et gliales sous contraintes mécaniques

La littérature fournit des données éparses et parfois contradictoires sur les propriétés mécaniques de l'environnement physiologique des cellules du cerveau et leurs conséquences sur l'adhésion et la prolifération des cellules gliales.

Nous avons donc mené une étude de la réponse des cellules gliales aux stimuli mécaniques. Nous avons montré que la sensibilité des cellules gliales aux propriétés mécaniques de leur environnement dépend des propriétés chimiques de celui-ci. Nous avons utilisé des motifs élastiques pour réaliser une analyse systématique de leur adhésion et prolifération en fonction des propriétés chimiques de leur substrat et du milieu utilisé pour les maintenir en culture *in vitro*. La chimie représente un élément essentiel pour la croissance des neurones aussi, mais aucune réponse remarquable n'a été observée en fonction des propriétés mécaniques du substrat. La présence de neurones ne semble pas avoir une influence significative sur la mécanosensibilité des cellules gliales.

La variation de la taille des motifs de rigidité a donné accès à une analyse à différentes échelles, des cellules isolées à des configurations plus collectives (avec des cellules gliales seules ou en interaction avec les neurones). Comme les meilleures conditions chimiques ne sont pas les mêmes pour les cellules neuronales et gliales, des moyens possibles pour étudier de façon plus approfondie comment la mécanosensibilité des cellules gliales est influencée par l'interaction entre ces deux types de cellules a été discutée.

Cette étude constitue une première étape phénoménologique vers une étude plus complète de la dépendance des cellules gliales aux propriétés mécaniques de leur environnement.

En conclusion, nous avons étudié la croissance des cellules neuronales et gliales avec de nouveaux dispositifs expérimentaux permettant de sélectionner les comportements de cellules spécifiques dans des microenvironnements contrôlés et à mettre l'accent sur des éléments clés ayant un rôle important dans leur croissance. Ces idées pourraient également contribuer à imaginer de nouveaux systèmes expérimentaux pour étudier le comportement des cellules du cerveau, par exemple, en conduisant à des architectures contrôlées mixtes *in vitro* de cellules gliales et neuronales.

Une approche vers des systèmes 3D, en particulier pour les cellules gliales, doit être envisagé à l'avenir pour se rapprocher du microenvironnement 3D et hétérogène de cellules *in vivo*.

Publications

Caterina Tomba, Céline Braïni, Beilun Wu, Nir S. Gov, and Catherine Villard. *Tuning the adhesive geometry of neurons: length and polarity control.* Soft Matter, 10(14):2381–2387, 2014.

Caterina Tomba, Catherine Villard. *Brain cells and neuronal networks: encounters with controlled microenvironments.* Microelectronic Engineering, invited review, 132:176–191, 2014.

Nora Dempsey, Damien Le Roy, Heidi Marelli-Mathevon, Gorky Shaw, André Dias, Roman Kramer, Mikhail Kustov, Luiz Fernando Zanini, Catherine Villard, Klaus Hasselbach, Caterina Tomba, and Frédéric Dumas-Bouchiat. *Micro-magnetic imprinting of high field gradient magnetic flux sources.* Applied Physics Letters, 104(26):262401, 2014.

Appendix A

Tables chapter IV: glial and neuronal cell densities

		PLL/LN			FN		
		Soft		Stiff	Soft		Stiff
		Soft 1 ($\sim 1\ kPa$)	Soft 2 ($< 0.5\ kPa$)	($45\ kPa$)	Soft 1 ($\sim 1\ kPa$)	Soft 2 ($< 0.5\ kPa$)	($45\ kPa$)
DMEMs	3 DIV	0.8 ± 1.9	1.1 ± 1.3	0.6 ± 1.5	0.0 ± 0.0	0.6 ± 1.8	27.9 ± 14.4
	7 DIV	31.0 ± 17.8	18.4 ± 13.5	12.3 ± 11.0	6.7 ± 6.0	0.0 ± 0.0	200.7 ± 84.6
	10 DIV	63.7 ± 25.1	48.9 ± 33.1	10.4 ± 17.0	15.9 ± 14.3	18.2 ± 34.1	336.5 ± 150.7
	14 DIV	105.8 ± 36.5	70.4 ± 36.3	23.6 ± 31.8	4.6 ± 9.0		
	17 DIV	154.2 ± 72.2	70.5 ± 33.4	28.1 ± 22.6	8.2 ± 19.0		
	21 DIV	180.0 ± 30.8		35.8 ± 7.5	0.0 ± 0.0		
NBs	3 DIV	2.7 ± 1.5	2.5 ± 3.2	0.9 ± 1.3	0.0 ± 0.0	0.3 ± 1.3	4.4 ± 6.8
	7 DIV	3.1 ± 1.8	7.5 ± 4.4	3.0 ± 2.9	0.0 ± 0.0	0.0 ± 0.0	5.5 ± 9.6
	10 DIV	6.9 ± 5.7	5.1 ± 3.4	1.3 ± 1.3	0.0 ± 0.0	0.6 ± 1.8	3.6 ± 5.3
	14 DIV	4.0 ± 3.4	0.0 ± 0.0	7.8 ± 8.9	0.0 ± 0.0	0.0 ± 0.0	10.0 ± 10.4
	17 DIV	6.9 ± 4.2	0.0 ± 0.0	8.4 ± 21.5	4.3 ± 9.9	0.0 ± 0.0	11.7 ± 11.3
	21 DIV	5.6 ± 1.0			0.0 ± 0.0		18.3 ± 2.5

Table A.1: **Glial cell density ($cells/mm^2$) in different culture conditions.** Mean value ± SD of glial cells on the soft (soft 1, $\sim 1\ kPa$, and soft 2, $< 0.5\ kPa$) and the stiff ($45\ kPa$) regions of "target" hydrogels in different conditions of medium and molecules of adhesion: PLL/LN coating or FN coating with NBs or DMEMs culture medium. Cells were observed between 3 and 21 DIV. Mean density values are calculated on a number of fields of view (surface of around $0.5\ mm^2$) varying from 4 to 12 and depending on the localization on the sample of the area of interest. This corresponds to an amount of counted cells from a few tens to more than 2000 (in the cases of high proliferation).

		PLL/LN			FN		
		Soft		Stiff	Soft		Stiff
		Soft 1 ($\sim 1\ kPa$)	Soft 2 ($< 0.5\ kPa$)	($45\ kPa$)	Soft 1 ($\sim 1\ kPa$)	Soft 2 ($< 0.5\ kPa$)	($45\ kPa$)
DMEMs	3 DIV	1.9 ± 6.0	2.6 ± 2.8	0.9 ± 1.6	0.0 ± 0.0	0.0 ± 0.0	3.1 ± 3.1
	7 DIV	11.4 ± 8.2	1.7 ± 1.4	2.8 ± 5.3	0.0 ± 0.0	0.0 ± 0.0	4.3 ± 2.2
	10 DIV	0.7 ± 0.9	0.4 ± 1.2	0.5 ± 1.1	0.0 ± 0.0	0.0 ± 0.0	1.9 ± 3.1
	14 DIV	3.2 ± 2.0	0.0 ± 0.0	0.0 ± 0.0	0.0 ± 0.0		0.0 ± 0.0
	17 DIV	1.5 ± 3.4	0.0 ± 0.0	0.0 ± 0.0	0.0 ± 0.0		0.0 ± 0.0
	21 DIV	0.0 ± 0.0		2.7 ± 1.2	0.0 ± 0.0		
NBs	3 DIV	88.8 ± 21.0	65.5 ± 51.4	51.6 ± 22.5	1.5 ± 4.4	0.0 ± 0.0	3.0 ± 8.4
	7 DIV	90.7 ± 14.5	77.5 ± 49.7	38.1 ± 21.3	0.0 ± 0.0	0.0 ± 0.0	0.0 ± 0.0
	10 DIV	89.4 ± 26.6	73.6 ± 57.8	51.4 ± 40.1	0.0 ± 0.0	0.0 ± 0.0	0.0 ± 0.0
	14 DIV	72.0 ± 22.6	72.7 ± 19.7	68.4 ± 47.1	0.0 ± 0.0	0.0 ± 0.0	0.0 ± 0.0
	17 DIV	76.0 ± 21.3	87.2 ± 3.5	45.2 ± 25.3	0.0 ± 0.0	0.0 ± 0.0	0.0 ± 0.0
	21 DIV	81.7 ± 12.6			0.0 ± 0.0		0.0 ± 0.0

Table A.2: **Neuron density ($cells/mm^2$) in different culture conditions.** Mean value ± SD of neurons on the soft (soft 1, $\sim 1\ kPa$, and soft 2, $< 0.5\ kPa$) and the stiff ($45\ kPa$) regions of "target" hydrogels in different conditions of medium and molecules of adhesion: PLL/LN coating or FN coating with NBs or DMEMs culture medium. Cells were observed between 3 and 21 DIV. Means density values are calculated on a number of fields of view (surface of around 0.5 mm^2) varying from 4 to 12 and depending on the localization on the sample of the area of interest. This corresponds to an amount of counted cells from a few tens to some hundreds (in the cases of high adhesion and survival).

			DMEMs		NBs
			PLL/LN	FN	FN
Soft	Soft 1 ($\sim 1\ kPa$)	2 DIV	7.2 ± 6.4	1.7 ± 3.7	3.5 ± 5.8
		6 DIV	21.7 ± 20.6	1.2 ± 2.6	1.4 ± 1.9
		8 DIV	33.5 ± 28.0	0.0 ± 0.0	0.0 ± 0.0
		13 DIV	30.0 ± 18.9	0.0 ± 0.0	0.9 ± 1.9
		17 DIV	31.7 ± 17.9	0.0 ± 0.0	0.8 ± 1.7
	Soft 2 ($< 0.5\ kPa$)	2 DIV	7.0 ± 8.7	0.0 ± 0.0	0.0 ± 0.0
		6 DIV	15.7 ± 14.1	0.0 ± 0.0	0.3 ± 0.7
		8 DIV	19.2 ± 25.6	0.0 ± 0.0	0.0 ± 0.0
		13 DIV	31.9 ± 23.2	0.0 ± 0.0	0.0 ± 0.0
		17 DIV	26.2 ± 14.3	0.0 ± 0.0	0.0 ± 0.0
Stiff ($45\ kPa$)		2 DIV	0.0 ± 0.0	23.9 ± 25.0	32.4 ± 28.1
		6 DIV	0.2 ± 0.5	54.2 ± 39.3	46.2 ± 33.7
		8 DIV	0.0 ± 0.0	74.3 ± 44.6	36.6 ± 27.6
		13 DIV	0.0 ± 0.0	56.8 ± 37.4	34.1 ± 27.8
		17 DIV	1.5 ± 3.8	55.0 ± 35.3	31.1 ± 26.5

Table A.3: **Glial cell density ($cells/mm^2$) in different culture conditions.** Mean value ± SD of glial cells on the soft (Soft 1, $\sim 1\ kPa$, and Soft 2, $< 0.5\ kPa$) and the stiff ($45\ kPa$) regions of "target" hydrogels in different conditions of medium and molecules of adhesion: PLL/LN coating or FN coating with NBs or DMEMs culture medium. Cells were observed between 2 and 17 DIV. Mean values are calculated on a number of fields of view (surface of around 0.5 mm^2) varying from 4 to 12 and depending on the localization on the sample of the area of interest. This corresponds to an amount of counted cells from a few tens to some hundreds (in the cases of high proliferation).